UNIVERSITÉ PIERRE ET MARIE CURIE - PARIS VI
Ecole Doctorale de Paris Centre - UFR 929
Laboratoire Jacques-Louis Lions

Modélisation, simulation et assimilation de données autour d'un problème de couplage hydrodynamique-biologie

Thèse pour obtenir le grade de

Docteur de l'Université Pierre et Marie Curie
(Spécialité Mathématiques Appliquées)

présentée et soutenue par

Anne-Céline BOULANGER

le 13 Septembre 2013 devant le jury composé de

Christophe Berthon	Professeur	Rapporteur
Tomas Chacon Rebollo	Professeur	Rapporteur
Olivier Bernard	Directeur de recherche	Examinateur
Marie-Odile Bristeau	Directeur de recherche	Examinateur
Edwige Godlewski	Professeur	Examinateur
Philippe Moireau	Chercheur	Examinateur
Benoit Perthame	Professeur	Directeur
Jacques Sainte-Marie	Directeur de Recherche	Directeur

Année 2013 Université Pierre et Marie Curie

Remerciements

Je tiens d'abord à remercier mes deux directeurs de thèse pour le sujet passionnant qu'ils m'ont proposé, ainsi que la liberté qu'ils m'ont accordée pour m'y épanouir pleinement.

Jacques Sainte-Marie m'a initiée avec beaucoup d'enthousiasme au monde des équations hydrodynamiques à surface libre et à leurs nombreuses applications. Je le remercie de m'avoir fait voyager en dehors des frontières pour découvrir cette communauté mathématique dans laquelle je m'inscris, mais aussi de sa présence et de son soutien sans faille.

Encouragée par Benoit Perthame, je me suis plongée dans la théorie cinétique des lois de conservation. Malgré ses nombreuses obligations, il a su me consacrer un temps incroyablement précieux afin de me guider à la fois dans ma recherche mais aussi dans mes choix pour l'après-thèse. Pour cela je lui en suis extrêmement reconnaissante.

Je tiens ensuite à remercier chaleureusement Christophe Berthon et Tomas Chacon Rebollo pour avoir accepté d'endosser le rôle de rapporteur de ma thèse. Leurs conseils et remarques avisés m'ont permis de grandement améliorer ce manuscrit. Je suis également très heureuse qu'Olivier Bernard, Marie-Odile Bristeau, Edwige Godlewski et Philippe Moireau me fassent l'honneur de participer à mon jury.

C'est avec Olivier Bernard que j'ai découvert la problématique des biocarburants à base de microalgues, c'est grâce à Marie-Odile Bristeau que le développement d'un code 3D n'a plus de secrets pour moi, et enfin, c'est avec Philippe Moireau que mon intérêt pour l'assimilation de données s'est développé. Pour cela, je leur adresse tous trois un second remerciement.

Même si le travail qui en a découlé n'apparaît pas dans ce manuscrit, je souhaite remercier Clément Cancès, Hélène Mathis et Nicolas Seguin de m'avoir accueillie dans leur projet de recherche au Cemracs 2011 et de m'avoir expliqué avec beaucoup de patience ce qu'était un schéma Asymptotic Preserving. J'ai trouvé le sujet captivant et j'ai énormément apprécié cette collaboration.

Merci aux membres du laboratoire Jacques-Louis Lions et de l'INRIA de m'avoir permis d'effectuer ma thèse dans un environnement d'excellence, stimulant et chaleureux. Merci à mes camarades du bureau 301 tout d'abord, pour l'ambiance studieuse mais décontractée qui y régnait : Charles, Dorian, Guilhem, Haidar, Long, Mamadou, Nicole, Rahma, Sara, Sylvain et Vincent. Merci au bureau 324, le fameux : Benjamin, Magali, Quang, Stéphanie et Wafaâ, et j'ose y ajouter Ib'. Merci aussi à tous les autres : Paul, Justine, Juliette... et

j'en oublie tant, avec qui j'ai partagé repas et pauses café ! Je ne saurais m'arrêter sans remercier de tout coeur les membres ou ex-membres du bâtiment 16 : Annabelle, Anne-Claire, Asven, Cristobal, Emanuele, François, Frédérique, Grégory, Luna, Nick, Saverio, William... Nombreux sont les gens sus-nommés qui sont maintenant des amis.

Merci à mes amis (les autres) d'avoir été là, physiquement ou moralement (oui parce que les ingés ça voyage beaucoup !) pour parsemer ma vie de moments de bonheur et de détente inoubliables. Parmi les plus présents, je dois citer sans les nommer un certain groupe qui s'est doté du nom étrange Télavion ainsi que la joyeuse bande de l'ENSTA. J'ai une pensée particulière pour toi, Marion, pour nos discussions existentielles profondes (du moins le croit-on), loin des contingences vulgaires de l'existence...

Merci à ma famille, qui a toujours été d'un soutien inconditionnel, malgré le mystère profond qui subsiste autour de mon goût pour les mathématiques. Je pense à mes parents, que j'aime énormément et qui me prennent sans hésiter dans leurs valises quand j'ai besoin de changer d'air. Je pense à mon très cher frère Valentin (BBE), à nos fous rires et à nos retrouvailles express, à Lille, Paris, Marseille, Bordeaux ou ailleurs...et que je remercie surtout d'avoir relu mon introduction...ou pas ! Et enfin je pense à mes chers cousins et cousines Astrid (Objection !), Boris, Luis et Félix, grâce à qui les réunions de famille sont toujours emplies de joie de vivre ! Vous êtes un peu ma madeleine de Proust.

Mes derniers remerciements sont pour Raphaël, qui a l'immense tâche de me supporter au quotidien. Merci pour ton soutien, ta patience et ton optimisme, alors même que tu traversais, en même temps que moi, les périodes de joie et de doutes inhérentes à l'entreprise de la thèse. Sans toi, rien de tout cela n'aurait eu la même saveur, et j'ai l'audace de croire que la réciproque est vraie.

Abstract

This thesis is built around a biological and industrial problem: the simulation of the coupling of hydrodynamics and biology in the context of industrial microalgae culture in outdoor raceways. The numerical modeling is addressed with the use of a multilayer vertical discretization of hydrostatic Navier-Stokes equations coupled with a light sensitive Droop model. Numerically, kinetic schemes allow for the development of efficient, positivity preserving, well balanced and entropy satisfying schemes. Simulations are carried out in 2D and 3D. From a practical point of view, this model is capable of accounting for the utility of a paddlewheel and exhibits Lagrangian trajectories underwent by algae. Hence providing hints on the light history of algae in the pond, which is a key information to biologists, since it enables them to adapt their phytoplankton growth models to those particular, non natural conditions.

In order to validate the models and strategies, two solutions are explored. The first one consists in providing analytical solutions to free surface Euler equations. Besides, a specific biological model is designed to permit an analytical coupling. The second one is the use of data assimilation. In order to take advantage of the kinetic description of conservation laws already used for the building of efficient schemes, an innovative data assimilation method for hyperbolic balance laws based in a Luenberger observer on the kinetic equation is developed. It provides a nice theoretical framework for scalar conservation laws, for which we study the cases of complete observations, partial observations in space, in time, and noisy observations. As far as systems are concerned, we focus on the Saint-Venant system, which is hyperbolic, nonlinear and has a topographic source term. We build an observer based only on water depths measurements. Numerical simulations are provided in the case of scalar laws and systems, in one and two dimensions, which validate the efficiency of the method.

Keywords: free surface Navier-Stokes equations, multilayer model, hydrodynamics-biology coupling, Droop model, finite volumes, kinetic schemes, data assimilation, kinetic formulation of conservation laws, Luenberger observer, nudging.

Résumé

Les sujets abordés dans cette thèse s'articulent autour de la modélisation numérique du couplage entre l'hydrodynamique et la biologie pour la culture industrielle de microalgues dans des raceways. Ceci est fait au moyen d'un modèle multicouches qui discrétise verticalement les équations de Navier-Stokes hydrostatiques couplé avec un modèle de Droop photosensible pour représenter la croissance des algues, notamment la production de carbone. D'un point de vue numérique, une méthode volumes finis avec schémas cinétiques est appliquée. Elle permet d'obtenir un schéma équilibre qui préserve la positivité de la hauteur d'eau et des quantités biologiques et qui satisfait une inégalité d'énergie. Des simulations sont effectuées en 2D et en 3D, au moyen d'un code C++ développé à cet effet. Du point de vue de l'intérêt pratique de ce travail, ces simulations ont permis de mettre en évidence l'utilité de la roue à aube présente dans les raceways, mais aussi d'exhiber les trajectoires lagrangiennes réalisées par les microalgues, qui permettent de connaitre l'historique lumineux des algues, information d'une grande importance pour les biologistes car elle leur permet d'adapter leurs modèles de croissance phytoplanctoniques à ce contexte très particulier et non naturel. Afin de valider les modèles et les stratégies numériques employées, deux pistes on été explorées. La première consiste à proposer des solutions analytiques pour les équations d'Euler à surface libre, ainsi qu'un modèle biologique spécifique permettant un couplage analytique. La deuxième consiste à faire de l'assimilation de données. Afin de tirer partie de la description cinétique des lois de conservation hyperboliques, une méthode innovante basée sur la construction d'un observateur de Luenberger au niveau cinétique est développée. Elle permet d'obtenir un cadre théorique intéressant pour les lois de conservation scalaires, pour lesquelles on étudie les cas d'observations complètes, partielles en temps, en espace, et bruitées. Pour les systèmes, on se concentre particulièrement sur le système de Saint-Venant, système hyperbolique non linéaire et un observateur basé sur l'observation des hauteurs d'eau uniquement est construit. Des simulations numériques dans les cas scalaires et systèmes, en 1D et 2D sont effectuées et valident l'efficacité de la méthode.

Keywords: équations de Navier-Stokes à surface libre, modèle multicouches, couplage hydrodynamique - biologie, modèle de Droop, volumes finis, schémas cinétiques, assimilation de données, formulation cinétique des lois de conservation, observateur de Luenberger, nudging.

Contents

List of Figures

List of Publications

The work done during this Ph.D. lead to the following publications.

Peer-reviewed articles

- Analytical solutions for the free surface hydrostatic Euler equations. A.-C. Boulanger, M.-O. Bristeau, J. Sainte-Marie. Com. in Math. Sci., 11(4):993-1010, 2013.

- A 2D model for hydrodynamics and biology coupling applied to algae growth simulations. O.Bernard, A.-C. Boulanger, M.-O. Bristeau, J. Sainte-Marie. M2AN, 2013. doi: http://dx.doi.org/10.1051/m2an/2013072

- Data Assimilation for hyperbolic conservation laws. A Luenberger observer approach based on a kinetic description. A.-C. Boulanger, P. Moireau, B. Perthame, J. Sainte-Marie, 2013. Submitted.

Proceedings

- OSAMOAL: Optimized Simulations by Adapted MOdels using Asymptotic Limits. A.-C. Boulanger, C. Cancès, H. Mathis, K. Saleh, N. Seguin. ESAIM Proceedings, 38:183-201, 2012. doi: http://dx.doi.org/10.1051/proc/201238010

1 Introduction (Français)

Non-French speakers please go directly to Chapter 2, an english version of the introduction is provided there.

1.1 Acteurs du projet

L'idée de cette thèse est née du constat suivant : dans les océans aussi bien que dans les retenues lacustres ou encore les "raceways" industriels, la prise en compte du couplage entre l'hydrodynamique et la biologie est un enjeu essentiel car de nombreux phénomènes sont directement influencés par ce couplage - flux de carbone, eutrophisation, migration ou croissance de certaines espèces biologiques. Le caractère multi-échelles du système couplé et la nécessaire utilisation de modèles et méthodes sophistiqués pour sa résolution numérique rendent ce couplage délicat à traiter. Il nécessite aussi la collaboration entre mathématiciens, biologistes et océanographes, ce dont j'ai pu bénéficier durant ces trois années. Bien sûr, de par ma formation d'ingénieur en mathématiques appliquées, la couleur de cette thèse sera clairement plus mathématique.

J'ai donc effectué mon doctorat sous la direction de Benoit Perthame et Jacques Sainte-Marie au sein du projet Ange - auparavant intégré à Bang-, une équipe commune CETMEF - INRIA - CNRS/UPMC. Les activités de recherche de ce groupe sont principalement dédiées à la simulation numérique d'écoulements géophysiques à surface libre, comme les rivières, les lacs ou les zones côtières. J'ai également collaboré avec des scientifiques d'autres domaines, notamment des ingénieurs et des biologistes. Je cite entre autres Olivier Bernard et Antoine Sciandra, de l'équipe Biocore (équipe conjointe INRIA, INRA et CNRS/UPMC) de Villefranche sur Mer, spécialistes de la croissance du phytoplancton. Mais aussi Bruno Sialve, ingénieur de recherche chez Naskéo, une entreprise spécialisée en méthanisation qui a bâti un raceway expérimental à l'INRA de Narbonne, et grâce à

qui nous avons eu accès à des données expérimentales. Ces scientifiques sont maintenant membres d'un Institut d'Excellence sur les Energies Décarbonées nommé GreenStars et qui regroupe de nombreux acteurs de la filière de valorisation des micro-algues.

1.2 Contexte du problème

1.2.1 Contribution à l'étude des écoulements géophysiques

Histoire des modèles d'écoulements géophysiques Alors que l'année 2013 a été déclarée par l'UNESCO *Année des Mathématiques de la planète Terre*[1], nous voudrions que cette thèse s'inscrive comme contribution au vaste champ de l'étude des écoulements géophysiques gravitaires. Sans rentrer dans les détails qui seront donnés Section 1.5.1, ce paragraphe a pour but de rappeler les avancées scientifiques historiques dans ce domaine, les défis actuels et d'y situer notre travail.

Pour les présenter brièvement, les écoulements géophysiques sont communément représentés par les équations de la mécanique des fluides incompressibles à surface libre: les équations d'Euler [46, 139], proposées en 1757 dans l'ouvrage *Principes généraux du mouvement des fluides* ou de Navier-Stokes [137], décrites en 1840. Les secondes peuvent être vues comme un extension des premières au cas de fluides visqueux. Néanmoins, dans le cas d'écoulements géophysiques, lorsque le fluide considéré est l'eau (écoulement de rivières, lacs, océans), les effets visqueux, bien que présents, ont une importance faible en comparaison des phénomènes de convection ou de pression. Aussi, on peut considérer que les équations d'Euler représentent bien la dynamique des fluides géophysiques. Une partie de ce travail de thèse leur est d'ailleurs dévouée, qui consistera à proposer des solutions analytiques nouvelles dans le but essentiel de valider des codes de calcul. Cependant, les dimensions caractéristiques des problèmes étudiés justifient l'utilisation de modèles plus simples que ceux précédemment cités, tant au niveau de l'analyse mathématique que pour l'aspect numérique. En effet, la présence récurrente d'une surface libre dans ce type d'écoulements complique grandement la simulation (topologie du domaine variante, maillage mobile requis). Parmi les modèles simplifiés qui permettent un traitement plus aisé de la surface libre, les plus importants sont ceux décrivant les écoulements peu profonds. C'est en ce sens qu'un troisième système d'équations fait son apparition en 1871, le système de Saint-Venant [19]. Ce système peut être retrouvé à partir des équations d'Euler sur la base de deux hypothèses [61] :

Hypothèse (1) : la vitesse horizontale du fluide est bien représentée par sa moyenne selon la direction verticale,

Hypothèse (2) : la pression du fluide est hydrostatique.

Il présente de nombreux avantages dans les problèmes d'écoulements à surface libre, car il permet de simuler un problème tridimensionnel sur un domaine variable en temps à l'aide

[1] http://mpe2013.org/

d'un système bidimensionnel posé sur un domaine instationnaire. L'analyse mathématique et numérique des équations de Saint-Venant, qui nécessite des outils de la théorie des lois de conservation hyperboliques, n'est pas triviale. Néanmoins, bien que certaines questions restent ouvertes (préservation d'équilibres non triviaux, entropie discrète des schémas), les enjeux et besoins sont ailleurs. Ils proviennent notamment de la volonté de s'affranchir de l'hypothèse restrictive (1) qui ne permet pas de représenter des écoulements stratifiés et de se rapprocher ainsi plus précisément des équations d'Euler ou de Navier-Stokes. Les premiers modèles qui apparaissent sont de type multi-couches et décrivent le fluide comme une superposition de systèmes de Saint-Venant [2, 30]. Mais cette modélisation revient à considérer chaque couche comme étant constituée d'un fluide non-miscible et s'avère donc trop limitée. Une approche voisine [9, 10], que nous utiliserons dans cette thèse, consiste en une décomposition de type Galerkin selon la verticale de toutes les variables du problèmes (vitesse horizontale, verticale, hauteur d'eau) de Navier-Stokes hydrostatique, suivi d'une intégration sur chaque couche. Les variables sont alors constantes par couche et non plus uniformes sur toute la hauteur et permettent de retrouver une hétérogénéité selon la verticale. Enfin, un autre type de modèle consiste à réintégrer l'accélération verticale pour se défaire non pas de l'hypothèse (1), mais de l'hypothèse (2) [36, 37]. Ces derniers modèles représenteront mieux le déferlement de tsunami près des côtes par exemple.

Couplages Les problèmes rencontrés dans les géosciences font naturellement apparaitre des couplages. Il peut s'agir d'un couplage entre fluides miscibles mais stratifiés par leur densité (eau froide, eau chaude), d'un couplage entre un fluide et une structure (vague contre une digue), ou d'un couplage entre un fluide et une quantité biologique (algues). Les préoccupations liées au développement durable font émerger d'importantes questions qui relèvent des mathématiques appliquées et qui impliquent la modélisation de ces couplages. Parmi les secteurs d'activité en plein essor, on peut citer les énergies marines, qui vont chercher à produire de l'électricité en récupérant l'énergie des vagues, des marées, des courants, au moyen d'hydroliennes ou en optimisant la bathymétrie d'un domaine géométrique. On peut mentionner aussi l'étude d'écosystèmes lacustres face aux forçages atmosphériques, climatiques ou à la pollution, qui permettent de mieux comprendre les phénomènes d'eutrophisation. Enfin, et c'est ce qui nous intéressera dans cette thèse, la culture de micro-algues est aussi très en vogue. Certaines espèces à forte teneur en lipides pourraient conduire à la production de biocarburants de troisième génération avec des rendements beaucoup plus importants que ceux de première et deuxième génération, fabriqués à partir de plantes supérieures. La modélisation de l'hydrodynamique du bassin de culture et de son couplage avec la biologie est capitale pour ce type de projets. Comme il sera exprimé plus tard dans ce travail, une grande hétérogénéité règne dans le bassin, du fait notamment d'un gradient d'intensité lumineuse très prononcé. Nous devons donc ici modéliser un problème d'écoulement à surface libre avec des inhomogénéités verticales non négligeables (ce qui exclut une modélisation de type Saint-Venant) contenant un modèle biologique de réaction-diffusion. Tout ceci en prenant en compte le fait que les constantes temporelles de la biologie sont bien plus élevées que celles de l'hydrodynamique et qu'une simulation typique est de l'ordre de

plusieurs jours. Il faut donc être efficace du point de vue du temps de calcul. Les modèles distribués sur la verticale présentés au paragraphe précédent permettront d'appréhender de manière adéquate ce problème.

Validation En géosciences, les phénomènes physiques sont abondants. En effet, même si nous n'avons évoqué que les problèmes faisant intervenir l'eau, les écoulements géophysiques peuvent aussi impliquer des fluides plus denses telles les phénomènes d'avalanche, de glissements de terrain, d'éruptions volcaniques. Cette multitude de phénomènes donne naissance à une multitude de modèles qu'il faut juger à la fois à la manière dont ils ont été dérivés au niveau continu, mais aussi à leur capacité à reproduire des données. Une fois le modèle choisi et validé, il est intéressant d'exploiter son caractère prédictif. Dans ce contexte, on est amené à s'intéresser à l'assimilation de données, qui permet d'améliorer les prédictions en utilisant les observations passées. Lorsqu'on étudie des systèmes à dominante hyperbolique non linéaire, comme le système de Saint-Venant, de nombreuses questions scientifiques restent ouvertes dans ce domaine, que nous aborderont de manière générale dans une partie de cette thèse.

A travers les précédents paragraphes, nous espérons avoir mis en perspective la place de ce travail de thèse dans le cadre des écoulements géophysiques et explicité son fil conducteur. Plongeons-nous maintenant plus spécifiquement dans les arcanes du problème de l'aquaculture destinée à la production de biocarburants.

1.2.2 Des objectifs européens

En décembre 2008, l'UE est parvenue à trouver un accord sur les énergies renouvelables : avant 2020, 10% des besoins en carburant dans le domaine des transports devront être satisfaits par des combustibles verts, de l'hydrogène ou de l'électricité verte. De plus, la directive précisait que le jour où elle entrerait en vigueur, les membres de l'UE devraient vérifier que la proportion de biocarburant utilisée permet une réduction de 35% des émissions de carbone par rapport à une utilisation d'énergie fossile. Cette réduction devrait atteindre 50% en 2017, 60% en 2018.

Derrière ces conditions, on perçoit l'inquiétude grandissante envers les biocarburants de première génération dérivés de sources telles que le sucre, les graisses animales ou les huiles végétales. Cependant, l'éthanol et le biodiesel ainsi produits sont accusés de faire s'envoler les cours alimentaires et de menacer la biodiversité. C'est pourquoi l'UE s'est tournée vers les biocarburants de deuxième génération. Ceux-ci sont obtenus par transformation de la lignocellulose des plantes. Alors que celles-ci sont composées de lignine et de cellulose, les technologies des biocarburants de deuxième génération permettent de séparer ces deux composants. La cellulose fermente alors pour donner de l'alcool. Quant à la lignine, elle est transformée en sucres, mais sa conversion requiert des technologies chères et encore non optimales. Pour cette raison, la deuxième génération n'est pas censée remplacer la première avant 2020.

Récemment, l'intérêt grandit pour les biocarburants de troisième génération, élaborés à

base d'algues.

1.2.3 Aquaculture

Les micro-algues et les cyanobactéries sont des organismes vivants dont la taille varie de 1 à 100 microns et que l'on trouve en abondance dans les lacs, les rivières, les océans. Il est couramment admis qu'il y a plus d'un million d'espèces d'algues. En comparaison, on ne compte de 250 000 plantes dites supérieures. Elles utilisent la lumière comme source d'énergie afin de fixer le dioxyde de carbone. Quelques espèces sont capables de stocker ce carbone sous forme de lipides. Par ailleurs, les espèces autotrophes n'ont besoin que de carbone inorganique pour croître. C'est la raison pour laquelle il est possible de les considérer comme une source potentielle de biocarburant. En 1973, le National Renewable Energy laboratory (NREL) avait commencé des études pour évaluer le potentiel de ce type de carburant. Mais le prix du baril de prétrole, 5 fois moins cher à l'époque, avait conduit à abandonner tout projet.

Un fort taux de croissance Une des caractéristiques principales des micro-algues est leur haut rendement photosynthétique. Défini comme le ratio entre l'énergie lumineuse incidente et l'énergie réellement stockée dans la plante, il est estimé qu'en conditions optimales, 10 moles de photons sont nécessaires pour fixer 1 mole de $C0_2$. Si ce ratio n'est pas différent d'autres espèces végétales, il parait plus facile de trouver les conditions optimales pour des micro-organismes vivant sous l'eau.

Synthèse des lipides Comme mentionné précédemment, les micro-algues et les cyanobactéries contiennent des lipides habituellement en proportions faibles. Néanmoins, il a été montré que quelques candidats sont capables d'augmenter considérablement leur production si elles sont soumises à certains stress, comme par exemple une privation d'azote ou des chocs thermiques. Ainsi, le niveau de lipide intrinsèque peut atteindre 80% de la matière sèche. Bien sûr, ces conditions de stress ne peuvent être appliquées impunément sans inhiber la croissance. Il faut donc trouver un compromis entre une croissance calme (multiplication des algues) et une croissance sous contraintes (production de lipides). Pour le moment, une proposition en deux temps a été faite : une croissance-multiplication des algues dans un photobioréacteur (Figure 1.1, à gauche) suivie des quelques jours en raceway (Figure 1.1, à droite), dans des conditions de manque d'azote.

Récolte et purification La récolte est une étape limitante pour la production de biocarburant. Les algues ne mesurent en effet que quelques microns et ont une densité proche de celle de l'eau. Il est possible pour certaines espèces d'utiliser des techniques de filtration, mais pour la plupart, la centrifugation est nécessaire. Cette étape est malheureusement très coûteuse en énergie. Ensuite, une fois la récolte effectuée, d'autres techniques doivent extraire les lipides. La plupart de ces méthodes utilisent actuellement des solvants, mais les chercheurs tentent d'en trouver de nouvelles.

Figure 1.1: Gauche: Photobioréacteur à IFREMER. Droite: Un raceway industriel (Innovalg, 85). Photo IFREMER.

Barrières actuelles Actuellement, certaines barrières doivent être levées pour permettre une large production de biocarburant à base de micro-algues. Nous en citons ici quelques unes :

- les micro-algues ne supportent pas un ensoleillement trop élevé, ni une chaleur ou un froid trop intenses. Les rendements théoriques attendus sont donc difficiles à atteindre. De plus, certains pays subissant des températures extrêmes ne pourront pas développer ces techniques.
- Comment optimiser le compromis croissance des algues *versus* synthèse de lipides ?
- D'importants coûts nécessitent d'être diminués, notamment les apports en vitamines et oligo-éléments, l'apport de nutriments tel que l'azote, mais aussi la récolte et l'extraction des lipides.
- Les risques de contamination dans le cas des raceways extérieurs sont grands.

Nous nous donnons donc pour objectif une modélisation du couplage hydrodynamique-biologie dans le cadre de la culture de micro-algues en raceway. Pour cela, nous choisissons un modèle hydrodynamique, qui est une discrétisation verticale des équations Navier-Stokes hydrostatiques, et un modèle biologique, le modèle de Droop, augmenté d'une dépendance à la lumière incidente.

1.3 Plan de la thèse

Le thème de départ de ce travail était donc l'étude du couplage hydrodynamique-biologie, dans le cas de la culture d'algues. Afin de mener à bien une modélisation correcte du

problème, plusieurs directions ont été envisagées dans cette thèse. Car une fois le modèle trouvé, le code développé et les résultats numériques obtenus, il est nécessaire de valider d'une part la partie schéma numérique à travers des solutions analytiques, et d'autre part la partie modèle à travers l'assimilation de données. La première partie de ce manuscrit, constituée du Chapitre 3 et résumée dans la Section 1.4 est consacrée à la recherche de solutions analytiques à la fois pour l'hydrodynamique à surface libre, modélisée par les équations d'Euler hydrostatiques, mais aussi pour la biologie, à l'aide d'un modèle simple de transport-réaction. Cette étude nous a permis de valider d'une part le code hydrodynamique qui a été produit par la suite, et d'autre part la méthode de couplage que nous utilisons. Ce travail a fait l'objet d'un article publié dans CMS.

La deuxième partie de la thèse, constituée des Chapitres 4 et Chapitre 5 et résumée dans la Section 1.5, traite de la modélisation et de la simulation du problème d'aquaculture dans les raceways. En deux dimensions, une étude complète a été menée et publiée dans M2AN. En trois dimensions, un code C++ a été développé, qui a permis d'avoir quelques résultats préliminaires encourageants. Ce code est d'ailleurs maintenu et étendu par Raouf Hamouda, ingénieur INRIA, afin de rester un outil phare dans l'équipe Ange.

Enfin, la troisième partie, composée du Chapitre 6 et résumée dans la Section 1.6 s'articule autour du thème de l'assimilation de données pour les lois de conservation hyperboliques. En exploitant les techniques de description cinétique de ces lois, on est capable de proposer une technique innovante en assimilation de données, construite autour d'un observateur de Luenberger. Ce travail fait l'objet d'une publication.

1.4 Solutions analytiques des équations d'Euler à surface libre

1.4.1 Etat de l'art

Les modèles mathématiques émanant de la dynamique des fluides, bien souvent issus des célèbres équations de Navier-Stokes, sont globalement complexes à analyser, aussi bien sur le plan analytique que numérique. Cela soulève des difficultés quand vient l'heure de valider des schémas numériques. Une solution intéressante, même si elle n'a pas valeur de preuve, est de confronter les simulations avec des solutions analytiques sur des cas tests. Dans le but d'étudier un couplage entre l'hydrodynamique et la biologie dans un bassin industriel, nous nous sommes attelés tout d'abord à la recherche de solutions analytiques aux équations d'Euler hydrostatiques et incompressibles à surface libre. Celles-ci correspondent en effet à une version non visqueuse des équations de Navier-Stokes, qui correspondent donc bien, comme rappelé précédemment, à des écoulements géophysiques. Puis nous avons cherché à obtenir un système biologique simple pour lequel le couplage analytique serait aussi possible.

En dynamique des fluides, de nombreux travaux portent sur une version simplifiée des équations de Navier-Stokes incompressibles dans le cadre d'écoulements en eau peu profonde. On l'appelle le système de Saint-Venant. Ce système hyperbolique non linéaire admet de par sa nature des solutions non régulières qui peuvent présenter des chocs. Il

est par conséquent nécessaire d'être capable de construire des schémas numériques qui capturent ces chocs. Dans le but de vérifier ce point, MacDonalds [99, 100] propose un ensemble de solutions analytiques présentant un ressaut hydraulique lors du passage d'un écoulement fluvial à un écoulement torrentiel. Nous suivrons d'ailleurs sa méthode pour obtenir des solutions stationnaires au problème d'Euler à surface libre au Chapitre 3. Nous pouvons aussi citer les travaux sur l'équation de Korteweg-de-Vries, qui modélise la propagation d'ondes en eau peu profonde. Cette équation admet des solutions exactes de type soliton [85]. Ces modèles étant plutôt valables en eau peu profonde, les travaux qui suivent permettent d'étendre ces outils à des solutions plus hétérogènes sur la dimension verticale. Néanmoins, ces solutions ne correspondent pas à des cas pratiques d'utilisation de ce modèle et sont en réalité destinées à la validation de schémas numériques.

1.4.2 Le système d'Euler incompressible à surface libre

Rappelons tout d'abord les équations d'Euler hydrostatiques et incompressibles à surface libre [34, 66] soumises à la gravité

$$\frac{\partial u}{\partial x} + \frac{\partial v}{\partial y} + \frac{\partial w}{\partial z} = 0, \tag{1.1}$$

$$\frac{\partial u}{\partial t} + u\frac{\partial u}{\partial x} + v\frac{\partial u}{\partial y} + w\frac{\partial u}{\partial z} + \frac{\partial p}{\partial x} = 0, \tag{1.2}$$

$$\frac{\partial v}{\partial t} + u\frac{\partial v}{\partial x} + v\frac{\partial v}{\partial y} + w\frac{\partial v}{\partial z} + \frac{\partial p}{\partial y} = 0, \tag{1.3}$$

$$\frac{\partial p}{\partial z} = -g, \tag{1.4}$$

où z représente la direction verticale. On considère ce système pour

$$t > 0, \quad (x, y) \in \Omega, \quad z_b(x, y) \leq z \leq \eta(x, y, t),$$

où Ω est un domaine borné de $\mathbb{R}^2$, $\eta(x, y, t)$ est l'élévation de la surface libre, $\mathbf{u} = (u, v, w)^T$ le vecteur vitesse. L'accélération gravitationnelle est notée g et p est la pression du fluide, tandis que z_b représente la topographie. Ainsi, la hauteur d'eau s'écrit $H = \eta - z_b$. Le système (1.1)-(1.4) est complété par des conditions aux bords. A la surface, on impose une condition cinématique (l'indice s ci-dessous signifiant que les variables sont prises à la surface),

$$\frac{\partial \eta}{\partial t} + u_s\frac{\partial \eta}{\partial x} + v_s\frac{\partial \eta}{\partial y} - w_s = 0, \tag{1.5}$$

ainsi qu'une condition d'équilibre avec la pression atmosphérique

$$p_s = p^a(x, y, t), \tag{1.6}$$

et au fond une condition de non pénétration du fluide (l'indice b ci-dessous signifiant que les variables sont prises au fond),

$$u_b \frac{\partial z_b}{\partial x} + v_b \frac{\partial z_b}{\partial y} - w_b = 0. \tag{1.7}$$

1.4.3 Solutions analytiques pour l'hydrodynamique

On se place dans le cadre stationnaire 2D, le domaine horizontal étant $\Omega = [0, L_x]$. Dans ce cas, les solutions satisfont :

$$\frac{\partial}{\partial x} \int_{z_b}^{\eta} u \; dz = 0, \tag{1.8}$$

$$w = -\frac{\partial}{\partial x} \int_{z_b}^{z} u \; dz, \tag{1.9}$$

$$u \frac{\partial u}{\partial x} + w \frac{\partial u}{\partial z} + g \frac{\partial \eta}{\partial x} = -\frac{\partial p^a}{\partial x}. \tag{1.10}$$

Solutions régulières stationnaires générales

La méthode est la suivante : on se donne une hauteur d'eau, un champ de vitesse admissible et on cherche la topographie qui correspond à la résolution du système d'Euler à surface libre. On peut alors trouver une famille de solutions régulières :

Proposition 1.4.1 (B., Bristeau, Sainte-Marie)**.** *Si α, β et $\overline{z}_b$ sont trois constantes réelles, H_0 une fonction réelle positive de classe $C^1(\Omega)$ telle que $\sin(\beta H_0(x)) \neq 0$ pour tout $x \in \Omega$, alors $u = u_{\alpha,\beta}$, $w = w_{\alpha,\beta}$ et z_b donnés respectivement par*

$$z_b = \overline{z}_b - H_0 - \frac{\alpha^2 \beta^2}{2g \sin^2(\beta H_0)}, \tag{1.11}$$

$$u_{\alpha,\beta} = \frac{\alpha\beta}{\sin(\beta H_0)} \cos(\beta(z - z_b)), \tag{1.12}$$

$$w_{\alpha,\beta} = \alpha\beta \left(\frac{\partial z_b}{\partial x} \frac{\cos(\beta(z - z_b))}{\sin(\beta H_0)} + \frac{\partial H_0}{\partial x} \frac{\sin(\beta(z - z_b)) \cos(\beta H_0)}{\sin^2(\beta H_0)} \right), \tag{1.13}$$

satisfont les équations d'Euler stationnaires (1.8)-(1.10) *avec $\eta = H_0 + z_b$.*

Solutions stationnaires à topographie donnée

Dans un deuxième temps, on étudie les solutions stationnaires à topographie donnée $z_b(x), x \in \Omega$. On propose encore une fois de choisir des solutions admissibles de type

$$\begin{aligned} u_{\alpha,\beta} &= \frac{\alpha\beta}{\sin(\beta H)} \cos(\beta(z - z_b)) \\ w_{\alpha,\beta} &= \alpha\beta \left(\frac{\partial z_b}{\partial x} \frac{\cos(\beta(z - z_b))}{\sin(\beta H)} + \frac{\partial H}{\partial x} \frac{\sin(\beta(z - z_b)) \cos(\beta H)}{\sin^2(\beta H)} \right) \end{aligned} \tag{1.14}$$

où on se donne $\alpha > 0$ et β et une valeur frontière pour H ($H(0)$ ou $H(L_x)$). Reste donc à déterminer la hauteur d'eau en tout point. On définit la fonction

$$F_{\alpha,\beta} \,:\, x \mapsto gx + \frac{\alpha^2\beta^2}{2\sin^2(\beta x)}. \tag{1.15}$$

Alors on a la proposition suivante qui permet de déterminer si une solution continue existe :

Proposition 1.4.2 (B., Bristeau, Sainte-Marie)**.** *Si pour tout $x \in \Omega$, le problème*

$$F_{\alpha,\beta}(H(x)) = F_{\alpha,\beta}(H_{lim}) + g(z_{b,lim} - z_b(x)) = C_{\alpha,\beta,lim} - gz_b(x) \tag{1.16}$$

a une solution $H(x) \geq 0$, alors $(H, u_{\alpha,\beta}, w_{\alpha,\beta})$ est solution de (1.8)-(1.10). Ce résultat peut s'énoncer aussi de la manière suivante : si le problème (1.16) admet une solution H_m au point $x = x_m$ où la topographie z_b est maximale, ou, de manière équivalente si

$$F^{min}_{\alpha,\beta} \leq C_{\alpha,\beta,lim} - gz_b(x_m),$$

alors il existe une solution pour tout $x \in \Omega$. De plus, il est facile de prouver que si $z_b \in C^k(\Omega)$, $k \geq 1$ alors $(H, u_{\alpha,\beta}) \in C^k(\Omega)$ et $w_{\alpha,\beta} \in C^{k-1}(\Omega)$.

Ensuite, on s'intéresse naturellement aux situations pour lesquelles il existe des points x pour lesquels le problème (1.16) n'a pas de solution. On note Ω_c l'ensemble de ces points. On suppose qu'il est non vide, et qu'il existe au moins un point x_c défini par

$$z_{b,c} = \max_{x\in\Omega} z_b(x), \tag{1.17}$$

$$\left.\frac{\partial z_b}{\partial x}\right|_{x=x_c} = 0. \tag{1.18}$$

Ce point est nécessairement dans Ω_c. Sans perte de généralité, on suppose que la topographie n'admet qu'une seule bosse. Le point x_c est donc unique. En amont de x_c la topographie est strictement croissante. En aval de x_c elle est strictement décroissante. Pour étudier une topographie plus générale, on peut couper le domaine en sous-domaines qui vérifient ces hypothèses. On se donne de plus $H_{lim} = H(L_x)$. On montre qu'on est capable de déterminer $H_c = H(x_c)$ analytiquement.

Lemme 1.4.3 (B., Bristeau, Sainte-Marie)**.** *Dans le cas où Ω_c est non vide, il contient au moins x_c le point intérieur de topographie maximale, et la hauteur d'eau en ce point est définie par*

$$H_c = \frac{\arcsin r_c^2}{\beta} \tag{1.19}$$

avec

$$r_c = \sqrt{\frac{\sqrt[3]{12\alpha^4}\beta^2}{6g}\frac{-\sqrt[3]{12\alpha^4}\beta^2 + \left(\sqrt[3]{9g + \sqrt{12\alpha^4\beta^6 + 81g^2}}\right)^2}{\sqrt[3]{9g + \sqrt{12\alpha^4\beta^6 + 81g^2}}}} \tag{1.20}$$

Sur $[x_c, L_x]$, la solution peut admettre un choc, à une abscisse que l'on nomme x_s. On montre qu'on est capable de trouver les hauteurs d'eau à droite et à gauche du choc, ainsi que sa position en déterminant des relations de saut pour les chocs stationnaires. Ainsi, x_s, $H_{s,l}$ et $H_{s,r}$ peuvent être trouvés grâce à la proposition suivante :

Proposition 1.4.4 (B., Bristeau, Sainte-Marie)**.** *Sur $[x_c, L_x]$, si un choc apparait, alors sa position x_s et les hauteurs d'eau de part et d'autre du choc sont définies par*

$$\left[\frac{g}{2}H^2 + \frac{\alpha^2\beta^2 H}{2\sin^2(\beta H)} + \frac{\alpha^2\beta}{2}\frac{\cos(\beta H)}{\sin(\beta H)}\right]_{H_{s,l}}^{H_{s,r}} = 0, \tag{1.21}$$

$$\frac{\alpha^2\beta^2}{2\sin^2(\beta H_c)} + g(H_c + z_{b,c}) = \frac{\alpha^2\beta^2}{2\sin^2(\beta H_{s,l})} + g(H_{s,l} + z_{b,s}), \tag{1.22}$$

$$\frac{\alpha^2\beta^2}{2\sin^2(\beta H_{lim})} + g(H_{lim} + z_{b,lim}) = \frac{\alpha^2\beta^2}{2\sin^2(\beta H_{s,r})} + g(H_{s,r} + z_{b,s}). \tag{1.23}$$

Puis, sur $[0, x_c]$, la solution étant continue, on utilise (1.16) pour déterminer les hauteurs d'eau en utilisant comme référence non plus la valeur au bord mais la valeur en x_c qui a pu être déterminée. Des illustrations de ces solutions analytiques sont données en fin de chapitre.

De nombreuses autres solutions pour l'hydrodynamique sont données dans le Chapitre 3, dont une extension au cas tridimensionnel ou à la présence d'une surface partiellement libre.

1.4.4 Solution analytique couplée pour l'hydrodynamique et la biologie

Finalement, on propose un modèle de couplage avec un traceur. Ce modèle réactif représente le transport d'une quantité biologique dans le champ de vitesse hydrodynamique des équations d'Euler, ainsi qu'un phénomène de réaction. Le terme de réaction n'a pas vocation à représenter un phénomène physique réel, mais juste de permettre une résolution analytique de l'équation suivante couplée aux équations d'Euler à surface libre précédemment étudiées :

$$u\frac{\partial T}{\partial x} + w\frac{\partial T}{\partial z} = \frac{T_0 - T}{\tau}, \tag{1.24}$$

où u et w sont les solutions du système (1.8)-(1.9) pour une fonction donnée H_0, décrites par les formules (1.12) et (1.13). La fonction

$$T(x,z) = e^{-(H_0(x)-(z-z_b(x)))}, \tag{1.25}$$

avec $T_0 = 0$ et

$$\frac{1}{\tau} = \alpha\beta\frac{\cos(\beta(z-z_b))}{\sin(\beta H_0)}\left(1 - \frac{\tan(\beta(z-z_b))}{\tan(\beta H_0)}\right)\frac{\partial H_0}{\partial x}, \tag{1.26}$$

convient. Cette solution nous servira à valider l'étude du Chapitre 4.

1.5 Couplage hydrodynamique et biologie pour la simulation de la culture de micro-algues en raceways

1.5.1 Etat de l'art hydrodynamique

Le problème exposé dans la Section 1.2 est un problème d'hydrodynamique à surface libre. L'eau est souvent considérée comme un fluide incompressible. Néanmoins, la surface libre implique des interactions avec l'atmosphère et donc des similitudes avec l'étude de fluides compressibles. De plus, le raceway ne correspond pas à des conditions naturelles d'évolution du fluide. Les concentrations en micro-algues sont très élevées et, même si on n'en tiendra pas compte en première approximation, cela pourrait avoir des effets sur la densité ou la viscosité du fluide.

Le système de Navier-Stokes

En mécanique des fluides newtoniens, le point de départ est le système de Navier-Stokes. Ces équations, si on pouvait les simuler numériquement aussi finement que nécessaire, modéliseraient les différents phénomènes hydrodynamiques possibles: diffusion, convection... Elles découlent en effet simplement de l'application de la seconde loi de Newton. On les écrit ici en deux dimensions pour un écoulement à surface libre soumis à la gravité:

$$\frac{\partial \rho}{\partial t} + \frac{\partial \rho u}{\partial x} + \frac{\partial \rho w}{\partial z} = 0, \tag{1.27}$$

$$\frac{\partial \rho u}{\partial t} + \frac{\partial \rho u^2}{\partial x} + \frac{\partial \rho uw}{\partial z} + \frac{\partial p}{\partial x} = \frac{\partial \Sigma_{xx}}{\partial x} + \frac{\partial \Sigma_{xz}}{\partial z}, \tag{1.28}$$

$$\frac{\partial \rho w}{\partial t} + \frac{\partial \rho uw}{\partial x} + \frac{\partial \rho w^2}{\partial z} + \frac{\partial p}{\partial z} = -\rho g + \frac{\partial \Sigma_{zx}}{\partial x} + \frac{\partial \Sigma_{zz}}{\partial z}, \tag{1.29}$$

et on considère les solutions pour $t > t_0, \quad x \in \mathbb{R}, \quad z_b(x) \leq z \leq \eta(x,t)$, où $\eta(x,t)$ représente l'élévation de la surface, $\mathbf{u} = (u,w)^T$ le vecteur vitesse, $p(x,z,t)$ est la pression, g l'accélération gravitationnelle et ρ la densité de l'eau. Le tenseur de contraintes est défini par

$$\Sigma_{xx} = 2\mu \frac{\partial u}{\partial x}, \quad \Sigma_{xz} = \mu \left(\frac{\partial u}{\partial z} + \frac{\partial w}{\partial x} \right), \quad \Sigma_{zz} = 2\mu \frac{\partial w}{\partial z}, \quad \Sigma_{zx} = \mu \left(\frac{\partial u}{\partial z} + \frac{\partial w}{\partial x} \right).$$

Evidemment, il faut compléter ce système avec des conditions aux bords. Pour la surface libre, on prendra souvent une condition cinématique

$$\frac{\partial \eta}{\partial t} + u_s \frac{\partial \eta}{\partial x} - w_s = 0, \tag{1.30}$$

où l'indice s désigne la valeur en surface. Considérant que la viscosité de l'air est négligeable par rapport à celle du fluide, la continuité des contraintes à la surface implique :

$$\Sigma_T \mathbf{n}_s = -p^a \mathbf{n}_s, \tag{1.31}$$

où $p^a = p^a(x,t)$ est la pression atmosphérique, donnée et Σ_T le tenseur global des contraintes (il contient les termes liés à la viscosité mais aussi à la pression). Pour le fond, il y a une condition cinématique de non pénétration :

$$\mathbf{u}_b.\mathbf{n}_b = 0, \quad \text{ou} \quad u_b \frac{\partial z_b}{\partial x} - w_b = 0. \tag{1.32}$$

Pour le tenseur des contraintes, on aura

$$\mathbf{t}_b.\Sigma_T \mathbf{n}_b = \kappa \mathbf{u}_b.\mathbf{t}_b, \tag{1.33}$$

où $\mathbf{t}_b$ est un vecteur unitaire satisfaisant $\mathbf{t}_b \cdot \mathbf{n}_b = 0$ et κ est un coefficient de friction.

Le fait que la viscosité de l'air soit faible implique que les contraintes en surface sont faibles, et la surface libre peut s'avérer complexe. Il existe différentes techniques pour capturer cette surface. Des méthodes de level set, des méthodes lagrangiennes, des méthodes de maillage mobiles...Mais elles sont très coûteuses et il faut perdre en précision pour obtenir des temps de calcul raisonnables.

Concernant les méthodes de simulation, Navier-Stokes est classiquement vue comme une équation parabolique. On lui applique donc des méthodes de type éléments finis. Cependant, même si quelques travaux étudient l'utilisation des éléments finis en hydrodynamique à surface libre [74, 82], ces techniques ne traitent pas efficacement

- les solutions non régulières,
- les problèmes d'interface sec-mouillé, lorsque la hauteur d'eau tend vers 0 ou que le domaine change de topologie,
- les besoins de conservation d'éventuels traceurs.

Dans notre cas, on ne va pas utiliser ce genre de méthode pour les équations de Navier-Stokes à surface libre. Comme indiqué en début d'introduction, les écoulements géophysiques gravitaires sont dominés par l'advection et les termes de pression et sont peu diffusifs. De plus, notre problème se caractérise par une faible profondeur (une trentaine de centimètres face à plusieurs dizaines de mètres de long) et un besoin de conservativité (notamment à cause des espèces biologiques présentes dans l'eau). Le système de Saint-Venant semble par exemple plus approprié.

Un modèle de complexité réduite

Le système de Saint-Venant a originellement été introduit en 1871 [19], par une analyse des forces qui s'exercent sur une section de fluide, dans un canal rectangulaire à fond plat. Quand il est complété par les termes sources adéquats, ce système a prouvé son efficacité pour une large classe de problèmes géophysiques comme les rivières, les domaines côtiers, les océans, ou même les avalanches. Il décrit les écoulements au moyen de deux variables: la hauteur d'eau $H(t,x,y)$ et la vitesse moyenne du fluide sur la verticale $\boldsymbol{u}(t,x,y)$. Nous

l'écrivons ici dans sa version bidimensionnelle qui inclut un terme source de topographie.

$$\partial_t H + \mathrm{div}(H\boldsymbol{u}) = 0, \tag{1.34}$$

$$\partial_t H\boldsymbol{u} + \mathrm{div}(H\boldsymbol{u} \otimes \boldsymbol{u}) + \nabla(\frac{g}{2}H^2) = -gH\nabla z_b, \tag{1.35}$$

où g désigne l'accélération gravitationnelle, $z_b(x, y)$ représente la topographie du fond, faisant de $H + z_b$ la côte de la surface libre. On voit clairement apparaitre ici un des intérêts majeurs du système de Saint-Venant. Il permet, grâce à son système de variables bien choisies, de simuler un problème à trois dimensions sur un domaine variable en temps à travers un système bidimensionnel posé sur un domaine stationnaire. Evidemment, ce gain ne se fait pas sans perte de précision, et il faut se poser la question du domaine de validité de ce système. Cela se fait en essayant de retrouver les équations de Saint-Venant à partir de systèmes plus généraux. Ainsi, dans [133] ou [142], les auteurs les dérivent formellement à partir des équation d'Euler. Puis, de nombreux travaux ont consisté à les retrouver à partir des équations de Navier-Stokes. La méthode, initiée dans [61] en une dimension pour aboutir à un système de Saint-Venant visqueux, a inspiré nombre de travaux en deux dimensions [50, 58, 101]. Dans ces études, on y apprend que les équations de Saint-Venant sont une bonne approximation des équations de Navier-Stokes dans le cas où deux hypothèses sont satisfaites. La première est l'hypothèse d'eau peu profonde, qui signifie que la longueur du domaine est bien plus grande que sa profondeur. La deuxième est l'hypothèse hydrostatique, qui stipule que l'accélération verticale est négligeable et que les variations verticales de pression du fluide sont essentiellement dues à la gravité. Par ailleurs, il est nécessaire aussi que les variations du fond soient de petite amplitude, que la viscosité soit faible, mais aussi que les frottements du fond soient peu importants. De nombreuses restrictions donc auxquelles il faut prêter attention pour ne pas faire de non-sens mathématique.

Mais attardons-nous un peu sur les techniques numériques adaptées au système de Saint-Venant, car elles soulèvent des points que nous estimons cruciaux dans notre propre modélisation. Le système de Saint-Venant s'exprime facilement comme une loi de conservation hyperbolique à laquelle on peut même ajouter une inégalité énergétique. D'où l'utilisation de méthodes volumes finis pour sa simulation [28, 62, 92]. Ces méthodes sont par nature conservatives et traitent particulièrement bien l'aspect discontinu des solutions. De plus, en comparaison des différences finies, elle sont utilisables sur des maillages non structurés. Rappelons brièvement qu'il s'agit de découper l'espace en cellules et d'intégrer les équations sur chaque cellule et sur un pas de temps. On voit alors apparaitre les moyennes des solutions sur chaque cellule et les termes de divergence sont convertis en intégrales de surface, qui représentent des flux échangés entre les cellules au niveau de leur interface. On peut résumer un schéma volume fini en une dimension d'espace comme ceci

$$U_i^{n+1} = U_i^n - \frac{\Delta t^n}{\Delta x_i}\left(F_{i+1/2}^n - F_{i-1/2}^n\right) + \Delta t^n S_i^n \tag{1.36}$$

Tout le travail repose sur la bonne détermination du flux $F_{i+1/2}^n$ entre les cellules C_i et C_{i+1}. Une revue des différents schémas possibles est disponible dans [62, 92, 139]. On voudra no-

tamment que ces schémas aient de bonnes propriétés de consistance et de stabilité, et pour les équations de Saint-Venant, cela signifie surtout que l'on veut assurer la positivité de la hauteur d'eau, et que l'on veut préserver les états d'équilibre au repos. Malheureusement, si les schémas volumes finis sont appropriés à la bonne détermination des flux, ils le sont beaucoup moins à la discrétisation des termes sources. Théoriquement, le schéma de Godunov exact vérifie ces propriétés [90], mais il est trop coûteux à mettre en oeuvre dans des simulations. De nombreuses méthodes sont alors proposées pour construire des schémas équilibres [59, 67, 81, 91] mais peu sont capables d'assurer aussi une hauteur d'eau positive. Parmi ces derniers, un des plus connus, et que nous utiliserons par la suite, est le travail de reconstruction hydrostatique initié par Audusse *et al.* [3]. On trouve aussi dans [55] une proposition basée sur une discrétisation de type Galerkin Discontinue, ou dans [108], une modification du solveur de Roe permet de garantir la positivité de la hauteur d'un flot granulaire.

Le système de Saint-Venant est finalement un système qui a fait ses preuves expérimentalement, en ce sens que les ingénieurs observent sa précision dans de nombreux cas, même quand les hypothèses nécessaires à son utilisation ne sont pas toutes vérifiées. Il a aussi initié de nombreux travaux d'analyse théorique ou numérique pour aboutir à des techniques de discrétisation sophistiquées et qui présentent de moins en moins d'aberrations. Malgré tout, nous voudrions, pour notre problème qui peut être très hétérogène sur la verticale, lever la limitation d'uniformité des vitesses.

Un modèle distribué sur la verticale

L'idée est en fait de chercher un système intermédiaire entre Navier-Stokes et Saint-Venant, qui permette de conserver l'efficacité de Saint-Venant en terme de réduction de dimension, mais aussi de simplification de domaine géométrique, tout en récupérant de l'information sur les profils de vitesses verticaux. Pour cela, on introduit un système de Saint-Venant multicouches. Plusieurs versions sont disponibles à ce jour. Dans une des premières, introduite par Audusse *et al.* [2, 7, 8], les deux hypothèses d'hydrostaticité et d'eau peu profonde sont faites. Mais chaque couche est ensuite décrite par sa propre hauteur, sa propre vitesse, et est advectée par le flot. Il en résulte un écoulement qui se fait sans échanges de masse entre couches, qui s'apparente donc plutôt à un système de fluides non miscibles, tels qu'étudiés dans [38, 39, 105]. Plus récemment, un autre modèle distribué sur la verticale est proposé [9, 10], qui se base sur une discrétisation verticale des variables de type Galerkin, mais pour lequel seule l'hypothèse de non-hydrostaticité est faite. Une intégration des équations de Navier-Stokes hydrostatiques projetées sur cette base mène à une formulation de type Saint-Venant multicouches pour laquelle des termes d'échange de masse apparaissent. Nous détaillons ici sa dérivation car c'est ce modèle que nous utiliserons.

On commence par écrire les équations de Navier-Stokes hydrostatiques à densité con-

stante ρ_0

$$\frac{\partial u}{\partial x}+\frac{\partial w}{\partial z}=0, \tag{1.37}$$

$$\frac{\partial u}{\partial t}+\frac{\partial u^2}{\partial x}+\frac{\partial uw}{\partial z}+\frac{1}{\rho_0}\frac{\partial p}{\partial x}=\frac{1}{\rho_0}\left(\frac{\partial \Sigma_{xx}}{\partial x}+\frac{\partial \Sigma_{xz}}{\partial z}\right), \tag{1.38}$$

$$\frac{\partial p}{\partial z}=-\rho_0 g+\frac{\partial \Sigma_{zx}}{\partial x}+\frac{\partial \Sigma_{zz}}{\partial z}. \tag{1.39}$$

On choisit pour tenseur des contraintes visqueuses

$$\Sigma_{xx}=2\mu\frac{\partial u}{\partial x},\quad \Sigma_{xz}=\mu\frac{\partial u}{\partial z},\quad \Sigma_{zz}=2\mu\frac{\partial w}{\partial z},\quad \Sigma_{zx}=\mu\frac{\partial u}{\partial z}$$

et on complète bien sûr avec des conditions cinématiques en surface et des conditions de non pénétration au fond. L'intervalle $[z_b,\eta]$ est divisé en N couches $\{L_\alpha\}_{\alpha\in\{1,\dots,N\}}$ de hauteur $l_\alpha H(x,t)$ où chaque couche L_α comprend les points vérifiant $z\in L_\alpha(x,t)=[z_{\alpha-1/2},z_{\alpha+1/2}]$ avec

$$\begin{cases} z_{\alpha+1/2}(x,t)=z_b(x,t)+\displaystyle\sum_{j=1}^{\alpha} l_j H(x,t), \\ \\ h_\alpha(x,t)=z_{\alpha+1/2}(x,t)-z_{\alpha-1/2}(x,t)=l_\alpha H(x,t), \quad \alpha\in[0,\dots,N] \end{cases} \tag{1.40}$$

avec $l_j>0,\quad \sum_{j=1}^{N} l_j=1$.

Puis, on considère l'espace $\mathbb{P}_{0,H}^{N,t}$ de fonctions continues par morceaux définies par

$$\mathbb{P}_{0,H}^{N,t}=\left\{\mathbb{I}_{z\in L_\alpha(x,t)}(z),\quad \alpha\in\{1,\dots,N\}\right\},$$

où $\mathbb{I}_{z\in L_\alpha(x,t)}(z)$ est la fonction caractéristique de la couche $L_\alpha(x,t)$. Les projections de u, w et T sur $\mathbb{P}_{0,H}^{N,t}$ sont alors (pour $X=u$, $X=w$ ou $X=T$)

$$X^N(x,z,\{z_\alpha\},t)=\sum_{\alpha=1}^{N}\mathbb{I}_{[z_{\alpha-1/2},z_{\alpha+1/2}]}(z)X_\alpha(x,t). \tag{1.41}$$

Pour faciliter la compréhension, les notations sont rappelées sur la Figure 1.2. Alors, en omettant la viscosité pour des questions de simplicité, on peut énoncer le résultat suivant [9]

Proposition 1.5.1 (Audusse, Bristeau, Pelanti, Sainte-Marie)**.** *La formulation faible des*

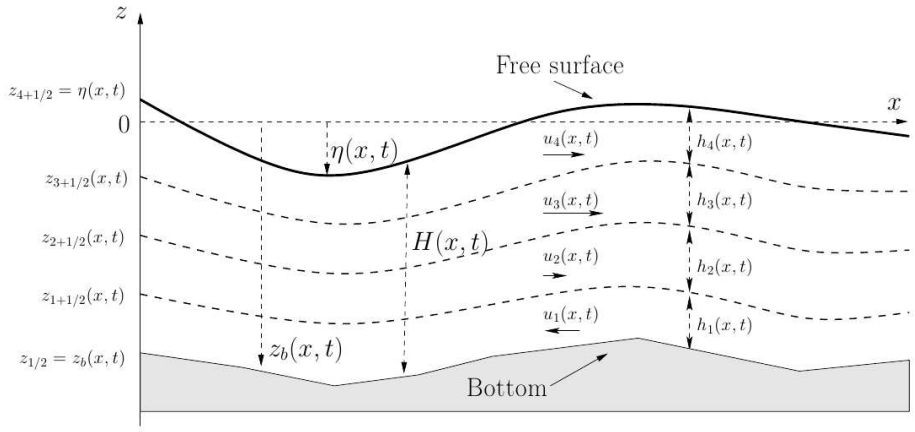

Figure 1.2: Notations de l'approche multicouches.

Eqs. (1.37)-(1.39) sur $\mathbb{P}_{0,H}^{N,t}$ *conduit au système*

$$\sum_{\alpha=1}^{N} \frac{\partial l_\alpha H}{\partial t} + \sum_{\alpha=1}^{N} \frac{\partial l_\alpha H u_\alpha}{\partial x} = 0, \tag{1.42}$$

$$\frac{\partial h_\alpha u_\alpha}{\partial t} + \frac{\partial}{\partial x}\left(h_\alpha u_\alpha^2 + h_\alpha p_\alpha\right) = u_{\alpha+1/2} G_{\alpha+1/2} - u_{\alpha-1/2} G_{\alpha-1/2} + \frac{1}{\rho_0}\left(\frac{\partial z_{\alpha+1/2}}{\partial x} p_{\alpha+1/2} - \frac{\partial z_{\alpha-1/2}}{\partial x} p_{\alpha-1/2}\right), \tag{1.43}$$

$\alpha \in [1, \ldots, N]$,

avec

$$G_{\alpha+1/2} = \sum_{j=1}^{\alpha} \frac{\partial h_j}{\partial t} + \sum_{j=1}^{\alpha} \frac{\partial h_j u_j}{\partial x} \tag{1.44}$$

$$G_{1/2} = G_{N+1/2} = 0, \tag{1.45}$$

$$p_\alpha = \rho_0 g \left(\frac{h_\alpha}{2} + \sum_{j=\alpha}^{N} h_j\right), \tag{1.46}$$

$$p_{\alpha+1/2} = \rho_0 g \sum_{j=\alpha+1}^{N} h_j, \tag{1.47}$$

$$u_{\alpha+1/2} = \begin{cases} u_\alpha & \text{if } G_{\alpha+1/2} \geq 0, \\ u_{\alpha+1} & \text{if } G_{\alpha+1/2} < 0. \end{cases} \tag{1.48}$$

Récapitulons les différents avantages d'un tel formalisme pour notre problème:

- le système multicouches permet de modéliser un problème non homogène sur la ver-

ticale;

- comme dans un système de Saint-Venant classique, il n'y a plus de dérivée selon la verticale;
- comme dans un système de Saint-Venant classique, le domaine géométrique est complètement déterminé une fois que la hauteur d'eau $H(t,x)$ l'est. La simulation d'un problème bidimensionnel se fait sur un maillage 1D, la simulation d'un problème tridimensionnel se fait sur un maillage 2D;
- le système obtenu a la structure d'un système de lois de conservation avec terme source qui ressemble fort au modèle de Saint-Venant. On va donc pouvoir utiliser les techniques décrites dans la section précédente, notamment volumes finis et reconstruction hydrostatique et bénéficier des bonnes propriétés de stabilité qu'elles garantissent (hauteur d'eau positive, fronts sec/mouillé bien représentés).

Un mot sur les schémas cinétiques

Comme précisé dans la section précédente, le modèle multicouches va être discrétisé par la méthode des volumes finis. Il faut donc choisir un solveur de Riemann pour résoudre, de manière exacte ou approchée, les problèmes aux interfaces des cellules et calculer les flux. Dans la plupart des cas, ces solveurs sont basés sur le calcul de valeurs propres et vecteurs propres du système hyperbolique étudié. Mais la preuve de l'hyperbolicité du système de Saint-Venant multicouches est encore un problème ouvert (excepté dans le cas bicouches), et nous n'avons pas d'accès analytique aux valeurs propres du système.

Les schémas cinétiques vont nous donner le moyen de contourner cette limitation. De plus, ils permettent d'obtenir de bonnes propriétés de stabilité discrète. Les premiers schémas cinétiques font leur apparition dans les années 70, pour l'étude de la dynamique des gaz [120, 127]. Mais en 1990, dans [111], Perthame introduit une nouvelle idée: la Maxwellienne habituellement utilisée dans la description cinétique des équations peut être remplacée par un équilibre de Gibbs à support compact. Celui-ci permet d'obtenir de meilleures propriétés théoriques sur le schéma [84, 111]. Il est aussi plus simple à implémenter et permet de réduire le temps de calcul.

Pour des raisons de simplicité, nous allons décrire le processus de construction d'un schéma cinétique sur l'équation de Saint-Venant avec termes sources de topographie. Ce qui sera fait dans le Chapitre 4 sera une adaptation multicouches de ce procédé. L'idée de base des schémas cinétiques est d'utiliser le lien qui existe entre les équations macroscopiques de la dynamique des fluides - comme Navier-Stokes, Euler ou Saint-Venant - avec les équations cinétiques de type Boltzmann [41], qui décrivent l'évolution d'une densité de particules, à un niveau plus mésoscopique. La première étape est de définir un équilibre de Gibbs, c'est à dire une densité de particules. Une particule est repérée par sa position x et sa vitesse ξ au temps t. Ainsi, si on définit l'équilibre ainsi :

$$M(t,x,\xi) = M(H(t,x), \xi - \boldsymbol{u}(t,x)) = \frac{H(t,x)}{c^2}\chi\left(\frac{\xi - \boldsymbol{u}(t,x)}{c}\right), \tag{1.49}$$

où $c = \sqrt{\frac{gH}{2}}$ et χ est une fonction paire qui vérifie

$$\int_{\mathbb{R}} \begin{pmatrix} 1 \\ \xi^2 \end{pmatrix} \chi(\xi) d\xi = \begin{pmatrix} 1 \\ 1 \end{pmatrix}, \tag{1.50}$$

alors on peut énoncer le théorème suivant :

Théorème 1.5.1 (Audusse)**.** *Les fonctions $(H, H\boldsymbol{u})$ sont solutions du système de Saint-Venant homogène si et seulement si $M(t,x,\xi)$ est solution de l'équation cinétique*

$$\partial_t M + div(\xi M) = Q(t,x,\xi), \tag{1.51}$$

pour un terme de collision $Q(t,x,\xi)$ qui satisfait pour presque tout (t,x),

$$\int_{\mathbb{R}} Q d\xi = 0, \quad \int_{\mathbb{R}} \xi Q d\xi = 0 \tag{1.52}$$

La preuve se fait simplement en remarquant qu'une intégration de (1.51) contre $\begin{pmatrix} 1 \\ \xi \end{pmatrix}$ donne le système de Saint-Venant (1.34) - (1.35) sans terme source de topographie. A ξ fixé, et si on omet dans un premier temps le terme de collision, l'équation (1.51) est une équation d'advection linéaire. On peut alors la discrétiser par la méthode des volumes finis en utilisant un simple schéma upwind:

$$f_i^{n+1-} = M_i^n - \frac{\Delta t^n}{\Delta x_i} \xi_+ \left(M_i^n - M_{i-1}^n \right) - \frac{\Delta t^n}{\Delta x_i} \xi_- \left(M_{i+1}^n - M_i^n \right), \tag{1.53}$$

où

$$\xi^+ = \max(\xi, 0), \quad \text{et} \quad \xi^- = \min(\xi, 0) \tag{1.54}$$

Le terme de collision est pris en compte dans un deuxième temps. Il est vu comme une projection de f_i^{n+1-} sur l'ensemble des équilibres de Gibbs admissibles (de la forme (1.49) par exemple). En intégrant le schéma numérique (1.53), on obtient pour (1.36) une expression des flux macroscopiques:

$$F_{i+1/2}^n = \int_{\xi \leq 0} \xi \begin{pmatrix} 1 \\ \xi \end{pmatrix} M_{i+1}^n d\xi + \int_{\xi \geq 0} \xi \begin{pmatrix} 1 \\ \xi \end{pmatrix} M_i^n d\xi \tag{1.55}$$

Remarque 1.5.2. *Les conditions (1.50) autorisent un grand nombre de choix pour l'équilibre de Gibbs. Souvent, on prendra une fonction à support compact qui soit intégrable analytiquement pour faciliter le calcul du flux.*

Remarque 1.5.3. *Plus de détails sur la théorie cinétique seront donnés dans le Chapitre 6. Ici, nous nous intéressions uniquement au côté pratique de cette théorie pour construire des*

schémas numériques.

1.5.2 Etat de l'art de la modélisation de la croissance phytoplanctonique

Phytoplancton

Après avoir présenté dans la partie précédente le modèle hydrodynamique que nous choisirons pour le Chapitre 4, nous abordons la partie biologie. Dans un premier temps, nous allons définir un peu plus clairement ce qu'est le phytoplancton, et les différents phénomènes auxquels il est confronté. Pour plus de détails, le lecteur pourra se référer à [57].

Définition 1.5.4. *Le terme* phytoplancton *est dérivé des mots grecs* phyto *(plante) et* planktos *(itinérant). Le phytoplancton est composé de micro organismes vivant dans un environnement aquatique. L'eau peut être salée ou douce. Il existe de nombreuses variétés de phytoplancton, avec différentes formes, tailles, propriétés.*

Comme les plantes terrestres, le phytoplancton est doté de chlorophylle pour capturer la lumière du soleil, et la transformer en énergie chimique par la photosynthèse (cf Définition 1.5.5). Il consomme du dioxyde de carbone et relâche de l'oxygène. La croissance du phytoplancton dépend de la disponibilité en nutriments, en dioxyde de carbone et de la quantité d'énergie lumineuse incidente. Les nutriments nécessaires sont: nitrate, phosphate, silicate, calcium, fer. D'autres facteurs influencent la croissance du phytoplancton: température, salinité, profondeur de la hauteur d'eau, vent, zooplancton.

Le phytoplancton est important car il est à l'origine de la plupart des transferts de dioxyde de carbone de l'atmosphère vers les océans. Le dioxyde de carbone est consommé pendant la photosynthèse, et le carbone est incorporé dans le phytoplancton. La majorité du carbone intrinsèque retourne dans les eaux de surface quand le phytoplancton est mangé ou se décompose, mais une partie tombe dans les profondeurs des océans.

Dans notre cas, on n'étudie pas le phytoplancton dans son environnement naturel, mais dans un lieu où les conditions sont optimisées pour la croissance.

Définition 1.5.5. *La photosynthèse est un procédé qui convertit le dioxyde de carbone en composés organiques, plus spécialement en sucres, en utilisant l'énergie solaire. La photosynthèse a lieu dans les plantes, les algues, et de nombreuses espèces de bactéries. L'équation de la réaction est*

$$6\,CO_2 + H_2O \underset{+Lumière}{\Rightarrow} C_6H_{12}O_6 + 6\,O_2 \tag{1.56}$$

Les électrons nécessaires à la réaction sont capturés par des protéines qui se situent dans des organelles appelés chloroplastes et qui contiennent la chlorophylle. La chlorophylle absorbe la lumière bleue, rouge, mais pas verte, ce qui explique sa couleur.

Définition 1.5.6. *La respiration est un procédé permettant, la nuit, de récupérer l'énergie stockée par la photosynthèse en journée. Celle-ci est alors utilisée pour conduire les processus intracellulaires, parmi lesquels la croissance prend une part significative.*

Les algues doivent garder un équilibre entre l'énergie capturée du soleil et l'énergie utilisée pour la fixation du carbone. Face aux variations lumineuses quotidiennes et saisonnières, les organismes répondent par des changements physiques, biophysiques, biochimiques et physiologiques.

Définition 1.5.7. *La photoacclimatation est la réponse phénotypique des algues à des changements d'irradiance dans le but d'optimiser la photosynthèse. Au niveau cellulaire, cela se traduit par des changements de concentration et de composition en pigments. Au niveau physiologique, le quantum minimum requis pour la photosynthèse varie aussi en fonction de la lumière perçue.*

Durant la photosynthèse, certains complexes de protéines sont responsables de réactions dépendant de la lumière. Parmi ceux-ci, le complexe Photosystem II (PS II) va intervenir dans le processus de photoacclimatation. Il peut être dans trois états: ouvert (prêt à recevoir un électron), fermé (il travaille) et endommagé (il ne peut plus travailler). Bien évidemment, quand un site est endommagé, il n'y a plus de transfert d'électron possible et la photosynthèse est stoppée. L'inactivation est irréversible mais la protéine peut cependant être restaurée. On liste deux types de photoacclimatation :

- la photoacclimatation à court terme. Ce sont des processus courts (de la seconde à moins d'une heure). La première défense de l'algue est la désactivation des excitons par la dissipation thermique.
- la photoacclimatation à long terme. Ce sont des processus qui peuvent durer entre une heure et plusieurs jours. Quand l'algue est exposée à des quantités lumineuses inadaptées et que la photoacclimatation à long terme ne peut suffire, l'algue peut faire varier la quantité de chlorophylle dans le PS II. Elle peut aussi changer le nombre de PS II.

Définition 1.5.8. *La photoinhibition est la réduction de la capacité de photosynthèse d'une plante due à une trop forte intensité lumineuse.*

Parfois, les mécanismes de photoacclimatation décris ci-dessus ne sont pas assez efficaces pour protéger l'algue de lésions photoniques. C'est le cas par exemple ci celle-ci a été exposée longtemps à une irradiance élevée. Elle peut alors désactiver ses centres de réaction PS II, c'est la photoinhibition.

Modéliser la dynamique du phytoplancton

La dynamique du phytoplancton est encore décrite plus ou moins empiriquement. La raison en est que les processus physiologiques mentionnés dans la section précédente sont encore mal compris. Ce manque de compréhension est une des raisons pour lesquelles tant d'alternatives existent pour modéliser la croissance phytoplanctonique. Dans cette section, inspirée de [16] et [106], nous donnons un aperçu des différents choix de modélisation possibles jusqu'à maintenant. Classiquement, il y a deux types de modèles: les modèles empiriques et les modèles mécanistiques. Les premiers conviennent parfaitement aux situations

pour lesquelles on bénéficie de données. Mais un modèle réglé sur un site spécifique peut difficilement être appliqué à un autre site. De plus, ces modèles font intervenir des paramètres qui sont souvent éloignés de toute signification physique. Au contraire, les modèles mécanistiques essaient de retranscrire les processus biogéochimiques en équations. Ainsi, ils sont plus flexibles d'une situation à l'autre et ils utilisent des paramètres significatifs physiquement ou biologiquement (on peut ainsi les mesurer par l'expérience). Néanmoins, cela se paie par une complexité plus importante (parfois 15 variables, 17 paramètres).

Quoi qu'il en soit, peu importe le type de modèle choisi, une bonne modélisation devra représenter à la fois les processus gouvernés par la lumière (photosynthèse, photoacclimatation...) et ceux gouvernés par les nutriments (croissance, consommation, respiration...).

Modélisation des processus de photosynthèse et photoacclimatation La lumière est la variable principale impliquée dans la photosynthèse. Dans les modèles, la mesure de la lumière est l'irradiance, notée E, parfois intégrée sur un intervalle spectral, car la chlorophylle n'est en réalité sensible qu'aux longueurs d'onde d'amplitude 400-700 μm. La sortie importante des modèles de photosynthèse est le taux de production primaire, souvent noté μ (taux de production de composés organiques à partir du dioxyde de carbone atmosphérique ou aquatique). Ce taux de production est fonction à la fois de la lumière, mais aussi des nutriments. Concentrons-nous tout d'abord sur la partie qui dépend de la lumière.

Les modèles empiriques essaient d'ajuster une fonction à des données expérimentales. On construit une fonction $f(E)$ telle que $f(0) = 0$, qui prend ou non en compte la photoinhibition (Définition 1.5.8), et à laquelle le taux de production primaire sera proportionnel. Mentionnons par exemple:

- La fonction de Monod (1950) : $f(x) = \frac{x}{1+x}$, pas de photoinhibition
- La fonction de Steele (1962) : $f(x) = x.e^{1-x}$, photoinhibition
- La fonction de Klepper (1962) : $f(x) = \frac{(2+A)x}{1+Ax+x^2}$, photoinhibition

Les modèles mécanistiques ont une autre approche, basée sur la physique. Si on suit ce qu'on a expliqué à la section précédente à propos de la photoacclimatation et la photoinhibition, une courbe représentant le taux de croissance comme fonction de la lumière doit avoir les caractéristiques suivantes :

- En faible irradiance, la courbe de production primaire est croissante. Le facteur limitant est la lumière.
- Un plateau caractérisant un rendement maximal.
- En haute irradiance, la courbe de production primaire est décroissante. Le facteur limitant est le transfert des nombreux électrons excités par les photons.

A l'échelle microscopique, cela s'explique par le fonctionnement des PS II lors des processus de photoacclimatation (Définition 1.5.7). Jusqu'à présent, les processus à court terme n'ont

pas été inclus dans les modèles. Mais plusieurs modèles prennent en compte les processus à long terme: Zonneveld (1994) et Han (2002) construisent des modèles dans lesquels PS II peut être trouvé dans trois états: ouvert, fermé ou photoinhibé. Concentrons-nous par exemple sur le modèle de Han. Nous appelons n_o, n_c et n_{in} les probabilités pour un PS II d'être ouvert, fermé ou inhibé. L'équation d'équilibre cinétique est donc

$$\text{Site ouvert} \underset{\tau^{-1}}{\overset{\sigma_{PSII}.E}{\leftrightarrows}} \text{Site fermé} \underset{k_r}{\overset{k_d}{\leftrightarrows}} \text{Site inhibé}, \tag{1.57}$$

où $\sigma_{PSII}.E$, τ^{-1}, k_r et k_d sont les constante de réaction. Le système s'écrit alors :

$$\begin{cases} \dfrac{dn_o}{dt} = -\sigma_{PSII}.E.n_o + \dfrac{n_c}{\tau}, & (1.58) \\ \dfrac{dn_c}{dt} = \sigma_{PSII}.E.n_o - \dfrac{n_c}{\tau} - k_d\sigma_{PSII}En_c, & (1.59) \\ n_{in} = 1 - n_o - n_c. & (1.60) \end{cases}$$

La fonction $f(E)$ et *a fortiori* le taux de production primaire sont ensuite proportionnels au nombre de sites ouverts.

Un autre indicateur de l'état de photoacclimatation de l'algue est le ratio chlorophylle-carbone. S'il est faible, l'algue a probablement été dans une situation d'éclairement intense peu auparavant; s'il est haut, l'algue est certainement dans la première phase de la courbe de photosynthèse. Les modèles empiriques considèrent souvent un ratio constant (comme le ratio de Redfield), mais c'est loin de la réalité. Pour améliorer cette approximation, Cloern (1995) propose une formulation empirique du ratio, estimée grâce à 219 publications. En désignant la concentration en chlorophylle par Chl et celle en carbone par C, il trouve, en fonction de la température T et de l'irradiance E

$$\frac{Chl}{C} = 0.003 + 0.0154.e^{0.050T}.e^{-0.059E}. \tag{1.61}$$

Les modèles mécanistiques sont nombreux à traiter cette partie. Le modèle de Zonneveld (1998) décompose la cellule en trois compartiments: un volume permanent, et deux zones transitoires pour le carbone et les nutriments. Dans des conditions de limitation de nutriments, la production de chlorophylle est proportionnelle à la taille de la zone qui contient l'azote. Geider (1997) propose un modèle alternatif basé sur l'introduction d'une équation d'état indépendante pour la chlorophylle.

Modélisation des processus contrôlés par les nutriments En plus de lumière, les algues ont besoin de nutriments pour croitre. Avant l'introduction des modèles en quota (Droop 1968), il était communément admis d'utiliser le ratio de Redfield pour la modélisation. Ce ratio, déterminé expérimentalement, stipule que le ratio moléculaire carbone, azote et phosphore est égal à 106:16:1 partout. Ainsi, on déduit de la connaissance d'une variable, la valeur des deux autres. Mais ce modèle échoue dans de nombreuses situations et la nécessité de construire des modèles multi-variables, et d'introduire le concept de colimitation

est apparue.

Selon Flynn (2003), il existe trois stratégies de modélisation de la croissance liée aux nutriments: croissance de type Monod, en quota ou mécanistique. La loi de Monod est empirique et affirme que le taux de production primaire est proportionnel à

$$f_{growth} = \frac{X_e}{K + X_e}, \tag{1.62}$$

où X_e représente le nutriment limitant et K est une constante. Mais ce modèle n'est pas satisfaisant pour deux raisons:

- la croissance s'arrête quand il n'y a plus de nutriments (ce qui est faux en pratique),
- il représente mal les interactions avec plusieurs nutriments.

Par la suite Droop [52, 53] a introduit les modèles en quota. Il affirme qu'une algue est capable de stocker des nutriments dans des compartiments intracellulaires. Ces nutriments sont utilisés pour la croissance, c'est pourquoi en absence de nutriments extracellulaires, la croissance ne cesse pas instantanément. Le quota $Q = \frac{X}{C}$, où X est la concentration en nutriments, C celle en carbone, est inclus dans le ratio de production primaire μ, qui est alors proportionnel à

$$f_{growth} = \frac{Q - Q_{min}}{Q}. \tag{1.63}$$

Il y a deux possibilités pour la modélisation d'interactions avec plusieurs nutriments dans le processus de croissance. La première est la loi du minimum de Liebig. Elle postule que la croissance est gouvernée par le facteur le plus limitant. Dans le cas d'une loi de Monod, on aurait alors

$$f_{growth} = \min_i \left(\frac{X_i^e}{K_{X_i} + X_i^e} \right). \tag{1.64}$$

L'autre approche consiste à considérer plutôt des effets cumulatifs en multipliant les contributions. On aurait alors

$$f_{growth} = \prod_i \left(\frac{X_i^e}{K_{X_i} + X_i^e} \right) \tag{1.65}$$

Mais aucune de ces approches n'a été capable de reproduire les effets couplés de l'azote et de la silice sur les diatomées (Davidson et Gurney (1999)). D'autres modèles sont proposés mais ils n'admettent pas de formulation générale et ne fonctionnent que dans des conditions restreintes.

Finalement, on s'intéresse à l'absorption des nutriments. Le taux d'absorption d'un nutriment est souvent décrit par un modèle de type Michaelis-Menten

$$f_{upt} = A. \frac{X_e}{K_X + X_e}. \tag{1.66}$$

Modélisation de la respiration Les modèles empiriques établissent que le taux de respiration est divisé en deux composantes

$$R = R_m + R_g.$$

R_m est appelée la respiration de maintenance, alors que R_g varie avec la production primaire. Ces valeurs sont déterminées expérimentalement. Mais la plupart du temps, on prend un taux de respiration constant. Les modèles mécanistiques, comme celui proposé par Han (1991) détaillent les étapes de la respiration en introduisant des variables qui sont les concentrations des protéines impliquées dans le processus.

Modèle de Droop

Pour finir, venons-en à notre choix de modèle. Il ne s'agit pas ici de modéliser le plus précisément possible les phénomènes biologiques. Il s'agit de coupler un modèle hydrodynamique avec un modèle biologique simple, mais qui contient tout de même la majorité des phénomènes expliqués dans les paragraphes précédents pour en tirer des premières conclusions. Nous avons expliqué plus haut que parmi les modèles les plus simples de croissance, les modèles en quota sont plus adaptés que des modèles de type Monod. Nous optons donc pour un modèle de Droop pour les variables suivantes

- Le carbone phytoplanctonique, C_1,
- L'azote phytoplanctonique, C_2,
- Les nutriments extracellulaires, C_3.

En notant $Q = \dfrac{C_2}{C_1}$, on en déduit que le coefficient de croissance est proportionnel au quota Q de la manière suivante :

$$\mu(q, I) = \bar{\mu}(I)(1 - \frac{Q_0}{Q}), \tag{1.67}$$

et on inclut la photoinhibition comme suit

$$\bar{\mu}(I) = \tilde{\mu}\frac{I}{I + K_{sI} + \frac{I^2}{K_{iI}}}. \tag{1.68}$$

Enfin, l'absorption de la lumière lumière captée par l'algue dépend de la profondeur mais aussi de la quantité de chlorophylle rencontrée:

$$I(z) = I_0 e^{-\int_0^z (aChl(z) + b)dz}, \tag{1.69}$$

où $Chl(z) = \gamma(I^*)C_2$ est la concentration en chlorophylle, et I^* est la quantité de lumière moyenne observée dans la colonne d'eau la journée précédente. C'est la quantité de chlorophylle qui traduit la photoacclimatation de l'algue. La respiration est supposée constante

égale à R, et l'absorption des nutriments suit classiquement une loi de Michaelis-Menten (1.66) avec un taux de consommation des nutriments λ :

$$\lambda(C^3, q) = \overline{\lambda}\frac{C^3}{C^3 + K_3}(1 - \frac{q}{Q_l}). \tag{1.70}$$

Ce qui nous conduit au système spatialisé avec réaction, transport, diffusion dans l'eau

$$\begin{cases} \partial_t C_1 + \nabla \cdot (\mathbf{u} C_1) = \nu C_1 \Delta C_1 + \mu(q, I) C_1 - R C_1, \\ \partial_t C_2 + \nabla \cdot (\mathbf{u} C_2) = \nu C_2 \Delta C_2 + \lambda(C_3, q) C_1 - R C_2, \\ \partial_t C_3 + \nabla \cdot (\mathbf{u} C_3) = \nu C_3 \Delta C_3 - \lambda(C_3, q) C_1, \end{cases} \tag{1.71}$$

où $\mathbf{u}$ est la vitesse du fluide dans lequel les micro-algues sont immergées, ν est le coefficient de viscosité.

1.5.3 Résultats de l'étude

Finalement, nous résumons ici les apports de l'étude. La version multicouche du modèle hydrodynamique et sa discrétisation [9, 10], a été enrichie d'une force volumique afin de modéliser l'effet de la roue à aube dans le bassin. Celle ci est intégrée à la dérivation multicouches et change principalement les termes de pression dans chaque couche (Proposition 1.5.1). L'étude est faite tout d'abord en deux dimensions, sur un domaine périodique, pour reproduire la dynamique cyclique d'un raceway.

Intéressons-nous au traitement du modèle de Droop. La première chose à effectuer est la dérivation du modèle multicouches, que nous donnons dans cette proposition:

Proposition 1.5.9 (Bernard, B., Bristeau, Sainte-Marie)**.** *Version multicouches du modèle de Droop avec photoacclimatation. Avec les notations de la Proposition 1.5.1, la formulation faible du système* (1.71) *sur* $\mathbb{P}^{N,t}_{0,H}$ *mène à un système de la forme*

$$\begin{aligned} \frac{\partial h_\alpha C^1_\alpha}{\partial t} + \frac{\partial}{\partial x}\left(h_\alpha C^1_\alpha u_\alpha\right) &= C^1_{\alpha+1/2} G_{\alpha+1/2} - C^1_{\alpha-1/2} G_{\alpha-1/2} \\ &\quad + h_\alpha(\mu(q_\alpha, I_\alpha) C^1_\alpha - R C^1_\alpha), \qquad (1.72) \\ \frac{\partial h_\alpha C^2_\alpha}{\partial t} + \frac{\partial}{\partial x}\left(h_\alpha C^2_\alpha u_\alpha\right) &= C^2_{\alpha+1/2} G_{\alpha+1/2} - C^2_{\alpha-1/2} G_{\alpha-1/2} \\ &\quad + h_\alpha(\lambda(C^3_\alpha, q_\alpha) C^1_\alpha - R C^2_\alpha), \qquad (1.73) \\ \frac{\partial h_\alpha C^3_\alpha}{\partial t} + \frac{\partial}{\partial x}\left(h_\alpha C^3_\alpha u_\alpha\right) &= C^3_{\alpha+1/2} G_{\alpha+1/2} - C^3_{\alpha-1/2} G_{\alpha-1/2} \\ &\quad - h_\alpha \lambda(C^3_\alpha, q_\alpha) C^1_\alpha, \qquad (1.74) \\ & \qquad\qquad \alpha \in [1, \ldots, N], \end{aligned}$$

avec $q_\alpha = \frac{C^2_\alpha}{C^1_\alpha}$ *et* $C^j_{\alpha+1/2}$, $j = 1 \ldots 3$ *défini en fonction du signe des échanges de masse représentés par les* $G_{\alpha+1/2}$.

Puis, on obtient une description cinétique du modèle de biologie multicouches sans les

termes de réaction. Ceux-ci sont intégrés par la suite, grâce à un schéma numérique de type splitting. On définit donc des équilibres de Gibbs par couche

$$U_\alpha^j(x,t,\xi) = C_\alpha^j(x,t) M_\alpha(x,t,\xi), \quad \alpha = 1,\dots,N, \quad j = 1,\dots,3, \tag{1.75}$$

$$V_{\alpha+1/2}^j(x,t,\xi) = C_{\alpha+1/2}^j(x,t) N_{\alpha+1/2}(x,t,\xi), \quad \alpha = 0,\dots,N, \quad j = 1,\dots,3, \tag{1.76}$$

où $N_{\alpha+1/2}(x,t,\xi)$ est defini par

$$N_{\alpha+1/2}(x,t,\xi) = G_{\alpha+1/2}(x,t)\ \delta\left(\xi - u_{\alpha+1/2}(x,t)\right), \tag{1.77}$$

pour $\alpha = 0,\dots,N$ et où δ désigne la distribution de Dirac. On a alors la proposition suivante :

Proposition 1.5.10 (Bernard, B., Bristeau, Sainte-Marie)**.** *Les fonctions (C^j) sont des solutions fortes du système (1.72) -(1.74) sans terme de réaction si et seulement si les équilibres de Gibbs $\{U_\alpha^j(x,t,\xi)\}_{\alpha=1}^N$ definis par (1.75) sont solutions des équations cinétiques*

$$\frac{\partial U_\alpha^j}{\partial t} + \xi \frac{\partial U_\alpha^j}{\partial x} - V_{\alpha+1/2}^j + V_{\alpha-1/2}^j = Q_{U_\alpha^j}, \tag{1.78}$$

pour $\alpha = 1,\dots,N$, $j = 1\dots3$ avec $\{N_{\alpha+1/2}(x,t,\xi), V_{\alpha+1/2}^j(x,t,\xi)\}_{\alpha=0}^N$ vérifiant (1.77)-(1.76).

Les quantités $Q_{U_\alpha^j} = Q_{U_\alpha^j}(x,t,\xi)$ sont des termes de collision nuls au niveau macroscopique, c'est à dire qu'ils satisfont, pour presque tout (t,x)

$$\int_{\mathbb{R}} Q_{U_\alpha^j} d\xi = 0, \quad \int_{\mathbb{R}} \xi Q_{U_\alpha^j} d\xi = 0, \quad \textit{et} \qquad \int_{\mathbb{R}} \xi^2 Q_{U_\alpha^j} d\xi = 0. \tag{1.79}$$

Finalement, une discrétisation des équations cinétiques, comme expliquée sur le modèle de Saint-Venant dans la Section 1.5.1 aboutit à un schéma numérique qui, sous une certaine condition CFL, assure positivité de la hauteur d'eau, conservation des quantités physiologiques. Les simulations exposées dans cette thèse sont effectuées à l'ordre deux en espace par une méthode de reconstruction des variables et on améliore l'ordre en temps par un schéma de Heun. Elles montrent principalement l'état de l'hydrodynamique du bassin et les courbes de production de carbone et de consommation d'azote.

L'étude porte ensuite sur les trajectoires lagrangiennes générées par ces simulations et qui sont d'une grande aide pour les biologistes. En effet, comme exprimé plus haut, il existe de nombreux modèles de photosynthèse, variant entre eux par le niveau de détail qu'ils proposent. La connaissance des variations lumineuses subies par les algues, qui est donnée par la reconstruction des trajectoires lagrangiennes, permet alors de mieux déterminer les constantes de temps en jeu et les phénomènes prédominants. Ainsi, une meilleure version pourrait être proposée en lieu et place du modèle de Droop étudié dans cette thèse.

Enfin, un code tridimensionnel a été élaboré et les premiers résultats son exposés dans le Chapitre 5.

1.6 Assimilation de données pour les lois de conservation hyperboliques admettant une description cinétique

1.6.1 Etat de l'art

L'assimilation de données est un terme qui désigne une large classe de méthodes destinées à estimer l'état et les paramètres d'un système en combinant à la fois les informations fournies par un modèle numérique, et celles apportées par des observations. La necessité de combiner modèle et données est d'abord apparue dans les domaines de la météorologie et de l'océanographie. Une des premières tentatives de prédiction de la météo fut faite en 1922 par Richardson et sa "forecast factory" [122]. Afin d'avoir une donnée initiale complète pour lancer son modèle de prédiction numérique, il interpole les données au temps 0. Mais l'interpolation ne respecte pas les contraintes physiques du modèle et la notion de CFL n'a pas encore été introduite dans la résolution numérique des équations : les résultats sont mauvais. Puis, dans les années 50, l'analyse de Cressman [48] introduit l'idée qu'il faut pondérer l'action des observations et du modèle en respectant un rayon d' influence des observations. Mais là encore la méthode est trop simple pour donner des résultats satisfaisants. Dans les années 70, Hoke et Anthes [75] modifient pour la première fois les équations pour les contraindre vers les données. Ils créent, sans le nommer, un observateur de Luenberger, qui sera plus tard repris dans la communauté d'assimilation de données par le terme de *nudging* [11, 13]. Enfin, les méthodes plus élaborées apparaissent, que l'on peut classer en deux catégories: les méthodes séquentielles et les méthodes variationnelles. Les premières, un peu comme le fait l'observateur de Luenberger, consistent à incorporer dans la dynamique du système un terme de correction basé sur l'écart entre les données et le modèle. On s'attend à converger en temps vers le système réel, mais on ne retrouve pas la condition initiale. L'observateur le plus populaire est le filtre de Kalman, optimal dans le cas de systèmes linéaires [21]. Mais l'inconvénient est qu' il manipule des matrices pleines dont la taille dépend de la dimension du problème et des observations. Les méthodes variationnelles quant à elles sont des méthodes de minimisation sous contraintes. L'algorithme le plus répandu est le 4D-VAR, qui minimise une fonction coût du type

$$J(x) = (x - x_b)^T \boldsymbol{B}^{-1} (x - x_b) + \sum_{i=0}^{n} (y_i - H[x_i])^T \boldsymbol{R_i}^{-1} (y_i - H[x_i]), \tag{1.80}$$

où $\boldsymbol{B}$ est la matrice de covariance des erreurs d'ébauche, $\boldsymbol{R_i}$, y_i, x_i sont respectivement la matrice de covariance d'erreurs d'observation, le vecteur observation au temps et le vecteur d'état au temps t_i, x_b est le terme d'ébauche (condition initiale précédemment trouvée ou conjecturée), et x la condition initiale et H est l'opérateur d'observation. La résolution de ce problème nécessite alors le calcul du gradient de J, en résolvant une équation adjointe qui peut nécessiter de nombreuses itérations.

Les deux dernières méthodes sont de nos jours les plus populaires, mais comme exprimé plus haut, elles peuvent être difficiles à mettre en oeuvre. Nous nous intéressons plutôt à l'observateur de Luenberger introduit il y a plus longtemps, mais qui a récemment regagné

de l'intérêt par sa simplicité. Des améliorations sont proposées, comme le Back and Forth Nudging [11, 13], afin de pouvoir déterminer la meilleure donnée initiale, ou l'optimisation des coefficients de nudging [145]. Le Chapitre 6 ne propose pas une amélioration de cette méthode, mais plutôt un nouveau cadre pour l'utiliser sur des systèmes de lois de conservation hyperboliques. Ce nouveau cadre est lié à la description cinétique des lois de conservation, qui a déjà été utilisée dans cette thèse dans le Chapitre 4 pour la création de schémas numériques.

Les principaux résultats de ce chapitre se classent en deux parties. Les premiers vont concerner des résultats de convergence pour les lois de conservation scalaires, et les seconds sont des résultats sur le système de Saint-Venant. Comme il sera exprimé plus tard dans le Chapitre 6, la méthode de nudging cinétique, quand elle est appliquée aux lois de conservations scalaires, offre certes un cadre théorique avantageux, mais ne permet pas en pratique de construire de nouveaux schémas numériques pour l'équation de l'observateur. Par contre, la portée de ce travail est bien plus importante en ce qui concerne les équations de Saint-Venant, car il offre une méthode constructive d'un nouvel observateur.

Dans la suite, on désignera par V_p l'espace $L^p(\mathbb{R}^d_x \times \mathbb{R}_\xi)$.

1.6.2 Lois de conservation scalaires en données complètes

Sans s'attarder sur les preuves, car cela sera fait dans le Chapitre 6, on donne ici les principaux résultats pour les lois de conservation scalaires du type

$$\begin{aligned} \partial_t u + \sum_{i=1}^{d} \partial_{x_i} A_i(u) = 0, \\ u(t=0,x) = u_0(x). \end{aligned} \tag{1.81}$$

La théorie de la description cinétique [112] nous indique que (1.81), augmentée de toutes ses inégalités d'entropie est équivalente à

$$\begin{cases} \partial_t M(t,x,\xi) + a(\xi)\cdot \nabla_x M(t,x,\xi) = \nabla_\xi m(t,x,\xi) \\ M(0,x,\xi) = \chi(\xi, u_0(x)) \end{cases} \tag{1.82}$$

où $M(t,x,\xi) = \chi(\xi, u(t,x))$ vérifie

$$\chi(\xi,u) = \begin{cases} +1, & \text{for } 0 < \xi < u \\ -1, & \text{for } u < \xi < 0 \\ 0, & \text{sinon,} \end{cases} \tag{1.83}$$

m est une mesure bornée positive et

$$a(\xi) = \left(A_1'(\xi), A_2'(\xi), \dots, A_d'(\xi)\right).$$

On considère une solution exacte de (1.82), et on écrit l'équation vérifiée par un observateur de Luenberger:

$$\begin{cases} \dfrac{\partial}{\partial t} f(t,x,\xi) + a(\xi)\cdot\nabla_x f(t,x,\xi) + \lambda f(t,x,\xi) = \lambda M(t,x,\xi), \\ f(t,x,\xi=0) = f_0(x,\xi). \end{cases} \tag{1.84}$$

On va alors distinguer plusieurs cas de figures pour énoncer des résultats de convergence, tout d'abord en données complètes. Le premier résultat concerne les cas où les données sont très régulières. Dans ce cas, on peut considérer que les collisions sont nulles ($m = 0$) et on obtient facilement cette proposition

Proposition 1.6.1 (B., Moireau, Perthame, Sainte-Marie)**.** *Soit $M \in C([0,T], V_1)$ vérifiant (1.82) avec $m(t,x,\xi) = 0$ et $f \in C(\mathbb{R}^+; V_1)$ vérifiant (1.84), alors*

$$\|f - M\|_{V_1} \underset{t\to+\infty}{\longrightarrow} 0, \tag{1.85}$$

et la décroissance est exponentielle en temps avec un taux de convergence λ.

Remarque 1.6.2. *Ce résultat montre la convergence des densités au niveau cinétique. Pour avoir la convergence des données macroscopiques, il faut encore intégrer en ξ. Mais cela ne pose pas problème car les densités sont prises à support compact en ξ.*

Une deuxième proposition consiste à considérer encore une fois que les données proviennent exactement de l'équation (1.82) mais qu'elles ne sont pas régulières. La présence du terme de collision Q nous empêche d'avoir une propriété de convergence aussi forte en temps. Néanmoins, on peut prouver une convergence quand le coefficient de nudging tend vers l'infini grâce à la borne supérieure donnée par ce théorème:

Théorème 1.6.1 (B., Moireau, Perthame, Sainte-Marie)**.** *Soit $M \in C([0,T], V_1)$ vérifiant (1.82) avec $u_0 \in L^1(\mathbb{R}^d)$ et $f \in C(\mathbb{R}^+; V_1)$ vérifiant (1.84) avec $f_0 \in V_1$, alors, pour un module de continuité $\omega(T,\cdot)$*

$$\|f(T) - M(T)\|_{V_1} \le \|f_0 - f_{\lambda,0}\|_{V_1} e^{-\lambda T} + \omega(T, \frac{1}{\lambda}). \tag{1.86}$$

De plus, si $u_0 \in L^\infty \cap L^1 \cap BV(\mathbb{R}^d)$, la dépendance en λ peut être précisée:

$$\|f(T) - M(T)\|_{V_1} \le \|f_0 - f_{\lambda,0}\|_{V_1} e^{-\lambda T} + C(d)\|a\|_{L^\infty(-K,K)} \sqrt{\frac{T\|u_0\|_{BV(\mathbb{R}^d)}}{\lambda}}. \tag{1.87}$$

Enfin, le dernier théorème concernant l'assimilation de données dans la cas idéal d'observations complètes est fait pour le cas de données inconnues (on ne connait plus l'équation (1.82)), mais régulières tout de même:

Théorème 1.6.2 (B., Moireau, Perthame, Sainte-Marie)**.** *Soit $p = 1$ ou $p = 2$. Soit $M(t,x,\xi) \in C([0,T],V_p)$ et $f(t,x,\xi) \in C([0,T],\, V_p)$ la solution de*

$$\begin{aligned} &\frac{\partial}{\partial t} f(t,x,\xi) + a(\xi)\cdot\nabla_x f(t,x,\xi) + \lambda f(t,x,\xi) = \lambda M(t,x,\xi), \\ &f(t=0,x,\xi) = f_0(x,\xi), \end{aligned} \tag{1.88}$$

avec f_0 et M_0 in L^p. Supposons de plus $\dfrac{\partial M}{\partial t} + a(\xi)\cdot\nabla_x M = Q \in C([0,T],V_p)$. Alors,

$$\|f(T) - M(T)\|_{V_p} \le \|f_0 - M_0\|_{V_p} e^{-\lambda T} + \frac{1-e^{-\lambda T}}{\lambda} \sup_{0\le t\le T} \|Q(t)\|_{V_p}$$

Ce théorème a été étendu au cas de données moins régulières par une méthode de régularisation par convolution.

1.6.3 Lois de conservation scalaires en données incomplètes ou bruitées

Par la suite, nous allons nous intéresser à des situations plus réelles, avec des données bruitées, ou incomplètes. On commence tout d'abord par ajouter un bruit sur l'équation de l'observateur. Ce bruit est supposé d'amplitude non négligeable dans une norme L^2, mais sera plus faible dans une norme adaptée. Par des effets régularisants bien connus des équations cinétiques, on pourra alors déduire une borne supérieure sur la moyenne en ξ de l'erreur. C'est à dire une borne sur l'erreur entre les variables macroscopiques.

On considèrera la situation où le coefficient d'advection est linéaire en ξ (comme c'est le cas par exemple pour l'équation de Burgers), puis celle où il ne l'est pas. Le cas linéaire s'écrit comme suit:

$$\xi\cdot\nabla_x f(x,\xi) + \lambda f(x,\xi) = \lambda M(x,\xi) + \lambda \frac{\partial^\alpha E}{\partial x^\alpha} \tag{1.89}$$

avec

$$\xi\cdot\nabla_x M(x,\xi) = Q(x,\xi) \in V_2, \tag{1.90}$$

où α est un multi-indices $(\alpha_1,\alpha_2,\dots\alpha_n)$ qui satisfait $\alpha = \alpha_1+\alpha_2+\ldots+\alpha_n$,

$$\frac{\partial^\alpha E}{\partial x^\alpha} \;=\; \frac{\partial^\alpha E}{\partial x_1^{\alpha_1} x_2^{\alpha_2}\dots x_n^{\alpha_n}}$$

représente le bruit, et $E(t,x,\xi) \in V_2$. On désigne

$$\rho_\psi(t,x) = \int_{\mathbb{R}_\xi} \left(f(x,\xi) - M(x,\xi)\right)\psi(\xi)d\xi \tag{1.91}$$

la moyenne en ξ de l'erreur entre le modèle et les données. Alors on montre que pour un λ optimal, ρ appartient à un espace plus régulier que L^2 et on obtient une borne supérieure différente de celle obtenue dans L^2:

Théorème 1.6.3 (B., Moireau, Perthame, Sainte-Marie)**.** *Soit $M(x,\xi) \in V_2$ la solution de (1.90) et $f(x,\xi) \in V_2$ la solution du problème d'assimilation de données bruitées (1.89) pour $|\alpha| < \frac{1}{2}$. Alors $\exists\ \gamma$, $0 < \gamma \leq 1 - 2|\alpha|$ et une constante K telle que*

$$\|\dot{\hat{\rho}}_\psi\|^2_{H^{\gamma/2}(\mathbb{R}_x)} \leq K\|\partial^\alpha E\|^2_{V_2}\left(\frac{\|\hat{E}\|_{\hat{V}_2}}{\|\partial^\alpha E\|^2_{V_2}}\right)^{\frac{\gamma}{1-|\alpha|}} + \mathrm{o}\left(\|\hat{E}\|_{V_2}^{\frac{2+\gamma}{1-|\alpha|}}\right) \tag{1.92}$$

qui tend alors vers 0 quand $\|\hat{E}\|_{V_2}$ tends vers 0. Cette inégalité est obtenue pour la valeur optimale de λ,

$$\lambda_{opt} = K\|\hat{Q}\|_{\hat{V}_2}\left(\frac{\|\partial^\alpha E\|^{2\alpha}_{V_2}}{\|\hat{E}\|_{\hat{V}_2}}\right)^{\frac{1}{1-\alpha}}, \tag{1.93}$$

où K est une constante.

La démonstration est basée sur une analyse de Fourier, et quelques résultats classiques dans la théorie des lemmes de moyenne pour les équations cinétiques [29, 51, 65, 79, 116]. Ensuite, dans le cas où le coefficient n'est pas linéaire, on travaille à partir de cette équation:

$$a(\xi)\cdot\nabla_x f(x,\xi) + \lambda f(x,\xi) = \lambda M(x,\xi) + \lambda\frac{\partial^\alpha E}{\partial x^\alpha} \tag{1.94}$$

avec

$$a(\xi)\cdot\nabla_x M(x,\xi) = Q(x,\xi) \in L^2(\mathbb{R}^N_x \times \mathbb{R}_\xi), \tag{1.95}$$

où a est un flux non dégénéré. Alors,

Théorème 1.6.4. *Soit $M(x,\xi) \in V_2$ solution de (1.95) et $f(x,\xi) \in V_2$ solution du problème d'assimilation de données bruitées (1.94). Alors, il existe β, $0 < \beta < 1$, γ, $0 < \gamma < \beta - 2|\alpha|$ et une constante K telle que*

$$\|\dot{\hat{\rho}}_\psi\|^2_{H^{\gamma/2}(\mathbb{R}_x)} \leq K_1\|\partial^\alpha E\|^2_{V_2}\left(\frac{\|\hat{E}\|^{2-\beta}_{\hat{V}_2}}{\|\partial^\alpha E\|^2_{V_2}}\right)^{\frac{\gamma}{(|\alpha|+1)\beta-2|\alpha|}} + \mathrm{o}\left(\|\hat{E}\|_{V_2}^{\frac{(2-\beta)\gamma}{(|\alpha|+1)\beta-2|\alpha|}}\right) \tag{1.96}$$

qui est obtenue pour un λ optimal

$$\lambda_{opt} = K_2\|\hat{Q}\|_{\hat{V}_2}\left(\frac{\|\partial^\alpha E\|^{2\alpha}_{V_2}}{\|\hat{E}\|^{\beta}_{\hat{V}_2}}\right)^{\frac{1}{(\alpha+1)\beta-2\alpha}} \tag{1.97}$$

où K_1 et K_2 sont des constantes.

Ces deux études ont été adaptées au cas non stationnaire. Cela fait intervenir quelques autres résultats intermédiaires et les estimations sont moins évidentes.

Dans une autre étude, nous nous intéressons au cas de données non complètes en temps. On estime qu'on a accès, pour des temps discrets t_k, à une moyenne temporelle des vari-

ables d'états, sur un petit intervalle de taille σ. Néanmoins, on considère que l'on connait l'équation vérifiée par les données:

$$\partial_t M(t,x,\xi) + a(\xi)\cdot\nabla_x M(t,x,\xi) = Q(t,x,\xi). \tag{1.98}$$

L'observateur satisfait l'équation

$$\partial_t f(t,x,\xi) + a(\xi)\cdot\nabla_x f(t,x,\xi) + \lambda\sum_{k\in I}\varphi_\sigma(t-t_k)f(t_k,x,\xi) = \lambda\sum_{k\in I}\varphi_\sigma(t-t_k)M(t_k,x,\xi), \tag{1.99}$$

où φ_σ est un noyau régularisant de support σ et $\{t_k,\, k\in I\}$ sont les temps d'observation. Alors,

Théorème 1.6.5 (B., Moireau, Perthame, Sainte-Marie)**.** *Supposons M solution de* (1.98) *et f solution de* (1.99)*. Si* $\mathrm{Card}(k, t_k \le T-\sigma) \neq 0$*, alors*

$$\begin{aligned}\|f(T)-M(T)\|_{V_1} \le{}& \|f_0-M_0\|_{V_1} e^{-\lambda\,\mathrm{Card}(k,t_k\le T-\sigma)}\\ &+\sigma\|\partial_t(f-M)\|_{L^\infty_t(M^1_x(\mathbb{R}_x),L^1(\mathbb{R}_\xi))}\left(1-e^{-\lambda\,\mathrm{Card}(k,t_k\le T+\sigma)}\right)\\ &+\sup_{0<t\le T}\|Q(t)\|_{V_1}\frac{1-e^{-\lambda\,\mathrm{Card}(k,t_k\le T+\sigma)}}{\lambda}\end{aligned} \tag{1.100}$$

Enfin, la dernière étude sur les lois de conservation scalaires a consisté à tenir compte d'observations partielles en espace. Ce travail mérite encore approfondissement. Pour l'instant, on peut considérer les résultats préliminaires d'observabilité et de stabilité exponentielle de l'erreur dans un cas unidimensionnel périodique, pour des solutions régulières des équations:

$$\begin{cases}\partial_t f(t,x,\xi) + a(\xi)\cdot\nabla_x f(t,x,\xi) = \lambda\mathbb{1}_{[a,b]}(x)(M(t,x,\xi)-f(t,x,\xi)),\\ f(0,x,\xi) = f_0(x,\xi),\\ f(t,0,\xi) = f(t,1,\xi),\end{cases} \tag{1.101}$$

où les observations proviennent du modèle

$$\begin{cases}\partial_t M(t,x,\xi) + a(\xi)\cdot\nabla_x M(t,x,\xi) = Q(t,x,\xi),\\ M(0,x,\xi) = M_0(x,\xi),\\ f(t,0,\xi) = f(t,1,\xi).\end{cases} \tag{1.102}$$

On définit le temps

$$X_{t,\xi}(x) = \int_0^t \mathbb{1}_{[a,b]}(x+a(\xi)s)ds, \tag{1.103}$$

qui représente le temps que la particule dont la position initiale était x passe dans l'intervalle $[a,b]$ entre 0 et t. Alors on peut énoncer la proposition suivante:

Proposition 1.6.3 (B., Moireau, Perthame, Sainte-Marie)**.** *Le problème* (1.101) *est observable* $\Leftrightarrow X^{inf}_{t,\xi} = \min_x X_{t,\xi} > 0$.

Et le résultat de stabilité suit:

Proposition 1.6.4 (B., Moireau, Perthame, Sainte-Marie)**.** *Soit* $f(t,x,\xi)$ *solution de* (1.101) *et* $M(t,x,\xi)$ *solution de* (1.102) *où* $Q(t,x,\xi) = 0$*. Si le problème d'assimilation de données* (1.101) *est observable, la stabilité exponentielle en temps est assurée dès que* $\lambda \geq \frac{t}{X^{inf}_t}$*, i.e.*

$$\|g(t)\|_{V_2} \leq \|g_0\|_{V_2} e^{-\lambda X^{inf}_t}. \tag{1.104}$$

Pour terminer la partie sur les lois de conservation scalaires, nous proposons une étude numérique sur l'équation de Burgers. Elle illustre les convergences dans le cas de données partielles en temps et espace, mais aussi l'existence d'un λ optimal dans le cas de données bruitées.

1.6.4 Système de Saint-Venant

Les résultats théoriques précédents sont motivés par des tests numériques sur l'équation de Saint-Venant qui donnent des premiers résultats de qualité surprenante compte tenu de la simplicité de l'approche. On s'intéresse donc dans cette partie au système de Saint-Venant unidimensionnel (déjà évoqué Section 1.5.1) mais que l'on rappelle:

$$\frac{\partial H}{\partial t} + \frac{\partial}{\partial x}\big(Hu\big) = 0, \tag{1.105}$$

$$\frac{\partial (Hu)}{\partial t} + \frac{\partial (Hu^2)}{\partial x} + \frac{g}{2}\frac{\partial H^2}{\partial x} = -gH\frac{\partial z_b}{\partial x}. \tag{1.106}$$

L'interprétation cinétique associée comprend, contrairement à ce qu'on a fait jusqu'ici, un terme source :

$$\partial_t M(t,x,\xi) + \xi \cdot \nabla_x M(t,x,\xi) - g\frac{\partial z_b}{\partial x}\partial_\xi M(t,x,\xi) = Q(t,x,\xi), \tag{1.107}$$

où

$$M(t,x,\xi) = \frac{H}{c}\chi\left(\frac{\xi - u}{c}\right), \tag{1.108}$$

et χ est une fonction à support compact qui vérifie

$$\begin{cases} \chi(a) = \chi(-a) \geq 0, \\ \displaystyle\int \chi(z)dz = \int z^2\chi(z)dz = 1. \end{cases} \tag{1.109}$$

Nous voulons montrer ici que la convergence de l'observateur vers une solution du système de Saint-Venant est possible si on n'observe que la hauteur d'eau. L'équation de l'observateur

cinétique devient

$$\partial_t f(t,x,\xi) + \xi \cdot \nabla_x f(t,x,\xi) - g\frac{\partial z_b}{\partial x}\partial_\xi f(t,x,\xi) = \lambda(\widetilde{M}(t,x,\xi) - f(t,x,\xi)), \tag{1.110}$$

où

$$\widetilde{M}(t,x,\xi) = \frac{H}{c}\chi\left(\frac{\xi-\hat{u}}{c}\right), \tag{1.111}$$

et $\hat{u}$ est la vitesse déduite de l'observateur f qui est en fait sous la forme:

$$f(t,x,\xi) = \frac{\hat{H}}{\hat{c}}\chi\left(\frac{\xi-\hat{u}}{\hat{c}}\right). \tag{1.112}$$

Et on prouve

Proposition 1.6.5 (B., Moireau, Perthame, Sainte-Marie)**.** *Soit* $(H(t,x),u(t,x)) \in L^\infty([0,T]\times\mathbb{R}_x)$ *solution de* (1.105) - (1.106)*, et* $M(t,x,\xi)$ *l'équilibre de Gibbs* (1.108)*. Soit* $f(t,x,\xi)$ *satisfaisant* (1.110)*. Si* $\widetilde{M}$ *possède la régularité définie par*

$$\partial_t\widetilde{M} + \xi\cdot\nabla_x\widetilde{M} + g\frac{\partial z_b}{\partial x}\left(\frac{\xi-u}{c^2}\right)\widetilde{M} = Q \in C([0,T],V_1), \tag{1.113}$$

alors

$$\|f(T) - M(T)\|_{V_1} \underset{\lambda\to+\infty}{\longrightarrow} 0. \tag{1.114}$$

Avec ce nouvel observateur, on est capable de construire un schéma entropique pour l'assimilation de données sur les équations de Saint-Venant. On l'étend même aux équations de Saint-Venant non-hydrostatiques avec des résultats numériques satisfaisants.

1.7 Conclusion et Perspectives

Le problème de modélisation de l'aquaculture destinée à la production de biocarburants conduit à la simulation de systèmes de lois de conservations de type Saint-Venant. Ceux-ci mènent à se poser des questions théoriques inattendues et difficiles sur les formulations cinétiques. Nous y avons apporté quelques outils qui permettent de simuler le cas du raceway, et de le valider, que ce soit par la recherche de solutions analytiques ou par une technique innovante d'assimilation de données. Par ailleurs, la construction d'un code C++ pour simuler les écoulements à surface libre tridimensionnels a permis de démontrer l'intérêt de notre démarche aux biologistes, qui l'utilisent déjà pour simuler des trajectoires lagrangiennes de particules. Ce code continue d'être validé, maintenu et amélioré au sein de l'équipe Ange par un ingénieur INRIA, Raouf Hamouda.

1.7.1 Perpsectives pour le couplage hydrodynamique - biologie

Amélioration du code C++ Jusqu'à présent, les équations simulées sont hydrostatiques. En première approche, nous avons pu justifier cette hypothèse. Néanmoins, il reste vrai que la roue à aube induit des effets non hydrostatiques qui sont suceptibles de modifier les trajectoires lagrangiennes. La théorie est déjà disponible dans [126]. Reste à trouver un bon schéma numérique et à l'implémenter. Par ailleurs, les validations analytiques ne sont pas encore possibles.

Modélisation d'autres phénomènes Les raceways sont des domaines bien plus complexes que ce que nous avons pour l'instant modélisé. La température, et par voie de conséquence l'évaporation de l'eau jouent un grand rôle dans la physiologie des algues. De même, la sédimentation des nutriments va accélérer l'hétérogénéité qui peut apparaitre quand le bassin n'est pas assez agité. Ce genre de phénomènes mérite d'être intégré au modèle pour améliorer son réalisme.

Amélioration du mélange Dans [134], Strook *et al.* décrivent un système de mélange innovant en microfluidique. Ils rencontrent en effet le problème de flots laminaires dans les microtubes dans des conditions usuelles d'utilisation. Au moyen de bas-relief implantés sur le sol, ils parviennent à créer des turbulences qui homogénéisent le fluide. On peut penser à introduire de tels fonds dans le code pour en observer l'effet.

Adaptation du code à d'autre situations Le modèle est capable de rentre compte d'autres situations impliquant des interactions hydrodynamique biologie. Citons par exemple la simulation de l'invasion d'algues dans certaines régions côtières du monde, comme le Chili ou la Guadeloupe.

1.7.2 Perpsectives pour l'assimilation de données de systèmes hyperboliques

Termes sources Tous les résultats du Chapitre 6 ne concernent pas les lois de conservation scalaires avec termes source. Une proposition est faite sur le traitement du terme de topographie pour le système de Saint-Venant mais cela peut être généralisé.

Filtre de Kalman Le formalisme cinétique permet de travailler sur une équation linéaire à ξ fixé. Toute la non-linéarité se retrouve à la fois dans l'écriture de l'équilibre de Gibbs à partir des variables macroscopiques mais aussi dans le terme de collisions que l'on nomme souvent Q. Nous voudrions étudier la faisabilité d'un filtre de Kalman au niveau cinétique, que l'on pourrait par la suite moyenner en ξ pour obtenir un vrai filtre de Kalman macroscopique.

Entropie relative L'entropie relative est un outil qui permet d'étudier le comportement de deux solutions l'une par rapport à l'autre, qui est souvent utilisé pour montrer des

convergences et qui est bien rodé pour le cas scalaire. Le formalisme cinétique des systèmes de conservation hyperboliques peut permettre de bien utiliser cet outil mathématique pour prouver la convergence des observateurs.

Assimilation de données dans le code hydro-bio Bien évidemment, il sera intéressant d'inclure les données hydrodynamiques collectées par l'INRA et NASKÉO sur le raceway expérimental de Narbonne pour contraindre le modèle et récupérer ainsi des trajectoires lagrangiennes plus exactes.

2 Introduction (English)

2.1 The project

The idea of this thesis was born with the following observation: in oceans, lakes or industrial raceways, there is an essential need to study the coupling between hydrodynamics and biology, as many phenomena are directly influenced by it - carbon fluxes, eutrophication, migration or growth of many biological species. Because of the multiscale properties of the system and the use of sophisticated models and method for its numerical simulation, the coupling is delicate to handle. It also requires the joint efforts of mathematicians, biologists or oceanographers. That is what I benefited through the three years of my thesis. I completed my Ph.D thesis under the supervision of Benoit Perthame and Jacques Sainte-Marie, in the team ANGE (a CETMEF - INRIA - CNRS/UPMC joint team). This group is devoted to the study of free surface geophysical flows, such as river, lakes or coastal areas. I also had the opportunity to collaborate with scientists from other domains, especially engineers and biologists. Among them, let me mention Olivier Bernard and Antoine Sciandra, from team BIOCORE (INRIA - INRA - CNRS/UPMC joint team) from Villefranche-sur-Mer, who are experts in phytoplankton growth. I would also mention Bruno Sialve who is research engineer at Naskéo. Those scientists are now members of a large research and development project based in France and entitled GreenStars. It involves, scientists and companies whose aim is to explore the use of micro-algae to produce third generation biofuels.

2.2 Context of the problem

2.2.1 Contribution to the study of geophysical flows

Brief history of geophysical flows As the year 2013 has been declared year for the *Mathematics of Planet Earth*[1], we would like to incorporate this thesis in the vast framework of free surface geophysical flows. Without many details, we will recall in the following paragraphs the historical scientific breakthroughs in this domain, the current challenges and we will set our work with regards to those informations.

Geophysical flows are commonly represented by the free surface incompressible fluid mechanics equations: Euler equations[46, 139], suggested in 1757 in its publication *Principes généraux du mouvement des fluides*, or Navier-Stokes equations [137], described in 1840. The latter ones can be considered as an extension of the first ones in the case of viscous fluids. Nevertheless, when dealing with geophysical flows of water, viscous effects, though real, have few importance comparing to convection or pressure phenomena. Hence we can consider that geophysical flows are well represented by Euler equations. A part of this work is dedicated to them: we propose a new set of analytical solutions that will enable us to test numerical codes. However, given the characteristic dimensions of the problems, the use of simplified models must be investigated, both at the analytical and numerical level. In this type of flows indeed, the free surface raises non trivial problems for the numerical simulation (varying topology of the domain, moving meshes). Among simplified models, some permit an easy treatment of the free surface, and the most important from them are the ones describing shallow water flows. In 1871, Barré de Saint-Venant comes up with a new system: the Saint-Venant system [19]. It has been proved later that this system is an approximation of Euler equations when assuming two hypotheses [61]:

Hyp (1): the horizontal velocity of the fluid is well represented by its mean along the vertical dimension,

Hyp (2): the fluid pressure is hydrostatic.

Those new equations exhibit the main advantage of being able to represent a tridimensional problem on a time varying domain through a bidimensional system on an stationary domain. The mathematical analysis of Saint-Venant equations requires tools from the theory of hyperbolic conservation laws. It is not trivial and several questions are still open (preservation of non trivial equilibria, obtaining of a discrete entropy). However, the needs and challenges are elsewhere. They come from the necessity to free oneself from the restrictive hypothesis (1) that prevents from representing stratified flows, and get closer to the original Euler or Navier-Stokes equations. The first models appearing in this sense are multilayer models that describe the fluid as a superimposition of Saint-Venant systems [2, 30]. But this modeling reduces to considering each layer as a non-miscible fluid, which is another important limitation. Another approach [9, 10], that we use in this thesis, consists in applying a Galerkin decomposition of each variable along the vertical dimension (horizontal

[1] http://mpe2013.org

velocity, vertical velocity, water height), followed by an integration of Navier-Stokes (or Euler) equations over each layer so defined. The variables are thus constant by layers and not uniform along the whole water depth anymore. This allows for the description of vertically heterogeneous flows. Eventually, another class of models tries to reintegrate the vertical acceleration in order to avoid hypothesis (2) [36, 37]. Those non-hydrostatic models will for instance better represent the breaking of a tidal wave on the shores.

Coupling Problems arising in geosciences naturally lead to the study of coupled systems. It can either be the coupling between two miscible fluids stratified by their density (cold water and hot water), or between a fluid and a structure (wave breaking on an embankment), but also between a fluid and a biological entity (algae). As the society gets always more concerned about sustainable development, important questions involving applied mathematics skills arise, especially concerning those couplings. Among the sectors of activity enjoying a notable boom, we can mention marine energies, which try to produce electricity from wave energy, tides and currents using watermills or optimizing the bathymetry of a geometric domain. We can also cite the study of lacustrian ecosystems facing atmospheric, climatic or pollution forcings. This enables to better understand important phenomenon such as eutrophication. Eventually, and this is what we will be focusing on in this thesis, microalgae culture is in vogue. Some species are capable of storing large amounts of lipids and could lead to the production of third generation biofuels with a better productivity as superior plants did for first generation biofuels. The modeling of the raceway hydrodynamics and its coupling with biology is of high importance for the success of such a project. As it will be explained later on, a high heterogeneity reigns in the pond, essentially due to a strong light intensity gradient. We therefore have to model a free surface flow problem with non negligible vertical inhomogeneities (which rules out any Saint-Venant modeling), and containing a reaction diffusion biological model. Besides, we need to take into account the fact that the time constants of the biological model are far greater than the hydrodynamical ones. A typical simulation should last several days and we need efficiency on the computation time. Distributed models exhibited in the previous paragraph will enable a suitable handling of the problem.

Validation In geosciences, physical phenomena are plentiful. We only evoked problems involving water, but geophysical flows can also bring into play more dense fluids for example in avalanches, landslides or eruptions. This multitude of phenomena gives rise to a multitude of models, whose relevance should be judged regarding on the one hand the way they are derived from the original equations, and on the other hand their ability to reproduce real life data. Once the model is chosen and validated, it is indeed interesting to exploit its forecasting efficiency. In that context, data assimilation is a key tool, to improve predictions using past observations. For systems with nonlinear hyperbolic features, like the Saint-Venant system, lots of questions remain open, that we will tackle in this work.

With the previous paragraphs, we wanted to put in perspective this thesis in the frame-

work of geophysical flows. This is indeed the common thread of every chapter. Let us focus now on the aquaculture problem for biofuel production.

2.2.2 European objectives

In December 2008, the EU comes to the following agreement concerning renewable energies: before the year 2020, 10% of the needs of carburant in the transport field should be provided by green fuels, hydrogene or green electricity. Moreover, the directive precises that the day it will come into force, the EU members should check that the proportion of biofuel already used by them enables a reduction of 35% in carbon emission compared to fossil fuels. This reduction should reach 50% in 2017, 60% in 2018.

Behind those conditions, we perceive the growing concerns about the current first generation biofuels.The first generation biofuels refer to the fuels that have been derived from sources like starch, sugar, animal fats and vegetable oil. The oil is obtained using the conventional techniques of production. Some of the most popular types of first generation biofuels are: biodiesel, vegetable oil, biogas...However, ethanol and biodiesel for instance are accused of making alimentation grow up in price whereas they threaten biodiversity. That is the reason why the EU got involved in the second generation biofuels. Second generation biofuels are derived from lignocellulosic crops. Plants are made from lignin and cellulose. Technology allows these two components of a plant to be split. Then the cellulose can be fermented into alcohol in the same way as a first generation biofuel. However, the conversion of the lignin biomass into sugar requires expensive technologies, with preliminary treatments and a fermentation with special enzymes, which prevents it from being produced at a large scale. For those reasons, this technology is not supposed to replace first generation biofuels before 2020, and if it does, it will require a lot of biomass.

Thus, the last step are biofuels of the third generation such as algae and phytoplankton.

2.2.3 Aquaculture

Microalgae and cyanobacteries are bioorganisms whose size vary from 1 micron to 100 microns and are found in abundance in oceans, rivers, lakes...It is commonly admitted that there are more than 1 million algae species, compared to the 250000 superior plants ones. They use light as a source of energy in order to fix carbon dioxyde. Some species are able to store this carbon in the form of lipid. Moreover, autotroph species (as opposed to heterotroph species) only need inorganic carbon to grow. That is the reason why is it possible to consider them as a potential source of biofuel. After the 1973 energy crisis, the National Renewable Energy Laboratory (NREL) carried out studies to assess the potential of this kind of fuel. But the petrol baril was 5 times cheaper than today and the project was declared unprofitable.

High growth rate One of the most interesting caracteristics of microalgae is their high photosynthetic output rate. Defined as the ratio between the incident light energy and the energy actually stored in the plant, it is estimated that for optimal conditions, 10 moles of

photons are required to fix 1 mole of CO_2. Though this ratio is not different from other superior plants, it is easier to find optimal conditions in case of microorganisms living under water. Besides, in terrestrial vegetables, a non negligible part of CO_2 is used to create lignocellulosic molecules which cannot be used as a source of fuel (cf second generation biofuels). Those high output rates lead to high productivities.

Lipid synthesis As already mentioned before, microalgae and cyanobacteries contain lipids, usually in low proportions. Nevertheless, it has been shown that some candidates can significantly increase their lipid production under stress. Techniques such as nitrogen deficiency, thermal or osmotic shocks proved to be efficient. Thus, the intrinsic lipid level can reach 80% of the dry matter. Of course, those stress conditions cannot be applied indefinitely without inhibiting the growth. As a matter of fact, a compromise need to be found between calm growth (multiplication of the algae) and stressed growth (oil production). Propositions in two steps have been made to optimize it: algae grow in a photobioreactor (high output rate, no contamination...) (Figure 2.1 on the left) and then spend 2 days in a raceway (Figure 2.1 on the right), under nitrogen deficiency.

Figure 2.1: Left: Photobioreactor in IFREMER. Right: industrial raceway (Innovalg, 85). Photo IFREMER.

Harvest and purification The crop constitutes a limiting step for the production of biofuel since the algae are no more than a few microns large and have a density close to water. It is possible for some species to use only filtration but for most of them centrifugation techniques have to be carried out. Thus, this step is really energy demanding. Once the algae is collected, other techniques have to extract the lipids. In addition to classical methods using solvents, alternate methods are currently a research field.

Current barriers Let us mention here some of the barriers that have to be broken in order to make the algal biofuel ready for a wide production:

- microalgae do not withstand high illumination, cold or heat;
- microalgae have to contain a weighty amount of lipid while continuing to grow and divide. This is the compromise we already mentioned between lipid synthesis and growth;
- high costs need to be reduced: vitamins and oligo elements input, collection of algae, extraction of oil;
- contamination risks in the case of outdoor raceways;

Our objective is thus to model and study the coupling between hydrodynamics and biology, in the framework of aquaculture in raceways. For that purpose we choose a vertically distributed hydrodynamic model coming from hydrostatic Navier-Stokes equations and a Droop model for the biology, which will be improved with a light sensitivity. But more explanation will come later in that introduction.

2.3 Outline of the thesis

The theme of the thesis is thus the contribution to the study of geophysical flows through the particular problem of modeling algae growth in raceways. In order to achieve a good modeling of the problem, several directions have been studied during those three years. Once the model is chosen, the code developed and the numerical results obtained, it is indeed necessary to validate the numerical treatment of the model through analytical solutions and to improve the model itself through data assimilation.

The first part of the manuscript, consisting of Chapter 3 and summed up in Section 2.4 is dedicated to the research of analytical solution for both the hydrodynamics, modeled by the hydrostatic Euler equations, and the biology, modeled by a mere model of transport-reaction. This work enabled us to validate one the one hand our hydrodynamics code and on the other hand the coupling method we use. This study has been published in CMS.

The second part of the manuscript, consisting of Chapter 4 and Chapter 5 and summed up in Section 2.5, deals with the modeling and the simulation of the aquaculture problem in raceways. A complete study has been carried out in two dimensions and was published in M2AN. In three dimensions, a C^{++} code has been developed, which gave encouraging numerical results for the hydrodynamics of the pond. Besides, this code is currently maintained and extended by Raouf Hamouda, a computer scientist at INRIA, in order to remain a key tool in the ANGE project.

Eventually, the third part, consisting of Chapter 6 and summed up in Section 2.6, revolves around the theme of data assimilation for hyperbolic conservation laws. Making the most of the kinetic description methods of this kind of equations, we are capable of proposing an innovative strategy for data assimilation built from a Luenberger observer. This work is also the object of a publication.

2.4 Analytical solutions for free surface Euler equations

2.4.1 State of the art

Mathematical models arising from fluid dynamics often come from the well-known Navier-Stokes equations. They are globally difficult to analyze, both at the analytical and numerical level. Therefore it is tricky to validate the numerical schemes. An interesting solution, even if it cannot serve as a proof, is to compare the simulations with analytical solutions on test cases. For the purpose of studying the coupling between hydrodynamics and biology in an industrial pond, we first attempted to find analytical solutions to the hydrostatic and incompressible free surface Euler equations. The latter correspond to an inviscid version of Navier-Stokes equations, which is coherent with the study of geophysical flows. Then we looked for a plain biological system for which the analytical coupling would be possible.

In fluid dynamics, many contributions deal with a simplified version of the incompressible Navier-Stokes equations in the framework of shallow water flows. It is called the Saint-Venant system. Because of its nonlinear hyperbolic nature, this system admits non smooth solutions for which shocks can occur. Therefore it is necessary to build numerical schemes which are able to capture those shocks. With the aim of checking this point, MacDonalds [99, 100] proposes a set of analytical solutions showing a hydraulic jump when the fluvial flow becomes torrential. We follow his method in Chapter 3 to obtain stationary solutions for the free surface Euler equations. We also mention the works on Korteweg-de-Vries equation, which models the wave propagation when the water depth is low. This equation admits soliton type solutions [85]. Nonetheless, those models are only valid for shallow water flows, and the work we propose enables to extend the tools to solutions which are more heterogeneous along the vertical dimension. We point out the fact that those solutions do not correspond to any physical and realistic situation and mainly aim at the validation of numerical schemes.

2.4.2 Free surface incompressible Euler equations

Let us recall first the tridimensional incompressible and hydrostatic free surface Euler equations [34, 66] with gravity

$$\frac{\partial u}{\partial x} + \frac{\partial v}{\partial y} + \frac{\partial w}{\partial z} = 0, \tag{2.1}$$

$$\frac{\partial u}{\partial t} + u\frac{\partial u}{\partial x} + v\frac{\partial u}{\partial y} + w\frac{\partial u}{\partial z} + \frac{\partial p}{\partial x} = 0, \tag{2.2}$$

$$\frac{\partial v}{\partial t} + u\frac{\partial v}{\partial x} + v\frac{\partial v}{\partial y} + w\frac{\partial v}{\partial z} + \frac{\partial p}{\partial y} = 0, \tag{2.3}$$

$$\frac{\partial p}{\partial z} = -g, \tag{2.4}$$

where z represents the vertical direction. We consider this system for

$$t > 0, \quad (x, y) \in \Omega, \quad z_b(x, y) \leq z \leq \eta(x, y, t),$$

where Ω is a bounded domain of $\mathbb{R}^2$, $\eta(x,y,t)$ is the free surface elevation, $\mathbf{u}=(u,v,w)^T$ the velocity vector. Gravity is denoted g, p is the fluid pressure and z_b the topography. Thus the water height writes $H=\eta-z_b$. The system (2.1)-(2.4) is completed with boundary conditions. At the free surface, we impose a kinematic condition (the index s means that the variables are considered at the surface),

$$\frac{\partial \eta}{\partial t}+u_s\frac{\partial \eta}{\partial x}+v_s\frac{\partial \eta}{\partial y}-w_s=0, \tag{2.5}$$

but also a balance condition with the atmospheric pressure

$$p_s=p^a(x,y,t). \tag{2.6}$$

At the bottom we prescribe a no penetration condition (the index b means that the variables are considered at the bottom),

$$u_b\frac{\partial z_b}{\partial x}+v_b\frac{\partial z_b}{\partial y}-w_b=0. \tag{2.7}$$

2.4.3 Analytical solutions for hydrodynamics

We consider the bidimensional stationary case, with the horizontal domain $\Omega=[0,L_x]$. Hence the previous equations satisfy:

$$\frac{\partial}{\partial x}\int_{z_b}^{\eta} u\ dz=0, \tag{2.8}$$

$$w=-\frac{\partial}{\partial x}\int_{z_b}^{z} u\ dz, \tag{2.9}$$

$$u\frac{\partial u}{\partial x}+w\frac{\partial u}{\partial z}+g\frac{\partial \eta}{\partial x}=-\frac{\partial p^a}{\partial x}. \tag{2.10}$$

General smooth stationary solutions

The method is the following: given a water height and an admissible velocity field, we are looking for the topography that corresponds to the resolution of the free surface Euler system. Then, we find a family of smooth solutions:

Proposition 2.4.1 (B., Bristeau, Sainte-Marie)**.** *If α, β and $\overline{z}_b$ are three real constants, H_0 a non-negative real-valued function of class $C^1(\Omega)$ such that for all $x\in\Omega$ $\sin(\beta H_0(x))\neq 0$ then $u=u_{\alpha,\beta}$, $w=w_{\alpha,\beta}$ and z_b respectively defined by*

$$z_b = \overline{z}_b-H_0-\frac{\alpha^2\beta^2}{2g\sin^2(\beta H_0)}, \tag{2.11}$$

$$u_{\alpha,\beta} = \frac{\alpha\beta}{\sin(\beta H_0)}\cos(\beta(z-z_b)), \tag{2.12}$$

$$w_{\alpha,\beta} = \alpha\beta\left(\frac{\partial z_b}{\partial x}\frac{\cos(\beta(z-z_b))}{\sin(\beta H_0)}+\frac{\partial H_0}{\partial x}\frac{\sin(\beta(z-z_b))\cos(\beta H_0)}{\sin^2(\beta H_0)}\right), \tag{2.13}$$

satisfy the stationary Euler equations (2.8)-(2.10) *with* $\eta = H_0 + z_b$.

Stationary solutions with given topography

Afterwards, we study the stationary solutions for a given topography $z_b(x), x \in \Omega$. Once again, we propose to choose admissible solutions of type:

$$\begin{aligned} u_{\alpha,\beta} &= \frac{\alpha\beta}{\sin(\beta H)}\cos(\beta(z-z_b)) \\ w_{\alpha,\beta} &= \alpha\beta\left(\frac{\partial z_b}{\partial x}\frac{\cos(\beta(z-z_b))}{\sin(\beta H)} + \frac{\partial H}{\partial x}\frac{\sin(\beta(z-z_b))\cos(\beta H)}{\sin^2(\beta H)}\right) \end{aligned} \tag{2.14}$$

where $\alpha > 0$, β and a boundary value H ($H(0)$ or $H(L_x)$) are given. It remains to identify the water height at any point. In order to do so, we define the function

$$F_{\alpha,\beta} \,:\, x \mapsto gx + \frac{\alpha^2\beta^2}{2\sin^2(\beta x)}. \tag{2.15}$$

Then we state the following proposition which enables to determine if a continuous solution exists:

Proposition 2.4.2 (B., Bristeau, Sainte-Marie)**.** *If for any* $x \in \Omega$*, the problem*

$$F_{\alpha,\beta}(H(x)) = F_{\alpha,\beta}(H_{lim}) + g(z_{b,lim} - z_b(x)) = C_{\alpha,\beta,lim} - gz_b(x) \tag{2.16}$$

has a solution $H(x) \geq 0$*, then* $(H, u_{\alpha,\beta}, w_{\alpha,\beta})$ *is solution of (2.8)-(2.10). This is also expressed in the following manner: if the problem (2.16) admits a solution* H_m *in* $x = x_m$ *where the topography* z_b *is maximal, or equivalently if*

$$F^{min}_{\alpha,\beta} \leq C_{\alpha,\beta,lim} - gz_b(x_m),$$

then there exists a solution for any $x \in \Omega$*. Moreover, it is easy to prove that if* $z_b \in C^k(\Omega)$*,* $k \geq 1$ *then* $(H, u_{\alpha,\beta}) \in C^k(\Omega)$ *and* $w_{\alpha,\beta} \in C^{k-1}(\Omega)$.

Then, we naturally focus on situations when there exists some points x for which (2.16) has no solution. We denote by Ω_c the set of those points. We assume it is non empty, and that there exists at least one point x_c satisfying

$$z_{b,c} = \max_{x\in\Omega} z_b(x), \tag{2.17}$$

$$\left.\frac{\partial z_b}{\partial x}\right|_{x=x_c} = 0. \tag{2.18}$$

This point is necessarily in Ω_c. Without any loss of generality, we suppose that the topography admits only one bump. The point x_c is therefore unique. Upstream this point the topography is increasing. Downstream it is decreasing. For a more general topography, we shall divide the domain into several subdomains satisfying those constraints. We define also $H_{lim} = H(L_x)$ and we show that we are able to determine analytically $H_c = H(x_c)$.

Lemma 2.4.3 (B., Bristeau, Sainte-Marie)**.** *If Ω_c is non-empty, it contains at least x_c the interior point of maximum topography, and the water height at this point is defined by*

$$H_c = \frac{\arcsin r_c^2}{\beta}, \tag{2.19}$$

where

$$r_c = \sqrt{\frac{\sqrt[3]{12\alpha^4}\beta^2}{6g}\frac{-\sqrt[3]{12\alpha^4}\beta^2 + \left(\sqrt[3]{9g+\sqrt{12\alpha^4\beta^6+81g^2}}\right)^2}{\sqrt[3]{9g+\sqrt{12\alpha^4\beta^6+81g^2}}}}. \tag{2.20}$$

Over $[x_c, L_x]$, the solution might present a shock at an abscissa denoted x_s. We are capable of finding the water heights on either side of the shock, as well as its position by solving jump relations for stationary shocks. Hence, x_s, $H_{s,l}$ and $H_{s,r}$ are defined with the following proposition:

Proposition 2.4.4 (B., Bristeau, Sainte-Marie)**.** *Over $[x_c, L_x]$, if a shock occurs, then its position x_s and the water heights on both sides of it are defined through*

$$\left[\frac{g}{2}H^2 + \frac{\alpha^2\beta^2 H}{2\sin^2(\beta H)} + \frac{\alpha^2\beta}{2}\frac{\cos(\beta H)}{\sin(\beta H)}\right]_{H_{s,l}}^{H_{s,r}} = 0, \tag{2.21}$$

$$\frac{\alpha^2\beta^2}{2\sin^2(\beta H_c)} + g(H_c + z_{b,c}) = \frac{\alpha^2\beta^2}{2\sin^2(\beta H_{s,l})} + g(H_{s,l} + z_{b,s}), \tag{2.22}$$

$$\frac{\alpha^2\beta^2}{2\sin^2(\beta H_{lim})} + g(H_{lim} + z_{b,lim}) = \frac{\alpha^2\beta^2}{2\sin^2(\beta H_{s,r})} + g(H_{s,r} + z_{b,s}). \tag{2.23}$$

Then, over $[0, x_c]$, the solution is continuous and we use (2.16) to determine the water heights, using this time the value in x_c instead of the boundary value (in $x = L$) as a reference. Illustrations of those analytical solutions are given at the end of Chapter 3.

Many other hydrodynamics solutions are given in Chapter 3, among them an extension to the tridimensional case where the presence of the free surface is only partial.

2.4.4 Coupled analytical solutions for hydrodynamics and biology

Eventually, we propose a coupling with a tracer. This model represents the advection of a biological quantity in the hydrodynamic velocity field of free surface Euler equations and a reaction phenomenon. We do not pretend that the reaction term reproduces a real and physical situation. It rather allows to have an analytical solution of the equation presented hereafter coupled to the free surface Euler solutions studied previously:

$$u\frac{\partial T}{\partial x} + w\frac{\partial T}{\partial z} = \frac{T_0 - T}{\tau}, \tag{2.24}$$

where u and w are solutions of (2.8)-(2.9) for a given function H_0, defined by formulae (2.12) et (2.13). The function

$$T(x,z) = e^{-(H_0(x)-(z-z_b(x)))}, \tag{2.25}$$

with $T_0 = 0$ and

$$\frac{1}{\tau} = \alpha\beta \frac{\cos(\beta(z-z_b))}{\sin(\beta H_0)} \left(1 - \frac{\tan(\beta(z-z_b))}{\tan(\beta H_0)}\right) \frac{\partial H_0}{\partial x}, \tag{2.26}$$

is just right for it. This solution will be used to validate the study in Chapter 4.

2.5 Hydrodynamics and biology coupling for the simulation of microalgae culture in raceways

2.5.1 Hydrodynamics state of the art

The problem exhibited in Section 2.2 is a free surface hydrodynamics problem. The water is often considered as an incompressible fluid. However, the presence of the free surface implies interactions with the atmosphere and thus similarities with the study of compressible fluids. Besides, the raceway does not correspond to natural evolution conditions of the fluid. Though we will not take it into account as a first approximation, the microalgae concentrations are so high that it could induce effects on the water density.

The Navier-Stokes system

In the field of newtonian fluid dynamics, the starting point is the Navier-Stokes system. They contain almost every possible hydrodynamical phenomena: diffusion, convection...They stem indeed from the application of Newton's second law. We write them in in two dimensions for a free surface gravitational flow:

$$\frac{\partial \rho}{\partial t} + \frac{\partial \rho u}{\partial x} + \frac{\partial \rho w}{\partial z} = 0, \tag{2.27}$$

$$\frac{\partial \rho u}{\partial t} + \frac{\partial \rho u^2}{\partial x} + \frac{\partial \rho uw}{\partial z} + \frac{\partial p}{\partial x} = \frac{\partial \Sigma_{xx}}{\partial x} + \frac{\partial \Sigma_{xz}}{\partial z}, \tag{2.28}$$

$$\frac{\partial \rho w}{\partial t} + \frac{\partial \rho uw}{\partial x} + \frac{\partial \rho w^2}{\partial z} + \frac{\partial p}{\partial z} = -\rho g + \frac{\partial \Sigma_{zx}}{\partial x} + \frac{\partial \Sigma_{zz}}{\partial z}, \tag{2.29}$$

and we consider solutions for $t > t_0, \quad x \in \mathbb{R}, \quad z_b(x) \leq z \leq \eta(x,t)$, where η represents the surface elevation, $\mathbf{u} = (u,w)^T$ the velocity vector, $p(x,z,t)$ is the pressure, g is the gravitational force and ρ is the water density. The stress tensor is defined by

$$\Sigma_{xx} = 2\mu \frac{\partial u}{\partial x}, \quad \Sigma_{xz} = \mu \left(\frac{\partial u}{\partial z} + \frac{\partial w}{\partial x}\right), \quad \Sigma_{zz} = 2\mu \frac{\partial w}{\partial z}, \quad \Sigma_{zx} = \mu \left(\frac{\partial u}{\partial z} + \frac{\partial w}{\partial x}\right).$$

Evidently, we complete this system with boundary conditions. For the free surface, we have a kinematic boundary condition

$$\frac{\partial \eta}{\partial t} + u_s \frac{\partial \eta}{\partial x} - w_s = 0, \tag{2.30}$$

where the subscript s denotes the surface value. Considering that the air viscosity is negligible compared to the fluid viscosity, the stress continuity at the surface implies

$$\Sigma_T \mathbf{n}_s = -p^a \mathbf{n}_s, \tag{2.31}$$

where $p^a = p^a(x,t)$ is the given atmospheric pressure and Σ_T is the total stress tensor (it contains not only the viscosity terms, but also the pressure ones). At the bottom, there is classically a no-penetration condition:

$$\mathbf{u}_b.\mathbf{n}_b = 0, \quad \text{ou} \quad u_b \frac{\partial z_b}{\partial x} - w_b = 0. \tag{2.32}$$

For the stress tensor we will have:

$$\mathbf{t}_b.\Sigma_T \mathbf{n}_b = \kappa \mathbf{u}_b.\mathbf{t}_b, \tag{2.33}$$

where $\mathbf{t}_b$ is a unit vector satisfying $\mathbf{t}_b \cdot \mathbf{n}_b = 0$ and κ is a friction coefficient.

Since the air viscosity is negligible, the surface constraints are low and the free surface might happen to show a complex geometry. There exists several methods to capture this surface. Level-set methods, Lagrangian methods, moving meshes methods...But they prove to be costly and a precision loss is required to achieve reasonable computation times.

As far as simulation methods are concerned, the Navier-Stokes equations are traditionally considered as a parabolic system. Consequently, finite element methods are preferably used. However, even if those methods have already been applied to free surface flows [74, 82], they do not treat efficiently:

- non-smooth solutions,
- drying and flooding phenomena, when the water height tends to zero or the topology of the domain varies,
- the conservation of potential tracers.

In our case, we will not use that kind of method on Navier-Stokes equations. As pointed out in the beginning of this introduction, advection and pressure terms prevail on diffusion in gravity driven geophysical flows. Furthermore, our problem is characterized by a small water depth (around thirty centimeters versus several dozen meters long) and by an absolute need for conservativity (because of the biological species in the water). We could think of the saint-Venant system as a more suitable model.

A simplified model

The Saint-Venant system was originally introduced in 1871 [19] by an analysis of the forces applied to a fluid section, in a rectangular canal with a flat bottom. When completed with adequate source terms, this system has proved its effectiveness for a wide class of geophysical problems such as rivers, coastal areas, oceans or even avalanches. It describes flows via two variables: the water height $H(t,x,y)$ and the mean vertical velocity of the fluid $\boldsymbol{u}(t,x,y)$. It is written here in its two-dimensional version that includes a topographical source term.

$$\partial_t H + \operatorname{div}(H\boldsymbol{u}) = 0, \tag{2.34}$$

$$\partial_t H\boldsymbol{u} + \operatorname{div}(H\boldsymbol{u}\otimes\boldsymbol{u}) + \nabla(\frac{g}{2}H^2) = -gH\nabla z_b, \tag{2.35}$$

where g denotes the g-force and $z_b(x,y)$ the bottom topography, thus making $H + z_b$ the altitude of the free surface. The benefit of the Saint-Venant systems are clear: it allows, thanks to its well chosen variable system, to simulate a tridimensional problem on a time-varying domain via a bidimensional system on a fixed domain.

Naturally this comes with a price, namely a loss in precision, and the question of the validity domain of such system arises. Answers may be obtained by retrieving the Saint-Venant system from more generic systems. Indeed in [133] or [142], it is shown that it can be derived from the Euler equations. Other works [50, 58, 101] focused on its link with the Navier-Stokes equations. These articles derive from [61] in which a method is proposed to reduce the two-dimensional Navier-Stokes equations to a viscous Saint-Venant system. In particular, we learn from those works that the Saint-Venant system is a good approximation of the Navier-Stokes equations provided two assumptions hold. First, the hypothesis of shallow water assumes that the domain length is much larger than its depth. Second, the hydrostatic assumption claims that the vertical acceleration should be negligible and vertical variations of the fluid pressure are mainly due to gravity. Furthermore, other restrictions apply when one wants to avoid mathematical pitfalls: variations of the bottom should be of low magnitude, and viscosity as well as bottom friction must be weak.

We then discuss the numerical methods adapted to the Saint-Venant system, as they raise some points that we deem paramount in our own modeling. The Saint-Venant system can be easily expressed as a hyperbolic conservation law to which we may even add an energy inequality, hence the use of finite volume methods for its simulation [28, 62, 92]. These methods are by nature conservative and handle particularly well the solutions discontinuities. Moreover, unlike finite differences approaches, they can be used on unstructured meshes. Let us recall that such methods consist in splitting the domain in cells and integrating the equations on each cell over a time step. They thus involve local averages of the solution in each cell, while divergence terms are converted in surface integrals that represent the exchanged flux between the different cells. We can sum up a one-dimensional

finite volume scheme as follows

$$U_i^{n+1} = U_i^n - \frac{\Delta t^n}{\Delta x_i}\left(F_{i+1/2}^n - F_{i-1/2}^n\right) + \Delta t^n S_i^n \tag{2.36}$$

The whole work lies in the determination of the flux $F_{i+1/2}^n$ between cells C_i and C_{i+1}. Reviews of different schemes are available in [62, 92, 139]. Such schemes should have good properties of consistency and stability. For Saint-Venant equations, this translates in the guarantee of a positive water height and the preservation of equilibria at rest. Unfortunately, while finite volume schemes are adequate for a good assessment of flux, they are not adapted to the discretization of source terms. Godunov's exact scheme shows theoretically both properties [90] but is computationally untractable in many applications. A number of methods were then proposed to build equilibrium schemes [59, 67, 81, 91] but few are able to guarantee a positive water height. Among the most well-known of them, we will use hydrostatic reconstruction initially proposed by Audusse *et al.* [3]. However we also mention a method proposed in [55] based on a discontinuous Galerkin discretization and the work of Pelanti *et al.* [108] that modifies the Roe solver to provide such a guarantee in the case of a granular flow.

Eventually, the Saint-Venant system has already proved to be useful in practice (since engineers do observe its accuracy in a number of applications), even if the theoretical assumptions associated to it do not hold. It also leads to numerous works in the field of both theoretical and numerical analysis, in order to build sophisticated and realistic discretization techniques. Nevertheless, as our problem can be very heterogeneous vertically, we would like to relax the limitation on velocities uniformity.

A vertically distributed model

The idea is to find an intermediate system between Navier-Stokes and Saint-Venant equations, that would preserve the efficiency of the shallow water system in terms of dimension reduction, geometric domain simplification and in the same time allow to retrieve information about the vertical velocities profile. For that reason, several vertically distributed models have been proposed. The first ones are multilayer systems, introduced by Audusse *et al.* [2, 7, 8]. In those models, both hypotheses of hydrostaticity and shallow water are made. But every layer is described by its own height, velocity and is advected by the flow. As a result, we obtain a flow with no mass exchanges between the layers, which would rather suit the situation of non-miscible fluids as investigated in [38, 39, 105]. More recently, another vertically distributed system has been suggested [9, 10]. It is based on a Galerkin vertical discretization of the variables for which only the non-hydrostaticity assumption is made - no shallow water hypothesis. An integration of Navier-Stokes equations projected on this Galerkin basis leads to a system similar to the previous multilayer Saint-Venant but this time mass exchange terms appear. We detail hereafter its derivation since this is the model used in this thesis.

Let us begin with the bidimensional hydrostatic Navier-Stokes equations with constant

density ρ_0:

$$\frac{\partial u}{\partial x} + \frac{\partial w}{\partial z} = 0, \tag{2.37}$$

$$\frac{\partial u}{\partial t} + \frac{\partial u^2}{\partial x} + \frac{\partial uw}{\partial z} + \frac{1}{\rho_0}\frac{\partial p}{\partial x} = \frac{1}{\rho_0}\left(\frac{\partial \Sigma_{xx}}{\partial x} + \frac{\partial \Sigma_{xz}}{\partial z}\right), \tag{2.38}$$

$$\frac{\partial p}{\partial z} = -\rho_0 g + \frac{\partial \Sigma_{zx}}{\partial x} + \frac{\partial \Sigma_{zz}}{\partial z}. \tag{2.39}$$

The viscous stress tensor is chosen as follows

$$\Sigma_{xx} = 2\mu\frac{\partial u}{\partial x}, \quad \Sigma_{xz} = \mu\frac{\partial u}{\partial z}, \quad \Sigma_{zz} = 2\mu\frac{\partial w}{\partial z}, \quad \Sigma_{zx} = \mu\frac{\partial u}{\partial z}$$

and we complete with kinematic boundary conditions at the surface and at the bottom. The interval $[z_b, \eta]$ is divided into N layers $\{L_\alpha\}_{\alpha\in\{1,\dots,N\}}$ of height $l_\alpha H(x,t)$ where each layer L_α contains the points $z \in L_\alpha(x,t) = [z_{\alpha-1/2}, z_{\alpha+1/2}]$ with

$$\begin{cases} z_{\alpha+1/2}(x,t) = z_b(x,t) + \displaystyle\sum_{j=1}^{\alpha} l_j H(x,t), \\ \\ h_\alpha(x,t) = z_{\alpha+1/2}(x,t) - z_{\alpha-1/2}(x,t) = l_\alpha H(x,t), \quad \alpha \in [0,\dots,N], \end{cases} \tag{2.40}$$

with $l_j > 0$, $\quad \sum_{j=1}^{N} l_j = 1$.

Then we consider the space $\mathbb{P}_{0,H}^{N,t}$ of piecewise continuous functions defined by

$$\mathbb{P}_{0,H}^{N,t} = \left\{\mathbb{I}_{z\in L_\alpha(x,t)}(z), \quad \alpha \in \{1,\dots,N\}\right\},$$

where $\mathbb{I}_{z\in L_\alpha(x,t)}(z)$ is the characteristic function of the layer $L_\alpha(x,t)$. The projections of u, w and T on $\mathbb{P}_{0,H}^{N,t}$ are then (for $X = u$, $X = w$ or $X = T$)

$$X^N(x,z,\{z_\alpha\},t) = \sum_{\alpha=1}^{N} \mathbb{I}_{[z_{\alpha-1/2},z_{\alpha+1/2}]}(z) X_\alpha(x,t). \tag{2.41}$$

To facilitate the comprehension, notations are recalled on Figure 2.2. Omitting the viscosity terms for the sake of simplicity, we formulate the result from [9]

Proposition 2.5.1 (Audusse, Bristeau, Pelanti, Sainte-Marie)**.** *The weak formulation of*

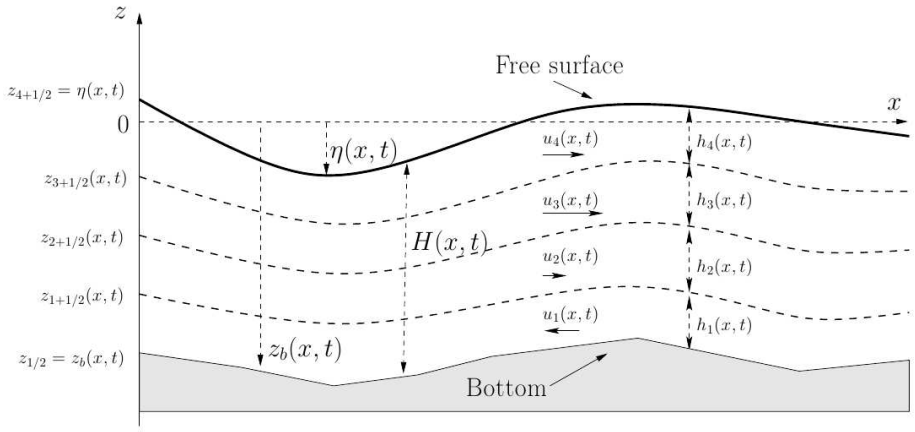

Figure 2.2: Notations for the multilayer approach.

Eqs. (2.37)-(2.39) over $\mathbb{P}_{0,H}^{N,t}$ *leads to the system*

$$\sum_{\alpha=1}^{N} \frac{\partial l_\alpha H}{\partial t} + \sum_{\alpha=1}^{N} \frac{\partial l_\alpha H u_\alpha}{\partial x} = 0, \tag{2.42}$$

$$\frac{\partial h_\alpha u_\alpha}{\partial t} + \frac{\partial}{\partial x}\left(h_\alpha u_\alpha^2 + h_\alpha p_\alpha\right) = u_{\alpha+1/2} G_{\alpha+1/2} - u_{\alpha-1/2} G_{\alpha-1/2} + \frac{1}{\rho_0}\left(\frac{\partial z_{\alpha+1/2}}{\partial x} p_{\alpha+1/2} - \frac{\partial z_{\alpha-1/2}}{\partial x} p_{\alpha-1/2}\right), \tag{2.43}$$

$\alpha \in [1, \ldots, N]$,

with

$$G_{\alpha+1/2} = \sum_{j=1}^{\alpha} \frac{\partial h_j}{\partial t} + \sum_{j=1}^{\alpha} \frac{\partial h_j u_j}{\partial x} \tag{2.44}$$

$$G_{1/2} = G_{N+1/2} = 0, \tag{2.45}$$

$$p_\alpha = \rho_0 g \left(\frac{h_\alpha}{2} + \sum_{j=\alpha}^{N} h_j\right), \tag{2.46}$$

$$p_{\alpha+1/2} = \rho_0 g \sum_{j=\alpha+1}^{N} h_j, \tag{2.47}$$

$$u_{\alpha+1/2} = \begin{cases} u_\alpha & \text{if } G_{\alpha+1/2} \geq 0, \\ u_{\alpha+1} & \text{if } G_{\alpha+1/2} < 0. \end{cases} \tag{2.48}$$

Let us recall the different advantages of such a formalism for our problem

- the vertically discretized system enables the modeling of a problem showing inhomo-

geneities over the vertical dimension;

- similarly to a Saint-Venant system, there are no more z-derivatives;

- similarly to the Saint-Venant system, the geometric domain is completely determined when the water height is known. The simulation of a bidimensional problem is made on a 1D mesh, a tridimensional problem is studied on a 2D mesh;

- the obtained system has the structure of a conservation law with source terms resembles the Saint-Venant model. Thus we will be able to use the numerical techniques described in the previous section, especially finite volumes and hydrostatic reconstruction, and benefit from the important stability properties they guarantee (positive water height, dry/wet interfaces well represented).

A word about kinetic schemes

As it was mentioned in the previous section, the multilayer model will be discretized by a finite volume method. We need to choose a Riemann solver to solve, exactly or approximately the interfaces problems and compute the fluxes in (2.36). In most cases, the solvers are based on the computation of eigenvalues and eigenvectors of the hyperbolic system of interest. Nonetheless, the vertically discretized hydrostatic Navier-Stokes equations exposed in Section 2.5.1 have not proved to be hyperbolic (apart from the two layers case) and we do not have access to the eigenelements of the problem.

Kinetic schemes provide a way to circumvent this apparent limitation. Moreover, they lead to good discrete stability properties. The first kinetic schemes appear in the seventies, for the study of gas dynamics [120, 127]. But in 1990, in [111], Perthame introduces a new idea: the Maxwellian commonly used in the kinetic description of the equations can be replaced by a compactly supported Gibbs equilibria. This latter yields better theoretical properties on the scheme [84, 111]. It is also easier to implement and it reduces the computation cost.

In the interest of clarity, we will describe the process for the building of a kinetic scheme on the Saint-Venant equations with a topography source term. In Chapter 4 we will make a multilayer adaptation of this method. The basic idea for kinetic schemes is to use the link existing between the macroscopic equations of fluid dynamics - like Navier-Stokes, Euler or Saint-Venant - with the kinetic equations of Boltzmann type [41], describing the evolution of a particle density at a mesoscopic level. The first step is then to define a Gibbs equilibria, that is to say a particle density. A particle is identified by its position x and its velocity ξ at time t. If we choose the equilibria:

$$M(t,x,\xi) = M(H(t,x), \xi - \boldsymbol{u}(t,x)) = \frac{H(t,x)}{c^2}\chi\left(\frac{\xi - \boldsymbol{u}(t,x)}{c}\right), \tag{2.49}$$

where $c = \sqrt{\frac{gH}{2}}$ and χ is an even function satisfying

$$\int_{\mathbb{R}} \begin{pmatrix} 1 \\ \xi^2 \end{pmatrix} \chi(\xi) d\xi = \begin{pmatrix} 1 \\ 1 \end{pmatrix}, \tag{2.50}$$

then we can formulate the following theorem

Theorem 2.5.2 (Audusse)**.** *The functions $(H, H\boldsymbol{u})$ are solutions to the homogeneous Saint-Venant system if and only if $M(t,x,\xi)$ is solution of the kinetic equation*

$$\partial_t M + div(\xi M) = Q(t,x,\xi), \tag{2.51}$$

for a collision term $Q(t,x,\xi)$ satisfying for almost every (t,x),

$$\int_{\mathbb{R}} Q d\xi = 0, \quad \int_{\mathbb{R}} \xi Q d\xi = 0 \tag{2.52}$$

The proof consists in integrating (2.51) against $\begin{pmatrix} 1 \\ \xi \end{pmatrix}$ to recover the Saint-Venant system (2.34) - (2.35) without the topography source term. For a fixed ξ, and omitting in a first phase the collision term Q, (2.51) is a linear advection equation. We are able to discretize it simply by a finite volume method using an upwind scheme:

$$f_i^{n+1-} = M_i^n - \frac{\Delta t^n}{\Delta x_i}\xi_+ \left(M_i^n - M_{i-1}^n\right) - \frac{\Delta t^n}{\Delta x_i}\xi_- \left(M_{i+1}^n - M_i^n\right), \tag{2.53}$$

where

$$\xi^+ = \max(\xi, 0), \quad \text{et} \quad \xi^- = \min(\xi, 0). \tag{2.54}$$

The collision term is taken into account in a second phase. It is interpreted as a projection of f_i^{n+1-} on the set of admissible Gibbs equilibria (for instance of the form (2.49)). The integration of the numerical scheme (2.53) yields an expression of the macroscopic fluxes for (2.36):

$$F_{i+1/2}^n = \int_{\xi \le 0} \xi \begin{pmatrix} 1 \\ \xi \end{pmatrix} M_{i+1}^n d\xi + \int_{\xi \ge 0} \xi \begin{pmatrix} 1 \\ \xi \end{pmatrix} M_i^n d\xi \tag{2.55}$$

Remark 2.5.3. *More details about the kinetic theory will be provided in Chapter 6. We were only exhibiting the practical use of this theory for the construction of efficient numerical schemes.*

2.5.2 State of the art of phytoplankton growth modeling

Phytoplankton

After the presentation of the hydrodynamic model we are going to use in Chaper 4, we tackle the biological part. First and foremost, we describe more precisely what phytoplankton is and the different phenomena it undergoes. For more details, the reader can refer to [57].

Definition 2.5.4. ***Phytoplankton*** *Derived from the Greek words phyto (plant) and plankton (made to wander or drift), phytoplankton are microscopic organisms that live in watery environments, both salty and fresh. There exists many varieties of phytoplankton, with different shapes, sizes, properties*

Like land plants, phytoplankton have chlorophyll to capture sunlight, and they use photosynthesis to turn it into chemical energy. They consume carbon dioxide, and release oxygen. Phytoplankton growth depends on the availability of carbon dioxide, sunlight, and nutrients. The nutrients required are : nitrate, phosphate, silicate (for instance for the shell of the diatoms), calcium, iron. Other factors can influence the growth of phytoplankton: temperature, salinity, water depth, wind, zooplankton.

Phytoplankton is important since it is at the origin of most of the transfer of carbon dioxide from the atmosphere to the ocean. Carbon dioxide is consumed during photosynthesis, and the carbon is incorporated in the phytoplankton. Most of the carbon is returned to near-surface waters when phytoplankton are eaten or decompose, but some fall into the ocean depths.

In our case, we will not study phytoplankton in its natural environment but in an place optimized for growth (which we still have to determine), since we will exploit the oil stored in phytoplankton during photosynthesis.

Definition 2.5.5. ***Photosynthesis*** *Photosynthesis is a process that converts carbon dioxide into organic compounds, especially sugars, using the energy from sunlight. Photosynthesis occurs in plants, algae, and many species of bacteria. In plants, algae, and cyanobacteria, photosynthesis uses carbon dioxide and water, releasing oxygen as a waste product. The reaction equation is:*

$$6\,CO_2 + H_2O \underset{+Light}{\Rightarrow} C_6H_{12}O_6 + 6\,O_2 \tag{2.56}$$

The electrons required for the reaction are captured by proteins in organelles called chloroplasts and containing chlorophyll. Chlorophyll absorbs light in the blue and red portion but not in the green, that explains the color.

Définition 2.5.6. *Respiration is a process enabling, at night, to recover the energy that has been stored during the day thanks to photosynthesis. This energy is then used to carry on the intracellular mechanisms, among which growth takes an important part.*

Algae have to keep a balance between the energy captured from sunlight and the energy used for carbon fixation (or other metabolic reactions). Since daily and seasonal variations

in light intensity induce stresses, organisms respond with physical, biophysical, biochemical and physiological changes.

Definition 2.5.7. ***Photoacclimation*** *Photoacclimation is the phenotypic response of algae to changes in irradiance in order to optimize photosynthesis. At the cellular level this implies changes in the concentration and composition of pigments. At the physiological level, the minimum quantum for photosynthesis is also function of the light intensity.*

During photosynthesis, several proteins complex come into the picture. They carry out reactions that are either light-dependent or independent. Among the light-dependent machinery, the protein complex Photosystem II intervenes in the photoacclimation process. It can have three states: open (ready to receive an electron), closed (working) or damaged (cannot work anymore). Of course, when a site is damaged, no electron transfer occurs, and photosynthesis is stopped. The inactivation is irreversible and can only be restored by the degradation and synthesis of the D1 protein. Two kinds of photoacclimation are listed:

- Short-term photoacclimation : these are short-term processes from a few seconds to less than an hour(the limit of the hour is given by physiological constraints: the minimum time for synthesizing new proteins or pigments is 30-60 min). The first defense of the algae is the deactivation of excitons through thermal dissipation. It can also begin the process of photorespiration.
- Long-term photoacclimation : processes from an hour to several days. When algae are exposed to unfavourable light conditions and short term acclimation is not efficient enough to protect it from damage, it can:
  - alterate the amount of chlorophyll per photosystem unit
  - change the number of photosystem units.

Sometimes neither a short nor a long-term photoacclimation strategy are efficient to protect an algae from photodamage. It is the case when the algae undergoes a high irradiance for a long time. Then it can inactivate its PSII reaction centers.

Definition 2.5.8. ***Photoinhibition*** *Photoinhibition is a reduction in the photosynthetic ability of a plant or algae induced by light.*

Modeling phytoplankton dynamics

Phytoplankton dynamics are still described more or less empirically. This is mainly due to the fact that the physiological processes mentioned in the previous section remain quite misunderstood. This lack of knowledge is also the reason of the emergence of so many alternative formulations for phytoplankton growth. In this paragraph, we will try to give the main directions in phytoplankton modeling and also some ideas on how it has been carried out until now, based mainly on [16] and [106]. Basically, there are two kinds of models: empirical models and mechanistic models. The first ones are particularly suitable

for situations where data can be acquired. But a model tuned on one site cannot be easily extended to another site. Moreover, those models associate parameters that are often physically or biologically meaningless. On the contrary, mechanistic models try to translate the biogeochemical processes into equations. Thus, they are flexible from one site to another and they use physically and biologically meaningful parameters (that we can measure in experiences). Their main drawback is their complexity (sometimes up to 15 variables and 70 parameters). However, we can imagine that once those models give results, those results can be used to design larger scale models as asymptotical behaviour of the detailed one. But anyway, whatever concept of modeling is chosen, it will have to represent the processes governed by light (photosynthesis, photoacclimation...) and those governed by nutrients (growth, uptake, respiration).

Growth controlled by photosynthesis and photoacclimation Light is the main variable involved in photosynthesis. In the models, the measure of light is the irradiance E, sometimes integrated over a spectral range (since chlorophyll is sensitive to wavelength of magnitude 400-700 μm). The important output in a photosynthesis model is the primary production rate (the production rate of organic compounds from atmospheric or aquatic carbon dioxide), which is a function of light. Empirical models try to fit an expression of this primary production rate to experimental data, given the light exposure. They build a function $f(E)$ satisfying $f(0) = 0$, taking or not into account photoinhibition (Definition 2.5.8. The primary production rate will be proportional to $f(E)$. We can mention for example:

- The Monod function(1950) : $f(x) = \frac{x}{1+x}$, no photoinhibition
- The Steele function(1962) : $f(x) = x.e^{1-x}$, photoinhibition
- The Klepper function(1962) : $f(x) = \frac{(2+A)x}{1+Ax+x^2}$, photoinhibition

Mechanistic models have another approach, based on the physics. Following what we explained in the previous section about photoacclimation/photoinhibition, any curve representing the growth rate as a function of light in the presence of photoinhibition should have three phases:

- low irradiance, increase of primary production. The limiting factor is light;
- light saturation index;
- high irradiance, decrease of primary production. The limiting factor is the transfer of the numerous electrons excited by photons.

This is explained at the microscopic level by the functioning of Photosystem II (see photoacclimation definition) in short-term or long-term processes. Until now, short-term processes have never been introduced in models. But long-term processes are. Zonneveld (1997) and Han (2002) built models relying on the fact that PSU can be found in three different states: open, closed or photoinhibited. Let us zoom on Han's model. It assumes

that each PSU contains only one PSII, which has a probability of being open, close or inhibited, denoted respectively n_0, n_c and n_{in}. Thus, with kinetics coefficients, the balance equation becomes:

$$\text{Open site} \underset{\tau^{-1}}{\overset{\sigma_{PSII}.E}{\leftrightarrows}} \text{Closed site} \underset{k_r}{\overset{k_d}{\leftrightarrows}} \text{inhibited site}, \tag{2.57}$$

where $\sigma_{PSII}.E$, τ^{-1}, k_r and k_d are the reaction constants. Hence the system writes:

$$\begin{cases} \dfrac{dn_0}{dt} = -\sigma_{PSII}.E.n_0 + \dfrac{n_c}{\tau} & (2.58) \\ \dfrac{dn_c}{dt} = \sigma_{PSII}.E.n_0 - \dfrac{n_c}{\tau} - k_d\sigma_{PSII}En_c & (2.59) \\ n_{in} = 1 - n_0 - n_c & (2.60) \end{cases}$$

Then, he states that the primary production rate is proportional to the number of opened sites.

Finally, the Chl:C ratio is important since it allows converting two biomass units, but it is also an indicator of the photoacclimation state of the algae (if it is low it can be photoinhibited, if it is high, it is in the first phase of the photosynthesis curve). Empirical models often consider a constant ratio (like the Redfield ratio), but this is far from the truth. To improve this first order approximatiom, Cloern(1995) propose an empirical formulation of the ratio estimated thanks to 219 publications. He finds :

$$\frac{Chl}{C} = 0.003 + 0.0154.e^{0.050T}.e^{-0.059E}. \tag{2.61}$$

Mechanistic models are numerous for this part. Zonneveld's (1998) model decomposes a cell in three variables: a permanent volume and two transient pools for carbon and nutrients. Under nutrient limited conditions, the production rate of chlorophyll is proportional to the nitrogen pool. Geider (1997) proposed an alternative model based on an independent mass balance equation for chlorophyll (which becomes then a state variable).

Growth controlled by nutrients

Apart from light supply, algae need nutrients for growth. Before the introduction of quota models (Droop, 1968) it was commonly admitted that Redfield ratio could be used. This ratio, determined experimentally by Redfield stipulates that the molecular ratio of carbon, nitrogen and phosphorus in phytoplankton was equal to $106 : 16 : 1$ everywhere. Thus, one variable lead to both others. But this model fails in many situations and it is necessary to build multi-elements models and introduce the concept of colimitation.

According to Flynn (2003), there exists three modeling strategies for phytoplankton nutrient-related growth: Monod, quota and mechanistic. Monod law is empirical and states

that the primary production rate is proportional to:

$$f_{growth} = \frac{X_e}{K + X_e}, \tag{2.62}$$

where X_e represents the limiting nutrient and K is a constant. This model however turns out to be unsatisfactory for two reasons:

- Growth stops when there is no more nutrients (which proves to be wrong)
- It represents badly multiple nutrients interactions

Then, quota models were introduced, first by Droop [52, 53]. It states that an algae can store nutrients in intracellular pools. These nutrients are used for growth. Thus, an absence of extracellular nutrient does not lead instantly to a growth stop. The quota $Q = \frac{X}{C}$ is included in the model in the primary production rate, which becomes proportional to:

$$f_{growth} = \frac{Q - Q_{min}}{Q}. \tag{2.63}$$

There are two possibilities for the modeling of multi-nutrients interactions in growth processes. the first one is the Liebig's law of the minimum. It postulates that growth is governed by the most limiting factor. Thus, the primary production rate is proportional to(in case of Monod laws):

$$f_{growth} = \min_i \left(\frac{X_i^e}{K_{X_i} + X_i^e} \right). \tag{2.64}$$

The other approach rather considers a cumulation of the effects of the limiting factors by multiplying their contributions to the growth rate:

$$f_{growth} = \prod_i \left(\frac{X_i^e}{K_{X_i} + X_i^e} \right) \tag{2.65}$$

Since none of those formulations proved to be capable of reproducing the coupled effects of nitrogen and silica on diatoms (Davidson and Gurney (1999)), new models have been proposed. Unfortunately, none of them could be generalized and worked only in restricted conditions. Eventually, we focus on nutrient uptake. Usually a Michaelis-Menten model for nutrient uptake is used:

$$f_{upt} = A.\frac{X_e}{K_X + X_e}. \tag{2.66}$$

Respiration modeling Empirical models state that the respiration rate is divided into two components:

$$R = R_m + R_g.$$

R_m is called the maintenance respiration while R_g varies with the primary production. Those values are determined experimentally. Nevertheless, most of the time, a constant respiration rate is taken into account. Mechanistic models, like the one proposed by Han(1991)

detail the steps of respiration by introducing three state variables which are the concentrations of the mains proteins involved in the process.

Droop model To conclude, let us come to our model choice. The goal is not to model as precisely as possible the biological phenomena. It is more about being able to couple a hydrodynamical model with a simple biological one, that would still encompass the main features out forward in the previous sections, in order to draw the first conclusions. We have just explained that quota models are more adapted that Monod type models. We opt for a Droop model with the following variables;

- the phytoplanktonic carbon C_1,
- the phytoplanktonic nitrogen C_2,
- the extracellular nutrients C_3.

Denoting $Q = \dfrac{C_2}{C_1}$, we deduce that the growth coefficient is proportional to the nutrient quota Q in the following manner:

$$\mu(q, I) = \bar{\mu}(I)(1 - \frac{Q_0}{Q}), \tag{2.67}$$

and we include photoinhibition as follows:

$$\bar{\mu}(I) = \tilde{\mu}\frac{I}{I + K_{sI} + \frac{I^2}{K_{iI}}}. \tag{2.68}$$

Finally, absorption of light depends not only on the water depth, but also on the amount of chlorophyll encountered:

$$I(z) = I_0 e^{-\int_0^z (aChl(z) + b)dz}, \tag{2.69}$$

where $Chl(z) = \gamma(I^*)C_2$ is the chlorophyll concentration, and I^* is the mean light observed in the water column the day before. The varying chlorophyll quantity shows the photoacclimation process. Respiration is assumed constant equal to R and uptake of nutrients follows a Michaelis-Menten law (1.66) with an uptake rate λ:

$$\lambda(C^3, q) = \overline{\lambda}\frac{C^3}{C^3 + K_3}(1 - \frac{q}{Q_l}). \tag{2.70}$$

This eventually leads to the spatialized reaction, transport and diffusion system

$$\begin{cases} \partial_t C_1 + \nabla \cdot (\mathbf{u}C_1) = \nu C_1 \Delta C_1 + \mu(q, I)C_1 - RC_1, \\ \partial_t C_2 + \nabla \cdot (\mathbf{u}C_2) = \nu C_2 \Delta C_2 + \lambda(C_3, q)C_1 - RC_2, \\ \partial_t C_3 + \nabla \cdot (\mathbf{u}C_3) = \nu C_3 \Delta C_3 - \lambda(C_3, q)C_1, \end{cases} \tag{2.71}$$

where $\mathbf{u}$ is the fluid velocity in which algae are immersed, ν is the viscosity coefficient.

2.5.3 Study results

To conclude, we sum up hereafter the study results. The vertically discretized version of the hydrostatic Navier-Stokes equations [9, 10], has been enriched by a volumic force mimicking the effect of the paddlewheel in the pond. It has been integrated to the multilayer derivation and changes principally the pressure terms in each layer (Proposition 2.5.1). The investigation is made in two dimensions, on a periodic domain, to reproduce the cyclic dynamics of a raceway.

Let us focus first on the handling of the Droop model. We derive it in its multilayer version in the proposition:

Proposition 2.5.9 (Bernard, B., Bristeau, Sainte-Marie)**.** *Multilayer version of the Droop model with photoacclimation. With the notations of Proposition 2.5.1, the weak formulation of the system (2.71) on $\mathbb{P}^{N,t}_{0,H}$ leads to a system of the form*

$$\begin{aligned}
\frac{\partial h_\alpha C^1_\alpha}{\partial t} + \frac{\partial}{\partial x}\left(h_\alpha C^1_\alpha u_\alpha\right) &= C^1_{\alpha+1/2} G_{\alpha+1/2} - C^1_{\alpha-1/2} G_{\alpha-1/2} \\
&\quad + h_\alpha(\mu(q_\alpha, I_\alpha) C^1_\alpha - R C^1_\alpha), \qquad (2.72)\\
\frac{\partial h_\alpha C^2_\alpha}{\partial t} + \frac{\partial}{\partial x}\left(h_\alpha C^2_\alpha u_\alpha\right) &= C^2_{\alpha+1/2} G_{\alpha+1/2} - C^2_{\alpha-1/2} G_{\alpha-1/2} \\
&\quad + h_\alpha(\lambda(C^3_\alpha, q_\alpha) C^1_\alpha - R C^2_\alpha), \qquad (2.73)\\
\frac{\partial h_\alpha C^3_\alpha}{\partial t} + \frac{\partial}{\partial x}\left(h_\alpha C^3_\alpha u_\alpha\right) &= C^3_{\alpha+1/2} G_{\alpha+1/2} - C^3_{\alpha-1/2} G_{\alpha-1/2} \\
&\quad - h_\alpha \lambda(C^3_\alpha, q_\alpha) C^1_\alpha, \qquad (2.74)\\
&\qquad\qquad \alpha \in [1, \dots, N],
\end{aligned}$$

with $q_\alpha = \frac{C^2_\alpha}{C^1_\alpha}$ and $C^j_{\alpha+1/2}$, $j = 1 \dots 3$ defined following the sign of the mass exchanges represented by $G_{\alpha+1/2}$.

Then, we obtain a kinetic description of the multilayer biological model without reaction terms. Those latter are included subsequently thanks to a splitting numerical scheme. We define, as in the hydrodynamical case, Gibbs equilibria for each layer

$$U^j_\alpha(x,t,\xi) = C^j_\alpha(x,t) M_\alpha(x,t,\xi), \quad \alpha = 1, \dots, N, \quad j = 1, \dots, 3, \qquad (2.75)$$

$$V^j_{\alpha+1/2}(x,t,\xi) = C^j_{\alpha+1/2}(x,t) N_{\alpha+1/2}(x,t,\xi), \quad \alpha = 0, \dots, N, \quad j = 1, \dots, 3, \qquad (2.76)$$

where $N_{\alpha+1/2}(x,t,\xi)$ is defined by

$$N_{\alpha+1/2}(x,t,\xi) = G_{\alpha+1/2}(x,t)\ \delta\left(\xi - u_{\alpha+1/2}(x,t)\right), \qquad (2.77)$$

for $\alpha = 0, \dots, N$ and where δ denotes the Dirac distribution. We have the following proposition:

Proposition 2.5.10 (Bernard, B., Bristeau, Sainte-Marie). *The functions* (C^j) *are strong solutions of the system (2.72) -(2.74) without reaction terms if and only if the Gibbs equilibria* $\{U_\alpha^j(x,t,\xi)\}_{\alpha=1}^N$ *defined in* (2.75) *are solutions of the kinetic equations*

$$\frac{\partial U_\alpha^j}{\partial t} + \xi \frac{\partial U_\alpha^j}{\partial x} - V_{\alpha+1/2}^j + V_{\alpha-1/2}^j = Q_{U_\alpha^j}, \tag{2.78}$$

for $\alpha = 1,\dots,N$, $j = 1\dots3$ *with* $\{N_{\alpha+1/2}(x,t,\xi), V_{\alpha+1/2}^j(x,t,\xi)\}_{\alpha=0}^N$ *satisfying (2.77)-(2.76).*

The quantities $Q_{U_\alpha^j} = Q_{U_\alpha^j}(x,t,\xi)$ *are collision terms satisfying at the macroscopic level for almost every* (t,x)

$$\int_{\mathbb{R}} Q_{U_\alpha^j} d\xi = 0, \quad \int_{\mathbb{R}} \xi Q_{U_\alpha^j} d\xi = 0, \quad et \quad \int_{\mathbb{R}} \xi^2 Q_{U_\alpha^j} d\xi = 0. \tag{2.79}$$

Eventually, a discretization of the kinetic equation, as explained on the Saint-Venant system in Section 2.5.1 is performed and leads to a numerical scheme which, under a certain CFL condition, ensures positivity of the water height and conservation of physiological quantities. The simulations proposed in this thesis are carried out at the second order in space thanks to the reconstruction of variables and we improve the time order with the Heun method. They mostly show the hydrodynamical state of the raceway and plots of the production of carbon and the uptake of nitrogen.

Afterwards, the study deals with the lagrangian trajectories generated by the simulations. They are of great interest for biologists. There exists indeed many photosynthesis models, differing from each other in the details they take into account (Section 2.5.2). The knowledge of the light variations given by the reconstruction of lagrangian trajectories, enables to better determine the time constants coming into play and the prevailing phenomena. Hence, a better version could be proposed instead of the Droop model studied in this thesis.

Besides, a tridimensional code has been developed and the first hydrodynamical results are provided in Chapter 5.

2.6 Data assimilation for hyperbolic conservation laws admitting a kinetic description

2.6.1 Etat de l'art

Data assimilation encompasses a broad class of methods aimed at estimating the state and the parameters of a system by jointly combining information from a numerical simulation and actual observations. The need for this combination first appeared in the fields of meteorology and oceanography. One of the first attempts at doing so was made in 1922 by Richardson with his "forecast factory" [122]. In order to get a complete initial data,

necessary to run his prediction numerical model, he interpolates the data at time 0. However such an interpolation does not comply with the physical constraints of the model and the notion of CFL has not been introduced yet at that time: results are disappointing. In the 1950s, Cressman analysis [48] introduces the idea of weighting the influence of the observations with respect to the model, by defining a radius of influence for all observations. But once again, the method is too simple to provide satisfying results. In 1976, Hoke et Anthes [75] modify the equations to constrain the solution towards the data. Thus they create, without naming it, a Luenberger observer that will be reintroduced in the data assimilation community as *nudging* [11, 13]. Finally, more sophisticated methods appear and can be classified into two categories: sequential methods and variational methods. The former ones consist, like a Luenberger observer, in including within the system dynamics a correction term based on the difference between the data and the model. One expects the solution to converge in time, but not to retrieve the initial condition. The most popular observer is the Kalman filter which is optimal for linear systems [21]. Unfortunately, it requires the use of very large non-sparse matrices whose dimension depends on the size of the problem and the observations. The latter are denoted variational methods as they are minimization approaches subject to some constraints. The most well-known algorithm is 4D-VAR that minimizes a cost functional of the type

$$J(x) = (x - x_b)^T \boldsymbol{B}^{-1} (x - x_b) + \sum_{i=0}^{n} (y_i - H[x_i])^T \boldsymbol{R_i}^{-1} (y_i - H[x_i]), \tag{2.80}$$

where $\boldsymbol{B}$ is the covariance matrix of background errors and $\boldsymbol{R_i}$, y_i, x_i are respectively the covariance matrix of observation errors, the observation vector and the state vector at time t_i; x_b denotes the background term (initial condition previously found or assumed) while x is the initial condition and H the observation operator. Solving this problem needs the computation of the gradient of J by solving an adjoint equation that may require numerous iterations.

The last two methods are nowadays among the most popular ones but as aforementioned, they may be difficult to use in practice. We rather focus on the Luenberger observer that was introduced longer ago but recently regained interest due to its simplicity. Improvements have been proposed, such as the Back and Forth Nudging [11, 13] that allows the determination of the best initial condition or the optimization of nudging coefficients [145]. The aim of Chapter 6 is not to propose yet another enhancement of this method, but rather a framework to use it on systems of hyperbolic conservation laws. This novel framework relies on the kinetic description of conservation laws (that has already been used in Chapter 4 of this thesis to design numerical schemes).

This chapter presents convergence results on both scalar conservation laws and the Saint-Venant system. As it will be detailed in Chapter 6, the kinetic nudging method (when applied to scalar conservation laws) presents a theoretical framework but does not enable the construction of new numerical schemes for the observer's equation. However, the significance of our work is much more important regarding Saint-Venant equations, as

we propose a constructive method leading to a new observer.

In the remainder, we denote V_p the space $L^p(\mathbb{R}^d_x \times \mathbb{R}_\xi)$.

2.6.2 Scalar conservation laws with complete data

Without dwelling upon the proofs, since they are written in Chapter 6, we hereby give the main results for scalar conservation laws of the form:

$$\begin{aligned} \partial_t u + \sum_{i=1}^{d} \partial_{x_i} A_i(u) = 0, \\ u(t=0,x) = u_0(x). \end{aligned} \tag{2.81}$$

The theory of kinetic description [112] indicates that (2.81) augmented with all its entropies is equivalent to:

$$\begin{cases} \partial_t M(t,x,\xi) + a(\xi)\cdot\nabla_x M(t,x,\xi) = \nabla_\xi m(t,x,\xi) \\ M(0,x,\xi) = \chi(\xi,u_0(x)) \end{cases} \tag{2.82}$$

where $M(t,x,\xi) = \chi(\xi,u(t,x))$ satisfies

$$\chi(\xi,u) = \begin{cases} +1, & \text{for } 0<\xi<u \\ -1, & \text{for } u<\xi<0 \\ 0, & \text{sinon,} \end{cases} \tag{2.83}$$

m is a non-negative bounded measure and

$$a(\xi) = \left(A_1'(\xi), A_2'(\xi), \ldots, A_d'(\xi)\right).$$

We consider the exact solution of (2.82), and we write the equation verified by the Luenberger observer

$$\begin{cases} \dfrac{\partial}{\partial t} f(t,x,\xi) + a(\xi)\cdot\nabla_x f(t,x,\xi) + \lambda f(t,x,\xi) = \lambda M(t,x,\xi), \\ f(t,x,\xi=0) = f_0(x,\xi). \end{cases} \tag{2.84}$$

We distinguish between several situations to formulate convergence results with complete data in space and time. The first result concerns smooth data. In that case, we can consider that there are no collision ($m=0$) and we get easily to that proposition

Proposition 2.6.1 (B., Moireau, Perthame, Sainte-Marie)**.** *Let $M \in C([0,T],V_1)$ satisfy (2.82) with $m=0$ and $f \in C(\mathbb{R}^+;V_1)$ satisfying (2.84), then*

$$\|f-M\|_{V_1} \underset{t\to+\infty}{\longrightarrow} 0, \tag{2.85}$$

and the decrease in exponential in time with a convergence rate proportional λ.

Remark 2.6.2. *This results shows the convergence of the kinetic densities. For the convergence of microscopic quantities, we still need to integrate in ξ. This does not cause any problem as the densities are compactly supported in ξ.*

A second proposition consists in considering that data still come from (1.82) but are non-smooth. The presence of the collisions ($m \neq 0$) prevents us from getting such a strong convergence property in time as in the previous case. Nonetheless, it is possible to play on the nudging coefficient λ to recover interesting results, summed up in this theorem:

Theorem 2.6.3 (B., Moireau, Perthame, Sainte-Marie)**.** *Let $M \in C([0,T], V_1)$ satisfy (2.82) with $u_0 \in L^1(\mathbb{R}^d)$ and $f \in C(\mathbb{R}^+; V_1)$ satisfy (2.84) with $f_0 \in V_1$, then, for some modulus of continuity $\omega(T,\cdot)$*

$$\|f(T) - M(T)\|_{V_1} \leq \|f_0 - f_{\lambda,0}\|_{V_1} e^{-\lambda T} + \omega(T, \frac{1}{\lambda}). \tag{2.86}$$

Moreover, if $u_0 \in L^\infty \cap L^1 \cap BV(\mathbb{R}^d)$, the λ dependency can be specified:

$$\|f(T) - M(T)\|_{V_1} \leq \|f_0 - f_{\lambda,0}\|_{V_1} e^{-\lambda T} + C(d)\|a\|_{L^\infty(-K,K)} \sqrt{\frac{T\|u_0\|_{BV(\mathbb{R}^d)}}{\lambda}}. \tag{2.87}$$

Finally, the last theorem concerns data assimilation in the case of complete but unknown observations (we cannot relate them to (2.82) anymore). In a first step, we assume regularity on them anyway:

Theorem 2.6.4 (B., Moireau, Perthame, Sainte-Marie)**.** *Let $p = 1$ or $p = 2$. Let $M(t,x,\xi) \in C([0,T], V_p)$ and $f(t,x,\xi) \in C([0,T],\ V_p)$ be solution of*

$$\begin{aligned} &\frac{\partial}{\partial t} f(t,x,\xi) + a(\xi)\cdot\nabla_x f(t,x,\xi) + \lambda f(t,x,\xi) = \lambda M(t,x,\xi), \\ &f(t=0,x,\xi) = f_0(x,\xi), \end{aligned} \tag{2.88}$$

with f_0 and M_0 in L^p. Let us assume moreover $\dfrac{\partial M}{\partial t} + a(\xi)\cdot\nabla_x M = Q \in C([0,T], V_p)$. Then,

$$\|f(T) - M(T)\|_{V_p} \leq \|f_0 - M_0\|_{V_p} e^{-\lambda T} + \frac{1 - e^{-\lambda T}}{\lambda} \sup_{0\leq t\leq T} \|Q(t)\|_{V_p}$$

This theorem admits an extension for less smooth data by means of a regularization by convolution method.

2.6.3 Scalar conservation laws for incomplete or noisy data

In the following, we focus on more realistic situations, with noisy or incomplete data. We begin with the addition of a noise on the observer equation. This noise is supposed to

be on non negligible magnitude in a classical L^2 norm, but smaller in a weaker one. By regularizing effects which are common in kinetic theory, we can deduce an upper bound on the macroscopic error mean.

For the sake of simplicity, we will deal first with the case of a linear advection coefficient $\xi \in \mathbb{R}^d$(as it is the case for the Burgers equation):

$$\xi \cdot \nabla_x f(x,\xi) + \lambda f(x,\xi) = \lambda M(x,\xi) + \lambda \frac{\partial^\alpha E}{\partial x^\alpha} \tag{2.89}$$

with

$$\xi \cdot \nabla_x M(x,\xi) = Q(x,\xi) \in V_2, \tag{2.90}$$

where α is a multi-index $(\alpha_1, \alpha_2, \dots \alpha_n)$ verifying $\alpha = \alpha_1 + \alpha_2 + \ldots + \alpha_n$,

$$\frac{\partial^\alpha E}{\partial x^\alpha} = \frac{\partial^\alpha E}{\partial x_1^{\alpha_1} x_2^{\alpha_2} \dots x_n^{\alpha_n}}$$

represents the noise, and $E(t,x,\xi) \in V_2$. We denote

$$\rho_\psi(t,x) = \int_{\mathbb{R}_\xi} \left(f(x,\xi) - M(x,\xi)\right) \psi(\xi) d\xi \tag{2.91}$$

the ξ-mean of the error between the model and the data. Then we show that for an optimal λ, ρ belongs to a more regular space than L^2 and we obtain a different upper-bound than the one we would have obtained in L^2:

Theorem 2.6.5 (B., Moireau, Perthame, Sainte-Marie)**.** *Let $M(x,\xi) \in V_2$ be the solution of (2.90) and $f(x,\xi) \in V_2$ satisfy the noisy data assimilation problem (2.89) for $|\alpha| < \frac{1}{2}$. Then $\exists\ \gamma$, $0 < \gamma \leq 1 - 2|\alpha|$ and a constant K_1 such that*

$$\|\dot{\hat{\rho}}_\psi\|^2_{H^{\gamma/2}(\mathbb{R}_x)} \leq K_1 \|\partial^\alpha E\|^2_{V_2} \left(\frac{\|\hat{E}\|_{\hat{V}_2}}{\|\partial^\alpha E\|^2_{V_2}} \right)^{\frac{\gamma}{1-|\alpha|}} + \mathrm{o}\left(\|\hat{E}\|_{V_2}^{\frac{2+\gamma}{1-|\alpha|}} \right), \tag{2.92}$$

and tends to zero when $\|\hat{E}\|_{V_2}$ tends to 0. This inequality is obtained for an optimal value of λ,

$$\lambda_{opt} = K_2 \|\hat{Q}\|_{\hat{V}_2} \left(\frac{\|\partial^\alpha E\|^{2\alpha}_{V_2}}{\|\hat{E}\|_{\hat{V}_2}} \right)^{\frac{1}{1-\alpha}}, \tag{2.93}$$

where K_2 is a constant.

The proof is based on Fourier analysis and some classical results in the theory of velocity averaging lemmas for kinetic equations [29, 51, 65, 79, 116]. Later, we consider the case when the advection is not linear in ξ ($\xi \in \mathbb{R}$). We start with the stationary equation:

$$a(\xi) \cdot \nabla_x f(x,\xi) + \lambda f(x,\xi) = \lambda M(x,\xi) + \lambda \frac{\partial^\alpha E}{\partial x^\alpha} \tag{2.94}$$

with

$$a(\xi)\cdot\nabla_x M(x,\xi)=Q(x,\xi)\in L^2(\mathbb{R}^N_x\times\mathbb{R}_\xi), \tag{2.95}$$

where a is a non-degenerate flux. Then,

Theorem 2.6.6. *Let $M(x,\xi)\in V_2$ be solution of (2.95) and $f(x,\xi)\in V_2$ satisfy the noisy data assimilation problem (2.94). Then, there exists β, $0<\beta<1$, γ, $0<\gamma<\beta-2|\alpha|$ and a constant K such that*

$$\|\dot{\hat{\rho}}_\psi\|^2_{H^{\gamma/2}(\mathbb{R}_x)}\leq K_1\|\partial^\alpha E\|^2_{V_2}\left(\frac{\|\hat{E}\|^{2-\beta}_{\hat{V}_2}}{\|\partial^\alpha E\|^2_{V_2}}\right)^{\frac{\gamma}{(|\alpha|+1)\beta-2|\alpha|}}+\mathrm{o}\left(\|\hat{E}\|_{V_2}^{\frac{(2-\beta)\gamma}{(|\alpha|+1)\beta-2|\alpha|}}\right) \tag{2.96}$$

which is obtained for an optimal λ

$$\lambda_{opt}=K_2\|\hat{Q}\|_{\hat{V}_2}\left(\frac{\|\partial^\alpha E\|^{2\alpha}_{V_2}}{\|\hat{E}\|^{\beta}_{\hat{V}_2}}\right)^{\frac{1}{(\alpha+1)\beta-2\alpha}} \tag{2.97}$$

where K_1 and K_2 are constants.

Both studies have been extended to the evolution cases in Chapter 6 and in Appendix B. They require some other intermediate lemmas and the results are not so obvious.

In a further section, we focus on data that are sampled in time. We consider that we have access at discrete times t_k to a temporal mean of the state variables. Moreover, we will consider that we know the equation satisfied by the data:

$$\partial_t M(t,x,\xi)+a(\xi)\cdot\nabla_x M(t,x,\xi)=Q(t,x,\xi). \tag{2.98}$$

The observer is solution of:

$$\partial_t f(t,x,\xi)+a(\xi)\cdot\nabla_x f(t,x,\xi)+\lambda\sum_{k\in I}\varphi_\sigma(t-t_k)f(t_k,x,\xi)=\lambda\sum_{k\in I}\varphi_\sigma(t-t_k)M(t_k,x,\xi), \tag{2.99}$$

where φ_σ is a regularizing kernel of support σ and $\{t_k,\,k\in I\}$ are the observation times. Then,

Theorem 2.6.7 (B., Moireau, Perthame, Sainte-Marie)**.** *Let us assume that M is solution of (2.98) and f satisfies (2.99). If* $\mathrm{Card}(k,t_k\leq T-\sigma)\neq 0$*, then*

$$\begin{aligned}\|f(T)-M(T)\|_{V_1}\leq{}&\|f_0-M_0\|_{V_1}e^{-\lambda\,\mathrm{Card}(k,t_k\leq T-\sigma)}\\&+\sigma\|\partial_t(f-M)\|_{L^\infty_t(M^1_x(\mathbb{R}_x),L^1(\mathbb{R}_\xi))}\left(1-e^{-\lambda\,\mathrm{Card}(k,t_k\leq T+\sigma)}\right)\\&+\sup_{0<t\leq T}\|Q(t)\|_{V_1}\frac{1-e^{-\lambda\,\mathrm{Card}(k,t_k\leq T+\sigma)}}{\lambda}\end{aligned} \tag{2.100}$$

Eventually, the last study on scalar conservation laws consists in considering partial observations in space. This work still needs an in-depth study. Until now, we only present preliminary result of observability and stability on the unidimensional periodic problem for smooth solutions ($Q = 0$). The observer's equation writes

$$\begin{cases} \partial_t f(t,x,\xi) + a(\xi)\cdot\nabla_x f(t,x,\xi) = \lambda \mathbb{1}_{[a,b]}(x)(M(t,x,\xi) - f(t,x,\xi)), \\ f(0,x,\xi) = f_0(x,\xi), \\ f(t,0,\xi) = f(t,1,\xi), \end{cases} \tag{2.101}$$

where observations come from

$$\begin{cases} \partial_t M(t,x,\xi) + a(\xi)\cdot\nabla_x M(t,x,\xi) = Q(t,x,\xi), \\ M(0,x,\xi) = M_0(x,\xi), \\ f(t,0,\xi) = f(t,1,\xi). \end{cases} \tag{2.102}$$

Denoting

$$X_{t,\xi}(x) = \int_0^t \mathbb{1}_{[a,b]}(x + a(\xi)s)ds, \tag{2.103}$$

the time, for a particle starting at position x, spent in the interval $[a,b]$ between 0 and t. Thus we state the following proposition

Proposition 2.6.8 (B., Moireau, Perthame, Sainte-Marie)**.** *The problem* (2.101) *is observable* $\Leftrightarrow X_{t,\xi}^{inf} = \min_x X_{t,\xi} > 0$.

And subsequently the stability result follows:

Proposition 2.6.9 (B., Moireau, Perthame, Sainte-Marie)**.** *Let* $f(t,x,\xi)$ *be the solution of* (2.101) *and* $M(t,x,\xi)$ *satisfy* (2.102) *where* $Q(t,x,\xi) = 0$*. If the data assimilation problem* (2.101) *is observable, exponential stability in time is ensured as soon as* $\lambda \geq \frac{t}{X_t^{inf}}$*, i.e.*

$$\|g(t)\|_{V_2} \leq \|g_0\|_{V_2} e^{-\lambda X_t^{inf}}. \tag{2.104}$$

To conclude the part about scalar conservation laws, we propose a numerical study on Burgers' equation. It illustrates convergences in the case of partial data in time and space, but also the existence of an optimal λ when data are noisy.

2.6.4 The Saint-Venant system

The theoretical results formulated above are motivated by numerical tests on the Saint-Venant system which give first results of astonishing qulity regarding the simplicity of the approach. In this part, we are interested in the unidimensional shallow water system

(already evoked in Section 2.5.1) but that we recall here:

$$\frac{\partial H}{\partial t} + \frac{\partial}{\partial x}\big(Hu\big) = 0, \tag{2.105}$$

$$\frac{\partial (Hu)}{\partial t} + \frac{\partial (Hu^2)}{\partial x} + \frac{g}{2}\frac{\partial H^2}{\partial x} = -gH\frac{\partial z_b}{\partial x}. \tag{2.106}$$

Opposite to what has been done in the previous section, the kinetic interpretation of this system contains a source term:

$$\partial_t M(t,x,\xi) + \xi \cdot \nabla_x M(t,x,\xi) - g\frac{\partial z_b}{\partial x}\partial_\xi M(t,x,\xi) = Q(t,x,\xi), \tag{2.107}$$

where

$$M(t,x,\xi) = \frac{H}{c}\chi\left(\frac{\xi - u}{c}\right), \tag{2.108}$$

and χ is a compactly supported function satisfying

$$\begin{cases} \chi(a) = \chi(-a) \geq 0, \\ \displaystyle\int \chi(z)dz = \int z^2\chi(z)dz = 1. \end{cases} \tag{2.109}$$

We show that the convergence of the observer towards a solution of the shallow water system is possible when we only benefit from data on the water height. The equation of the observer becomes

$$\partial_t f(t,x,\xi) + \xi \cdot \nabla_x f(t,x,\xi) - g\frac{\partial z_b}{\partial x}\partial_\xi f(t,x,\xi) = \lambda(\widetilde{M}(t,x,\xi) - f(t,x,\xi)), \tag{2.110}$$

where

$$\widetilde{M}(t,x,\xi) = \frac{H}{c}\chi\left(\frac{\xi - \hat{u}}{c}\right), \tag{2.111}$$

and $\hat{u}$ is the velocity deduced from the observer f which writes under the form:

$$f(t,x,\xi) = \frac{\hat{H}}{\hat{c}}\chi\left(\frac{\xi - \hat{u}}{\hat{c}}\right). \tag{2.112}$$

And we prove

Proposition 2.6.10 (B., Moireau, Perthame, Sainte-Marie)**.** *Let $(H(t,x), u(t,x)) \in L^\infty([0,T]\times \mathbb{R}_x)$ be solution of (2.105) - (2.106), and $M(t,x,\xi)$ be the Gibbs equilibrium (2.108). Let $f(t,x,\xi)$ satisfy (2.110). If $\widetilde{M}$ has the regularity defined by*

$$\partial_t \widetilde{M} + \xi \cdot \nabla_x \widetilde{M} + g\frac{\partial z_b}{\partial x}\left(\frac{\xi - u}{c^2}\right)\widetilde{M} = Q \in C([0,T], V_1), \tag{2.113}$$

then

$$\|f(T) - M(T)\|_{V_1} \underset{\lambda\to+\infty}{\longrightarrow} 0. \tag{2.114}$$

With this new observer, we are capable of building an entropic numerical scheme for data assimilation on the macroscopic variables. We event extend it to the non-hydrostatic Saint-Venant system with satisfactory numerical results.

2.7 Conclusion and Future Work

The problem of aquaculture modeling for the optimization of biofuel production leads to the simulation of systems of conservation laws similar to the Saint-Venant equations. Unexpected and tricky theoretical questions on kinetic formulations arise from such models. In this thesis, we provided some tools enabling the simulation (and validation) of the raceway case via both the search of closed-form solutions and the proposal of a novel method for data assimilation. Furthermore, the development of a C++ code to simulate three-dimensional free-surface flows proved the interests of our approach to biologists, who are already using it to compute Lagrangian trajectories of particles. This code is currently validated, maintained and improved by Raouf Hamouda (INRIA Engineer, team Ange).

2.7.1 Future work for the hydrodynamics/biology coupling

C++ code improvement Until now, simulated equations are hydrostatic. We showed that this assumption coarsely holds. However the paddlewheel does induce non-hydrostatic effects susceptible to modify Lagrangian trajectories. While theoretical material to account for those effects is available in [126], efficient numerical schemes are still to be found and implemented. Moreover, analytical validations are not possible yet.

Modeling of other phenomena Raceways are actually more complicated that what we have modeled for now. Temperature, and therefore water evaporation, are paramount in algae physiology. Likewise, nutrient sedimentation speeds up the heterogeneity that appears when the pond is not stirred enough. By taking into account such phenomena in the model, one could improve its realism.

Mixing modeling In [134], Strook *et al.* described an innovating mixing system for microfluids. Indeed they faced the same problem of laminar flows in standard use conditions of microtubes. Using low relief implanted in the ground, they managed to create turbulences that homogenize the fluid. Such an approach could be tested with our code by introducing similar bottoms.

Code adaptation for further applications The proposed model is able to represent other situations when hydrodynamic/biology interactions occur. One such application would be the algae invasion in several coastal regions like Chile and Guadeloupe.

2.7.2 Future work for data assimilation in hyperbolic systems

Source terms All results from Chapter 6 do not concern scalar conservation laws with source terms. A proposition on the processing of the topographical term for Saint-Venant equations was introduced. We believe that it could be generalized.

Kalman filter The kinetic formulation enables us to work on a linear equation when ξ is fixed. The whole non-linearity thus lies both in the Gibbs equilibrium written with macroscopic variables and the collision term (often denoted Q). We would like to study the feasibility of a Kalman filter at a kinetic level, that we could subsequently average with respect to ξ to obtain a proper macroscopic Kalman filter.

Relative entropy Relative entropy is a tool allowing the study of the behaviour of two solutions relatively to each other. It is often used to prove convergences and is well settled for the scalar case. Kinetic formulations of hyperbolic conservation law systems are compatible with such a concept and we could exploit it to prove observers convergences.

Data assimilation in the hydrodynamic/biology code Naturally, it will be interesting to take into account the real hydrodynamical data collected by INRA and NASKÉO from the raceway in Narbonne. This could constrain the model that will then provide more realistic Lagrangian trajectories.

Analytical solutions for free surface hydrostatic Euler equations

3

Dans ce chapitre, nous proposons un vaste ensemble de solutions analytiques, pour les équations d'Euler hydrostatiques et incompressible, à la fois en 2D et en 3D. Nous les appelons FRESH-ASSESS. Nous nous intéressons majoritairement à des situations d'écoulements à surface libre, mais quelques exemples ne le sont que partiellement. La principale utilité de ce travail est de permettre la validation de schémas numériques.

Ce travail, issu d'une collaboration avec Marie-Odile Bristeau *et* Jacques Sainte-Marie*, est paru dans Communication in Mathematical Sciences sous le titre* Analytical solutions for the free surface hydrostatic Euler equations.

In this chapter we propose a vast set of analytical solutions the hydrostatic and incompressible Euler equations, in 2D and 3D. We call them FRESH-ASSESS. We are mainly interested in free surface flows but some examples are given which have only partially a free surface. The principal interest of this work is to enable the validation of numerical schemes.

This is a joint work with Marie-Odile Bristeau *and* Jacques Sainte-Marie*. It was published in Communication in Mathematical Sciences under the title* Analytical solutions for the free surface hydrostatic Euler equations

3.1 Introduction

Models arising in fluid dynamics often based on the Navier-Stokes equations are generally difficult to analyze both at the mathematical or numerical level. As a consequence the derivation of efficient numerical schemes and their validations are complex. A way to circumvent this difficulty is to have access to analytical solutions of the considered problem and to confront the simulated solutions with them. Even if this approach is not a complete validation of the numerical schemes, it enables to have a good knowledge of the behavior of the discrete schemes in front of typical and complex situations particularly when the family of analytical solutions is large enough. Moreover it makes possible the study of the convergence order of a simulated solution towards the reference one. Starting from the incompressible Navier-Stokes equations, much work has been done in the derivation of relatively simple mathematical models for shallow water flows and long non-linear water waves. For these models, analytical solutions are often available. Thus the Saint-Venant system [19] that is well suited for the modeling of river hydraulics has been widely studied by a lot of authors. In a chronological order, the most famous contributions are: analytical solutions for the dam break situation by Ritter [123], the nonlinear wave propagation in Shallow water open channels by Stoker [132], solutions of the Saint-Venant system for a flow respectively over a ridge and in parabolic bowl by Houghton [76] and Thacker [138]. MacDonald *et al.* [99, 100] have proposed a wide family of analytical solutions with bottom friction, hydraulic jumps and various open-channel cross-sections. Likewise for the Korteweg-de Vries equations [85] and related systems – generally corresponding to potential flows [93] – such as the Boussinesq system [33], the Green-Naghdi model [66], various analytical solutions of soliton type are available [27, 86, 88]. Unfortunately, the previously mentioned models correspond to averaged – along a spatial coordinate – or irrotational approximations of the Navier-Stokes equations. In this paper we propose various analytical solutions for the incompressible hydrostatic Euler equations in the following situations: stationary flows, transient flows, free (or partially free) surface, external forcing, simplified viscosity terms. These solutions are denoted hereafter by the acronym FRESH-ASSESS corresponding to FREE Surface Hydrodynamics Analytical SolutionS for Euler SystemS. The analytical solutions are available in 2d and 3d for a large class of bottom geometry. Some of these solutions admit entropic shocks that are characterized. The main concern of the authors is to exhibit reference solutions that can be used for the validation of numerical codes. In the case of a regular flow, the solution is analytic. For non smooth solutions e.g. with shocks, the solution is obtained via the resolution of a simple ODE. If the proposed analytical solutions correspond to physical phenomena, they do not correspond to useful situations for practical use of the models. The analytical solutions are obtained as in MacDonald *et al.* [99, 100], starting from a given water depth and an admissible velocity field, we derive the corresponding topography profile. The paper is organized as follows. Starting from the incompressible and hydrostatic Euler equations (Section 3.2), we present in Section 3.3 the 2d FRESH-ASSESS solutions in various configurations. The 3d extension of these solutions is given in Section 3.4. In Section 3.5, the various analytical solutions are

illustrated in typical situations.

3.2 The Euler equations

We start from the 3d hydrostatic and incompressible free surface Euler equations [34, 68] with gravity

$$\frac{\partial u}{\partial x} + \frac{\partial v}{\partial y} + \frac{\partial w}{\partial z} = 0, \tag{3.1}$$

$$\frac{\partial u}{\partial t} + u\frac{\partial u}{\partial x} + v\frac{\partial u}{\partial y} + w\frac{\partial u}{\partial z} + \frac{\partial p}{\partial x} = 0, \tag{3.2}$$

$$\frac{\partial v}{\partial t} + u\frac{\partial v}{\partial x} + v\frac{\partial v}{\partial y} + w\frac{\partial v}{\partial z} + \frac{\partial p}{\partial y} = 0, \tag{3.3}$$

$$\frac{\partial p}{\partial z} = -g, \tag{3.4}$$

where the z axis represents the vertical direction. We consider this system for

$$t > 0, \quad (x, y) \in \Omega, \quad z_b(x, y) \leq z \leq \eta(x, y, t),$$

where Ω is a bounded domain of $\mathbb{R}^2$, $\eta(x, y, t)$ represents the free surface elevation, $\mathbf{u} = (u, v, w)^T$ the velocity vector. The gravity acceleration is denoted g and p is the fluid pressure. The bottom geometry is z_b so the water depth is $H = \eta - z_b$, see Figure 3.1. Equation (3.1) represents the incompressibility (mass conservation equation) and Eqs. (3.2),(3.3) are respectively the momentum equilibria of forces along axis x and y. Because of the hydrostatic assumption, the momentum equilibrium of forces along the vertical axis reduces to (3.4).

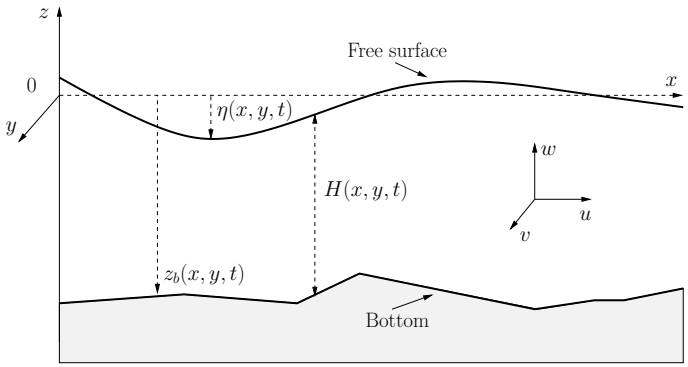

Figure 3.1: Notations: water height $H(x, y, t)$, free surface $\eta(x, y, t)$ and bottom $z_b(x, y)$.

The system (3.1)-(3.4) is completed with boundary conditions. Classically at the free surface we have the kinematic boundary condition

$$\frac{\partial \eta}{\partial t} + u_s\frac{\partial \eta}{\partial x} + v_s\frac{\partial \eta}{\partial y} - w_s = 0, \tag{3.5}$$

where the subscript s denotes the value of the considered quantity at the free surface. The dynamical condition at the free surface takes into account the equilibrium with the atmospheric pressure and we have

$$p_s = p^a(x, y, t), \tag{3.6}$$

where $p^a = p^a(x, y, t)$ is a given function corresponding to the atmospheric pressure. At the bottom, the kinematic boundary condition corresponds to a no-penetration condition

$$u_b \frac{\partial z_b}{\partial x} + v_b \frac{\partial z_b}{\partial y} - w_b = 0, \tag{3.7}$$

where the subscript b denotes the value of the considered quantity at the bottom.

The boundary condition (3.6) coupled with (3.4) gives

$$p = p^a + g(\eta - z),$$

so the hydrostatic Euler system (3.1)-(3.4) can be written under the form

$$\frac{\partial H}{\partial t} + \frac{\partial}{\partial x}\int_{z_b}^{\eta} u \, dz + \frac{\partial}{\partial y}\int_{z_b}^{\eta} v \, dz = 0, \tag{3.8}$$

$$w = -\frac{\partial}{\partial x}\int_{z_b}^{z} u \, dz - \frac{\partial}{\partial y}\int_{z_b}^{z} v \, dz, \tag{3.9}$$

$$\frac{\partial u}{\partial t} + u\frac{\partial u}{\partial x} + v\frac{\partial u}{\partial y} + w\frac{\partial u}{\partial z} + g\frac{\partial \eta}{\partial x} = -\frac{\partial p^a}{\partial x}, \tag{3.10}$$

$$\frac{\partial v}{\partial t} + u\frac{\partial u}{\partial x} + v\frac{\partial v}{\partial y} + w\frac{\partial u}{\partial z} + g\frac{\partial \eta}{\partial y} = -\frac{\partial p^a}{\partial y}. \tag{3.11}$$

Equation (3.8) results from an integration of the divergence free condition (3.1) along z from z_b to η coupled with the kinematic relation (3.5). Similarly Eq. (3.9) results from an integration of the divergence free condition from z_b to z where the boundary condition (3.7) is used. Notice that (3.8) and (3.9) are equivalent to (3.1), (3.5) and (3.7).

For smooth solutions, the hydrostatic Euler system (3.1)-(3.7) – or equivalently (3.8)-(3.11) – is completed with an energy equality namely,

$$\begin{aligned}\frac{\partial}{\partial t}\int_{z_b}^{\eta}(E + p^a) \, dz + \frac{\partial}{\partial x}\int_{z_b}^{\eta} u\big(E + g(\eta - z) + gz\big) \, dz \\ + \frac{\partial}{\partial y}\int_{z_b}^{\eta} u\big(E + g(\eta - z) + gz\big) \, dz = H\frac{\partial p^a}{\partial t},\end{aligned} \tag{3.12}$$

with

$$E = \frac{u^2}{2} + \frac{v^2}{2} + gz. \tag{3.13}$$

3.3 2d analytical solutions

For the sake of simplicity, we first restrict our presentation to 2d analytical solutions. The considered horizontal domain is $\Omega = [0, L_x]$. The 3d extension of the proposed solutions is given in Section 3.4.

In this section, we first propose stationary solutions for the system (3.1)-(3.4). The regularity of the solutions is examined in paragraphs 3.3.3 and 3.3.4. Then we exhibit analytical solutions for the Euler system in the following situations : external forcing, viscosity terms, reactive tracer, transient solutions, a partially free surface.

3.3.1 Main idea

We first consider the system (3.8)-(3.11) where all the variables are independent of y. Stationary solutions of this system have to fulfill

$$\frac{\partial}{\partial x}\int_{z_b}^{\eta} u \; dz = 0, \tag{3.14}$$

$$w = -\frac{\partial}{\partial x}\int_{z_b}^{z} u \; dz, \tag{3.15}$$

$$u\frac{\partial u}{\partial x} + w\frac{\partial u}{\partial z} + g\frac{\partial \eta}{\partial x} = -\frac{\partial p^a}{\partial x}. \tag{3.16}$$

Except in paragraphs 3.3.7 and 3.3.8, we assume in this section $p^a = Cst$.

From (3.16), it comes that

$$u\frac{\partial u}{\partial x} + w\frac{\partial u}{\partial z}, \tag{3.17}$$

has to be independent of z and this is the most difficult requirement to satisfy. The underlying idea for the derivation of the analytical solutions is the following. To satisfy (3.14), we seek for u under the form

$$u = \alpha\frac{\varphi'(z - z_b)}{\varphi(H)}, \tag{3.18}$$

with $\varphi(0) = 0$, $\alpha = Cst$. Then from (3.15), w is given by

$$w = -\alpha\frac{\partial}{\partial x}\frac{\varphi(z - z_b)}{\varphi(H)}, \tag{3.19}$$

and replacing the previous expressions for u and w in (3.16) implies (3.17) is independant of z when

$$(\varphi'(z - z_b))^2 - \varphi(z - z_b)\varphi''(z - z_b) = Cst,$$

that is ensured for

$$\varphi(z) = \sin(z). \tag{3.20}$$

3.3.2 General continuous stationary solutions

The following proposition gives smooth analytical solutions for the system (3.14)-(3.16).

Proposition 3.3.1. *If α, β and $\overline{z}_b$ are three real constants and H_0 a non negative real $C^1(\Omega)$ function such that $\sin(\beta H_0(x)) \neq 0$ for all $x \in \Omega$ then $u = u_{\alpha,\beta}$, $w = w_{\alpha,\beta}$ and z_b respectively given by*

$$z_b = \overline{z}_b - H_0 - \frac{\alpha^2\beta^2}{2g\sin^2(\beta H_0)}, \tag{3.21}$$

$$u_{\alpha,\beta} = \frac{\alpha\beta}{\sin(\beta H_0)}\cos(\beta(z-z_b)), \tag{3.22}$$

$$w_{\alpha,\beta} = \alpha\beta\left(\frac{\partial z_b}{\partial x}\frac{\cos(\beta(z-z_b))}{\sin(\beta H_0)} + \frac{\partial H_0}{\partial x}\frac{\sin(\beta(z-z_b))\cos(\beta H_0)}{\sin^2(\beta H_0)}\right), \tag{3.23}$$

satisfy the 2d stationary Euler equations (3.14)-(3.16) with $\eta = H_0 + z_b$.

Proof. Following (3.18),(3.20), we propose to choose u under the form

$$u = u_{\alpha,\beta} = \frac{\alpha\beta}{\sin(\beta H)}\cos(\beta(z-z_b)), \tag{3.24}$$

and from (3.19), w is given by

$$w = w_{\alpha,\beta} = \alpha\beta\left(\frac{\partial z_b}{\partial x}\frac{\cos(\beta(z-z_b))}{\sin(\beta H)} + \frac{\partial H}{\partial x}\frac{\sin(\beta(z-z_b))\cos(\beta H)}{\sin^2(\beta H)}\right), \tag{3.25}$$

then Eq. (3.16) reduces to

$$\frac{\partial}{\partial x}\left(\frac{\alpha^2\beta^2}{2\sin^2(\beta H)} + g(H+z_b)\right) = 0, \tag{3.26}$$

and the definition (3.21) for z_b with $H = H_0$ completes the proof. □

The previous proposition is only valid for smooth solutions. The regularity and uniqueness of the solutions and their derivation are discussed in the two following paragraphs.

3.3.3 Continuity of the solutions

Here we adopt a slightly different strategy considering we have a given topography $z_b(x)$, $x \in \Omega = [0, L_x]$, given values for $\alpha > 0$ and β and a boundary value for H namely, $H_{lim} = H(0)$ or $H_{lim} = H(L_x)$. $H(x)$ will be given by the solution of a simple ODE. We assume u satisfies (3.24), w satisfies (3.25) and it remains to solve (3.26) to obtain H.

We introduce the function

$$F_{\alpha,\beta}(x) \,:\, x \mapsto gx + \frac{\alpha^2\beta^2}{2\sin^2(\beta x)},$$

and we point out that $F_{\alpha,\beta}$ is not one-to-one (see Figure 3.2).

When considering smooth solutions – and with the notations of Figure 3.2 – the reso-

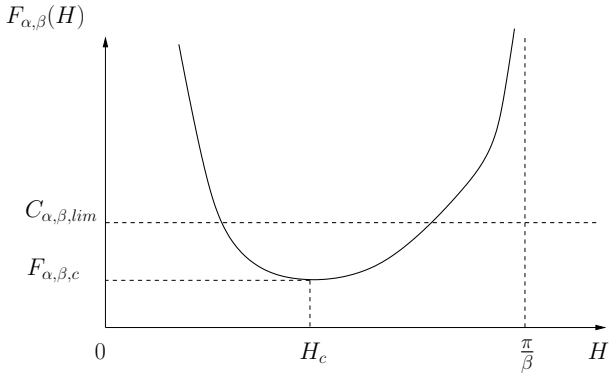

Figure 3.2: Function $H \mapsto F_{\alpha,\beta}(H)$.

lution of (3.26) is equivalent to find for all $x \in \Omega$ a solution to

$$F_{\alpha,\beta}(H(x)) + gz_b(x) = F_{\alpha,\beta}(H_{lim}) + gz_{b,lim}. \tag{3.27}$$

The previous results allow to write the following proposition

Proposition 3.3.2. *If for any $x \in \Omega$, the problem*

$$F_{\alpha,\beta}(H(x)) = F_{\alpha,\beta}(H_{lim}) + g(z_{b,lim} - z_b(x)) = C_{\alpha,\beta,lim} - gz_b(x) \geq 0, \tag{3.28}$$

has a solution $H(x) \geq 0$ then $(H, u_{\alpha,\beta}, w_{\alpha,\beta})$ are solutions of (3.14)-(3.16). This result can also be expressed in the following way: if the problem (3.28) admits a solution H_m in $x = x_m$, the point of maximum topography or equivalently if

$$F^{min}_{\alpha,\beta} \leq C_{\alpha,\beta,lim} - gz_b(x_m),$$

then it admits a solution for all $x \in \Omega$. And it is easy to prove that if $z_b \in C^k(\Omega)$, $k \geq 0$ then $(H, u_{\alpha,\beta}) \in C^k(\Omega)$ and $w_{\alpha,\beta} \in C^{k-1}(\Omega)$.

Let Ω_c be the subset of Ω containing the points x for which the problem (3.28) has no solution. We are now interested in situations where $\Omega_c \neq \emptyset$.

3.3.4 Discontinuous solutions

Let us consider now discontinuous solutions. We define the operator $[A] = A^+ - A^-$, where the superscripts $^+$ and $^-$ define the variables right after and before the discontinuity.

Stationary shocks of the system (3.12), (3.14) and (3.16) are characterized by

$$\left[\int_{z_b}^{\eta} u \; dz\right] = 0,$$
$$\left[\int_{x_0}^{x}\int_{z_b}^{\eta}\left(u\frac{\partial u}{\partial x} + w\frac{\partial u}{\partial z} + g\frac{\partial H}{\partial x}\right) dz\right] = 0,$$
$$\left[\int_{zb}^{\eta}\left(\frac{u^3}{2} + g\eta u\right) dz\right] = \mathcal{D},$$

that reduce to

$$\left[\frac{g}{2}H^2 + \frac{\alpha^2\beta^2 H}{2\sin(\beta H)^2} + \frac{\alpha^2\beta}{2}\frac{\cos(\beta H)}{\sin(\beta H)}\right] = 0, \tag{3.29}$$
$$\left[\frac{\alpha^3\beta^2}{2\sin^2(\beta H)} + g\alpha(H + z_b)\right] = \mathcal{D}, \tag{3.30}$$

since $u = u_{\alpha,\beta}$ and with $\mathcal{D} \leq 0$, the entropy dissipation.

If $\Omega_c = \Omega$, the parameters α, β and the boundary condition H_{lim} are not compatible so we assume $\Omega_c \neq \Omega$. Without loss of generality we assume $H_{lim} = H(L_x)$ and $\alpha \geq 0$. We also suppose here $z_b \in C^1(\Omega)$ with a unique $x_c \in \overset{\circ}{\Omega} =]0, L_x[$ such that

$$z_{b,c} = \max_{x\in\Omega} z_b(x), \tag{3.31}$$
$$\left.\frac{\partial z_b}{\partial x}\right|_{x=x_c} = 0. \tag{3.32}$$

The topography should also be strictly increasing before the maximum, and striclty decreasing after. If not, the domain should be divided into subdomains on which this property applies. If $\Omega_c \neq \emptyset$ then the problem (3.28) has no solution at least for $x = x_c \in \Omega_c$ and the solution will be discontinuous. Let us try to characterize the water height at this point. If the bottom profile is enough regular, apart from the shock Eq. (3.26) can be written under the form

$$\left(g - \alpha^3\beta^2\frac{\cos(\beta H)}{\sin^3(\beta H)}\right)\frac{\partial H}{\partial x} = -g\frac{\partial z_b}{\partial x}, \tag{3.33}$$

This previous equation remains well defined until the quantity

$$\left(g - \alpha^3\beta^2\frac{\cos(\beta H)}{\sin^3(\beta H)}\right),$$

vanishes to zero. It also corresponds to the vanishing of the derivative of $F_{\alpha,\beta}$, so a potential extremum. The critical water depth H_c satisfies

$$\frac{\cos(\beta H_c)}{\sin^3(\beta H_c)} = \frac{g}{\alpha^3\beta^2}. \tag{3.34}$$

So, we have now to study the function

$$f : x \to \frac{\cos(\beta x)}{\sin^3(\beta x)}$$

that is defined over $\mathbb{R} - \{n\pi/\beta\}, n \in \mathbb{Z}$, periodic with period π/β. It is a non increasing function over each intervall $I_{\beta,n} =]n\pi/\beta, (n+1)\pi/\beta[$. We can then conclude that for each intervall $I_{\beta,n}$, there exists only one solution for Eq. (3.34). Moreover, since the roots of f are easily defined as $(n+1/2)\pi/\beta$, we can conclude from the fact that $\frac{g}{\alpha^3\beta^2}$ is positive that the solution of Eq. (3.34) is in the intervall $]n\pi/\beta, (n+1/2)\pi/\beta[$. In the following we will consider $n = 0$.

Using the notations of Figure 3.2, we easily find that H_c solution of Eq. (3.34) satisfies

$$H_c = \frac{\arcsin r_c^2}{\beta}, \quad \text{and} \quad F_{\alpha,\beta,c} = gH_c + \frac{\alpha^2\beta^2}{2r_c^4}, \tag{3.35}$$

where r_c^2 is the unique real solution of the polynomial equation

$$P(X) = g^2X^3 + \alpha^4\beta^6X - \alpha^4\beta^6 = 0, \tag{3.36}$$

with

$$r_c = \sqrt{\frac{\sqrt[3]{12\alpha^4}\beta^2}{6g} \frac{-\sqrt[3]{12\alpha^4}\beta^2 + \left(\sqrt[3]{9g + \sqrt{12\alpha^4\beta^6 + 81g^2}}\right)^2}{\sqrt[3]{9g + \sqrt{12\alpha^4\beta^6 + 81g^2}}}}.$$

Since we have $P(0) \leq 0$ and $P(1) \geq 0$, we remark that $0 \leq r_c \leq 1$. From (3.32), for $x = x_c$ the solution H of

$$\left(g - \frac{\alpha^2\beta^3\cos(\beta H)}{\sin(\beta H)^3}\right)\frac{\partial H}{\partial x} = 0,$$

and the condition

$$\left.\frac{\partial H}{\partial x}\right|_{x=x_c} = 0, \quad \text{with} \quad g - \frac{\alpha^2\beta^3\cos(\beta H)}{\sin(\beta H)^3} \neq 0,$$

would give that a continuous solution exists over Ω that is contradictory with the assumption $x_c \in \Omega_c$. So $H_c = H(x_c)$ necessarily satisfies (3.34) that is equivalent to (3.36) and is given by (3.35). Over the interval $[0, x_c]$, the solution will be continuous and hence

$$\left[\frac{\alpha^3\beta^2}{2\sin^2(\beta H)} + g\alpha(H + z_b)\right]_{x=0}^{x=x_c} = 0.$$

Over the interval $[x_c, L_x]$, we have

$$\left[\frac{\alpha^3\beta^2}{2\sin^2(\beta H)} + g\alpha(H + z_b)\right]_{x=x_c}^{x=L_x} = \alpha(F_{\alpha,\beta}(H_{lim}) + gz_{b,lim} - F_{\alpha,\beta,c} - gz_{b,c}),$$

and by construction $F_{\alpha,\beta,c} + gz_{b,c} \geq C_{\alpha,\beta,lim}$ so we have $\mathcal{D} \leq 0$ in (3.30).

If a shock occurs, its abscissa x_s and the associated water depth are uniquely characterized by (3.29)-(3.30) that correspond to

$$\left[\frac{g}{2}H^2 + \frac{\alpha^2\beta^2 H}{2\sin^2(\beta H)} + \frac{\alpha^2\beta}{2}\frac{\cos(\beta H)}{\sin(\beta H)}\right]_{H_{s,l}}^{H_{s,r}} = 0, \tag{3.37}$$

$$\frac{\alpha^2\beta^2}{2\sin^2(\beta H_c)} + g(H_c + z_{b,c}) = \frac{\alpha^2\beta^2}{2\sin^2(\beta H_{s,l})} + g(H_{s,l} + z_{b,s}), \tag{3.38}$$

$$\frac{\alpha^2\beta^2}{2\sin^2(\beta H_{lim})} + g(H_{lim} + z_{b,lim}) = \frac{\alpha^2\beta^2}{2\sin^2(\beta H_{s,r})} + g(H_{s,r} + z_{b,s}), \tag{3.39}$$

where $z_{b,s}$ is the bottom topography at the abscissa of the shock and $H_{s,l}$, $H_{s,r}$ are the water depth at the left and right of the shock. If the solutions of the system (3.37)-(3.39) are continuous, this means the outflow boundary condition can not be satisfied. In this case, the torrential regime takes place from $x = x_c$ to $x = L_x$.

In practice, the solution $H(x)$ is obtained as follows. Starting from the value H_{lim} at abscissa x_{lim}, we calculate the solution of the algebraic equation (3.27) or equivalently the ODE (3.33). If no singularity appears, the problem is solved. If for one abscissa, Eq. (3.29) can not be solved then x_c has to be determined by (3.31),(3.32). Then (3.37)-(3.39) allow to build the whole solution over Ω.

An illustration of the analytical solutions obtained in the situations with and without shocks is given in paragraphs 3.5.1 and 3.5.2.

3.3.5 Solutions with external forcing

We consider the same hydrostatic Euler system with free surface as previously but we add an external forcing and a viscosity term (in the vertical direction). The governing equations of the considered system are

$$\frac{\partial}{\partial x}\int_{z_b}^{\eta} u \, dz = 0, \tag{3.40}$$

$$\frac{\partial u}{\partial x} + \frac{\partial w}{\partial z} = 0, \tag{3.41}$$

$$u\frac{\partial u}{\partial x} + w\frac{\partial u}{\partial z} + g\frac{\partial \eta}{\partial x} = f_x + \nu\frac{\partial^2 u}{\partial z^2}, \tag{3.42}$$

where f_x is a volumetric source term and the atmospheric pressure p^a is supposed to be constant. The following proposition holds

Proposition 3.3.3. *If we choose $f_x = \beta\nu u$ and $\beta \geq 0$ – that corresponds to an energy supply for the system – then for any bottom profile z_b of the form (3.21), the quantities $u = u_{\alpha,\beta}$, $w = w_{\alpha,\beta}$ given by (3.22) and (3.23) with $H = H_0$ are solutions of (3.40)-(3.42).*

Even if the situations encountered in this paragraph – with an equilibrium between the

external forcing and the viscosity – are different from those of the preceding paragraph, the resulting water depth and velocity fields are similar and we do not present any illustration for this situation.

3.3.6 Coupling with a reactive tracer

We consider in this paragraph the stationary hydrostatic Euler system governed by (3.14)-(3.15) with $p^a = Cst$ and coupled with an advection-reaction type equation of the form

$$u\frac{\partial T}{\partial x} + w\frac{\partial T}{\partial z} = \frac{T_0 - T}{\tau}. \tag{3.43}$$

The equation (3.43) models for example the transport and the reaction of a tracer.

In order to build solutions for the system (3.14)-(3.15) and (3.43) we use the analytical solutions proposed in paragraph 3.3.2. Thus, since the only remaining constraint for the choice of functions T, T_0 and τ is to satisfy (3.43), there exists a lot of solution for this problem. We present hereafter two distinct choices.

Let $x \mapsto H_0(x)$ be a continuous, non negative function defined on Ω and we choose the bottom topography z_b under the form defined by (3.21).

First choice

Suppose $T_0 = T_0(x)$ and $\tau = \tau(x)$ are defined by

$$\tau = \frac{\sin(\beta H_0(x))^2}{\alpha\beta^2 \cos(bH_0(x)\frac{\partial H_0}{\partial x}}, \quad \text{and} \quad T_0 = \alpha b \frac{\gamma(z - z_b(x))}{\sin(bH_0(x))},$$

with $\gamma = \gamma(x) = \frac{1}{\text{cotan}(x) - \text{csc}(x)}$. Then the velocity fields $u_{\alpha,\beta}$, $w_{\alpha,\beta}$ defined by (3.22) and (3.23) for $H = H_0$ and T defined by

$$T(x, z) = -\gamma(z - z_b(x))u_{\alpha,\beta}(x, z),$$

are solutions of (3.14)-(3.15) coupled with (3.43).

Second choice

Similarly, the velocity fields $u_{\alpha,\beta}$, $w_{\alpha,\beta}$ defined by (3.22) and (3.23) for $H = H_0$ and T defined by

$$T(x, z) = e^{-(H(x)-(z-z_b(x)))}$$

with $T_0 = 0$ and

$$\frac{1}{\tau} = \alpha\beta \frac{\cos(\beta(z - z_b))}{\sin(\beta H)} \left(1 - \frac{\tan(\beta(z - z_b))}{\tan(\beta H)}\right) \frac{\partial H}{\partial x},$$

are solutions of (3.14)-(3.15) coupled with (3.43).

3.3.7 Transient analytical solutions

The stationary solutions presented in the preceding paragraphs allow to validate spatial discretization techniques for the considered equations. In order to evaluate the accuracy of time schemes, transient solutions are necessary. In this paragraph we give two examples of time dependent analytical solutions.

First situation

We now consider the hydrostatic Navier-Stokes system defined by

$$\frac{\partial}{\partial x}\int_{z_b}^{\eta} u\ dz = 0, \tag{3.44}$$

$$w = -\frac{\partial}{\partial x}\int_{z_b}^{z} u\ dz, \tag{3.45}$$

$$\frac{\partial u}{\partial t} + u\frac{\partial u}{\partial x} + w\frac{\partial u}{\partial z} + g\frac{\partial \eta}{\partial x} = -\frac{\partial p^a}{\partial x} + \nu\frac{\partial^2 u}{\partial z^2}, \tag{3.46}$$

where $p = p^a$ is the atmospheric pressure at the free surface. We assume the velocity fields u,w can vary w.r.t. time t whereas the water depth $H = H(x)$ only depends on the spatial coordinate x.

As in paragraph 3.3.2, let $x \mapsto H_0(x)$ be a continuous, non negative function defined on Ω, we choose the bottom topography z_b under the form (3.21) and the external pressure p^a is given by

$$p^a = -\frac{\alpha^2\beta^2}{2\sin^2(\beta H_0)}\left(1 - e^{-\nu\beta^2 t}\right).$$

Then the velocity fields

$$\begin{aligned}
\tilde{u}_{\alpha,\beta} &= \frac{\alpha\beta}{\sin(\beta H_0)}\cos(\beta(z - z_b))e^{-\nu\beta^2 t}, \\
\tilde{w}_{\alpha,\beta} &= \frac{\alpha\beta e^{-\nu\beta^2 t}}{\sin^2(\beta H_0(x))}\left(\sin\left(\beta(z - z_b(x))\right)\cos\left(\beta H_0(x)\right)\frac{\partial H_0}{\partial x}\right. \\
&\quad \left. + \cos\left(\beta(z - z_b(x))\right)\frac{\partial z_b}{\partial x}\sin\left(\beta H_0(x)\right)\right)
\end{aligned}$$

and the water depth H_0 satisfy the equations (3.44)-(3.46).

This situation is very similar to what has been proposed in paragraph 3.3.2, the contribution of the horizontal and vertical velocities decreasing exponentially is replaced by the effects of the external pressure p^a. These analytical solutions are not illustrated.

The system (3.44)-(3.46) can admit discontinuous solutions but this would imply a discontinuous atmospheric pressure p^a that has no physical meaning.

Analytical solution with a travelling wave

In this paragraph, we consider that the bottom topography $z_b = z_b(x,t)$ can vary with respect to time and $p^a = Cst$. Let us consider the system

$$\frac{\partial H}{\partial t} + \frac{\partial}{\partial x}\int_{z_b}^{\eta} u \; dz = 0, \tag{3.47}$$

$$w = -\frac{\partial}{\partial x}\int_{z_b}^{z} u \; dz, \tag{3.48}$$

$$\frac{\partial u}{\partial t} + u\frac{\partial u}{\partial x} + w\frac{\partial u}{\partial z} + g\frac{\partial \eta}{\partial x} = f_x, \tag{3.49}$$

with f_x given by

$$f_x = -\frac{\partial z_b}{\partial t}\frac{\partial u}{\partial z}.$$

The energy balance associated with this system is

$$\frac{\partial}{\partial t}\int_{z_b}^{\eta} E \; dz + \frac{\partial}{\partial x}\int_{z_b}^{\eta} u\big(E + g(\eta - z) + gz\big) \; dz = -\frac{1}{2}\frac{\partial z_b}{\partial t}\left(u_s^2 - u_b^2\right),$$

with $E = \frac{u^2}{2} + gz$.

If $H_0(x)$ is a non negative quantity such that the bottom topography is given by (3.21) then $H(x,t) = H_0(x - c_0 t)$, $u_{\alpha,\beta}(x,z,t)$ given by

$$u_{\alpha,\beta}(x,z,t) = c_0 + \frac{\alpha\beta}{\sin(\beta H)}\cos(\beta(z - z_b)),$$

and w obtained from (3.23) are solutions of (3.47)-(3.49).

3.3.8 Interactions with structures

We are not only interested in situations of free surface flows, so we consider now situations without free surface or where only a part of the water surface is free.

2d analytical solutions with partially free surface

Such a situation can be obtained when the atmospheric pressure term p^a depends on the flow characteristics H, u, w. This corresponds to the case where the flow interacts with a lid. In such a situation, the closure of the system is ensured with a lid displacement law of the form

$$p^a = K(x)\left|\frac{\sqrt{\eta} - \sqrt{\eta_m}}{\sqrt{\eta_m}}\right|_+, \tag{3.50}$$

with $\eta = H + z_b$, $\eta_m = \eta_m(x)$ a given function and $K(.)$ a real nonnegative function. Such an expression for p^a mimics the interaction between a deformable lid and the free surface. For more informations about the origins and the mechanical justifications of formula (3.50), the reader can refer to [119].

Thus, if the water depth H satisfies the ODE

$$\frac{\partial}{\partial x}\left(\frac{\alpha^2\beta^2}{2\sin^2(\beta H)}+gH-K(x)\left|\frac{\sqrt{\eta}-\sqrt{\eta_m}}{\sqrt{\eta_m}}\right|\mathbf{1}_{H+z_b\geq\eta_m}\right)=-g\frac{\partial z_b}{\partial x}, \tag{3.51}$$

then H and $u_{\alpha,\beta}, w_{\alpha,\beta}$ given by (3.22) and (3.23) are solutions of the considered problem. In particular, if $H_0(x)$ is any non-negative function then $\overline{H}=\overline{\eta}-z_b$ with z_b given by (3.21) and

$$\overline{\eta}=\frac{K(x)(H_0+z_b)}{\left(\frac{\alpha^2\beta^2}{2\sin^2(\beta H_0)}+g(H_0+z_b)+K\right)^2},$$

satisfies (3.51).

Analytical solutions in cylindrical coordinates

We now consider the cylindrical representation of the incompressible Euler equations for an axisymmetric flow with the assumption of no tangential velocity. The gravity is also neglected. We denote u_x and u_r the velocities along the x axis and radial coordinate respectively. The continuity equation reads

$$\frac{1}{r}\frac{\partial r u_r}{\partial r}+\frac{\partial u_x}{\partial x}=0, \tag{3.52}$$

and the momentum equations reduces to

$$u_r\frac{\partial u_x}{\partial r}+u_x\frac{\partial u_x}{\partial x}+\frac{\partial p}{\partial x}=0, \tag{3.53}$$

$$\frac{\partial p}{\partial r}=0. \tag{3.54}$$

Suppose the flow takes place in a deformable pipe parallel to the x axis and of radius $R(x)$. The kinematic boundary condition at $r=R(x)$ ensuring the fluid does not leave the pipe is given by

$$\frac{\partial R}{\partial t}+\frac{\partial R}{\partial x}\,u_x|_{r=R}-u_r|_{r=R}=0. \tag{3.55}$$

Equation (3.54) gives $p=p(x)$ and as in paragraph 3.3.8, the system (3.52)-(3.55) is closed with a wall displacement law of the form

$$p(x)=K(x)\left(R(x)^\gamma-R_m(x)^\gamma\right),$$

where $K(.)$ and $R_m(.)$ are two non negative given functions and γ is a positive constant.

Using (3.52) and (3.55), the mass conservation in the pipe reads

$$\int_0^{R(x)} r u_x dr = Cst, \tag{3.56}$$

and the radial velocity u_r is given by

$$u_r = \frac{1}{r}\int_0^r r u_x dr. \tag{3.57}$$

Let us consider the velocity field u_x given by

$$u_x = \alpha\beta \frac{\cosh(\beta r^2)}{\sinh(\beta R(x)^2)},$$

then all the solutions $R(x)$ of

$$\frac{\partial}{\partial x}\left(\frac{\alpha^2\beta^2}{2\sinh^2(\beta R(x)^2)} + K(x)\left(R(x)^\gamma - R_m(x)^\gamma\right)\right) = 0, \tag{3.58}$$

are solutions of the system (3.52)-(3.57). In particular if $R_0(x)$ is any non-negative function then $\overline{R}(x)$ defined by

$$\overline{R}(x) = \left(\frac{\alpha^2\beta^2}{2K(x)\sinh^2(\beta R_0(x)^2)} + R_0(x)^\gamma\right)^{\frac{1}{\gamma}},$$

is solution. It has to be noticed that whatever the choices for the positive functions $K(x)$ and $R_m(x)$, all the solutions of (3.58) are necessarily continuous and no shock can occur.

An illustration of the situations proposed here is given in paragraph 3.5.3.

3.4 Analytical solutions in 3d

In this paragraph, we propose a 3d extension of the analytical solutions obtained in paragraph 3.3.2.

From (3.8)-(3.11), stationary solutions of the 3d Euler system with free surface have to fulfill

$$\frac{\partial}{\partial x}\int_{z_b}^{\eta} u\ dz + \frac{\partial}{\partial y}\int_{z_b}^{\eta} v\ dz = 0, \tag{3.59}$$

$$u\frac{\partial u}{\partial x} + v\frac{\partial u}{\partial y} + w\frac{\partial u}{\partial z} + g\frac{\partial \eta}{\partial x} = \frac{\partial p^a}{\partial x}, \tag{3.60}$$

$$u\frac{\partial v}{\partial x} + v\frac{\partial v}{\partial y} + w\frac{\partial v}{\partial z} + g\frac{\partial \eta}{\partial y} = \frac{\partial p^a}{\partial y}, \tag{3.61}$$

$$w = -\frac{\partial}{\partial x}\int_{z_b}^{z} u\ dz - \frac{\partial}{\partial y}\int_{z_b}^{z} v\ dz, \tag{3.62}$$

where we have considered $p^a = 0$. Let us introduce the velocity fields

$$u_{\alpha_1,\beta} = \frac{\alpha_1\beta}{\sin(\beta H)}\cos(\beta(z - z_b)), \tag{3.63}$$

$$v_{\alpha_2,\beta} = \frac{\alpha_2\beta}{\sin(\beta H)}\cos(\beta(z - z_b)), \tag{3.64}$$

then we clearly have

$$\int_{z_b}^{\eta} u_{\alpha_1,\beta}\, dz = \alpha_1, \quad \text{and} \quad \int_{z_b}^{\eta} v_{\alpha_2,\beta}\, dz = \alpha_2.$$

Using (3.62), we obtain

$$\begin{aligned} w_{\alpha_1,\alpha_2,\beta} &= \frac{\beta}{\sin^2(\beta H)} \left(\sin(\beta(z-z_b))\cos(\beta H) \left(\alpha_1 \frac{\partial H}{\partial x} + \alpha_2 \frac{\partial H}{\partial y} \right) \right. \\ &\quad \left. + \cos(\beta(z-z_b))\sin(\beta H) \left(\alpha_1 \frac{\partial z_b}{\partial x} + \alpha_2 \frac{\partial z_b}{\partial y} \right) \right), \end{aligned} \tag{3.65}$$

and the momentum equations along x and y (3.60)-(3.61) reduce to

$$\begin{aligned} g\frac{\partial \eta}{\partial x} - \alpha_1 \beta^3 \frac{\cos(\beta H)}{\sin^3(\beta H)} \left(\alpha_1 \frac{\partial H}{\partial x} + \alpha_2 \frac{\partial H}{\partial y} \right) = 0, \\ g\frac{\partial \eta}{\partial y} - \alpha_2 \beta^3 \frac{\cos(\beta H)}{\sin^3(\beta H)} \left(\alpha_1 \frac{\partial H}{\partial x} + \alpha_2 \frac{\partial H}{\partial y} \right) = 0, \end{aligned}$$

or equivalently

$$\frac{\partial}{\partial x} \left(gH + \frac{\alpha_1^2 \beta^2}{2\sin^2(\beta H)} \right) + \frac{\partial}{\partial y} \left(\frac{\alpha_1 \alpha_2 \beta^2}{2\sin^2(\beta H)} \right) = -g\frac{\partial z_b}{\partial x}, \tag{3.66}$$

$$\frac{\partial}{\partial x} \left(\frac{\alpha_1 \alpha_2 \beta^2}{2\sin^2(\beta H)} \right) + \frac{\partial}{\partial y} \left(gH + \frac{\alpha_2^2 \beta^2}{2\sin^2(\beta H)} \right) = -g\frac{\partial z_b}{\partial y}, \tag{3.67}$$

where H is the unknown. Therefore a necessary condition for the system (3.66)-(3.67) to admit a solution, is the water depth H being of the form

$$H(x,y) = H_0(\alpha_1 x + \alpha_2 y), \quad \text{or} \quad H(x,y) = H_0(\alpha_2 x - \alpha_1 y).$$

Only the second choice leads to non trivial solutions and thus for any non negative function $H_0(x)$, the bottom topography given by

$$z_b(x,y) = \overline{z}_b - H_0(\alpha_1 x + \alpha_2 y) - \frac{(\alpha_1^2 + \alpha_2^2)\beta^2}{2g\sin^2(\beta H_0(\alpha_1 x + \alpha_2 y))}, \tag{3.68}$$

and the velocity fields u, v and w respectively given by (3.63), (3.64) and (3.65) are solutions of (3.59)-(3.62). These 3d analytical solutions are illustrated in paragraph 3.5.4.

3.5 Illustrative examples

For some of the models investigated above, illustrations of the exhibited analytical solutions are given. In the following except for paragraphs 3.5.3 and 3.5.4, we always consider the situation of a $L_x = 20$ meter-long basin with constant width and vertical shores. Since the initial and boundary conditions do not depend on the variable y and the bottom geometry

satisfies $z_b = z_b(x)$, it is a 2d $(x - z)$ problem.

3.5.1 Stationary continuous solutions

In this paragraph we present typical analytical solutions for the problem examined in paragraph 3.3.2. Let us consider the bottom geometry $z_b(x)$ is defined by (3.21) where $H_0(x)$ is given by

$$H_0(x) = \frac{1}{2} + \frac{\pi}{2} + \frac{\alpha}{10}\tan^{-1}\left(\frac{N}{L_x}\left(x - \frac{L_x}{3}\right)\right) - e^{-\frac{N}{L_x^2}(x-\frac{3}{4L_x})^2},$$

with $N = 50$, $\alpha = 3.5$ and $\beta = 1$. The flow is fixed at inflow (left boundary) with $q_{in} = \alpha$ and the water height is prescribed at outflow (right boundary) with $H_{out} = H_0(L_x)$. Following the results of paragraph 3.3.2, the water depth $H = H_0$ and the velocity fields u, w given by (3.22),(3.23) are solutions of the considered problem. This situation where no shock occurs, is illustrated by Figure 3.3.

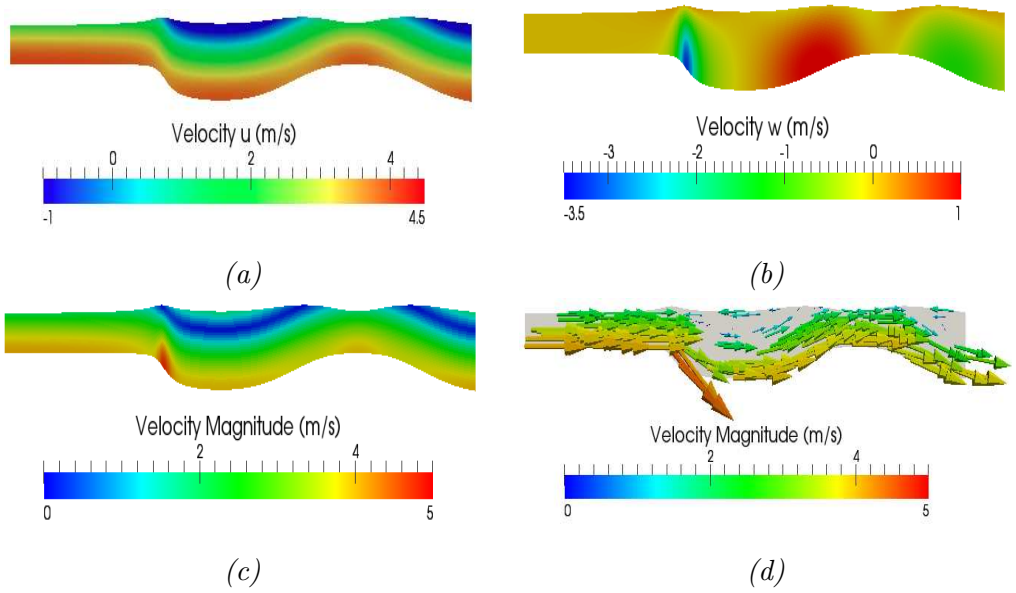

Figure 3.3: Surface level of the continuous solution and *(a)* horizontal velocity, *(b)* vertical velocity, *(c)* velocity norm, *(d)* velocity field (arrow).

3.5.2 Stationary solutions with a shock

Now we consider the situation decribed in paragraph 3.3.4. The bottom geometry is given by

$$z_b(x) = 0.2e^{-0.5(x-8)^2} - 0.4e^{-0.5(x-12)^2}. \tag{3.69}$$

With this geometry and $\alpha = 0.65$, $\beta = 2.5$ and $H(L_x) = 0.6$, the solution is discontinuous (cf. (3.28)) and governed by (3.29)-(3.30). The shock is characterized by (3.37)-(3.39)

and the vertical velocity w is obtained from(3.23). The obtained solution is depicted in Figure 3.4.

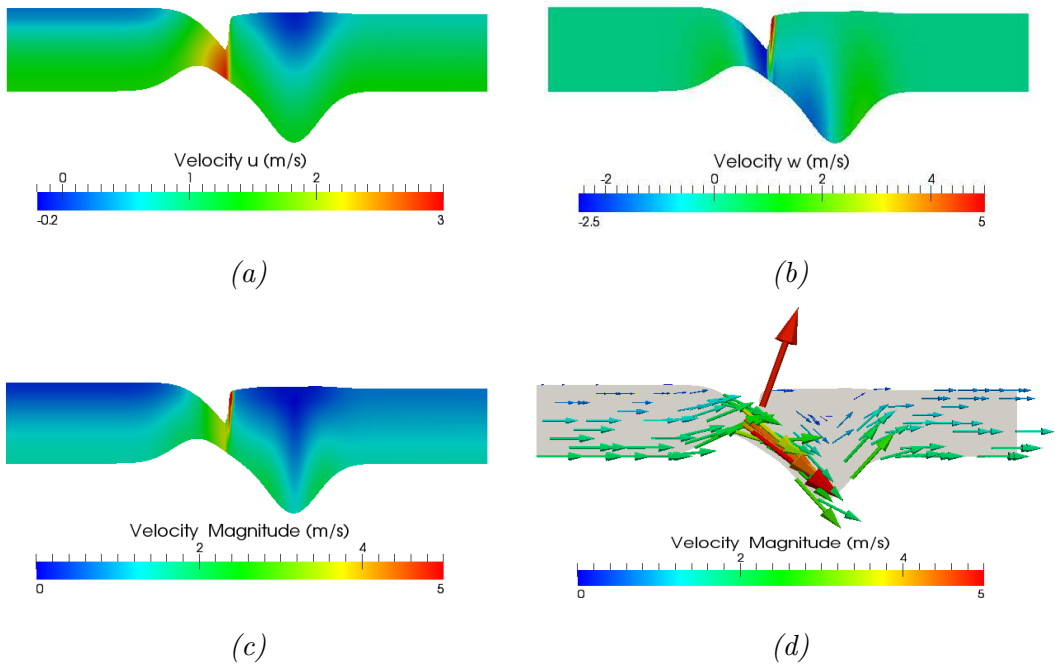

Figure 3.4: Surface level of the solution with shock and *(a)* horizontal velocity, *(b)* vertical velocity and *(c)* velocity norm, *(d)* velocity field (arrow).

3.5.3 Interactions with structures

Analytical solutions with partially free surface

The analytical solutions proposed in paragraph 3.3.8 are illustrated here in Figure 3.5.

We use the topography given by (3.69). As for Figure 3.4, we choose $\alpha = 0.65$ and $\beta = 2.5$. The external pressure p^a is given by (3.50) with $K(x) = 100x$ and $\eta_m(x) = \min(1.2, 0.2 + 0.04(x-14)^2)$.

Analytical solutions in cylindrical coordinates

The figure 3.6 depicts the analytical solution proposed in paragraph 3.3.8. It corresponds to a flow in a deformable cylinder of length $L_x = 10$ m with the parameters $\alpha = 2.5$, $\beta = 0.35$, $\gamma = 1$ and the functions

$$R_0(x) = 1 + 2e^{-(x-\frac{L_x}{3})^2} + e^{-(x-\frac{2L_x}{3})^2}, \quad \text{and} \quad K(x) = 1 - 0.6\sin\left(\frac{\pi}{20}\left(x - \frac{L_x}{2}\right)^2\right).$$

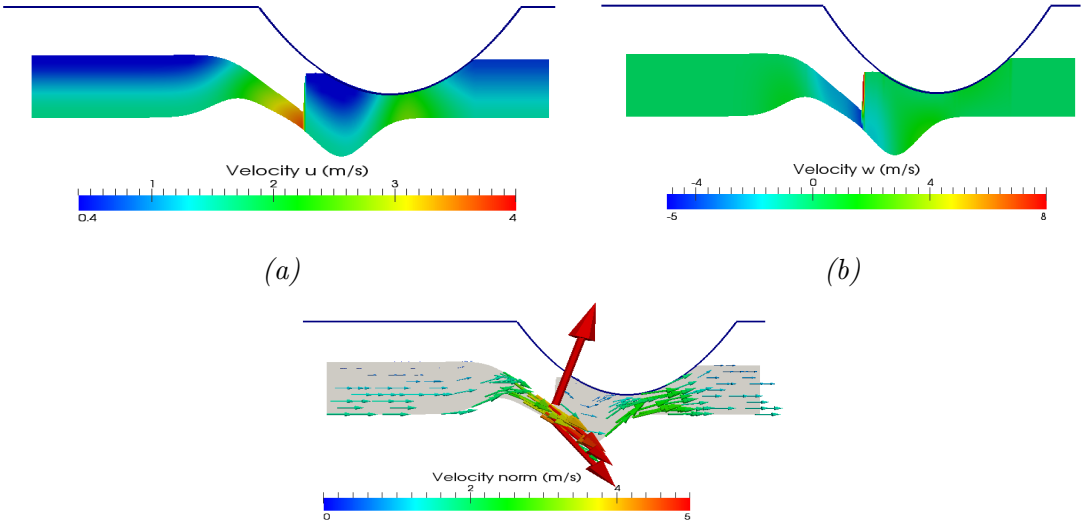

(a) *(b)*

(c)

Figure 3.5: Surface level of the solution with partially free surface *(a)* horizontal velocity u, *(b)* vertical velocity w and *(c)* velocity norm (with arrows).

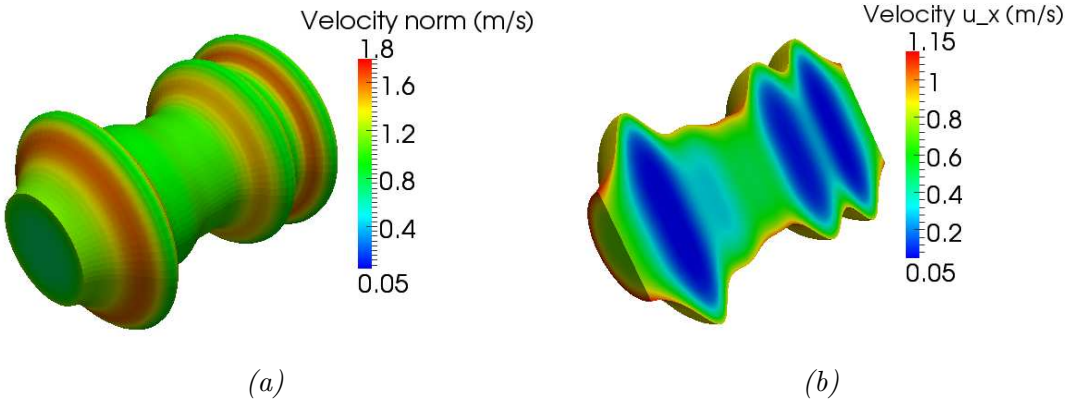

(a) *(b)*

Figure 3.6: Deformation of the cylinder and the velocity field *(a)* velocity norm, *(b)* slice along z with the velocity u_x.

3.5.4 Analytical solutions in 3d

In this paragraph we give an example of the 3d analytic solutions obtained in Section 3.4.

In this 3d situation, the water depth is given by

$$H(x,y) = H_0(\alpha_1 x + \alpha_2 y) = 1 + 0.3\sin(\beta(\alpha_1 x + \alpha_2 y)), \tag{3.70}$$

with $\alpha_1 = 1$,$\alpha_2 = 2$ and $\beta = 1$. The bottom geometry is given by (3.68). The bottom profile with 3090 vertices and 5978 triangles is depicted in Figure 3.7. The corresponding surface level and velocity fields u, v and w have been calculated from (3.63)-(3.65) and are presented in Figure (3.8).

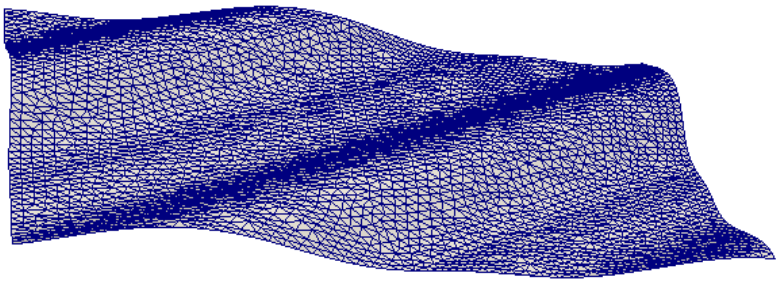

Figure 3.7: 3d bottom geometry.

3.6 Conclusion

We have proposed analytical solutions for the 2d and 3d incompressible and hydrostatic Euler system. The FRESH-ASSESS solutions have been obtained in various situations: free surface, partially free surface, shocks, transient regime,... and can be derived for a large class of geometrical domains.

The main interest of these analytical solutions is to allow the validation of numerical schemes. The authors have already checked that the numerical schemes they have proposed [9, 10] for the resolution of the incompressible and hydrostatic Euler system with free surface are able to recover the analytical solutions proposed here.

Acknowledgement. The authors want to thank Emmanuel Audusse and Benoît Perthame for helpful discussions that have allowed to greatly improve the paper.

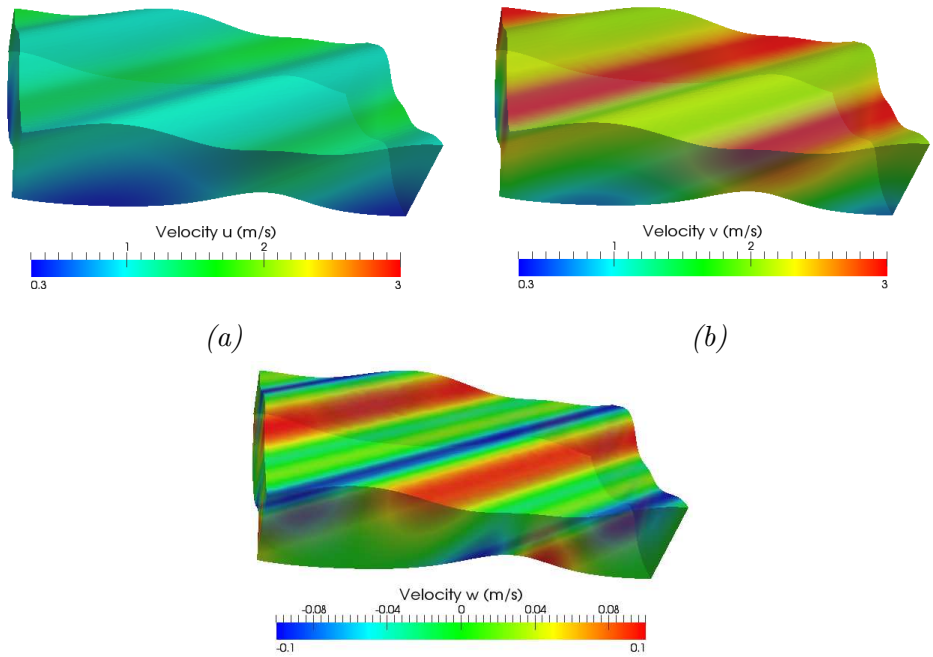

Figure 3.8: Surface level of the 3d solution and *(a)* and *(b)* horizontal velocities u and v and *(c)* vertical velocity w.

A 2D hydrodynamics and biology coupling applied to algae growth

4

La culture de microalgues oléagineuses dans des systèmes dédiés comme les raceways est considérée comme une voie prometteuse pour la production de biocarburant. Mais le processus est difficile à appréhender. Il couple une activité biologique non linéaire à une hydrodynamique complexe, et comporte un grand nombre de paramètres. Cela rend le problème d'optimisation délicat. Dans ce contexte, la modélisation mathématique peut apporter des solutions. Les raceways, bien que peu profonds, présentent une grande hétérogénéité selon la dimension verticale. De grandes variations sont observées concernant l'intensité lumineuse, la température ou la disponibilité des nutriments. Nous adoptons donc une approche multi-couches pour l'hydrodynamique et la biologie. Pour l'hydrodynamique à surface libre, nous utilisons un système de Saint-Venant multi-couches forcé par une représentation simplifiée d'une roue à aube. Pour la biologie, nous nous inspirons du modèle de croissance de Droop, sur lequel nous greffons l'action de la photosynthèse et que nous spatialisons aussi dans un modèle multi-couches. Nous donnons une interprétation cinétique du système couplé afin d'en dériver un schéma numérique efficace. Des simulations numériques en deux dimensions permettent de confirmer que l'approche discerne bien les situations dans lequel le bassin est agité des situations dans lesquelles il reste calme et hétérogène. De plus, la construction a posteriori des trajectoires lagrangiennes des algues permet de dégager un modèle de la quantité de lumière perçue par celles-ci et de mieux comprendre le processus de photosynthèse.

Cet article, issu d'une collaboration avec Olivier Bernard, Marie-Odile Bristeau *et* Jacques Sainte-Marie *est paru dans Mathematical Modelling and Numerical Analysis sous le titre* A 2D model for hydrodynamics and biology coupling applied to algae growth simulations. *DOI: http://dx.doi.org/10.1051/m2an/2013072.*

The culture of microalgae in dedicated systems such as raceways is seen as a promising way for the production of biofuel. But the process is difficult to handle. It couples a nonlinear biological activity with complex hydrodynamics and comprises a high number of parameters. It makes the optimization problem tricky. In that context, mathematical modeling can bring solutions. Raceways, though not so deep, show a high heterogeneity along the vertical dimension. Great variations are observed regarding light intensity, temperature or nutrients availability. We adopt a multilayer approach for hydrodynamics and biology. To model the free surface flows, we choose a vertically distributed version of hydrostatic Navier-Stokes equations, forced by a simplified version of a paddlewheel. For the biological system, we start from the Droop model that we improve with a light sensitivity and spatialization. It is also processed with a multilayer method. We provide a kinetic interpretation of the whole system which results in an efficient numerical scheme. Numerical simulations are provided in two dimensions. They confirm that our approach is capable of discriminating between a calm and a stirred raceway regarding the carbon productivity. Moreover, lagrangian trajectories of the algae are post-processed and give an idea of the light intensity they undergo through time, which is of high interest to build better biological models.

This is a joint work with Olivier Bernard, Marie-Odile Bristeau *and* Jacques Sainte-Marie. *It was published in Mathematical Modeling and Numerical Analysis with the title* A 2D model for hydrodynamics and biology coupling applied to algae growth simulations. *DOI: http://dx.doi.org/10.1051/m2an/2013072.*

4.1 Introduction

Recently, biofuel production from microalgae has proved to have a high potential for biofuel production [45, 143]. Several studies have demonstrated that some microalgae species could store more than 50% of their dry weight in lipids under certain conditions of nitrogen deprivency [45, 124, 144] leading to productivities in a range of order larger than terrestrial plants. In this article, we focus on microalgae cultivation in raceways (also called high rate ponds), whose hydrodynamics has been less studied than the photobioreactor culturing devices [98, 109, 110, 118, 125]. These annular shaped ponds of low depth (10 to 50 cm) are mixed with a paddlewheel (see Fig.4.3). Due to their inherent nonlinear and instationary properties, where hydrodynamics and biology are strongly coupled, managing and optimizing such processes is very tricky. Carrying out experiments on raceways is both expensive and time consuming. A model is thus a key tool to help in the optimal design of the process but also in its operation. The objective of this paper is to propose a new model describing the coupling between hydrodynamics and biology within a raceway.

The first dynamic model of a microalgal raceway pond was proposed by [135] assuming spatial homogeneity. The model was later consolidated by including time-discrete photoacclimation dynamics [136]. In parallel, other less elaborated models where proposed [69, 70]. Latter on, the coupling of biology with hydrodynamics in raceways was studied [77, 78], in order to optimize the raceway design. In [80], algae growth and transport is modelled and

several tests are performed in order to study for instance the effect of the water height or temperature control on the algae concentration evolution. However, those studies might not guarantee some key properties such as mass balance. We claim that the model we develop satisfies crucial mathematical properties such as the conservation of biochemical variables or positivity of the water height.

Our approach is the following. Hydrodynamics is governed by the Navier-Stokes equations. But for reasons of robustness and computational costs, we use a multilayer Saint-Venant system that is a good approximation of the Navier-Stokes equations for dominated advection flows. The accuracy and the stability properties of the multilayer approach are demonstrated in [9, 10, 126]. We add for our problem a specific forcing mimicking the effect of a paddlewheel. For the growth of microalgae, we utilize an improved version of the Droop model [22, 52, 53]. The Droop model has been widely studied and validated [23, 24, 87, 128]. It states that growth do not depend on the external nutrient concentration but on the internal cell quota of nutrients. The algae can indeed still grow a few days after exhaustion of the substrate thanks to their capacity to store nutrients. The enhanced Droop model [22] also takes into account the effect of light on phytoplankton. We then write the multi-layer version of the biological model, inspired from [9]. Afterwards, we give a kinetic interpretation of the whole system, allowing the derivation of a numerical scheme that has requested properties.

The outline is organized as follows. In Section 4.2 we describe and justify our system of partial differential equations. Afterwards, we derive the numerical scheme that we will use, based on a kinetic interpretation. We basically follow [9] and add the new state variables concerning biology. In Section 4.4 we explain how we model the raceway with the 2D code (the two dimensions being (x,z), respectively the length of the pond and the water depth) by adding periodic conditions. We also focus on the way agitation is introduced: we add a force mimicking a paddle-wheel and then we derive its contribution in the multilayer system, in the kinetic scheme and in the discrete scheme. We show that we have relevant results. Eventually, a last section deals with a Lagrangian approach of the algae tracking that could be useful regarding the elaboration of a better environment modeling for the algae.

4.2 The coupled model

We adopt and couple two continuous models, one for the representation of free surface hydrodynamics and the other for microalgae growth. We point out that it is a one way coupling: the biology is indeed advected and diffused by the water flow, but there is no retroaction of algae on the fluid. This is justified by the fact that the biological concentrations, even though greater in a raceway than they could be in an ocean or a lake, remain still much smaller than what is expected to change density or temperature of the raceway (let us recall for instance that the salinity of the seawater is around 37 $g.L^{-1}$ whereas we will never reach algae concentrations more than 1 or 2 $g.L^{-1}$).

4.2.1 The hydrodynamics model

Let us introduce first the hydrodynamics model in two dimensions. It will represent a free surface flow set into motion by a paddlewheel. As far as the modeling of geophysical free surface flows is concerned, two types of models and numerical techniques are usually investigated. On the one hand, when the flow is complex and no particular hypothesis can help simplify the model, finite differences or finite elements methods are used to solve the parabolic free surface Navier Stokes equations [40, 74]. But this treatment raises computational issues and, as far as the authors know, can hardly guarantee good properties such as positivity of the water depth, tracer conservation, wet/dry interface treatment shocks,.... On the other hand, when the shallow water hypothesis can be considered, a vertically averaged version of Navier-Stokes equations is often used: the Saint-Venant system [19],[61]. With an hyperbolic structure, numerical methods for shallow water flows consist in finite volume schemes and recent developments have allowed the recovery of properties such as the positivity of the water height. Let us cite the use of kinetic schemes introduced by B. Perthame [112] or the hydrostatic reconstruction by Audusse *et al.* in [4]. But those shallow water equations permit only the treatment of unstratified flows, which does not match our problem. We expect indeed to have high heterogeneities in our variables, due to the rapid light decline along the depth dimension. To sum up, because we want to tackle a complex realistic problem, we want to use a model that contains most of the phenomena expressed in Navier-Stokes equations, but which could be treated with Saint-Venant like tools, and this is what the multilayer Saint-Venant system provides. As stated in the introduction, efficiency of this new method has been proved in [9, 10, 126]. We allow us one hypothesis: the hydrostatic approximation. Whilst the vertical acceleration cannot be considered negligible around the paddlewheel, it is the case anywhere else in the raceway. Moreover the objective is not to reproduce the small scale perturbations of the paddlewheel over the flow but only to reproduce its first order effects. The paddlewheel applies a volumic force on the water:

$$F_{wheel}(x,z,t) = F_x(x,z,t)\overrightarrow{e_x} + F_z(x,z,t)\overrightarrow{e_z}.$$

More details are given in Section 4.4 about the formulation of the force.

Therefore, we begin with the 2D hydrostatic Navier-Stokes equations with varying density, on which we plug the paddlewheel force:

$$\frac{\partial \rho}{\partial t} + \frac{\partial \rho u}{\partial x} + \frac{\partial \rho w}{\partial z} = 0, \tag{4.1}$$

$$\frac{\partial \rho u}{\partial t} + \frac{\partial \rho u^2}{\partial x} + \frac{\partial \rho uw}{\partial z} + \frac{\partial p}{\partial x} = \frac{\partial \Sigma_{xx}}{\partial x} + \frac{\partial \Sigma_{xz}}{\partial z} + F_x(x,z,t), \tag{4.2}$$

$$\frac{\partial p}{\partial z} = -\rho g + \frac{\partial \Sigma_{zx}}{\partial x} + \frac{\partial \Sigma_{zz}}{\partial z} + F_z(x,z,t), \tag{4.3}$$

and we consider solutions of the equations for $t > t_0, \quad x \in \mathbb{R}, \quad z_b(x) \leq z \leq \eta(x,t)$, where $\eta(x,t)$ represents the free surface elevation, $\mathbf{u} = (u,w)^T$ the velocity vector, $p(x,z,t)$ is the pressure, g the gravity acceleration and $\rho(T)$ is the water density, depending on an

advected and diffused tracer T basically representing the temperature and which satisfies the advection diffusion equation:

$$\frac{\partial \rho T}{\partial t} + \frac{\partial \rho u T}{\partial x} + \frac{\partial \rho w T}{\partial z} = \mu_T \frac{\partial^2 T}{\partial x^2} + \mu_T \frac{\partial^2 T}{\partial z^2} \tag{4.4}$$

The flow height is $H = \eta - z_b$. The chosen form of the viscosity tensor is

$$\Sigma_{xx} = 2\mu \frac{\partial u}{\partial x}, \quad \Sigma_{xz} = \mu \frac{\partial u}{\partial z}, \quad \Sigma_{zz} = 2\mu \frac{\partial w}{\partial z}, \quad \Sigma_{zx} = \mu \frac{\partial u}{\partial z}$$

where μ is a dynamic viscosity.

Boundary conditions The system (4.1)-(4.3) is completed with boundary conditions. The outward and upward unit normals to the free surface $\mathbf{n}_s$ and to the bottom $\mathbf{n}_b$ are given by

$$\mathbf{n}_s = \frac{1}{\sqrt{1 + \left(\frac{\partial \eta}{\partial x}\right)^2}} \begin{pmatrix} -\frac{\partial \eta}{\partial x} \\ 1 \end{pmatrix}, \quad \mathbf{n}_b = \frac{1}{\sqrt{1 + \left(\frac{\partial z_b}{\partial x}\right)^2}} \begin{pmatrix} -\frac{\partial z_b}{\partial x} \\ 1 \end{pmatrix}.$$

Let Σ_T be the total stress tensor with

$$\Sigma_T = -pI_d + \begin{pmatrix} \Sigma_{xx} & \Sigma_{xz} \\ \Sigma_{zx} & \Sigma_{zz} \end{pmatrix}.$$

Free surface conditions At the free surface we have the kinematic boundary condition

$$\frac{\partial \eta}{\partial t} + u_s \frac{\partial \eta}{\partial x} - w_s = 0, \tag{4.5}$$

where the subscript s denotes the value of the considered quantity at the free surface. Provided that the air viscosity is negligible, the continuity of stresses at the free boundary implies

$$\Sigma_T \mathbf{n}_s = -p^a \mathbf{n}_s, \tag{4.6}$$

where $p^a = p^a(x,t)$ is a given function corresponding to the atmospheric pressure. In the following, we assume $p^a = 0$.

Bottom conditions The kinematic boundary condition is a classical no-penetration condition

$$\mathbf{u}_b.\mathbf{n}_b = 0, \quad \text{or} \quad u_b \frac{\partial z_b}{\partial x} - w_b = 0. \tag{4.7}$$

For the bottom stresses we consider a wall law

$$\mathbf{t}_b.\Sigma_T \mathbf{n}_b = \kappa \mathbf{u}_b.\mathbf{t}_b, \tag{4.8}$$

where $\mathbf{t}_b$ a unit vector satisfying $\mathbf{t}_b \cdot \mathbf{n}_b = 0$ and κ is a friction coefficient.

4.2.2 The biological model

Phytoplankton

Microalgae have pigments to capture sunlight, which is turned into chemical energy during the photosynthesis process. They consume carbon dioxide, and release oxygen. Phytoplankton growth depends on the availability of carbon dioxide, sunlight, and nutrients. Required nutrients are of various types, but here we focus on inorganic nitrogen, such as nitrate, whose deprivency is known to stimulate lipid production [102]. We consider the combined influence of nitrate and light on phytoplankton growth. The nutrient limitation is taken into account by a Droop formulation [52] of the growth rate. The light effect (photosynthesis and photoinhibition) is represented using a classical formulation from [107] embedded in the model proposed by [22].

Droop model with photoadaptation

The Droop model represents the growth of an algal biomass C^1 using a nutrient of concentration C^3 (nitrate under the form NO_3) in the medium. The concentration of particulate nitrogen (nitrogen contained in the algal biomass) is denoted C^2. Note that C^1 $(gC.m^{-3})$, C^2 $(gN.m^{-3})$ and C^3 $(gN.m^{-3})$ are three transportable quantities. In order to reproduce the coupling between nutrient uptake rate λ and growth rate μ, Droop introduced the cell quota, $q(t,x)$, defined as the amount of internal nutrients per biomass unit: $q = \frac{C^2}{C^1}$. Microalgae growth rate thus depends on the intra-cellular quota:

$$\mu(q) = \bar{\mu}(1 - \frac{Q_0}{q}), \tag{4.9}$$

where the constant $\bar{\mu}$ denotes the hypothetical growth rate for infinite quota, and Q_0 is the minimum internal nutrient quota required for growth.

The nitrate uptake rate is a function of the external nitrate [54]:

$$\lambda(C^3) = \bar{\lambda}\frac{C^3}{C^3 + K_3}, \tag{4.10}$$

where K_3 is the half saturation constant and $\bar{\lambda}$ the maximum uptake rate.

Finally, we will take into account both respiration and mortality, which are represented by a constant loss of the biomass with a factor R.

In line with [22], we modify this classical model in order to capture light and space variations.

Light along the raceway depth. The previous model only included nutrient limited growth. It can be improved by introducing a new data in the system: the light intensity, which will depend on the quantity of water and biomass above the algae. Light is indeed attenuated by the chlorophyll concentration. This concentration can be linked to nitrogen

through

$$Chl = \gamma(I^*)C^2$$

with

$$\gamma(I^*) = \frac{k_{I^*}}{I^* + k_{I^*}},$$

where k_{I^*} is a constant, I^* is the average light in the water column the day before(space and time average). $\gamma(I^*)$ is presumed constant over the day.

Let us assume that light intensity hitting the water surface is of the form

$$I_0 = I_0^{max} \max(0, \sin(2\pi t)), \tag{4.11}$$

Then the intensity at depth z can be described by

$$I(z) = I_0 e^{-\psi(C^2, I^*, z)}, \tag{4.12}$$

where

$$\psi(C^2, I^*, z) = \int_0^z (a\gamma(I^*)C^2(z) + b)dz, \tag{4.13}$$

$$\tag{4.14}$$

and I_0^{max} is a constant representing the maximum light intensity, a and b are also given constants.

The growth rate can then be computed to take into account light intensity, using Peeters and Eilers formalism [72, 107]

$$\mu(q, I) = \tilde{\mu}\frac{I}{I + K_{sI} + \frac{I^2}{K_{iI}}}(1 - \frac{Q_0}{q}),$$

with $\tilde{\mu}$, K_{sI}, K_{iI} three given constants derived from dedicated experiments. Finally, a down regulation by the internal quota of the uptake rate must be included to avoid infinite substrate(NO_3) uptake in the dark

$$\lambda(C^3, q) = \overline{\lambda}\frac{C^3}{C^3 + K_3}(1 - \frac{q}{Q_l})$$

where Q_l is the maximum achievable quota.

Adding advection and diffusion, the biological system writes in the end

$$\frac{\partial \rho C^1}{\partial t} + \frac{\partial \rho u C^1}{\partial x} + \frac{\partial \rho w C^1}{\partial z} = \mu_{C^1}\left(\frac{\partial^2 C^1}{\partial x^2} + \frac{\partial^2 C^1}{\partial z^2}\right) + \rho(\mu(q, I)C^1 - RC^1), \tag{4.15}$$

$$\frac{\partial \rho C^2}{\partial t} + \frac{\partial \rho u C^2}{\partial x} + \frac{\partial \rho w C^2}{\partial z} = \mu_{C^2}\left(\frac{\partial^2 C^2}{\partial x^2} + \frac{\partial^2 C^2}{\partial z^2}\right) + \rho(\lambda(C^3, q)C^1 - RC^2), \tag{4.16}$$

$$\frac{\partial \rho C^3}{\partial t} + \frac{\partial \rho u C^3}{\partial x} + \frac{\partial \rho w C^3}{\partial z} = \mu_{C^3}\left(\frac{\partial^2 C^3}{\partial x^2} + \frac{\partial^2 C^3}{\partial z^2}\right) - \rho\lambda(C^3, q)C^1, \tag{4.17}$$

where $q = \frac{C^2}{C^1}$, $\mu_{C^1}, \mu_{C^2}, \mu_{C^3}$ are diffusion coefficients and $(u,\ w)$ are the fluid velocities along x and z direction.

4.3 Multilayer model, kinetic interpretation and numerical scheme

4.3.1 Vertical space discretization: the multilayer model

The next step is the vertical discretization of (4.1)-(4.3) and (4.15)-(4.17) in order to obtain a multilayer system. For (4.1)-(4.3), such a derivation has already been performed in [9, 10], but in our case we have a source term representing the paddlewheel effect in equations (4.2) and (4.3). Since the resulting vertically discretized equations are not straightforward from those two previous papers, we detail it here. However, for the sake of simplicity, we choose to omit the viscosity terms. The spatial discretization of the multilayer viscous terms can be found in [10], Section 3.

Moreover, we will use the classical equation of state relating the density and the tracer identified here with the temperature

$$\rho(T) = \rho_0 \left(1 - \alpha(T - T_0)^2\right), \tag{4.18}$$

with $T_0 = 4^\circ$ C, $\alpha = 6.6310^{-6}\mathrm{C}^2$ and $\rho_0 = 10^3$ kg.m^{-3}. In the range of temperatures that we plan to use, it is easy to check that density variations are small. Hence we use the Boussinesq assumption which states that those density variations are taken into account in the gravitational force only. In any other equation the density is supposed to be ρ_0. Eventually, we end up with the hydrodynamic system

$$\frac{\partial u}{\partial x} + \frac{\partial w}{\partial z} = 0, \tag{4.19}$$

$$\frac{\partial u}{\partial t} + \frac{\partial u^2}{\partial x} + \frac{\partial uw}{\partial z} + \frac{1}{\rho_0}\frac{\partial p}{\partial x} = \frac{1}{\rho_0} F_x(x, z, t), \tag{4.20}$$

$$\frac{\partial p}{\partial z} = -\rho g + F_z(x, z, t), \tag{4.21}$$

$$\frac{\partial T}{\partial t} + \frac{\partial uT}{\partial x} + \frac{\partial wT}{\partial z} = 0 \tag{4.22}$$

with $\rho = \rho(T)$ given by (4.18) and the biological system

$$\frac{\partial C^1}{\partial t} + \frac{\partial uC^1}{\partial x} + \frac{\partial wC^1}{\partial z} = \mu(q, I)C^1 - RC^1, \tag{4.23}$$

$$\frac{\partial C^2}{\partial t} + \frac{\partial uC^2}{\partial x} + \frac{\partial wC^2}{\partial z} = \lambda(C^3, q)C^1 - RC^2, \tag{4.24}$$

$$\frac{\partial C^3}{\partial t} + \frac{\partial uC^3}{\partial x} + \frac{\partial wC^3}{\partial z} = -\lambda(C^3, q)C^1, \tag{4.25}$$

with $q = \frac{C^2}{C^1}$.

The process to obtain the multilayer system is described below. It is basically a Galerkin approximation of the variables followed by a vertical integration of the equations. The interval $[z_b, \eta]$ is divided into N layers $\{L_\alpha\}_{\alpha\in\{1,\dots,N\}}$ of thickness $l_\alpha H(x,t)$ where each layer L_α corresponds to the points satisfying $z \in L_\alpha(x,t) = [z_{\alpha-1/2}, z_{\alpha+1/2}]$ with

$$\begin{cases} z_{\alpha+1/2}(x,t) = z_b(x,t) + \sum_{j=1}^{\alpha} l_j H(x,t), \\ h_\alpha(x,t) = z_{\alpha+1/2}(x,t) - z_{\alpha-1/2}(x,t) = l_\alpha H(x,t), \quad \alpha \in [0,\dots,N] \end{cases} \tag{4.26}$$

with $l_j > 0, \quad \sum_{j=1}^{N} l_j = 1$.

Now let us consider the space $\mathbb{P}_{0,H}^{N,t}$ of piecewise constant functions defined by

$$\mathbb{P}_{0,H}^{N,t} = \left\{ \mathbb{I}_{z\in L_\alpha(x,t)}(z), \quad \alpha \in \{1,\dots,N\} \right\},$$

where $\mathbb{I}_{z\in L_\alpha(x,t)}(z)$ is the characteristic function of the interval $L_\alpha(x,t)$. Using this formalism, the projection of u, w and T onto $\mathbb{P}_{0,H}^{N,t}$ is a piecewise constant function defined by

$$X^N(x,z,\{z_\alpha\},t) = \sum_{\alpha=1}^{N} \mathbb{I}_{[z_{\alpha-1/2},z_{\alpha+1/2}]}(z) X_\alpha(x,t), \tag{4.27}$$

for $X \in (u,w,T)$. The density $\rho = \rho(T)$ inherits a discretization from the previous relation with

$$\rho^N(x,z,\{z_\alpha\},t) = \sum_{\alpha=1}^{N} \mathbb{I}_{[z_{\alpha-1/2},z_{\alpha+1/2}]}(z) \rho(T_\alpha(x,t)). \tag{4.28}$$

We have the following result.

Proposition 4.3.1. *The weak formulation of Eqs. (4.19)-(4.22) on $\mathbb{P}_{0,H}^{N,t}$ leads to a system of the form*

$$\sum_{\alpha=1}^{N} \frac{\partial l_\alpha H}{\partial t} + \sum_{\alpha=1}^{N} \frac{\partial l_\alpha H u_\alpha}{\partial x} = 0, \tag{4.29}$$

$$\begin{aligned} \frac{\partial h_\alpha u_\alpha}{\partial t} + \frac{\partial}{\partial x}\left(h_\alpha u_\alpha^2 + h_\alpha p_\alpha\right) &= u_{\alpha+1/2} G_{\alpha+1/2} - u_{\alpha-1/2} G_{\alpha-1/2} \\ &+ \frac{1}{\rho_0}\left(\frac{\partial z_{\alpha+1/2}}{\partial x} p_{\alpha+1/2} - \frac{\partial z_{\alpha-1/2}}{\partial x} p_{\alpha-1/2}\right) \\ &+ \frac{1}{\rho_0}\int_{z_{\alpha-1/2}}^{z_{\alpha+1/2}} F_x(x,z,t)dz, \end{aligned} \tag{4.30}$$

$$\frac{\partial h_\alpha T_\alpha}{\partial t} + \frac{\partial}{\partial x}\left(h_\alpha u_\alpha T_\alpha\right) = T_{\alpha+1/2} G_{\alpha+1/2} - T_{\alpha-1/2} G_{\alpha-1/2}, \tag{4.31}$$

$$\alpha \in [1,\dots,N].$$

with

$$G_{\alpha+1/2} = \frac{\partial z_{\alpha+1/2}}{\partial t} + u_{\alpha+1/2}\frac{\partial z_{\alpha+1/2}}{\partial x} - w_{\alpha+1/2} \tag{4.32}$$

$$G_{1/2} = G_{N+1/2} = 0. \tag{4.33}$$

The definitions of p_α, $p_{\alpha+1/2}$, $u_{\alpha+1/2}$, $T_{\alpha+1/2}$ *are given in the following proof.*

Proof. Since the demonstration for part of this proposal can be found in [9] and [10] , we will not detail it here. However, we will focus on the integration of the agitation terms in this multilayer system.

The horizontal term The horizontal term, in the x-projection of the momentum equation will be handled simply: since we plan to use an expression of the force that can be integrated analytically (see 4.4.2), we just add the integrated force in the right-hand-side of (4.30)

$$+\int_{z_{\alpha-1/2}}^{z_{\alpha+1/2}} F_x(x,z,t)dz, \qquad \alpha \in [1,\dots,N]. \tag{4.34}$$

The vertical term The handling of this term will require more steps. First of all, let us recall that in the situation where no additional source terms are present, (4.21) is used to compute the piecewise continuous state variable p, which is then introduced in (4.20) (see [9]). We basically proceed the same way.

From (4.21), we get:

$$p(x,z,t) = g\int_z^\eta \rho(x,z',t)dz' - \int_z^\eta F_z(x,z',t)dz' \tag{4.35}$$

If we project it on $\mathbb{P}_{0,H}^{N,t}$, we get for a z in layer α

$$p(x,z,t) = g\left(\sum_{j=\alpha+1}^{N}\rho_j h_j + \rho_\alpha(z_{\alpha+1/2} - z)\right) - \int_z^\eta F_z(x,z',t)dz'. \tag{4.36}$$

For the vertical integration of (4.20) we need to compute:

$$\int_{z_{\alpha-1/2}}^{z_{\alpha+1/2}} \frac{\partial p}{\partial x}dz = \frac{\partial h_\alpha p_\alpha}{\partial x} - \frac{\partial z_{\alpha+1/2}}{\partial x}p_{\alpha+1/2} + \frac{\partial z_{\alpha-1/2}}{\partial x}p_{\alpha-1/2}. \tag{4.37}$$

Since

$$p_\alpha = \frac{1}{h_\alpha}\int_{z_{\alpha-1/2}}^{z_{\alpha+1/2}} p(x,z,t)dz, \qquad p_{\alpha+1/2} = p(x,z_{\alpha+1/2},t), \tag{4.38}$$

we see that the vertical agitation force has an effect in p through (4.20). Let us precise the

expressions of $p_\alpha(x,t)$, $p_{\alpha+1/2}(x,t)$ and $p_{\alpha-1/2}(x,t)$.

$$\begin{aligned} p_\alpha(x,t) &= \frac{1}{h_\alpha}\int_{z_{\alpha-1/2}}^{z_{\alpha+1/2}} p(x,z,t)dz \\ &= g\left(\frac{\rho_\alpha h_\alpha}{2} + \sum_{j=\alpha+1}^{N}\rho_j h_j\right) - \frac{1}{h_\alpha}\int_{z_{\alpha-1/2}}^{z_{\alpha+1/2}}\int_z^\eta F_z(x,z',t)dz'dz, \end{aligned} \tag{4.39}$$

$$p_{\alpha+1/2}(x,t) = g\sum_{j=\alpha+1}^{N}\rho_j h_j - \int_{z_{\alpha+1/2}}^{\eta} F_z(x,z',t)dz', \tag{4.40}$$

$$p_{\alpha-1/2}(x,t) = g\sum_{j=\alpha}^{N}\rho_j h_j - \int_{z_{\alpha-1/2}}^{\eta} F_z(x,z',t)dz'. \tag{4.41}$$

The velocities $u_{\alpha+1/2}$, $\alpha = 1, ..., N-1$ are obtained using an upwinding with respect to the direction of the mass exchange:

$$u_{\alpha+1/2} = \begin{cases} u_\alpha & \text{if } G_{\alpha+1/2} \geq 0 \\ u_{\alpha+1} & \text{if } G_{\alpha+1/2} < 0. \end{cases} \tag{4.42}$$

We proceed in the same way for the tracer:

$$T_{\alpha+1/2} = \begin{cases} T_\alpha & \text{if } G_{\alpha+1/2} \geq 0 \\ T_{\alpha+1} & \text{if } G_{\alpha+1/2} < 0. \end{cases} \tag{4.43}$$

Notice that we also have [9]

$$G_{\alpha+1/2} = \sum_{j=1}^{\alpha}\frac{\partial h_j}{\partial t} + \sum_{j=1}^{\alpha}\frac{\partial h_j u_j}{\partial x},$$

which enables to define uniquely $u_{\alpha+1/2}$. □

In Prop. 4.3.1 the vertical velocity w no more appears, but we can derive relations for the discrete layer values of this variable by performing the Galerkin approximation of the continuity equation (4.19) multiplied by z. This leads to

$$\frac{\partial}{\partial t}\left(\frac{z_{\alpha+1/2}^2 - z_{\alpha-1/2}^2}{2}\right) + \frac{\partial}{\partial x}\left(\frac{z_{\alpha+1/2}^2 - z_{\alpha-1/2}^2}{2}u_\alpha\right) = h_\alpha w_\alpha + z_{\alpha+1/2}G_{\alpha+1/2} - z_{\alpha-1/2}G_{\alpha-1/2}, \tag{4.44}$$

where the w_α, $\alpha = 1, \ldots, N$, are the components of the Galerkin approximation of w on $\mathbb{P}_{0,H}^{N,t}$, see (4.27). Since all the quantities except w_α appearing in Eq. (4.44) are already defined by (4.29), (4.30), (4.32), (4.33), relation (4.44) allows obtaining the values w_α by post-processing. Note that we use the relation (4.44) rather than the divergence free

condition for stability purposes. We refer the reader to [9, 126] for more details.

Proposition 4.3.2. *Multilayer version of the Droop model with photoacclimation. The weak formulation of Eqs. (4.23)-(4.25) on $\mathbb{P}^{N,t}_{0,H}$ leads to a system of the form*

$$\begin{aligned}
\frac{\partial h_\alpha C^1_\alpha}{\partial t} + \frac{\partial}{\partial x}\left(h_\alpha C^1_\alpha u_\alpha\right) &= C^1_{\alpha+1/2} G_{\alpha+1/2} - C^1_{\alpha-1/2} G_{\alpha-1/2} \\
&\quad + h_\alpha(\mu(q_\alpha, I_\alpha) C^1_\alpha - R C^1_\alpha), \qquad (4.45)\\
\frac{\partial h_\alpha C^2_\alpha}{\partial t} + \frac{\partial}{\partial x}\left(h_\alpha C^2_\alpha u_\alpha\right) &= C^2_{\alpha+1/2} G_{\alpha+1/2} - C^2_{\alpha-1/2} G_{\alpha-1/2} \\
&\quad + h_\alpha(\lambda(C^3_\alpha, q_\alpha) C^1_\alpha - R C^2_\alpha), \qquad (4.46)\\
\frac{\partial h_\alpha C^3_\alpha}{\partial t} + \frac{\partial}{\partial x}\left(h_\alpha C^3_\alpha u_\alpha\right) &= C^3_{\alpha+1/2} G_{\alpha+1/2} - C^3_{\alpha-1/2} G_{\alpha-1/2} \\
&\quad - h_\alpha \lambda(C^3_\alpha, q_\alpha) C^1_\alpha, \qquad (4.47)\\
&\qquad\qquad \alpha \in [1, \dots, N],
\end{aligned}$$

with $q_\alpha = \frac{C^2_\alpha}{C^1_\alpha}$ and $C^j_{\alpha+1/2}$, $j = 1 \dots 3$ defined through the same upwinding as $u_{\alpha+1/2}$ and $T_{\alpha+1/2}$ (see 4.42, 4.43).

Proof. As for Eqs. (4.19)-(4.22), we use a Galerkin approximation of the biological variables on $\mathbb{P}^{N,t}_{0,H}$. The Galerkin approximation on $\mathbb{P}^{N,t}_{0,H}$ allows to write

$$Y^N(x, z, \{z_\alpha\}, t) = \sum_{\alpha=1}^{N} 1_{[z_{\alpha-1/2}, z_{\alpha+1/2}]}(z) Y_\alpha(x, t), \qquad (4.48)$$

for $Y \in (C^1, C^2, C^3)$. Then we perform an integration of Eqs. (4.23)-(4.25) over the layer α. Let us do it term by term.

$$\int_{z_{\alpha-1/2}}^{z_{\alpha+1/2}} \frac{\partial Y}{\partial t} dz = \frac{\partial h_\alpha Y_\alpha}{\partial t} - (Y_{\alpha+1/2} \frac{\partial z_{\alpha+1/2}}{\partial t} - Y_{\alpha-1/2} \frac{\partial z_{\alpha-1/2}}{\partial t}) \qquad (4.49)$$

For the transport terms it yields:

$$\int_{z_{\alpha-1/2}}^{z_{\alpha+1/2}} \frac{\partial uY}{\partial x} dz = \frac{\partial u_\alpha h_\alpha Y_\alpha}{\partial x} - (u_{\alpha+1/2} Y_{\alpha+1/2} \frac{\partial z_{\alpha+1/2}}{\partial x} - u_{\alpha-1/2} Y_{\alpha-1/2} \frac{\partial z_{\alpha-1/2}}{\partial x}) \qquad (4.50)$$

$$\int_{z_{\alpha-1/2}}^{z_{\alpha+1/2}} \frac{\partial wY}{\partial z} dz = w_{\alpha+1/2} Y_{\alpha+1/2} - w_{\alpha-1/2} Y_{\alpha-1/2} \qquad (4.51)$$

For the reaction terms we get:

$$\int_{z_{\alpha-1/2}}^{z_{\alpha+1/2}} (\mu(q,I)C^1 - RC^1)dz = h_\alpha(\mu(q_\alpha, I_\alpha)C^1_\alpha - RC^1_\alpha), \tag{4.52}$$

$$\int_{z_{\alpha-1/2}}^{z_{\alpha+1/2}} (\lambda(C^3,q)C^1 - RC^2)dz = h_\alpha(\lambda(C^3_\alpha, q_\alpha)C^1_\alpha - RC^2_\alpha), \tag{4.53}$$

$$\int_{z_{\alpha-1/2}}^{z_{\alpha+1/2}} -\lambda(C^3,q)X dz = -h_\alpha(\lambda(C^3_\alpha, q_\alpha)C^1_\alpha), \tag{4.54}$$

where

$$q = \frac{C^2}{C^1} \text{ and } q_\alpha = \frac{C^2_\alpha}{C^1_\alpha}.$$

Using the notation (4.32) and (4.33) we recover Eqs. (4.45)-(4.47). □

4.3.2 Kinetic interpretation

The kinetic approach consists in linking the behaviour of some macroscopic fluid systems - Euler or Navier-Stokes equations, Saint-Venant system - with Boltzmann type kinetic equations. Boltzmann equation was first introduced in gas dynamics. It represents the evolution of a density of particles in a gas. Kinetic schemes have been widely used for the resolution of Euler equations [32, 83]. Given the analogy between Euler and Saint-Venant equations, recent work has been carried out to adapt those schemes to the shallow water systems ([1]). The first step is the introduction of fictitious particles, the definition of a density of particles and the equation governing its evolution.

The process to obtain the kinetic interpretation of the multilayer hydrodynamic model (4.29)-(4.31) is similar to the one used in [9]. For that reason we will only detail the kinetic interpretation of the multilayer biological system (4.45)-(4.47).

For a given layer α, a distribution function $M_\alpha(x,t,\xi)$ of fictitious particles with microscopic velocity ξ is introduced to obtain a linear kinetic equation equivalent to the macroscopic model.

Let us introduce a real function χ defined on $\mathbb{R}$, compactly supported and which have the following properties

$$\begin{cases} \chi(-w) = \chi(w) \geq 0 \\ \int_{\mathbb{R}} \chi(w)\ dw = \int_{\mathbb{R}} w^2\chi(w)\ dw = 1. \end{cases} \tag{4.55}$$

Now let us construct a density of particles $M_\alpha(x,t,\xi)$ defined by a Gibbs equilibrium: the microscopic density of particles present at time t, in the layer α, at the abscissa x and with velocity ξ given by

$$M_\alpha = \frac{h_\alpha(x,t)}{c_\alpha}\chi\left(\frac{\xi - u_\alpha(x,t)}{c_\alpha}\right), \tag{4.56}$$

with

$$c^2_\alpha = p_\alpha,$$

and p_α defined by (4.39).

Likewise, we define $N_{\alpha+1/2}(x,t,\xi)$ by

$$N_{\alpha+1/2}(x,t,\xi) = G_{\alpha+1/2}(x,t)\ \delta\left(\xi - u_{\alpha+1/2}(x,t)\right), \tag{4.57}$$

for $\alpha = 0,\dots,N$ and where δ denotes the Dirac distribution.

The quantities $G_{\alpha+1/2}$, $0 \le \alpha \le N$ represent the mass exchanges between layers α and $\alpha+1$, they are defined in (4.32) and satisfy the conditions (4.33), so $N_{1/2}$ and $N_{N+1/2}$ also satisfy

$$N_{1/2}(x,t,\xi) = N_{N+1/2}(x,t,\xi) = 0. \tag{4.58}$$

For the Droop variables, we have the equilibria

$$U^j_\alpha(x,t,\xi) = C^j_\alpha(x,t)M_\alpha(x,t,\xi), \qquad \alpha = 1,\dots,N, \qquad j = 1,\dots,3 \tag{4.59}$$

$$V^j_{\alpha+1/2}(x,t,\xi) = C^j_{\alpha+1/2}(x,t)N_{\alpha+1/2}(x,t,\xi), \qquad \alpha = 0,\dots,N, \qquad j = 1,\dots,3 \tag{4.60}$$

With the previous definitions we write a kinetic representation of the multilayer biological system (4.45)-(4.47) **without biological reaction terms** and we have the following proposition:

Proposition 4.3.3. *The functions (C^j) are strong solutions of the system (4.45) -(4.47) without reaction terms if and only if the set of equilibria $\{U^j_\alpha(x,t,\xi)\}_{\alpha=1}^N$ are solutions of the kinetic equations*

$$\frac{\partial U^j_\alpha}{\partial t} + \xi\frac{\partial U^j_\alpha}{\partial x} - V^j_{\alpha+1/2} + V^j_{\alpha-1/2} = Q_{U^j_\alpha}, \tag{4.61}$$

for $\alpha = 1,\dots,N$, $j = 1\dots3$ with $\{N_{\alpha+1/2}(x,t,\xi), V^j_{\alpha+1/2}(x,t,\xi)\}_{\alpha=0}^N$ satisfying (4.57)-(4.60).

The quantities $Q_{U^j_\alpha} = Q_{U^j_\alpha}(x,t,\xi)$ are "collision terms" equal to zero at the macroscopic level i.e. which satisfy for a.e. values of (x,t)

$$\int_{\mathbb{R}} Q_{U^j_\alpha} d\xi = 0, \quad \int_{\mathbb{R}} \xi Q_{U^j_\alpha} d\xi = 0, \quad \text{and} \qquad \int_{\mathbb{R}} \xi^2 Q_{U^j_\alpha} d\xi = 0. \tag{4.62}$$

Proof. Using the definitions (4.56),(4.59) and the properties of the function χ, we have

$$l_\alpha H C^j_\alpha = \int_{\mathbb{R}} U^j_\alpha(x,t,\xi)d\xi, \qquad l_\alpha H C^j_\alpha u_\alpha = \int_{\mathbb{R}} \xi U^j_\alpha(x,t,\xi)d\xi. \tag{4.63}$$

From the definition (4.57) of $N_{\alpha+1/2}$ we also have

$$\int_{\mathbb{R}} N_{\alpha+1/2}(x,t,\xi)d\xi = G_{\alpha+1/2}, \tag{4.64}$$

A simple integration in ξ of the equations (4.61), always using (4.62), gives the biological equations (4.45)-(4.47). □

4.3.3 The numerical scheme

As in paragraph 4.3.2, we only detail the discretization of the biological part of the model. For the hydrodynamic part, the reader can refer to [9]. Using the multilayer system obtained in Prop. 4.3.2 we end up with a system of the form

$$\frac{\partial X}{\partial t} + \frac{\partial F(X)}{\partial x} = S_e(X) + S_{v,f}(X) + S_{bio}(X), \tag{4.65}$$

with $X = \left(k_1^1, \dots, k_N^1, k_1^2 \dots k_N^2, k_1^3 \dots k_N^3\right)^T$ and $k_\alpha^1 = l_\alpha HC_\alpha^1$, $k_\alpha^2 = l_\alpha HC_\alpha^2$, $k_\alpha^3 = l_\alpha HC_\alpha^3$. We denote $F(X)$ the flux of the conservative part, $S_e(X)$, $S_{v,f}(X)$ and $S_{bio}(X)$ the source terms, respectively the mass transfer, the viscous and friction effects and the biological reaction terms.

We introduce a $3N \times 3N$ matrix $\mathcal{K}(\xi)$ defined by $\mathcal{K}_{i,j} = \delta_{i,j}$ for $i, j = 1, \dots, N$ with $\delta_{i,j}$ the Kronecker symbol. Then, using Prop. 4.3.3, we can write

$$X = \int_\xi \mathcal{K}(\xi) \begin{pmatrix} U^1(\xi) \\ U^2(\xi) \\ U^3(\xi) \end{pmatrix} d\xi, \quad F(X) = \int_\xi \xi \mathcal{K}(\xi) \begin{pmatrix} U^1(\xi) \\ U^2(\xi) \\ U^3(\xi) \end{pmatrix} d\xi, \tag{4.66}$$

$$S_e(X) = \int_\xi \mathcal{K}(\xi) \begin{pmatrix} V^1(\xi) \\ V^2(\xi) \\ V^3(\xi) \end{pmatrix} d\xi, \tag{4.67}$$

with $U^j(\xi) = (U_1^j(\xi), \dots, U_N^j(\xi))^T$, and

$$V(\xi)^j = \begin{pmatrix} V_{3/2}^j(\xi) - V_{1/2}^j(\xi) \\ \vdots \\ V_{N+1/2}^j(\xi) - V_{N-1/2}^j(\xi) \end{pmatrix}, \quad \forall j \in 1..3.$$

We refer to [10] for the computation of $S_{v,f}(X)$.

To approximate the solution of (4.65) we use a finite volume framework. We assume that the computational domain is discretized by I nodes x_i. We denote C_i the cell of length $\Delta x_i = x_{i+1/2} - x_{i-1/2}$ with $x_{i+1/2} = (x_i + x_{i+1})/2$. For the time discretization, we denote $t^n = \sum_{k<n} \Delta t^k$ where the time steps Δt^k will be precised later through a CFL condition.

We denote

$$X_i^n = \left(k_{1,i}^{1,n}, \dots, k_{N,i}^{1,n}, k_{1,i}^{2,n}, \dots, k_{N,i}^{2,n}, k_{1,i}^{3,n}, \dots, k_{N,i}^{3,n}\right)^T$$

the approximate solution at time t^n on the cell C_i with $k_{\alpha,i}^{j,n} = l_\alpha H_i^n C_{\alpha,i}^{j,n}$.

Time splitting

For the time discretization, we apply a time splitting to the equation (4.65) and we write

$$\frac{\tilde{X}^{n+1} - X^n}{\Delta t^n} + \frac{\partial F(X^n)}{\partial x} = S_e(X^n, \tilde{X}^{n+1}) + S_{bio}(X^n), \tag{4.68}$$

$$\frac{X^{n+1} - \tilde{X}^{n+1}}{\Delta t^n} - S_{v,f}(X^n, X^{n+1}) = 0. \tag{4.69}$$

The conservative part of (4.68) is computed by an explicit kinetic scheme. The mass exchange terms are deduced from the kinetic interpretation. The biological reaction terms are not included in the kinetic interpretation but simply deduced from quadrature formulas. Eventually, the viscous and friction terms $S_{v,f}$ in (4.69) do not depend on the fluid density ρ. Thus, their vertical discretization and their numerical treatment do not differ from earlier works of the authors [10]. Due to potential dissipative effects, a semi-implicit scheme is adopted in the second step for reasons of stability.

Discrete kinetic equation

Starting from a piecewise constant approximation of the initial data, the general form of a finite volume discretization of system (4.68) is

$$\tilde{X}_i^{n+1} - X_i^n + \sigma_i^n \left[F_{i+1/2}^n - F_{i-1/2}^n\right] = \Delta t^n \mathcal{S}_{e,i}^{n+1/2} + \Delta t^n \mathcal{S}_{bio}^n, \tag{4.70}$$

where $\sigma_i^n = \Delta t^n / \Delta x_i$ is the ratio between space and time steps and the numerical flux $F_{i+1/2}^n$ is an approximation of the exact flux estimated at point $x_{i+1/2}$.

In order to find a good expression of the numerical fluxes, we need to make an incursion in the microscopic scale. Therefore we denote the discrete particle density at time n, cell i in the following manner:

$$M_{\alpha,i}^n(\xi) = l_\alpha \frac{H_i^n}{c_{\alpha,i}^n} \chi\left(\frac{\xi - u_{\alpha,i}^n}{c_{\alpha,i}^n}\right), \qquad \text{with } c_{\alpha,i}^n = \sqrt{p_{\alpha,i}^n}$$

and following (4.39)

$$p_{\alpha,i}^n = g\left(\frac{\rho_{\alpha,i}^n l_\alpha H_i^n}{2} + \sum_{j=\alpha+1}^{N} \rho_{j,i}^n l_j H_i^n\right) - \frac{1}{h_\alpha} \int_{z_{\alpha-1/2}}^{z_{\alpha+1/2}} \int_z^\eta F_z(x_i, z', t^n) dz' dz.$$

Then the equation (4.61) is discretized for each α by applying a simple upwind scheme

$$g_{\alpha,i}^{j,n+1}(\xi) = U_{\alpha,i}^{j,n}(\xi) - \xi\sigma_i^n \left(U_{\alpha,i+1/2}^{j,n}(\xi) - U_{\alpha,i-1/2}^{j,n}(\xi)\right) + \Delta t^n \left(V_{\alpha+1/2,i}^{j,n+1/2}(\xi) - V_{\alpha-1/2,i}^{j,n+1/2}(\xi)\right), \tag{4.71}$$

where

$$U_{\alpha,i+1/2}^{j,n} = \begin{cases} U_{\alpha,i}^{j,n} & \text{if } \xi \geq 0 \\ U_{\alpha,i+1}^{j,n} & \text{if } \xi < 0. \end{cases}$$

The quantity $g_{\alpha,i}^{j,n+1}$ is not an equilibrium but if we set

$$l_\alpha H_i^{n+1} C_{\alpha,i}^{j,n+1} = \int_{\mathbb{R}} g_{\alpha,i}^{j,n+1}(\xi) d\xi. \tag{4.72}$$

we recover the macroscopic quantities at time t^{n+1}.

Numerical flux of the finite volume scheme

In this section, we give some details for the computation of the fluxes introduced in the discrete equation (4.70). If we denote

$$F_{i+1/2}^n = F(X_i^n, X_{i+1}^n) = F^+(X_i^n) + F^-(X_{i+1}^n), \tag{4.73}$$

following (4.66), we define

$$F^-(X_i^n) = \int_{\xi\in\mathbb{R}^-} \xi\mathcal{K}(\xi) U_i^n(\xi) d\xi, \quad F^+(X_i^n) = \int_{\xi\in\mathbb{R}^+} \xi\mathcal{K}(\xi) U_i^n(\xi) d\xi \tag{4.74}$$

with $U_i^n(\xi) = (U_{1,i}^n(\xi), \ldots, U_{N,i}^n(\xi))^T$.

More precisely the expression of $F^+(X_i)$ can be written

$$F^+(X_i) = \Big(F_{k_1^1}^+(X_i), \ldots, F_{k_N^1}^+(X_i), F_{k_1^2}^+(X_i), \ldots, F_{k_N^2}^+(X_i), F_{k_1^3}^+(X_i), \ldots, F_{k_N^3}^+(X_i)\Big)^T, \tag{4.75}$$

with

$$F_{k_\alpha^j}^+(X_i) = C_{\alpha,i}^j l_\alpha H_i \int_{w \geq -\frac{u_{\alpha,i}}{c_i}} (u_{\alpha,i} + w c_{\alpha,i}) \chi(w)\, dw. \tag{4.76}$$

This kinetic method is interesting because it gives a very simple and natural way to propose a numerical flux through the kinetic interpretation. Indeed, choosing

$$\chi(w) = \frac{1}{2\sqrt{3}} 1_{|w|\leq\sqrt{3}}(w),$$

the integration in (4.76) can be done analytically.

However, this method proved to be numerically diffusive. That is why in practice, following [5, 9], we rather introduce the upwinding in the biological equations according to the sign of the total mass flux. We introduce then new biological fluxes that we will use instead of (4.76)

$$F^+_{k^j_\alpha}(X_i) = C^j_{\alpha,i+1/2} F^+_{h_\alpha} \tag{4.77}$$

with

$$F^+_{h_\alpha} = l_\alpha H_i \int_{w \geq -\frac{u_{\alpha,i}}{c_i}} (u_{\alpha,i} + w c_{\alpha,i}) \chi(w)\, dw$$

representing the mass flux in layer α at interface $i+1/2$ (see [9]) and the interfacial quantity being defined in the following manner

$$C^{j,n}_{\alpha,i+1/2} = \begin{cases} C^{j,n}_{\alpha,i} & \text{if } F^+_{h_\alpha} \geq 0 \\ C^{j,n}_{\alpha,i+1} & \text{if } F^+_{h_\alpha} < 0. \end{cases}$$

The source terms

We refer to [9] for the treatment of the mass exchanges terms $S_e(X^n, \tilde{X}^{n+1})$. For the reaction terms no difficulties occur since the biological variables and what they depend on, light for instance, are also projected on the same Galerkin basis. We write

$$\int_{z_{\alpha-1/2}}^{z_{\alpha+1/2}} \int_{x_{i-1/2}}^{x_{i+1/2}} R(x, z, t^n) = h_\alpha \Delta x_i R^n_i \tag{4.78}$$

where $R(x, z, t)$ represents one of the three reaction terms we have in the Droop model.

Properties

Although we are not going to provide any proof in this section we want to recall some important features of the model used in this paper (see [9, 10, 126] for the detailed proofs). First of all, under a certain CFL condition which means that the quantity of water leaving the cell during a time step is less than the current water volume of the cell, the water height and the biological concentrations remain non-negative. Second of all, [9] states that a passive tracer satisfies a maximum principle. Finally, we want to specify that a second order scheme in space and time is possible and has been performed in the simulations of Section 4.4. The second order in time is achieved through a classical Heun method. We apply a second order in space by a limited reconstruction of the variables [6] based on the prediction of the gradients in each cells, a linear interpolation followed by a limitation procedure.

4.4 Simulations

4.4.1 Analytical validation on non trivial steady states

In this section we show that we can find analytical solutions of the coupled problem, provided that we use Euler equations and a simplified model for biology. We want to emphasize the importance of this part. Validating a numerical code is indeed a complex but highly required task when it comes to non trivial situations. It is clear though that analytical solutions of the whole coupled problem cannot be found. However, we propose here a simplified version of a biological model that would be embedded in free surface Euler equations and for which we can find non trivial steady states.

Let (u,w) be the following vector field:

$$\begin{cases} u(x,z) = \alpha\beta \dfrac{\cos(\beta(z-z_b))}{\sin(\beta H)}, & (4.79) \\ w(x,z) = \dfrac{\alpha\beta}{\sin(\beta H)^2}\left[\sin(\beta(z-z_b))\cos(\beta H)\dfrac{\partial H}{\partial x} + \cos(\beta(z-z_b))\sin(\beta H)\dfrac{\partial z_b}{\partial x}\right] & (4.80) \end{cases}$$

with α, β being given constants, $z_b(x)$ being known and $H(x)$ being solution of the ordinary differential equation

$$\frac{\partial}{\partial x}\left(\frac{\alpha^2\beta^2}{2\sin^2(\beta H(x))} + gH\right) = -g\frac{\partial z_b}{\partial x}.$$

In [31], the authors show that it is an analytical solution of the Euler system of equations for free surface flows. In order to validate the coupling with biological equations which is performed in this paper, we propose a simplified stationary coupled model.

Let us consider the following scalar field

$$T(x,z) = e^{-(H-(z-zb))}.$$

We can check by simple calculation that T is solution of

$$\underbrace{\frac{\partial uT}{\partial x} + \frac{\partial wT}{\partial z}}_{\text{advection}} = \underbrace{f(x,z)T(x,z)}_{\text{reaction}} \tag{4.81}$$

where

$$f(x,z) = \alpha\beta\frac{\cos(\beta(z-z_b))}{\sin(\beta H)}\left(\frac{\tan(\beta(z-z_b))}{\tan(\beta H)} - 1\right)\frac{\partial H}{\partial x}. \tag{4.82}$$

Clearly, this equation is a simplified and alternate version of a biological model, with advection and reaction terms. Notice that solutions to (4.81) represent non trivial equilibria between advection and reaction terms.

Eventually, we compare analytical and numerical results of the following situation: a given hydrodynamic and biological flow is imposed at the left boundary of a 20m long raceway with topography $z_b = 0.2e^{(x-8)^2} - 0.4e^{(x-12)^2}$, a given water height is fixed at the right boundary. To solve this analytically we follow [31]: given the topography z_b, between

horizontal coordinates $x = 0$ and $x = 20$, we recover $H(x)$ and deduce $u(x, z)$ and $w(x, z)$ for $\alpha = 0.4$ and $\beta = 1.5$ thanks to the above formula (4.79, 4.80). Numerically, we impose the analytical flux at the left boundary, the analytical water depth at the right boundary, and run the code for 500s, with 300 nodes and 20 layers (thus 6000 vertices), while initial conditions were set up to zero for every variable (u, w, T). We see in Figure 4.1 that we recover numerically the hydrological and tracer steady states solutions for this simplified coupled model. Therefore,

we consider that our method and our code are likely to produce valid results.

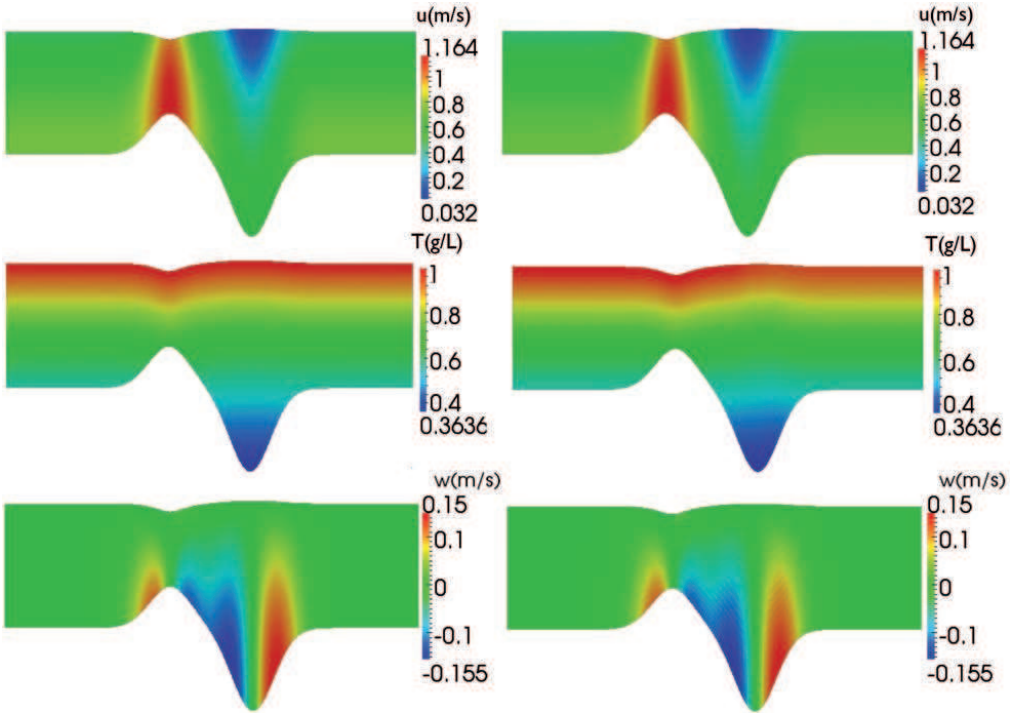

Figure 4.1: Analytical (left) and numerical (right) steady states solutions for hydrodynamics and tracer in case $\alpha = 0.4$, $\beta = 1.5$ and $z_b = 0.2e^{(x-8)^2} - 0.4e^{(x-12)^2}$. A given flow is imposed at the left boundary whereas the output boundary condition concerns the water height.

4.4.2 Numerical simulations of a raceway

Light

As explained in Section 4.2, the light intensity at a particular point will depend both on the amount of water above this point (i.e. related to the depth) and on the quantity of encountered chlorophyll (proportional to the concentration in intracellular nitrogen). Additionally, we explain in Section 4.3 that a Galerkin approximation of the variables is carried out. Hence light is also discretized along the depth by layers. We show in Figure 4.2 the light profile for different values of $\gamma(I^*)$. Recall that this value is related to the average irradiance perceived by microalgae the day before (photoadaptation phenomenon). The

Parameter	Value	Unit
$I_{0,max}$	500	$\mu mol.m^{-2}.s^{-1}$
a	16.2	$m^2.gChl^{-1}$
b	0.087	m^{-1}
C^2	5.0	$gN.m^{-3}$

Table 4.1: Parameters used for the computation of light.

parameters used are exposed in Table 4.1. We see for any curve the exponential decay. Moreover, this figure shows that the more exposed to light the microalgae were, the more receptive to it they are (no photoinhibition occurs in those ranges of irradiance).

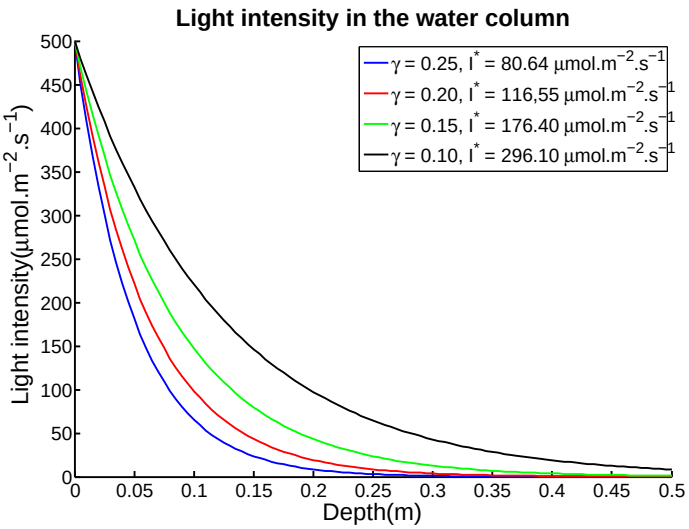

Figure 4.2: Light intensity in the water column for a concentration in nitrogen equal to 5.0 $gN.m^{-3}$. The figure shows the exponential decay of light with depth for different values of $\gamma(I^*)$.

Paddlewheel

We aim at representing the kind of raceway shown in Figure 4.3. In order to model it in 2D, periodic conditions are applied on a rectangular pond containing a paddlewheel in its first half (Figure 4.4). The wheel is not modelled physically but is represented by a force that is able to mimic its effect and give the system an equivalent energy. Therefore the

Figure 4.3: A typical raceway for cultivating microalgae. Notice the paddlewheel which mixes the culture suspension. Picture from INRA (ANR Symbiose project).

following expression is assumed:

$$\begin{cases} F_x(x,z,t) = F\cos\theta\left(\sqrt{(x-x_{wheel})^2+(z-z_{wheel})^2}\omega\right)^2 & (4.83) \\ F_z(x,z,t) = F\sin\theta\left(\sqrt{(x-x_{wheel})^2+(z-z_{wheel})^2}\omega\right)^2 & (4.84) \end{cases}$$

where F is a constant, θ is the angle between the blade and the vertical direction, $\omega = \dot{\theta}$. The force is normal to the blade and depends on the square of the velocity of the point on the blade: the further it is from the center of the wheel, the bigger is the force. Therefore, the energy provided by the wheel is be proportional to the cube of the velocity. To include it in the model, the process is similar to what is explained in Section 4.3.3: the force is added in the Navier-Stokes equations in order to derive again the multilayer model. This adds a source term in the x-momentum equation and change the expression of the pressure given by the z-momentum equation. We remind the reader that non-hydrostatic terms have not been taken into account in the derivation of the model (though it is described in [126]).

The obtained results in Figure 4.5 let us think that this may be appropriate to model the paddlewheel effect.

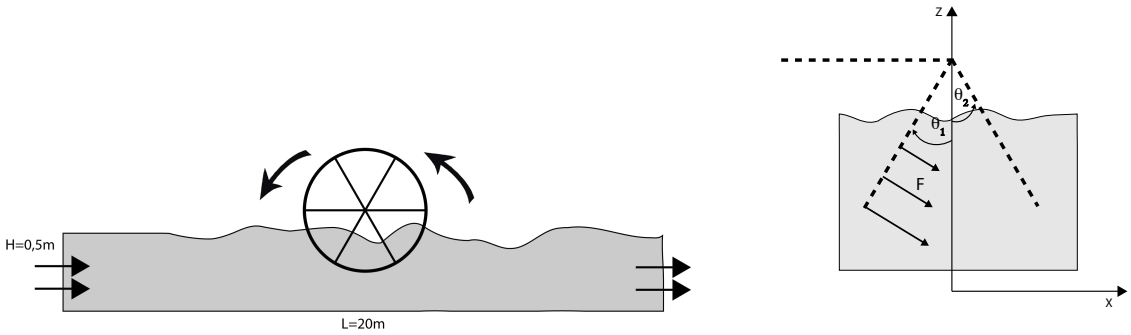

Figure 4.4: Left: Raceway and wheel dimensions and positions. Right: Outlook of the force applied to model the effect of the paddlewheel, supposed to be located in the first half of the raceway, with maximum efficiency at the end of the blade.

We performed several simulations for different paddlewheel angular velocities. We use a raceway with length 20m and height 0,5m. We show in Figure 4.5 that we are able to capture realistic hydrodynamics: a laminar flow of reasonable horizontal speed far from the wheel and a turbulent flow close to it. Concerning the hydrodynamics parameters, we take into account horizontal and vertical viscosity ($\mu = 0.001 m^2.s^{-1}$)and a Navier-type bottom friction($\kappa = 0.01 m.s^{-1}$). Besides, $\omega = 0.85$rad/s.

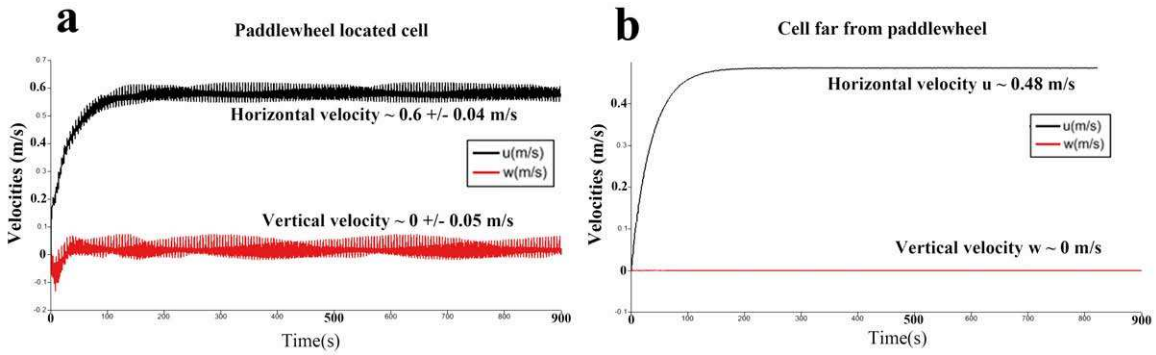

Figure 4.5: (a): Velocities along vertical and horizontal axis in a cell located near from the wheel rotating at angular speed $\omega = 0.8 rad/s$, with a force magnitude of $F = 10 N.m^{-3}$. The flow is very turbulent. (b): Velocities along vertical and horizontal axis in a cell located far from the wheel. An asymptotic value of $0.48 m.s^{-1}$ is reached.

In order to have a first idea of what is happening in the fluid, we add a tracer which is advected and slightly diffused. Figure 4.6 illustrates the effect of the wheel on the mixing. In particular, after several minutes, the pond seems well homogenized (here again $\omega = 0.85 rad/s$).

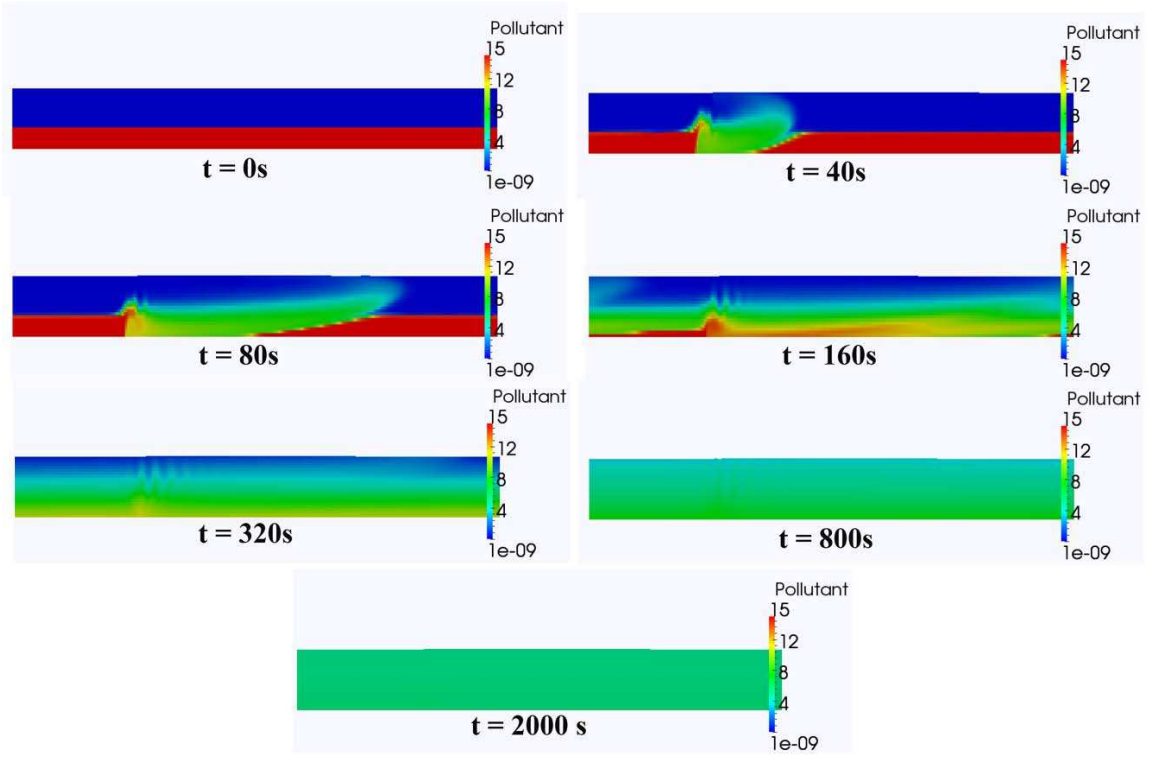

Figure 4.6: Snapshots of the tracer concentration in a raceway set into motion by a paddlwheel of angular velocity $\omega = 0.85 rad/s$. It is clear that after several minutes, the raceway is totally homogeneous. Therefore, the paddlewheel has indeed the required effect on the mixing.

4.4.3 Results

Eventually, we performed numerical simulations of the whole coupled model explained in Section 4.2 and discretized in Section 4.3. We use the same raceway with length 20m and height 0,5m. The height is chosen such that at the bottom of the pond, the respiration rate is close to the growth rate. We perform several 20 days simulations for different agitations, different initial conditions and we compare them to reference simulations i.e. without paddlewheel. The parameters used for the simulation (concerning the biological system) are exposed in Table 4.2. The relevant details of every simulation are in Table.4.3. The results are depicted in Figure 4.7.

The initial concentrations of particulate and dissolved nitrogen are the same for the six simulations. The initial microalgal carbon concentration varies (the initial internal nitrogen quota is therefore changing as well), and different agitation velocities are tested. The plots represent the average concentrations in the raceway (see local concentration comparison between upper and bottom layer in Figure 4.8). The carbon curves (Figure 4.7-a) show in every situation that agitation leads to better productivity. This is explained by the lack of nutrients in the upper layers at some point. However, regarding the initial internal quota

(Figure 4.7-b), the time when agitation actually enhances productivity varies. This phenomena is due to the fact that the internal nutrient pool, if not filled enough(low quota q), will tend to increase further by absorbing more external nitrogen. Thus leading two main consequences: the extracellular nutrient concentration diminishes and the intracellular nitrogen increases. Since chlorophyll is positively correlated with the latter biological variable, the light can not penetrate so deep anymore. We point out that the model is not able to differentiate between several agitation velocities. Ideas to explain and overcome this limitation are suggested in Section 4.5.

From these series of simulations we can conclude that our model is capable of reproducing coherent results, in the hydrodynamical part (adequate asymptotic velocity, turbulences near the wheel and laminar flow far from it) as well as in the biological concentrations. Nevertheless, we can only consider those results as preliminary, since no quantitative comparison with any data has been provided. Future work would include adaptation of the biological model given the hydrodynamical results obtained in this study. Moreover, other variables should be added to the system. For instance temperature, which could have a non negligible effect, sedimentation etc. Finally, experimental data should help us calibrate more accurately the raceway parameters and extend it to three dimensions.

Parameter	Value	Unit
$\tilde{\mu}$	1.7	day^{-1}
Q_0	0.050	$gN.gC^{-1}$
Q_l	0.25	$gN.gC^{-1}$
K_{iI}	295	$\mu mol.m^{-2}.s^{-1}$
K_{sI}	70	$\mu mol.m^{-2}.s^{-1}$
$\overline{\lambda}$	0.073	$gN.gC^{-1}.day^{-1}$
K_s	0.0012	$gN.m^{-3}$
R	0.0081	day^{-1}
$I_{0,max}$	500	$\mu mol.m^{-2}.s^{-1}$
$\gamma(I^*)$	0.25	$gChl.gN^{-1}$
a	16.2	$m^2.gChl^{-1}$
b	0.087	m^{-1}

Table 4.2: Parameters for the simulations.

	Simu 1	Simu 2	Simu 3	Simu 4	Simu 5	Simu 6
$C_0^1(g.m^{-3})$	25	25	50	50	83	83
$\left(\frac{C^2}{C^1}\right)_0 (gN.gC^{-1})$	0.2	0.2	0.1	0.1	0.06	0.06
$C_0^3(g.m^{-3})$	5	5	5	5	5	5
Agitation	no	yes	no	yes	no	yes
$C_f^1(g.m^{-3})$	60	74	79	103	100	129
$\left(\frac{C^2}{C^1}\right)_f (gN.gC^{-1})$	0.115	0.120	0.110	0.085	0.087	0.065
$C_f^3(g.m^{-3})$	3.77	0.0	0.0	0.0	0.0	0.0

Table 4.3: Initial conditions and final concentrations for the set of 6 simulations we performed. The differences lie on the one hand on the fact that the water is agitated or not and on the other hand on the initial carbon concentration, which changes the internal quota (nitrogen concentration is always equal to $5((g.m^{-3}))$

4.5 Lagrangian approach

So far, we have based our model on biological kinetics accounting for the photosynthesis process in conditions of light and nutrient limitations. We have used an extended version of the Droop model [22, 52, 53], but other models could have been used, differing by their level of details [15, 16, 60]. These models have been developped and experimentally validated for static conditions, i.e. for conditions where light was constant or slowly varying. However, the present study illustrates the fact that, due to hydrodynamics, each cell experiments a succession of light and dark phases, depending if it is close to surface or to the bottom. Such flashing light phenomenon has already been highlighted with photobioreactors [110]. Now the key question is to determine if the chosen model, with time scales in the range of hours, efficicently reproduces the photosynthesis dynamics at the cell scale, or if a more sophisticated model, accounting for the fast time scales of photosynthesis is required. Indeed, some models represent faster biological phenomena. For example, the Han model [73] represents the dynamics of the photosystems with time scales ranging from milliseconds to minutes. Such model would, of course, be more appropriate to account for photosynthesis in the context of rapid light fluctuations, with strong potential impact on the physiology [140]. As a consequence, it is now crucial to determine the typical light pattern received by a single cell. It is worth noting that such an information can only be obtained by simulation, since it would be very complex to measure experimentally the light along the trajectory of a microalgae. A Lagrangian approach derived from the previous model can lead to the reconstruction of cell trajectories. From this information, it is then possible to derive the light signals that microalgal cells undergo. We show hereafter that the velocity of the wheel does not influence much the light quantity perceived by an algae in a certain period of time, but it changes the way it receives it.

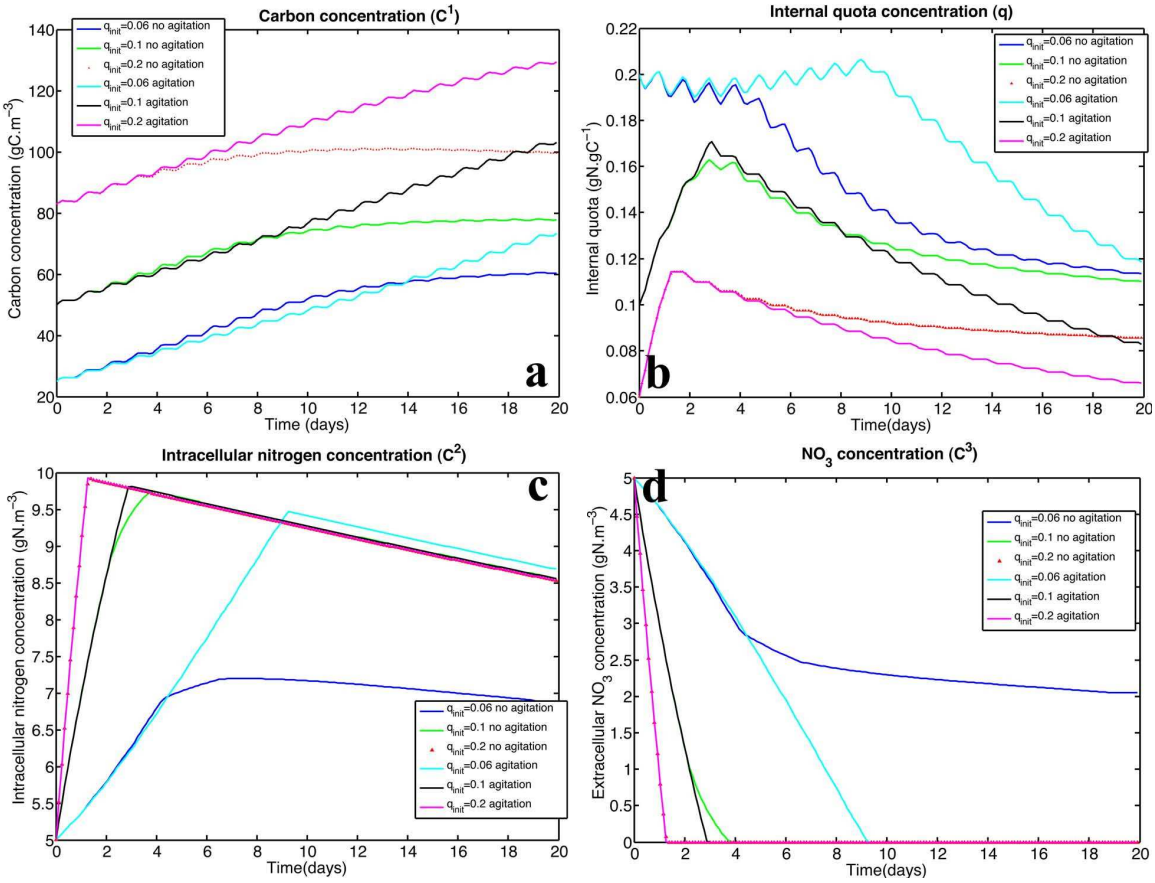

Figure 4.7: (a): Carbon concentration; (b): Internal quota q; (c): nitrogen concentration; (d): substrate concentration(NO_3). Those plots illustrate the average concentrations in the raceway for 6 simulations. Three were carried out without agitation, and the other three had the agitation term. In each situation, agitation, leading to homogenization leads to a better productivity. However, for certain initial conditions, the improvement is quite slow (after several days), since the biological variables do not evolve as quickly as hydrodynamics does.

In order to follow the position of a particle, we simply need to integrate the following equation. If $M(t)$ is the position of particle M at time t, then we have:

$$\frac{dM(t)}{dt} = v(M(t), t) \tag{4.85}$$

where $v(x, t)$ is the eulerian velocity field at position x, time t. We do not add to those particles any Brownian motion that would refer to the diffusion of biological concentrations at the macroscopic scale. Therefore, more realistic Lagrangian trajectories should look more noisy than what we get but the general behaviour is well represented.

For several angular velocities, we perform a one hour simulation and build the trajectories afterwards. One hundred particles are equally distributed in the raceway along the depth dimension. Fig.4.9 shows the distribution of particles against the percentage of time spent under more than 50% of the incident light (we will call it high enlightenment). We

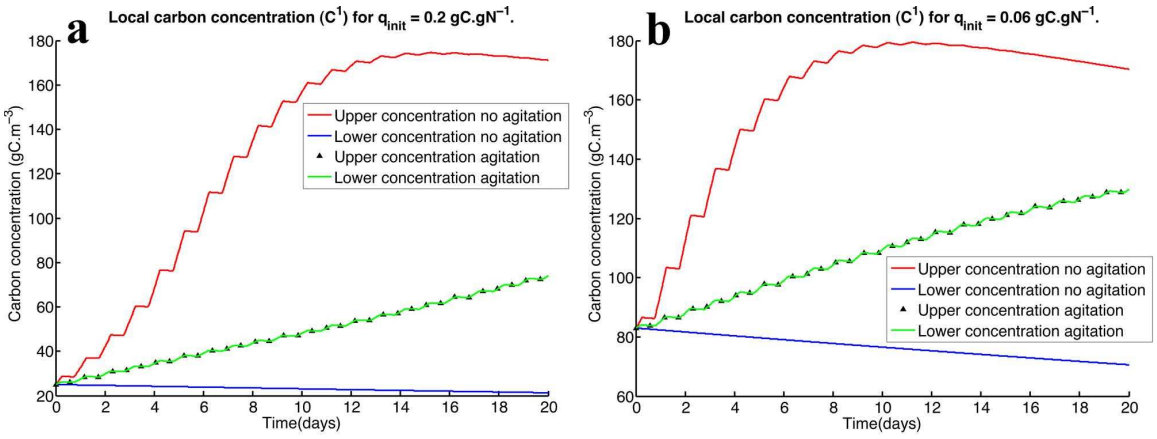

Figure 4.8: (a): Local carbon concentration when $q_{init} = 0.2gN.gC^{-1}$, in the bottom and upper layer, with and without agitation. (b): Local carbon concentration when $q_{init} = 0.06gN.gC^{-1}$, in the bottom and upper layer, with and without agitation. We see clearly the homogenization due to agitation. In both cases, we also see that the bottom layer when not agitated does not vary so much, which means that we are close to the point when respiration compensates growth.

notice that the wheel velocity has an influence on the number of particles which never undergo high enlightenment (38 particles over 100 for $\omega = 0.5$ and only 13 particles over 100 for $\omega = 1.0$). But globally, the particles are distributed around 20% of their time under high enlightenment. This is what we can expect from a good mixing since the light is exponentially decreasing and getting 50% of the incident light means being in the first 10cm from the surface of the raceway (over 50cm).

In Fig.4.10 we plot different indicators for eight velocities, established during a one hour simulation. First of all, Fig.4.10.a illustrates the average velocity at the end of the simulation. It turns out to lie in realistic ranges (0.2 $m.s^{-1}$ to 0.7 $m.s^{-1}$). Second of all Fig.4.10.b represents the average proportion of time spent for any particle under high enlightenment. From this curve we deduce that the global percentage of high enlightenment may not vary much between $\omega = 0.5$ and $\omega = 1$. The mixing is indeed well carried on (as shown in previous section) and in average, the particles have the same history. Finally, Fig.4.10.c depicts the number of times the particles switch from low enlightenment to high enlightenment during one hour. This last indicator gives insights about the duration of the high enlightenment periods. The greater it is, the shorter but more numerous were the high light instants (the particles switches more often).

Finally, the trajectories of three particles are depicted in Fig.4.11.a. From those trajectories we can extract two important informations. First of all, between two passages around the paddlewheel, the particle seems to stay at constant depth, thus enforcing the fact that the flow is laminar apart from the wheel. Second of all, we clearly see that the depth of the particle is suddenly modified by the wheel, giving rise to abrupt changes in the enlightenment. Fig.4.11.b shows the light received by those three particles in the case where the average intracellular nitrogen concentration is 5 $gN.m^{-3}$ and $\gamma(I^*) = 0.1$ $gChl.gN^{-1}$

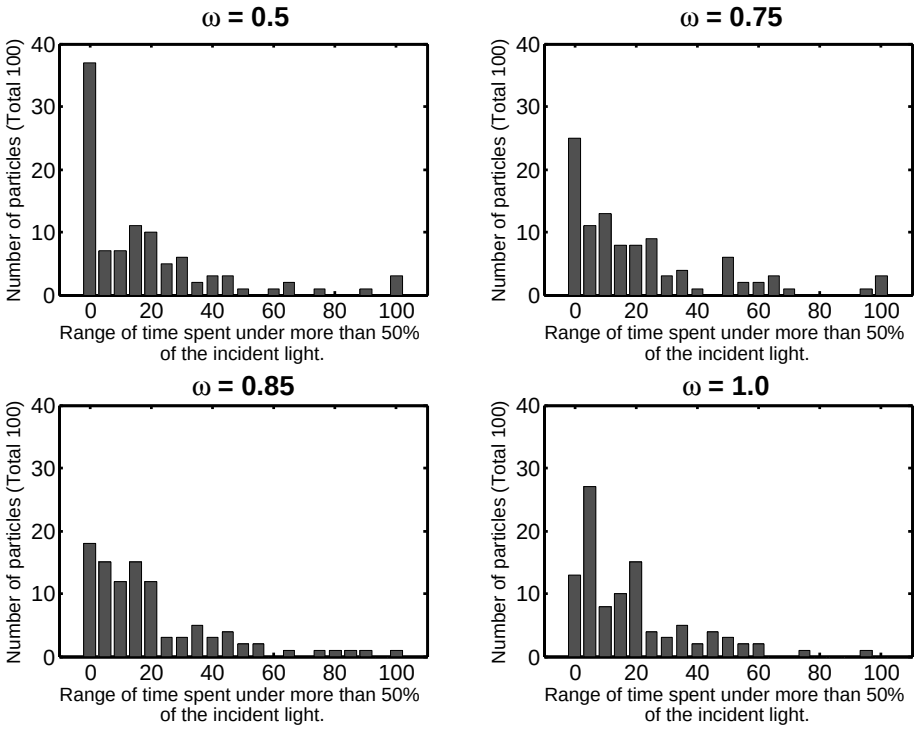

Figure 4.9: Number of particles for each class of enlightenment for four wheel angular velocities(0.5, 0.75, 0.85 and 1.0 $rad.s^{-1}$). One class represents a range of 5%. Being for instance in the class 20%-25% means that the particle spent between 20 and 25% of her time under hight enlightenment (more than 50% of the incident light).

(high irradiance the day before the simulation).

Fig.4.2 shows that light intensity is very low in the 20 deepest centimeters. Regarding our results on Fig.4.11, we assume that microalgae should spend one lap at high light and then several laps at low light. Since the asymptotic velocity is in the range $0.3m.s^{-1} - 0.8m.s^{-1}$, a whole lap is done in the order of a minute. Therefore, algae are faced to light changes with a time scale in the range of ten minutes. As regards our modeling problem, this tells us that a biological model valid for these fast time scale could lead to more precise results. Additional experiments forcing microalgae with typical light signal deduced from Figure 4.2 must therefore been carried out and support a microalgae modelling at fast time scale [56].

4.6 Conclusion

In this paper we derive a new model coupling hydrodynamics to biology in two dimensions. It provides new insights to better understand and represent this nonlinear and non stationary complex process. Except closed to the paddlewheel, the multilayer model seems to

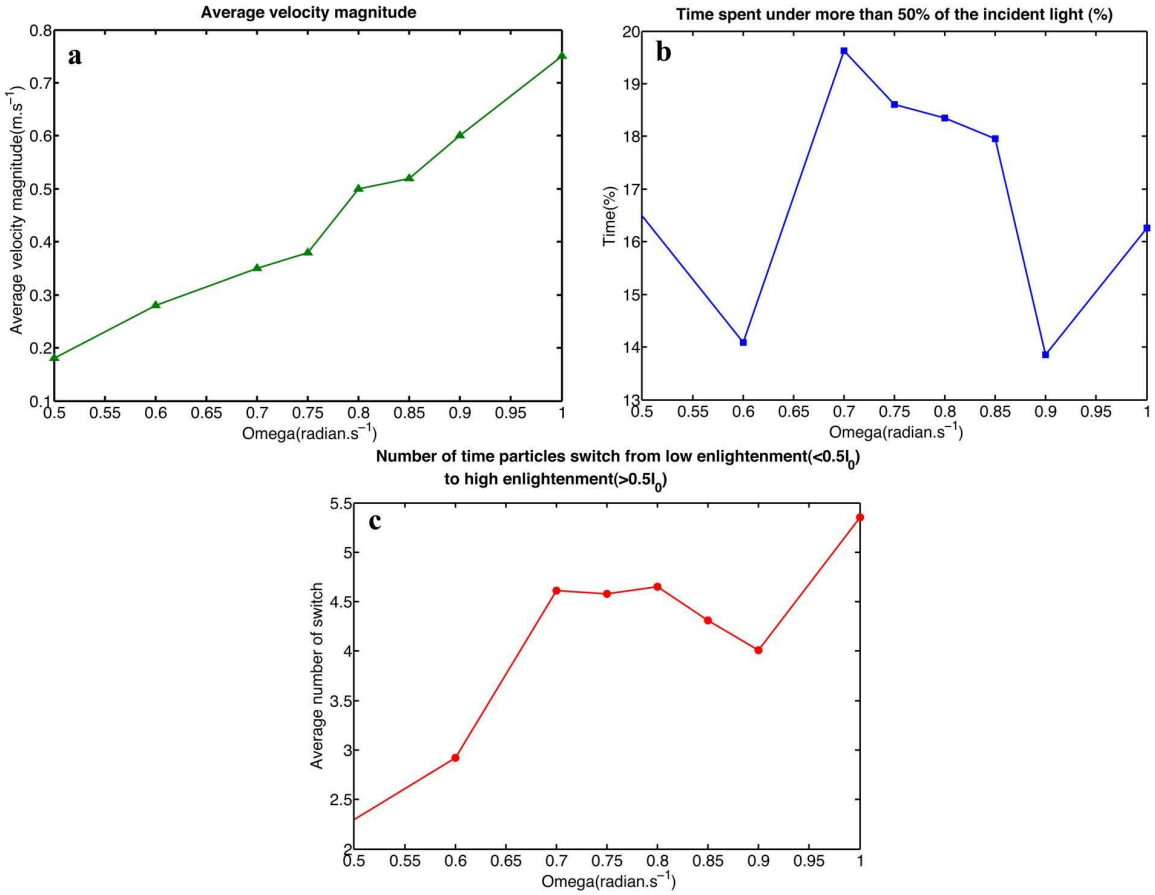

Figure 4.10: (a): Average velocity after one hour for 8 velocities. (b): Percentage of time spent under more than 50% of I_0. (c): Number of times a particles switches from a situation where it perceived less than 50% of light intensity to a situation where it perceives more during one hour.

adequately represent the vertical heterogeneity characterizing the agitated raceway. Notice that with our approach, we are able to provide analytical solutions which validated its numerical integration. The results show that water agitating through the paddlewheel has an effect on the growth of algae, particularly because of the lack of nutrients at the surface versus the lack of light around the raceway's floor. One of the outcome of this work is the identification of realistic light signals to which microalgae are faced. Lab scale experiments will be performed to assess the impact of such high frequency light signals on microalgae. It is worth remarking that similar works have been carried out for photobioreactor [109, 110], leading to the identification of much faster time scales in the range of the second. Of course, it is possible to improve the model around the wheel by relaxing the hydrostatic approximation. A robust an efficient scheme for the discretization of the non-hydrostatic terms is under development. Though theoretical results and first experiments have already been carried out ([36, 37]), this model has not yet been widely validated and requires the coding of much complex numerical schemes. Likewise a 3D model is necessary to take into account the effects of the bend of the hydrodynamics. The comparison with experimental data

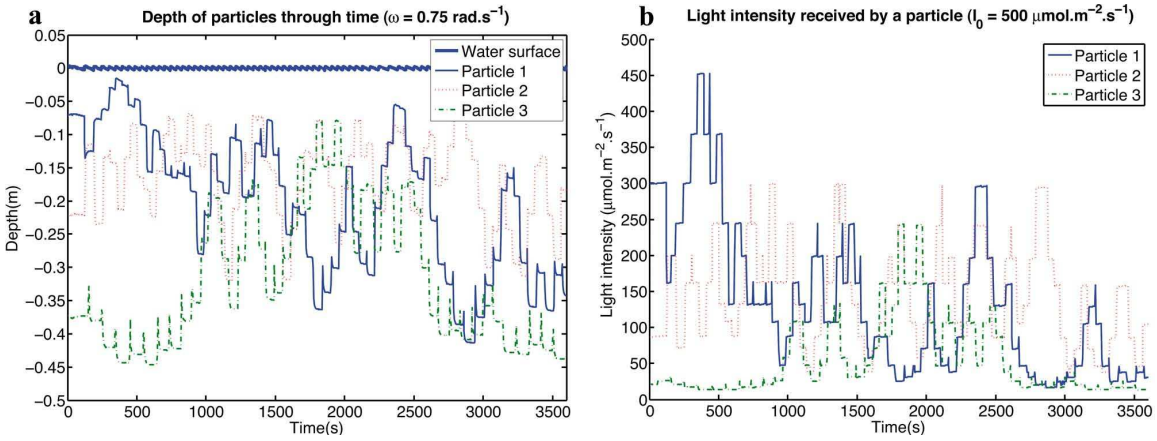

Figure 4.11: (a):Trajectories of three particles during the simulations. The large curve represents the water surface at the middle of the raceway. The other plot is the height of a given particle through time. The algae undergo sudden changes of depth every time it meets the wheel.(b): Perceived light from the microalgae. Particles are subject to even greater irradiance changes since the light is exponentially decaying.

would be of great relevance to better calibrate the hydrodynamics, and later on improve the biological predictions of the model. It is clear however that many parameters need to be taken into account in order to increase the model prediction capacity, for instance temperature. It was here considered as a passive tracer, only advected and diffused, with no particular effect on the biology (temperature does not appear in the growth or respiration rate). The sunlight effect on water temperature will be taken into account in a next stage since it deeply affects microalgae growth. Moreover, some microalgae species do not swim in the water and tend to sediment. This property could increase the beneficial effect of the wheel compared to a situation where the wheel is very slow or absent. Computational time is another issue which has to be improved in order to use the model *e.g.* for process optimal design. Up to now, schemes we are developing are only explicit. We are therefore constrained with a restrictive CFL condition. Improvement towards implicit schemes is also a future concern.

Acknowledgements. The authors would like to thank the support of INRIA ARC Nautilus (http://www-roc.inria.fr/bang/Nautilus/?page=accueil) together with the ANR Symbiose project (http://www.anr-symbiose.org).

Hydrodynamics of a raceway in 3D

5

Ce court chapitre fait suite au travail sur le couplage hydrodynamique-biologie 2D effectué dans le cadre de la production d'algues dans des raceways. Alors que la situation en deux dimensions était illustrée au moyen d'un code Fortran bidimensionnel dont la majeure partie hydrodynamique préexistait à cette thèse, un code hydrodynamique à surface libre tridimensionnel pour le système de Saint-Venant multi-couches a été développé en C++ pendant ces trois années. Nous présentons ici succinctement sa structure, sa documentation et les premiers résultats obtenus pour le problème qui nous intéresse.

This short chapter is the logical consequence of the hydrodynamics and biology coupling study carried out in 2D. Whereas the bidimensional situation is illustrated with a Fortran code whose main part was coded before this thesis, a tridimensional C++ code for the multilayer Saint-Venant system has been developed during those three years. We present here succinctly its structure, its documentation and the first 3D hydrodynamics results in the case of the raceway.

5.1 C^{++} code

Even if Fortran is a judicious choice to develop a scientific computing tool, it seemed preferable to us to start developing something better organized and well suited for a potential spreading of the code in the geophysical flow community. C++ (which is an object-oriented improvement of the language C), when used correctly, is now capable of competing with the good results of Fortran and tends to become always more popular in the applied mathematics community (think of *Freefem++* for a finite element tool or *Gmsh* for a meshing software). It enables indeed good computation speed, but it is also adapted for modularity (it is easier to add extensions in an object oriented program), and offers a wide variety of tools that facilitate the writing of the code and improve its efficiency: debugging tools (we used Valgrind), documentation tools (we used Doxygen), parallelization tools (we used OpenMP)...

5.1.1 Structure of the code

When beginning the writing of a C++ code, one has to organize the elements in several *classes* whose instantiations will define objects that interact with each other. Each class has *private attributes* (for instance the attributes of the mesh could be the dimensions of the domain, the number of points) and *public methods* (for instance the methods of the mesh object comprise the building of normals, the building of the dual mesh or the basis functions). We do not aim at providing too many explanations on this code as a documentation is available (see Section 5.1.2). We solely illustrate with a graph the interactions between the different objects on Figure 5.1, and the general algorithm of the code in Algorithm 5.1.1, with a zoom on the fluxes computation part in Algorithm 14. We can see on Figure 5.1 that 5 types of boundary conditions are implemented for the moment in the 3D multilayer system:

- sliding boundary conditions,
- fluvial boundary conditions, with either water height or flux imposed,
- torrential boundary conditions, either as input or output.

5.1.2 Documentation

The code has been regularly commented following specific rules for the documentation generator Doxygen. Therefore, an html documentation is available. This gives the list of classes. For each class, the members and methods are listed, with useful explanations. Figure 5.2 shows the homepage of the documentation, including a description of the project and basic informations to launch the simulation. Figure 5.3 is a screenshot of the class list, with standard information on each class. A click on the class name leads to a detailed description, like the one seen on Figure 5.4.

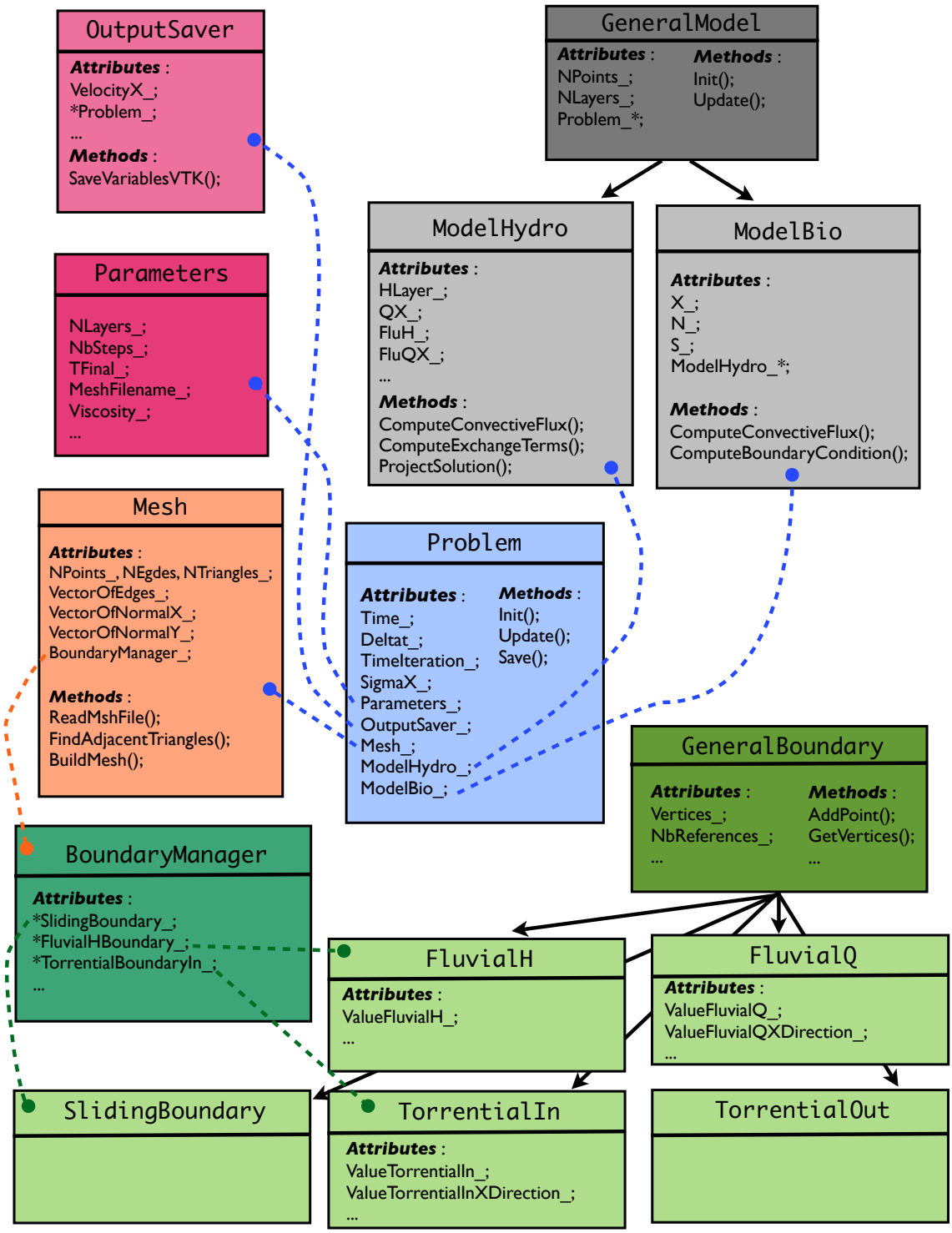

Figure 5.1: Global structure of the code.

Algorithm 5.1.1: Main algorithm in FreSHKiSS3D

Data: parameters, mesh, boundary conditions
Result: Evolution of the system until T_f
`/* Preprocessing part */`
Reading of parameters, mesh file, boundary conditions;
nbstep $\leftarrow$ maximum number of time steps, $T_f \leftarrow$ maximum time for simulation;
nver $\leftarrow$ number of vertices, nlay $\leftarrow$ number of layers;
$\partial\Omega \leftarrow$ boundary vertices ;
BuildMesh ; `// builds triangles, edges, normals, basis functions`
BuildModelHydro, BuildModelBio ; `// creates variables`
Initialization;
`/* Time loop */`
while *nstep* $<$ *nbstep* & $t < T_f$ **do**
  ComputeCFL: Δt;
  $t \leftarrow t + \Delta t$;
  nstep $\leftarrow$ nstep+1;
  `/* Computation of inner points fluxes - a * designates reconstructed variables */`
  ComputeConvectiveFluxes: $F(\boldsymbol{U}^*_{ij,\alpha}, \boldsymbol{U}^*_{ji,\alpha}, \boldsymbol{n}_{ij})$, $i = 1..$nver, $\alpha = 1..$nlay ;
  `/* Computation of boundary points fluxes */`
  ComputeBoundaryFluxes: $F(\boldsymbol{U}_{i,\alpha}, \boldsymbol{U}_{e,i,\alpha}, \boldsymbol{n}_i)$, $i = 1..\text{nver}, i \in \partial\Omega$, $\alpha = 1..$ nlay;
  `/* Computation of exchange terms */`
  ComputeExchangeTerms: $G_{i,\alpha+1/2}$, $i = 1..nver, i \in \partial\Omega$, $\alpha = 1..nlay$;
  `/* Update of the variables */`
  for $\alpha = 0$ **to** *nlay* **do** `// for each layer`
    for $i = 0$ **to** *nvertex* **do** `// for each vertex`

$$\boldsymbol{U}_{i,\alpha} \leftarrow \boldsymbol{U}_{i,\alpha} + \sum_{j \in \mathcal{K}} \sigma_{ij} F(\boldsymbol{U}^*_{ij,\alpha}, \boldsymbol{U}^*_{ji,\alpha}) - \sigma_i F(\boldsymbol{U}_{i,\alpha}, \boldsymbol{U}_{e,i,\alpha}, \boldsymbol{n}_i) + \Delta t G_{i,\alpha+1/2} \begin{pmatrix} 0 \\ u_{i,\alpha+1/2} \\ v_{i,\alpha+1/2} \end{pmatrix} - \Delta t G_{i,\alpha-1/2} \begin{pmatrix} 0 \\ u_{i,\alpha-1/2} \\ v_{i,\alpha-1/2} \end{pmatrix}$$

    end
  end
  `/* Computation of friction and vertical viscous terms */`
  ComputeFrictionTerms, ComputeViscousTerms;
  `/* Computation of forcing or reaction terms */`
  ComputeWheelEffects;
  `/* To ensure sliding boundary condition on the walls */`
  ProjectSolution;
end

5.1.3 An always improved and maintained code

This code is now an important key tool in the Ange team and it is currently maintained and improved by a computer scientist at Inria. Comparison with analytical solutions are

Algorithm 5.1.2: Computation of convective fluxes in FreSHKiSS3D. Hydrostatic reconstruction, rotation and flux vector splitting

Data: variables at time t^n
Result: convective fluxes for each vertex

for *edge = 1* **to** *nedge* **do** // for each edge
  i $\leftarrow$ first vertex of edge ;
  j $\leftarrow$ second vertex of edge ;
  for α *= 1* **to** *nlay* **do** // for each layer
    /* Hydrostatic reconstruction */
    $\boldsymbol{U}^*_{ij,\alpha}$, $\boldsymbol{U}^*_{ji,\alpha}$;
    /* Rotation of the coordinate system. 1D problem in the direction of the interface normal $\boldsymbol{n}_{ij} = (n_x, n_y)$ */
    $\boldsymbol{R} \leftarrow \begin{pmatrix} 1 & 0 & 0 \\ 0 & n_x & n_y \\ 0 & -n_y & n_x \end{pmatrix}$;
    $\hat{\boldsymbol{U}}_{i,\alpha} = \boldsymbol{R}\boldsymbol{U}_{i,\alpha}$;
    /* Computation of fluxes in this local basis */
    $F^+(\hat{\boldsymbol{U}}^*_{ij,\alpha}), F^-(\hat{\boldsymbol{U}}^*_{ji,\alpha})$;
    /* Inverse rotation */
    $F^+(\boldsymbol{U}^*_{ij,\alpha}) = \boldsymbol{R}^{-1}F^+(\hat{\boldsymbol{U}}^*_{ij,\alpha})$;
    $F^-(\boldsymbol{U}^*_{ij,\alpha}) = \boldsymbol{R}^{-1}F^-(\hat{\boldsymbol{U}}^*_{ij,\alpha})$;
    /* Add contribution of interface ij to total flux in i and j */
    TotalFlux[i, α] $\leftarrow$ TotalFlux[i, α] $-F^+(\boldsymbol{U}^*_{ij,\alpha}) - F^-(\boldsymbol{U}^*_{ji,\alpha})$;
    TotalFlux[j, α] $\leftarrow$ TotalFlux[j, α] $+ F^+(\boldsymbol{U}^*_{ij,\alpha}) + F^-(\boldsymbol{U}^*_{ji,\alpha})$;
  end
end

tested. Biologists from team BIOCORE at INRIA Sophia-Antipolis begin to use it in order to provide Lagrangian trajectories for different wheel velocities, wind conditions...This gives a great feedback to help fix the code.

FreSHKiSS3D v 1.0

Main Page Classes Files Search

FreSHKiSS3D Documentation

Introduction

The code solves the 3D hydrostatic Navier-Stokes equations coupled with a biological transport reaction diffusion system. It uses a finite volume scheme for the hyperbolic part of the equations with a kinetic solver. The diffusion operators are treated explicitely through finite element methods. We take into account variable density through the Boussinesq assumption.

Description of the project

To use the software:

- make clean: cleans every object file and executable
- make: compile (creates the executable)
- ./FreSHKiSS : execute code.

What you need to fill to execute your simulation:

- have the mesh contained in a .msh file, ex: test.msh
- parameter.ini : fill in parameters of simulation, names of files for mesh, boundary, initial conditions.
- configBoundary.ini (or name you gave to your boundary file) : indicates the boundaries type. Be careful, respect the syntax explained in the file.
- initialcondition.ini (or name you gave for your initial conditions file) : indicates the initial conditions (if homogeneous everywhere, else code your own init function in ***ModelHydro::Init()*** and ***ModelBio::Init()***)

Author:
A.-C. Boulanger

Generated on Tue Feb 14 2012 17:08:50 for FreSHKiSS3D by doxygen 1.7.3

Figure 5.2: Homepage of the html documentation generated by Doxygen.

FreSHKiSS3D v 1.0

Main Page Classes **Files** Search

Class List **Class Index** **Class Hierarchy** **Class Members**

Class List

Here are the classes, structs, unions and interfaces with brief descriptions:

BasisFunction	This class implements the basis functions of the domain (1 at one vertex, 0 at the neighbouring vertices). They are related to the finite element treatment of some terms in the code
BoundaryManager	This class implements the ***BoundaryManager*** object. **BoundaryManager** contains all information about the treatment of the boundary points. This class is initialized with a file. The allowed boundary conditions are for the moment: • Sliding condition, for solid boundaries, detailed in object ***SlidingBoundary*** • Fluvial flow with fixed height, detailed in object ***FluvialHBoundary*** • Fluvial flow with fixed flux, detailed in object ***FluvialQBoundary*** • Torrential inflow, detailed in object ***TorrentialInBoundary*** • Torrential outflow, detailed in object ***TorrentialOutBoundary***
Edge	This class implements the edge object. The edge here is between two triangle vertices. It contains: • a 2-int array containing the integer references of bothe vertices, • a boundary_ int telling if this is a boundary edge, • a 2-int array containing the references of both adjacent triangles(only one if boundary edge)
FluvialHBoundary	This class implements the fluvial flow with fixed height boundary condition. It inherits from the ***GeneralBoundary*** class. In addition to the ***GeneralBoundary*** class, this type of condition requires • the value of the imposed water height, • the value of the imposed tracer
FluvialQBoundary	This class implements the fluvial flow with fixed flow boundary condition. It inherits from the ***GeneralBoundary*** class. The additional attributes concern the flux we want to impose at the boundary (flow,direction,transition time). We also impose the tracer value
GeneralBoundary	This class implements the minimum framework to deal with any boundary type. Any class representing a more specific boundary should inherit from ***GeneralBoundary*** and implement the required virtual methods. There is no real instanciation of a **GeneralBoundary** object in the code
GeneralModel	This class implements the general framework for a model. It contains static variables that should be shared by all instanciated models (Mass flux, exchange terms). A lot of functions are pure virtual, which implies that this class is pure abstract (could never be instanciated) and the functions need be implemented in the children class
Mesh	This class implements the mesh object. A mesh is a based on a 2D triangulation of the domain computed with softwares like Freefem. The code here should be provided with a file in the same format as .msh files. The first line contains *NPoints_ NTriangles_ NBoundaryPoints*. The NPoints following lines contain the coordinate of point 'i' and its boundary reference (0 if interior point).

Figure 5.3: List of classes generated by Doxygen.

FreSHKiSS3D v 1.0

Main Page Classes Files Search

Class List Class Index Class Hierarchy Class Members

Public Member Functions | Private Attributes

Problem Class Reference

This class builds the framework for the resolution of one particular problem.
This problem should be filled with the following information:

- **Parameters**
- **Mesh**
- Topography
- Hydrodynamics equations
- Biological equations.

More...

`#include <problem.h>`

List of all members.

Public Member Functions

	Problem (**Parameters** *parameters, **Mesh** *mesh, **Topology** *topology, **ModelHydro** *modelhydro, **ModelBio** *modelbio) Constructor of the clas ***Problem***.
	~Problem () Destructor of the class ***Problem***.
double	**GetTime** () const Returns current time.
void	**SetTime** (double newtime) Sets current time to *newtime* .
double	**GetDeltat** () const Returns current time step.
void	**SetDeltat** (double newdeltat) Sets current time step to *newdeltat*.
double	**GetDeltat0** () const Returns deltat of first time iteration in case high order scheme in time.
void	**SetDeltat0** (double newdeltat0) Sets Deltat0 to newdeltat0.
double	**GetSigmax** () const Returns the space step.
void	**SetSigmax** (double newsigmax) Sets the space step to newsigmax.
int	**GetTimeIteration** () const Returns the time iteration.
void	**TimeIterationPlus** () Increments the time iteration.
int	**GetImprIteration** () const Returns the number of impressions carried out until current time.
Parameters *	**GetParameters** () const Returns the pointer on parameters.
Mesh *	**GetMesh** () const Returns th pointer on the mesh.

Figure 5.4: Example of class details generated by Doxygen. Here on the object Problem.

5.2 Numerical results on the raceway

5.2.1 Modeling

We eventually begin the modeling of the 3D raceway. We model a six blades paddlewheel whose angular velocity is $0.5 rad.s^{-1}$. We configure our parameters on the wheel in order to get, as in the bidimensionnal situation, an asymptotic value of $0.3 - 0.4 m.s^{-1}$. Figure 5.5 shows the velocity magnitude of the raceway after a ten minutes simulation. What is remarkable are the dead zones developing right after the turns. This phenomena are also observed in real situations and started to be investigated in [129] recently because it is something that should be avoided to optimize the algae growth.

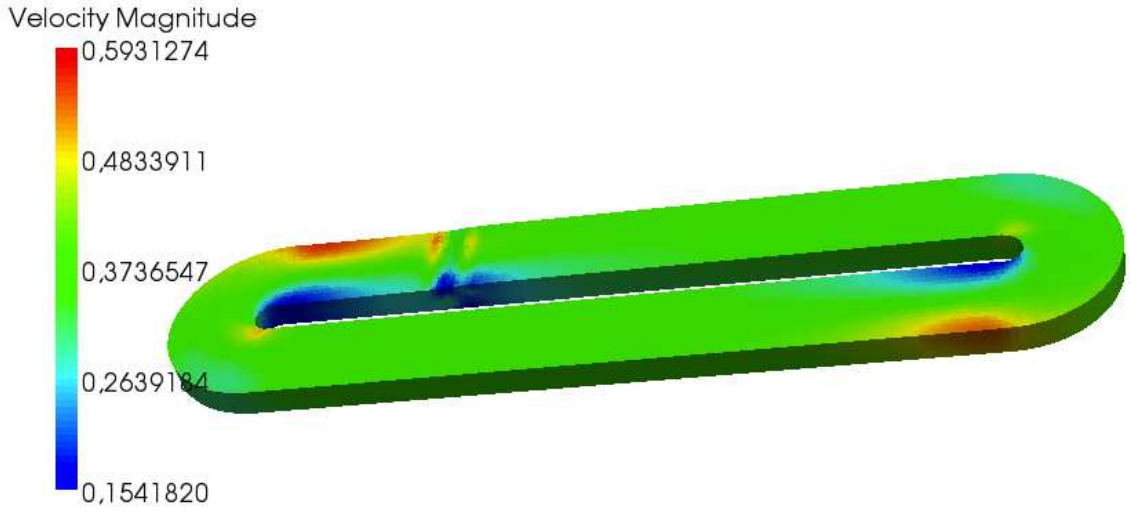

Figure 5.5: Velocity magnitude in the raceway after some time. Dead zones are observed right after the turns, as in real situations.

5.2.2 Data comparison

From a collaboration with INRA Narbonne and NASKÉO, we benefited from data on an experimental raceway. This raceway does not contain yet microalgae intended for biofuel but only water which enabled water velocity measures. The measurement points are explained in Figure 5.6. We reproduce this raceway with our code and launch simulations of a tracer advected and diffused by the flow until we meet a somewhat stationary state in order to compare our velocity values with the observed ones. Figure 5.7 shows a snapshot of this simulation. For the velocity comparisons, we test each series (denoted 1, 2 or 3 on Figure 5.6). The results are depicted in Figure 5.8, Figure 5.9 and Figure 5.10. Even though they do not exactly match, we are able to reproduce the global behaviour and the magnitudes are comparable. Figure 5.11 is the result of the simulation velocities around the pond for three different depths. It shows how the paddlewheel, at position 0 put the water

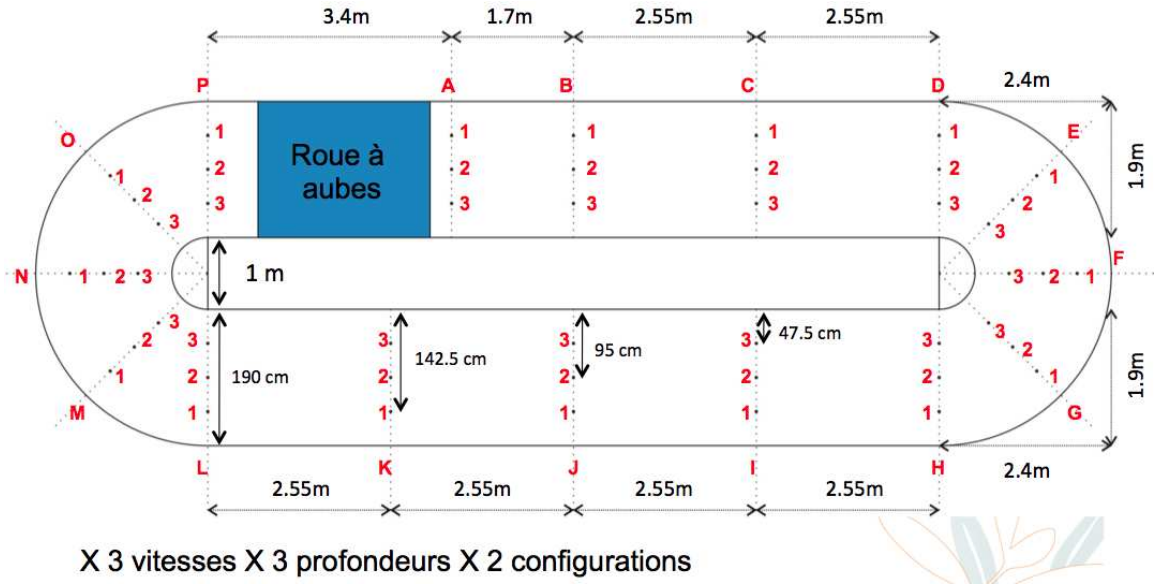

Figure 5.6: Dimensions of the raceway and measurement points for the velocity magnitude.

into motion, and how the energy is homogeneized in the raceway. We do not claim that our simulations match perfectly with reality. From those figures, we want, before everything to show the inhomogeneity of the velocity both along the vertical and the horizontal dimension. We also compare the evolution of the tracer concentration at some point in the pond through time. Figure 5.12 shows how the tracer is diffused in the pond. Data and simulations match quite well.

5.2.3 Lagrangian trajectories

In the end, as in the bidimensional case, biologists are interested in the lagrangian trajectories of microalgae in order to better understand the light dynamics that they undergo. Then, from each eulerian velocity field obtained in the simulation, we postprocess the resolution of equation

$$\frac{d\boldsymbol{M}(t)}{dt} = \boldsymbol{v}(\boldsymbol{M}(t)) \tag{5.1}$$

The experience we carry out is as follows. We have a 3 meters large 10 meters long and 0.5 meters deep raceway. We follow ten particles, located initially at the same (x, y) coordinates, but for different depths, uniformly split. We repeat this experiment for 6 initial y positions, $x_0 = 5$m, the paddlewheel is located at $x = 2$m. Then $y_0 = 0.3$m means that the particle is close to the inner wall of the raceway and $y_0 = 1.3$m means that the particle is rather located at the outer wall of the pond. Figure 5.13, Figure 5.14 and Figure 5.15 show the resulting x, y and z positions of the particles for the 6 experiments. The position in x does not tell much but the fact that the particles make approximately eight laps in 1000s, which gives a velocity of $0.16m.s^{-1}$. The position in y on Figure 5.14 shows that the particles do not follow exactly an ellipsoidal trajectory, but they switch from the inner wall to the

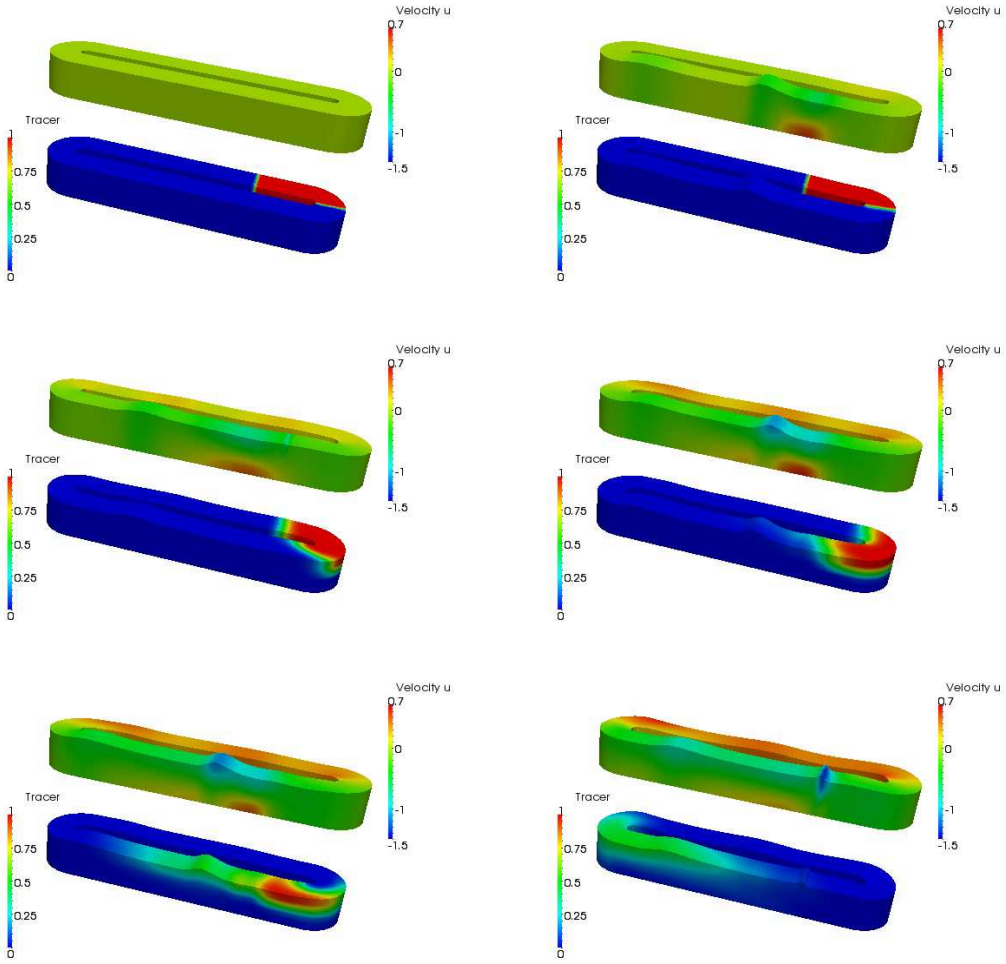

Figure 5.7: Snapshots of advection diffusion of a tracer.

outer wall regularly. Eventually, the depth in Figure 5.15 and Figure 5.16 shows that algae undergo great changes in their depth, no matter the initial condition. The 3D modeling brings us a new information on the trajectories of particles, especially with the y-position information. This could be due to spirals happening in the curves.

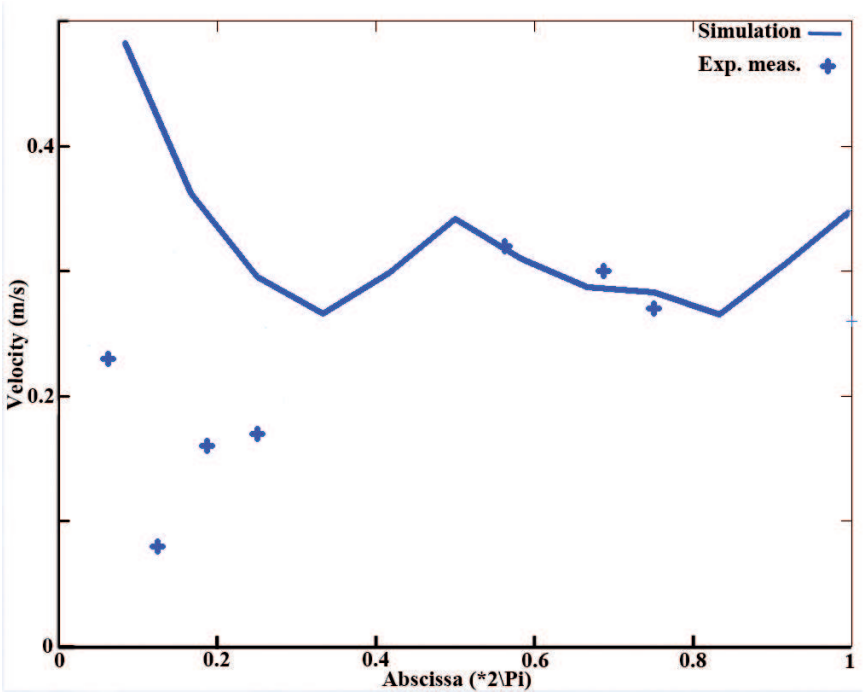

Figure 5.8: Velocity magnitude at the surface of the raceway after some time. First series (outer border of the pool). Abscissa 0 corresponds to point A. Abscissa 1 corresponds to point P.

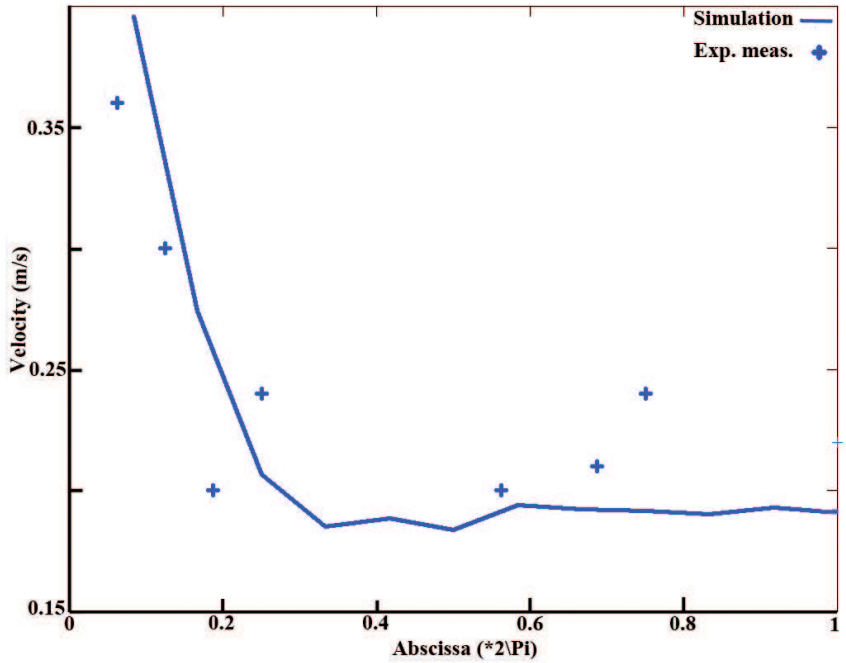

Figure 5.9: Velocity magnitude at the surface of the raceway after some time. Second series (middle of the pool).Abscissa 0 corresponds to point A. Abscissa 1 corresponds to point P.

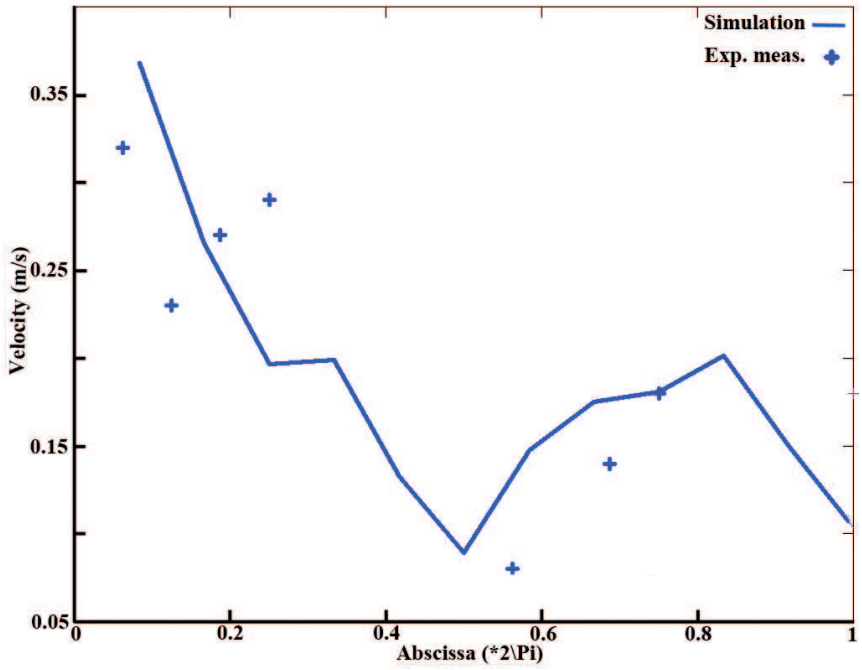

Figure 5.10: Velocity magnitude at the surface of the raceway after some time. Third series (inner border of the pool).Abscissa 0 corresponds to point A. Abscissa 1 corresponds to point P.

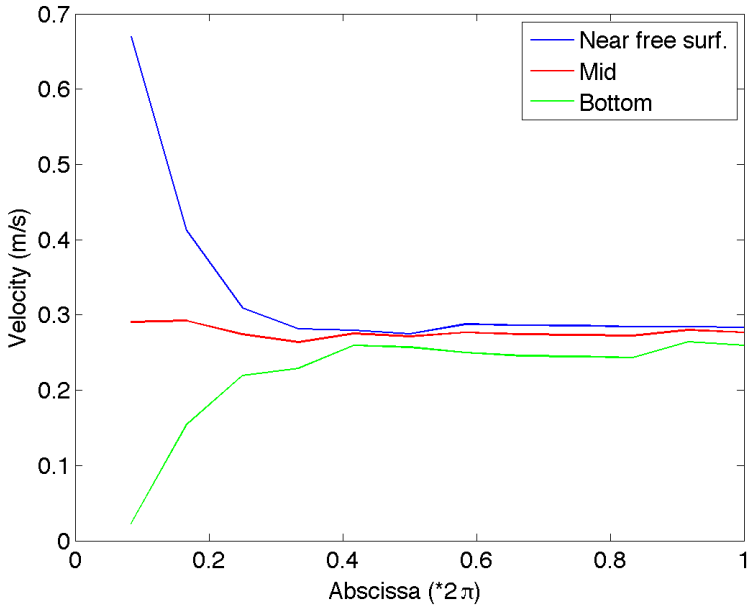

Figure 5.11: Velocity around the raceway at different depth: at the surface, in the middle and at the bottom. 0 is the position of the wheel.

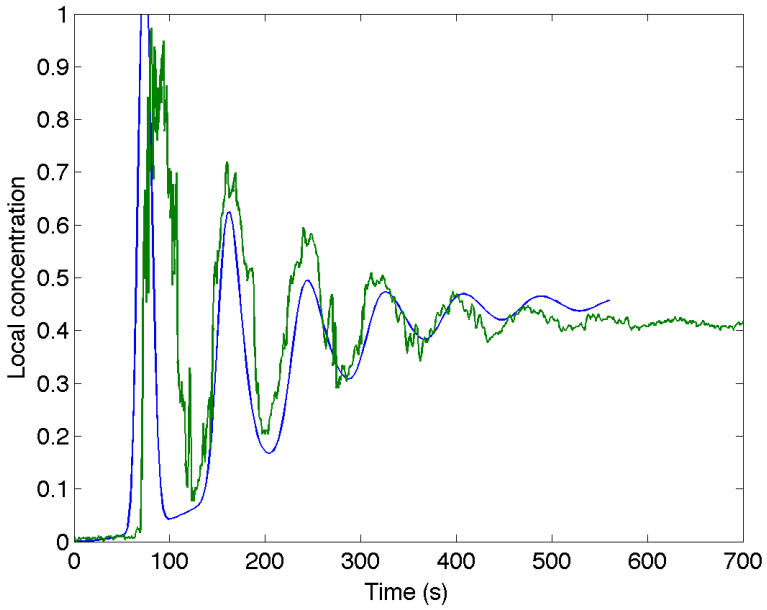

Figure 5.12: Tracer concentration evolution through time. Green curve plots the data. Blue curve represents the simulation.

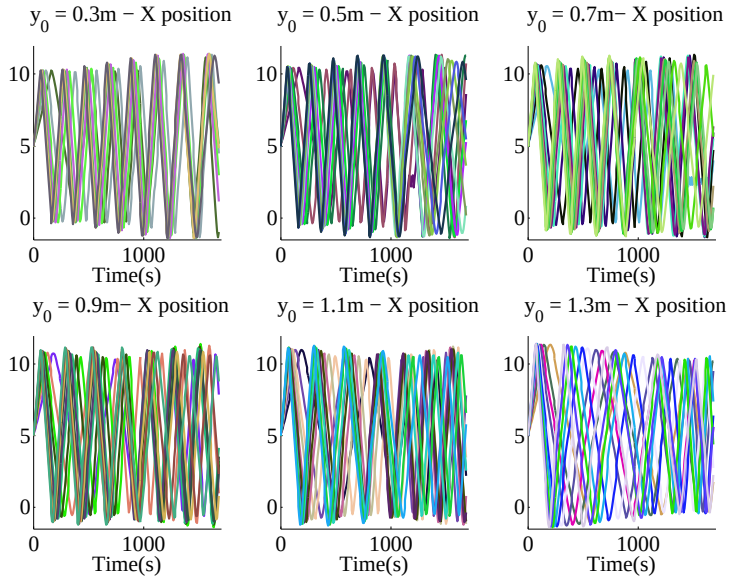

Figure 5.13: X-position of ten particles spread along the depth of the raceway for six different initial positions in y-dimension.

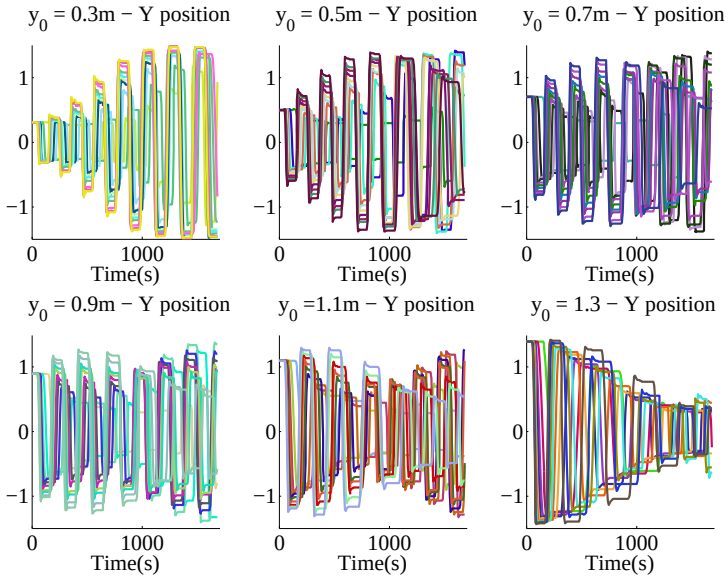

Figure 5.14: Y-position of ten particles spread along the depth of the raceway for six different initial positions in y-dimension.

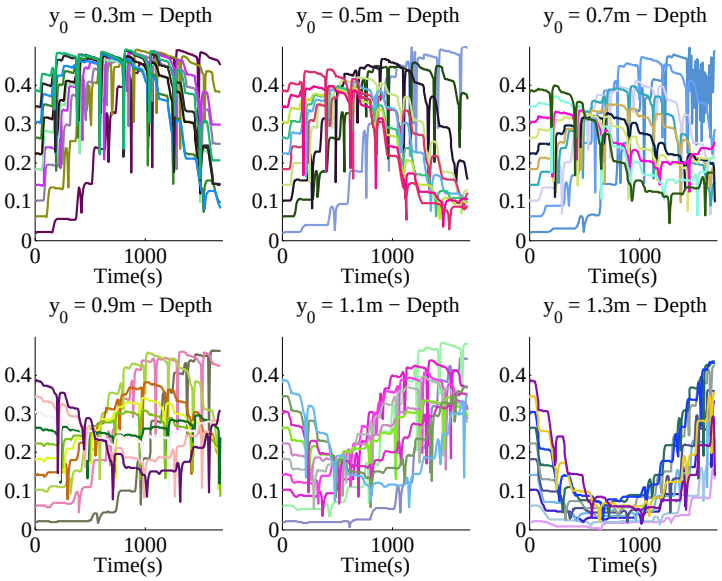

Figure 5.15: Z-position of ten particles spread along the depth of the raceway for six different initial positions in y-dimension.

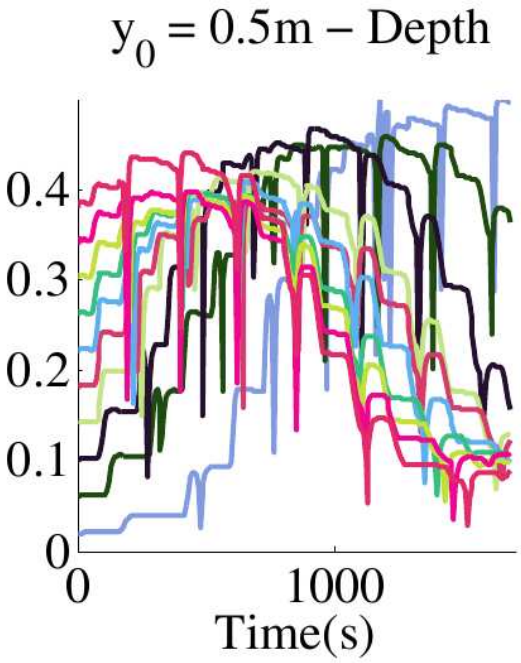

Figure 5.16: Z-position of ten particles spread along the depth of the raceway for different initial positions in y-dimension.

Data assimilation for hyperbolic conservation laws, Luenberger observer and kinetic description

6

L'assimilation de données pour des lois de conservation hyperboliques nécessite l'utilisation de méthodes robustes. En effet, ces EDP ne sont pas dissipatives et l'introduction d'information additionnelle dans les équations introduit des erreurs qui se propagent dans le temps et créent des chocs. Dans ce chapitre, nous proposons une nouvelle approche basée sur la description cinétique des lois de conservation. Une équation cinétique est une EDP du premier ordre, dans laquelle la vitesse d'advection est une variable libre. Dans certains cas, il est possible de prouver l'équivalence entre une loi de conservation non linéaire, augmentée de toutes ses inégalités d'entropies, et une unique équation cinétique scalaire linéaire sur une quantité non linéaire dépendant d'une nouvelle variable. L'assimilation de données est alors effectuée au niveau cinétique par un observateur de Luenberger. L'avantage de ce cadre de travail est que l'on travaille avec une unique équation de type BGK et le retour aux quantités macroscopiques est aisé. L'étude est essentiellement basée sur des techniques d'analyse fonctionnelle et considère des difficultés progressives. En premier lieu, on étudie la convergence dans le cas scalaire, en données complètes. Puis on ajoute du bruit pour étudier la stabilité, avant de passer à l'étude en données partielles, en temps et espace. Enfin, on s'intéresse au cas pratique du système de Saint-Venant. Des exemples numériques sont donnés dans les cas scalaire et système.

Ce travail est issu d'une collaboration avec Philippe Moireau, Benoit Perthame *et* Jacques Sainte-Marie *et sera publié sous le titre* Data Assimilation for hyperbolic conservation laws. A Luenberger observer approach based on a kinetic description.

Data assimilation for hyperbolic conservation laws requires the use of robust methods. Those PDEs indeed are not dissipative and the injection of additional information in the equations introduces errors which propagate with time and create shocks. In this chapter, we propose a novel strategy based on the kinetic description of conservation laws. A kinetic equation is a first order PDE in which the advection velocity is a free variable. In certain cases, it is possible to prove equivalence between a nonlinear conservation law plus all its entropy inequalities and a unique scalar kinetic equation on a nonlinear quantity depending on a new variable. Data assimilation is therefore carried out at the kinetic level using a Luenberger observer. The advantage of this framework is to work with a unique equation of BGK type, while getting back to the macroscopic variables is easy. The study is essentially based on functional analysis techniques and considers gradual difficulties. In a first step, we study the convergence of the observer when data are complete. In a second step, we add noise and consider partial data in space or time. Eventually, we focus on the Saint-Venant system. Numerical examples are provided in the scalar and system cases.

This is a joint work with Philippe Moireau, Benoit Perthame *and* Jacques Sainte-Marie. *It will be published under the title* Data Assimilation for hyperbolic conservation laws. A Luenberger observer approach based on a kinetic description.

6.1 Introduction

Data assimilation has become a popular strategy to refine the quality of numerical simulations of complex physical phenomena by taking into account available measurements. In particular numerous works in environmental sciences, but also life sciences – see [26, 44, 104] and references therein – have used data assimilation to deal with the various sources of error entering and propagating during a simulation and restricting the performance of a numerical prediction. This is particularly the case for hyperbolic systems in general, and especially for conservative systems where, in the absence of dissipation, even small numerical errors are likely to propagate and expand in time [43]. The main idea behind data assimilation is thus to improve the prediction by integrating additional information on the actual specific system considered, with the use of the measurements – also called observations – at our disposal.

We consider in this work a general class of conservation laws that may contain nonlinearities as typically illustrated by transport equations, Burgers' equation, the shallow-water or Euler systems and we focus especially on the non-viscous configurations. In data assimilation, two types of approaches are available: the variational and the sequential approach which both can be considered in a deterministic or a stochastic functional framework [21]. We rely, here, on a deterministic description which can be seen as a first step in the handling of more general uncertainties present in the system. On the one hand, the variational approach was popularized by the 4D-Var [89]. It consists in minimizing globally a – usually least-squares based – cost function representing a compromise during a period of

time between (1) the observation discrepancy computed between simulations of the model and the corresponding measurements and (2) an *a priori* confidence in the model. The cost function gradient is obtained through an adjoint model integration linked to the dynamical model constraint under which the cost function is minimized. Hence, the minimization is classically performed by a gradient descent algorithm involving numerous successive iterations of the combination of the model and adjoint dynamics during a fixed time window. Moreover, as optimal control theory often assumes differentiability, mathematical difficulties arise when viscosity is neglected and in the presence of discontinuities like shocks, see [17] and [18] where a formalism is defined to avoid incorrect computations of gradients (yet keeping the computation of the adjoint model). One the other hand, the sequential methods include in the definition of the approximating dynamics a correction term based on the observation discrepancy. The resulting system called observer – or estimator in the stochastic context – is then expected to converge in time to the actual system as it incorporates more and more data. Note that in the sequential approach the initial condition is classically not retrieved but only filtered so that we get an estimation at the final time in one forward simulation. In this context, the most popular observer is based on the Kalman filter which can be virtually defined on any model and shown to be equivalent to the variational approach at least for linear systems, ergo its denomination of optimal estimator [21]. However the Kalman filter, based on dynamic programing principles, is subject to the famous Bellman curse of dimensionality [20] which makes it numerically unpractical for partial differential equations (PDE). We rather follow the path introduced by Luenberger [96, 97] and popularized for PDE with the *nudging* appellation [75, 131] to define a sequential observer which converges to the actual system in one forward simulation and in which the correction term remains tractable in practice. The principle is to introduce the simplest possible correction so that the error between the actual observed trajectory and the simulated systems stabilizes rapidly to 0. This type of method has recently regained interest with applications to a large range of systems like conservation laws, waves, beams, elasticity or fluid-structure interaction [25, 42, 43, 95, 103] and with new general improvements, for example in the determination of the nudging coefficients [130, 141, 145] or for restoring the initial condition [12, 71, 121]. However, for conservation laws, despite some recent effort [14], the observer performances remain difficult to analyze in a general context, in particular in the presence of non-linearities. In this study, we propose a new nudging strategy which, for hyperbolic conservation laws admitting a kinetic description, can be thoroughly justified even for non-linear systems.

Let us consider the practical case of systems, with the illustrative example of the Saint-Venant system, which writes, without source term:

$$\partial_t H + \partial_x(Hu) = 0 \tag{6.1}$$

$$\partial_t Hu + \partial_x(Hu^2 + \frac{gH^2}{2}) = 0. \tag{6.2}$$

This system naturally comes with a single entropy inequality for the energy

$$E(H,u) = H\frac{u^2}{2} + \frac{gH^2}{2}, \tag{6.3}$$

which satisfies for weak solutions

$$\partial_t E + \nabla \cdot \left(u(E + \frac{gH^2}{2}) \right) \leq 0. \tag{6.4}$$

We expound here briefly the strategy of the kinetic Luenberger observer and set forth a crucial point justifying the interest to design such a method: the automatic decrease of energy that it guarantees. Naive data assimilation on the Saint-Venant system can indeed be written as follows:

$$\partial_t \widehat{H} + \partial_x(\widehat{H}\widehat{u}) = K(H - \widehat{H}) \tag{6.5}$$

$$\partial_t \widehat{H}\widehat{u} + \partial_x(\widehat{H}\widehat{u}^2 + \frac{g\widehat{H}^2}{2}) = 0 \tag{6.6}$$

where H represents data and $\left(\widehat{H}, \widehat{u}\right)$ the observer. The height is indeed usually the easiest variable to measure. With this system we associate the energy equation

$$\partial_t \widehat{E} + \nabla \cdot \left(\widehat{u}(\widehat{E} + \frac{g\widehat{H}^2}{2}) \right) \leq -K(H - \widehat{H}) \left(\frac{\widehat{u}^2}{2} - g\widehat{H} \right). \tag{6.7}$$

Unfortunately, the right hand side of the inequality has no obvious sign, and the decrease of energy is not assured. This is where we introduce the kinetic description of the Saint-Venant system. It consists in using the equivalence between the nonlinear system of conservation laws and a linear kinetic equation in a new variable ξ, the kinetic velocity. Formally, we have an equivalence between the macroscopic conservation law and its energy inequality and the kinetic equation. The shallow water system without source term ((6.1) -(6.2)) augmented of its entropy inequality (6.4) is equivalent to

$$\partial_t M(\widehat{H}, \widehat{u} - \xi) + \xi \cdot \nabla_x M(\widehat{H}, \widehat{u} - \xi) = Q(t,x,\xi). \tag{6.8}$$

where M satisfies the form

$$M(h, v - \xi) = \begin{cases} \dfrac{1}{2\pi g}, & \text{for } |\xi - v| < \sqrt{2gh} \\ 0, & \text{otherwise.} \end{cases} \tag{6.9}$$

and Q is what is called a collision operator that verifies

$$\int_{\mathbb{R}_\xi} Q(t,x,\xi)d\xi = \int_{\mathbb{R}_\xi} \xi Q(t,x,\xi)d\xi = 0, \quad \int_{\mathbb{R}_\xi} \frac{\xi^2}{2} Q(t,x,\xi)d\xi \leq 0. \tag{6.10}$$

The proof is done by simple integration in ξ of the first moments of (6.8).

In comparison to ((6.5) - (6.6)), the kinetic assimilated system writes ([112])

$$\partial_t f(\widehat{H}, \widehat{u} - \xi) + \xi \cdot \nabla_x f(\widehat{H}, \widehat{u} - \xi) = K\left(f(\widehat{H}, \widehat{u} - \xi) - M(H, u - \xi)\right). \tag{6.11}$$

where f and M satisfy the form (6.9). Thanks to the property of the collision operator, the energy equation, which is classically obtained by computing $\int_{\mathbb{R}_\xi} \frac{\xi^2}{2}(6.8)d\xi$ (see [112]) becomes

$$\partial_t \widehat{E} + \nabla \cdot \left(\widehat{u}(\widehat{E} + \frac{g\widehat{H}^2}{2})\right) \leq K(E - \widehat{E}). \tag{6.12}$$

This ensures by Gronwall's lemma the decrease of energy in L^1 norm. Unlike the macroscopic nudging (6.5), the Luenberger observer that we add at the kinetic level does not perturb the stability of the macroscopic system. With this simple example, we want to show that the kinetic Luenberger observer provides a nice framework to the development of a constructive data assimilation method. We will also demonstrate in the article the efficiency of this strategy through numerical results.

This efficacy encourages the development of a theoretical framework in the case of scalar conservation laws as usually made when dealing with hyperbolic PDEs. The kinetic formulation of them is indeed well understood [112]. For a scalar conservation law defined as follows

$$\begin{cases} \dfrac{\partial u}{\partial t}(t,x) + \nabla_x \cdot A(u)(t,x) = 0, \\ u(0,x) = u_0(x), \end{cases} \tag{6.13}$$

with the entropy inequalities

$$\frac{\partial S(u)}{\partial t}(t,x) + \nabla_x \cdot \eta(u)(t,x) \leq 0, \tag{6.14}$$

the kinetic description can be written

$$\begin{cases} \dfrac{\partial M}{\partial t}(t,x,\xi) + a(\xi) \cdot \nabla_x M(t,x,\xi) = Q(t,x,\xi), \\ M(0,x,\xi) = M_0(x,\xi). \end{cases} \tag{6.15}$$

u is the macroscopic variable, M is the density function which is related to u by its first moment:

$$u(t,x) = \int_{\mathbb{R}} M(t,x,\xi)\ d\xi.$$

Q is still the collision operator. Nonlinearities are hidden in the density function, and shocks are confined in the collision operator. But we emphasize the fact that for fixed ξ, the kinetic equation can be handled as a linear equation. The equivalence proof is based on simple integration of the kinetic equations. Then, the observer equations at the macroscopic level

$$\begin{cases} \dfrac{\partial \widehat{u}}{\partial t} + \nabla_x \cdot A(\widehat{u}) = \mathcal{K}[u - \widehat{u}], \\ \widehat{u}(0) = u_0 + \delta_0, \end{cases} \tag{6.16}$$

are transcribed at the kinetic level

$$\begin{cases} \dfrac{\partial f}{\partial t} + a(\xi) \cdot \nabla_x f = \mathcal{K}[M - f], \\ f(0) = M_0 + \gamma_0. \end{cases} \tag{6.17}$$

At the macroscopic level, the nonlinearity of the flux A prevents from easy convergence proofs of $\widehat{u}$ towards u. Possible techniques are based on L^1 contraction principle in the scalar case, but do not extend to systems. At the kinetic level, the equation gains linearity and we can even have the explicit writing of its solution:

$$f(t,x,\xi) = f_0(x - a(\xi)t, \xi)e^{-\mathcal{K}t} + \int_0^t e^{-\mathcal{K}s} M(t - sx - a(\xi)s, \xi)ds, \tag{6.18}$$

as soon as $M(t,x,\xi)$ can be generated from the measurements.

The outline is organized as follows. Section 6.3 exposes the theoretical framework of our novel method on a scalar hyperbolic conservation law. Convergence theorems are given in the case of complete observations, partial observations and noisy observations. Numerical experiments illustrate its efficiency on Burgers' equation in 1D. Afterwards, Section 6.4 introduces the more practical case of the shallow water equations. We emphasize the benefit of our method for the Saint-Venant system as we are able to build an efficient numerical assimilation scheme based on heights observations only. Once again, numerical simulations are carried out on bidimensional analytical solutions and an example in 3D is also provided.

Throughout the chapter, V_p stands for the Lebesgue space $L^p(\mathbb{R}^d_x \times \mathbb{R}_\xi)$ and we use the notation $\|f\|_{L^p(\mathbb{R}^d_x \times \mathbb{R}_\xi)} = \|f\|_{V_p}$.

6.2 Hyperbolic balance laws

For completeness and to present our notations, we recall briefly some essential notions. For a more detailed description, the reader can refer to ([112], [117], [113]). Let Ω be an open subset of $\mathbb{R}^p$, and let A_i, $1 \leq i \leq d$ be d smooth functions from Ω into $\mathbb{R}^p$. We consider in this chapter the initial value problem

$$\begin{cases} \partial_t \mathbf{u} + \displaystyle\sum_{i=1}^{d} \partial_{x_i} \mathbf{A_i}(\mathbf{u}) = 0 \\ \mathbf{u}(t=0,x) = \mathbf{u_0}(x) \end{cases} \tag{6.19}$$

where $\mathbf{u} = (u_1, \ldots, u_p)$ is a vector-valued function from $[0, +\infty[\times \mathbb{R}^d$ into Ω.

System (6.19) expresses the conservation of the quantities $u_1, \cdots, u_p$. Let us take indeed an arbitrary domain Ω of $\mathbb{R}^d$ and let $\mathbf{n} = (n_1, \cdots, n_d)$ be the outward unit normal to the

boundary Γ. Then, integration over the space and time variable of (6.19) yields

$$\frac{d}{dt}\int_{\Omega}\mathbf{u}dx+\sum_{i=1}^{d}\int_{\Gamma}\mathbf{A}_i(\mathbf{u})n_i dS=0. \tag{6.20}$$

Moreover, the system will be supposed hyperbolic: for any $i=1..d$, let us call

$$\mathbf{F}_i(\mathbf{u})=\left(\partial_{u_j}\mathbf{A}_i(\mathbf{u})\right)_{1\leq i,j\leq p} \tag{6.21}$$

the Jacobian matrix of $\mathbf{A}_i$, then for any $\mathbf{u}\in\Omega$ and any $\boldsymbol{\omega}=(\omega_1,\cdots,\omega_d)\in\mathbb{R}^d$, the matrix

$$\mathbf{F}(\mathbf{u},\boldsymbol{\omega})=\sum_{i=1}^{d}\omega_i\mathbf{F}_i(\mathbf{u})$$

has p real eigenvalues and p linearly independent corresponding eigenvectors. Solution to a nonlinear hyperbolic conservation law may exhibit shocks even if the initial condition is smooth. A classical $\mathcal{C}_1$ solution may not exist at any time. Thus, we define the concept of weak solution and the equation shall be interpreted in the distributional sense i.e. for any smooth function $\boldsymbol{\phi}\in C_0^1([0,+\infty[\times\mathbb{R}^d)^p$ and $\mathbf{u}_0\in L^{\infty}_{loc}(\mathbb{R}^d)^p$

$$\int\int\boldsymbol{\phi}_t\cdot\mathbf{u}+\sum_{i=1}^{d}\boldsymbol{\phi}_{\boldsymbol{x_i}}\cdot\mathbf{A_i}(\mathbf{u})dxdt+\int_{\mathbb{R}^d}\mathbf{u}_0(x)\cdot\boldsymbol{\phi}(0,x)dx=0, \tag{6.22}$$

where $\cdot$ designates the Euclidian inner product in $\mathbb{R}^p$. But in this sense, several weak solutions can satisfy (6.22). The supplementary condition required to select the appropriate one is called the entropy condition ([62]). The weak solution $\mathbf{u}$ of (6.19) is an entropy solution if

$$\partial_t S(\mathbf{u})+\sum_{i=1}^{d}\partial_{x_i}\eta_i(\mathbf{u})\leq 0 \tag{6.23}$$

in the sense of distribution and for any entropy pair $(S,\eta_i,i=1..d)$, where S is a convex entropy and η_i the corresponding entropy fluxes of the form

$$\nabla\eta_i(\mathbf{u})=\nabla S(\mathbf{u})\cdot F_i(\mathbf{u}) \tag{6.24}$$

6.3 Kinetic Luenberger observer on hyperbolic scalar conservation laws

In this section, we present the theoretical framework underlying the novel method we propose. It is based on the particular properties of hyperbolic balance laws and their kinetic formulation.

6.3.1 Kinetic formulation

The kinetic formulation, restricted to systems with many entropies, offers a way to represent full families of entropies by a single equation. An entropy, as explained is a conservation laws built on nonlinear functions of the unknown. The idea underlying the kinetic formulation is to parametrize those entropies, and consider the parameters as an additional variable. We call it the kinetic velocity ξ. After some manipulation, we end up with a linear equation in the best cases (for instance for scalar conservation laws). This linearity enables the use of functional analysis techniques such as convolution to regularize the solution or Fourier transform to perform further analysis.

We detail here the case of scalar conservation laws (p=1 in the previous section). Let us introduce the function χ such that for $\xi \in \mathbb{R}$

$$\chi(\xi, u) = \begin{cases} +1, & \text{for } 0 < \xi < u \\ -1, & \text{for } u < \xi < 0 \\ 0, & \text{otherwise.} \end{cases} \tag{6.25}$$

This function allows to represent any function $S(u)$ in the following manner

$$\int_{\mathbb{R}_\xi} S'(u)\chi(\xi, u)d\xi = S(u) - S(0). \tag{6.26}$$

Then, system (6.19) with its family of entropy inequalities (6.23) is equivalent to the kinetic formulation

$$\partial_t \chi(\xi, u(t,x)) + a(\xi) \cdot \nabla_x \chi(\xi, u(t,x)) = \nabla_\xi m(t,x,\xi), \tag{6.27}$$

where we have set

$$a_i(\cdot) = A_i'(\cdot), \tag{6.28}$$

$$a(\xi) = (a_1(\xi), \cdots, a_d(\xi)), \tag{6.29}$$

and for some nonnegative bounded measure $m(t,x,\xi)$, called kinetic entropy defect measure. A proof for this assertion is available in [94]. Though the converse is difficult to address, one implication can be easily computed by multiplying (6.27) by $S'(\xi)$ and integrating in ξ.

Remark 6.3.1. *The kinetic entropy defect measure m is unknown a priori and takes account of potential singularities in the solution. It can be seen as the Lagrange multiplier for the constraint $M(t,x,\xi) = \chi(\xi, u(t,x))$, similarly to the pressure term in the incompressible Navier-Stokes equation, which is a multiplier related to the constraint that the flow is divergence free. Three properties are worth notifying here:*

- *$m(t,x,\xi)$ depends on the macroscopic solution $u(t,x)$,*
- *in particular, $m(t,x,u(t,x)) = 0$,*
- *m vanishes where the solution is smooth.*

The system of isentropic gas dynamics, admitting a full entropy family can also be described by a kinetic formulation. But the resulting kinetic equation is 'less linear' than in the scalar case. More details can be found in ([112], section 1.3).

6.3.2 Kinetic level nudging in the scalar case for complete observations

As previously stated in the introduction, the nudging strategy carried out at the kinetic level offers the advantage of a linear framework and can guarantee the decay of the energy in such systems as the shallow water equations. In this section we develop theoretical results for this method. We begin with very ideal situations, among which smooth solutions or complete observations are studied. We are then able to state convergence results in the case of partial observations in space or time.

Let us consider that the observations derive from the scalar conservation law

$$\begin{cases} \partial_t u + \sum_{i=1}^{d} \partial_{x_i} A_i(u) = 0 \\ u(t=0,x) = u_0(x) \end{cases} \tag{6.30}$$

where $u(t,x)$ defined for $t \geq 0$ is a real-valued function, $x \in \mathbb{R}^d$. Following Section 6.3.1, (6.30) admits a kinetic formulation

$$\begin{cases} \partial_t M(t,x,\xi) + a(\xi) \cdot \nabla_x M(t,x,\xi) = \nabla_\xi m(t,x,\xi) \\ M(0,x,\xi) = \chi(\xi, u_0(x)) \end{cases} \tag{6.31}$$

where $M(t,x,\xi) = \chi(\xi, u(t,x))$ satisfies (6.26) and $a(\xi)$ is defined in (6.28)-(6.29). We recall that M is designed such that

$$u(t,x) = \int_{\mathbb{R}_\xi} M(t,x,\xi) d\xi.$$

We set the study in the case of complete observations for a fixed relaxation parameter λ. Hence, we are looking for the observer $f(t,x,\xi)$ satisfying the Boltzmann type equation

$$\begin{cases} \dfrac{\partial}{\partial t} f(t,x,\xi) + a(\xi) \cdot \nabla_x f(t,x,\xi) + \lambda f(t,x,\xi) = \lambda M(t,x,\xi), \\ f(t,x,\xi=0) = f_0(x,\xi). \end{cases} \tag{6.32}$$

We will also denote the macroscopic observer

$$\widehat{u}(t,x) = \int_{\mathbb{R}_\xi} f(t,x,\xi) d\xi.$$

First of all, let us precise that (6.32) admits a unique distributional solution (see [112], section 3.5, Th. 3.5.1)

Lemma 6.3.2. *Let $f_0 \in V_1, M \in C(0,T), L^1(\mathbb{R}^d_x \times \mathbb{R}_\xi))$ for all $T > 0$. Then, there exists a*

unique distributional solution to (6.32)*,* $f \in C(\mathbb{R}^+; V_1)$ *and it satisfies*

$$f = f_0(x - a(\xi)t)e^{-\lambda t} + \lambda \int_0^t e^{-\lambda s} M(t-s, \xi, x - a(\xi)s)ds.$$

Smooth data

In the case of smooth solutions, the kinetic defect measure m, whose role is to locate the discontinuities, disappears and the simple transport equation remains

$$\begin{cases} \partial_t M(t,x,\xi) + a(\xi) \cdot \nabla_x M(t,x,\xi) = 0, \\ M(0,x,\xi) = \chi(\xi, u_0(x)). \end{cases} \tag{6.33}$$

Therefore, we are able to state a very strong theorem in the simple case of smooth solutions to scalar conservation laws: the kinetic observer converges exponentially fast towards the data and so do the macroscopic variables.

Proposition 6.3.3. *Let* $M \in C([0,T], V_1)$ *satisfy* (6.33) *and* $f \in C(\mathbb{R}^+; V_1)$ *satisfy* (6.32)*, then*

$$\|f - M\|_{V_1} \underset{t \to +\infty}{\longrightarrow} 0, \tag{6.34}$$

and the decay is exponential in time with rate λ*. This is translated at the macroscopic level as:*

$$\|\widehat{u} - u\|_{L^1(R_x^d)} \underset{t \to +\infty}{\longrightarrow} 0, \tag{6.35}$$

with the same exponential decay.

Proof of Proposition 6.3.3. Subtracting (6.32) and (6.31), we obtain

$$\partial_t(f - M) + a(\xi) \cdot \nabla_x (f - M) + \lambda(f - M) = 0 \tag{6.36}$$

Applying Theorem 6.3.2 to (6.36) we can assert that

$$(f - M)(t, x, \xi) = (f - M)(0, x, \xi)e^{-\lambda t} \tag{6.37}$$

An integration in the space and velocity variables leads to the result. And for any $T > 0$

$$\|\widehat{u} - u\|_{L^1(R_x^d)} \underset{t \to +\infty}{\longrightarrow} 0, \tag{6.38}$$

□

Non-smooth data

Back in the situation of non-smooth solutions, the data are assumed to satisfy (6.31) with $u(t,x) = \int_{\mathbb{R}_\xi} M(t,x,\xi)$ and the kinetic observer $f(t,x,\xi)$ satisfies (6.32) since observations

are complete in space and time. The presence of the collision term prevents us from obtaining a time convergence as in Proposition 6.3.3. However, we can still obtain a convergence with respect to the nudging parameter λ. Thus, we claim the following

Theorem 6.3.4. *Let $M \in C([0,T], V_1)$ satisfy (6.31) with $u_0 \in L^1(\mathbb{R}^d)$ and $f \in C(\mathbb{R}^+; V_1)$ satisfy (6.32) with $f_0 \in V_1$, then for some modulus of continuity $\omega(T,\cdot)$*

$$\|f(T) - M(T)\|_{V_1} \leq \|f_0 - f_{\lambda,0}\|_{V_1} e^{-\lambda T} + \omega(T, \frac{1}{\lambda}). \tag{6.39}$$

Moreover, if $u_0 \in L^\infty \cap L^1 \cap BV(\mathbb{R}^d)$, the dependency in λ can be improved as:

$$\|f(T) - M(T)\|_{V_1} \leq \|f_0 - f_{\lambda,0}\|_{V_1} e^{-\lambda T} + C(d)\|a\|_{L^\infty(-K,K)} \sqrt{\frac{T\|u_0\|_{BV(\mathbb{R}^d)}}{\lambda}}. \tag{6.40}$$

Remark 6.3.5. *The rate of convergence in $\sqrt{\frac{T}{\lambda}}$ expresses the fact that discrepancy between the observations and the model variables tend to increase with time. The further we want to advance in time, the bigger we need to choose λ. Notice also that in this situation, and it will be the case in other situations of complete observations, the optimal λ is the greatest possible. Of course, it is not feasible numerically and a compromise need to be done (see Section 6.3.7 about numerical results).*

Proof of Theorem 6.3.4. In order to show the convergence of f towards M we introduce another integro-differential equation

$$\begin{cases} \dfrac{\partial}{\partial t} f_\lambda(t,x,\xi) + a(\xi) \cdot \nabla_x f_\lambda(t,x,\xi) + \lambda f_\lambda(t,x,\xi) = \lambda M_\lambda(t,x,\xi), \\ f_\lambda(0,x,\xi) = \chi(\xi, u_0(x)), \end{cases} \tag{6.41}$$

where $M_\lambda(t,x,\xi) = \chi_{u_\lambda}(\xi)$ and u_λ is only defined by the relation $u_\lambda = \int_{\mathbb{R}_\xi} f_\lambda d\xi$. We then use the triangular inequality

$$\|f(T) - M(T)\|_{V_1} \leq \|f(T) - f_\lambda(T)\|_{V_1} + \|f_\lambda(T) - M(T)\|_{V_1}. \tag{6.42}$$

On the one hand, in [112], the author study some properties of f_λ as λ tends to infinity, also called the hydrodynamic limit. They prove the following (Section 4.6, Thm 4.6.1):

- if $u_0 \in L^\infty \cap L^1 \cap BV(\mathbb{R}^d)$, and setting $K = \|u_0\|_{L^\infty}$,

$$\|u_\lambda(T) - u(T)\|_{L^1(\mathbb{R}^d)} \leq \|f_\lambda(T) - M\|_{V_1} \leq C(d)\|a\|_{L^\infty(-K,K)} \sqrt{\frac{T\|u_0\|_{BV(\mathbb{R}^d)}}{\lambda}}$$

- if only $u_0 \in L^1(\mathbb{R}^d)$ is assumed, we have for some modulus of continuity $\omega(T,\cdot)$:

$$\|u_\lambda(T) - u(T)\|_{L^1(\mathbb{R}^d)} \leq \|f_\lambda(T) - M(T)\|_{L^1(\mathbb{R}^d_x \times \mathbb{R}_\xi)} \leq \omega(T, \frac{1}{\lambda}).$$

On the other hand, according to (6.31) and (6.41), f and f_λ satisfy

$$\partial_t(f - f_\lambda) + a(\xi) \cdot \nabla_x(f - f_\lambda) + \lambda(f - f_\lambda) = \lambda(M - M_\lambda). \tag{6.43}$$

Therefore, we can use the representation formula of Theorem 6.3.2 and get

$$(f - f_\lambda)(t, x, \xi) = (f - f_\lambda)(0, x, \xi)e^{-\lambda t} + \lambda \int_0^t e^{-\lambda s}(M - M_\lambda)(t - s, \xi, x - a(\xi)s)ds. \tag{6.44}$$

We end up with

$$\|(f - f_\lambda)(T)\|_{V_1} \leq \|(f - f_\lambda)(0)\|_{V_1} e^{-\lambda T} + (1 - e^{-\lambda T})\|M(T) - M_\lambda(T)\|_{V_1}. \tag{6.45}$$

Since

$$\|M(T) - M_\lambda(T)\|_{V_1} = \|\chi_u(\xi) - \chi_{u_\lambda}(\xi)\|_{V_1} = \|u(T) - u_\lambda(T)\|_{L^1(\mathbb{R}_x)},$$

we can still use the convergence rates expressed above to upper bound

$$\|f(T) - f_\lambda(T)\|_{V_1} \leq \frac{\|f_0 - f_{\lambda,0}\|_{V_1}}{\lambda T} + C(d)\|a\|_{L^\infty(-K,K)}\sqrt{\frac{T\|u_0\|_{BV(\mathbb{R}^d)}}{\lambda}},$$

in the case $u_0 \in L^\infty \cap L^1 \cap BV(\mathbb{R}^d)$ and

$$\|f(T) - f_\lambda(T)\|_{V_1} \leq \frac{\|f_0 - f_{\lambda,0}\|_{V_1}}{\lambda T} + \omega(T, \frac{1}{\lambda})$$

otherwise. This concludes the proof. □

Unknown data

Let us assume that we have a state $M(t, x, \xi)$ that does not come from a kinetic formulation of (6.30). In practice, this means that we do not conjecture anything about the origin of the data, except maybe on its regularity. We are then interested in finding the closest admissible state $f(t, x, \xi)$ for the scalar law (6.30). The following theorem provides an upper bound, under a condition of regularity on the data, of the L^1 or L^2 norm of the discrepancy between the observer f and the data M. Moreover, as λ tends to infinity, the bound tends to zero. We begin with the following lemma

Lemma 6.3.6. *Let p=1, 2. Let $M(t, x, \xi) \in C([0, T], V_p)$ and $f(t, x, \xi) \in C([0, T], V_p)$ be the solution of*

$$\begin{cases} \dfrac{\partial}{\partial t} f(t, x, \xi) + a(\xi) \cdot \nabla_x f(t, x, \xi) + \lambda f(t, x, \xi) = \lambda M(t, x, \xi), \\ f(t = 0, x, \xi) = f_0(x, \xi), \end{cases} \tag{6.46}$$

with f_0 and M_0 in L^p. Let us assume that $\dfrac{\partial M}{\partial t} + a(\xi)\cdot\nabla_x M = Q \in C([0,T],V_p)$. *Then,*

$$\|f(T)-M(T)\|_{V_p} \le \|f_0-M_0\|_{V_p} e^{-\lambda T} + \frac{1-e^{-\lambda T}}{\lambda}\sup_{0\le t\le T}\|Q(t)\|_{V_p}$$

Remark 6.3.7. *This theorem is interpreted as follows: first of all, the error in the initial condition is forgotten with time. This is normal in the case of hyperbolic laws as those equations are irreversible. Second of all, the impact of the collision term is reduced as λ gets bigger. It acts like a filter and this raises the idea that is it theoretically possible to recover any situation, whatever big the discontinuities could be, by applying a great nudging coefficient. Of course, as we will see later, this is numerically intractable as λ has a negative effect on the time step.*

Proof of Lemma 6.3.6. First of all we recall the lemma

Lemma 6.3.8. *Let u be a C^1 function with values in $\mathbb{R}$ satisfying the differential inequality*

$$u'(t) \le a(t)u(t) + b(t), \quad \forall t \in [0,T]\,. \tag{6.47}$$

Then

$$u(t) \le u(0)e^{\int_0^t a(s)ds} + \int_0^t b(\tau)e^{\int_\tau^t a(s)ds}d\tau, \quad \forall t\in[0,T]\,. \tag{6.48}$$

Proof of Lemma 6.3.8. Indeed, multiplying (6.47) by $e^{\int_0^t -a(s)ds}$, we find

$$\frac{d}{dt}\left(u(t)e^{\int_0^t -a(s)ds}\right) \le b(t)e^{\int_0^t -a(s)ds}.$$

An integration between 0 and t leads to the result. □

From (6.46) we write:

$$\frac{\partial}{\partial t}\left(f(t,x,\xi)-M(t,x,\xi)\right) + a(\xi)\cdot\nabla_x\left(f(t,x,\xi)-M(t,x,\xi)\right) + \lambda\left(f(t,x,\xi)-M(t,x,\xi)\right) = -Q(t,x,\xi). \tag{6.49}$$

Multiplying by $(f-M)^{p-1}\operatorname{sgn}((f-M)^p)$,

$$\frac{1}{p}\frac{\partial}{\partial t}|f(t,x,\xi)-M(t,x,\xi)|^p + \frac{1}{p}a(\xi)\cdot\nabla_x|f(t,x,\xi)-M(t,x,\xi)|^p + \lambda|f(t,x,\xi)-M(t,x,\xi)|^p \le |Q||f(t,x,\xi)-M(t,x,\xi)|^{p-1}. \tag{6.50}$$

Integrating in the space and velocity variable,

$$\frac{1}{p}\frac{d}{dt}\|f(t,x,\xi)-M(t,x,\xi)\|_{V_p}^p+\lambda\|f(t,x,\xi)-M(t,x,\xi)\|_{V_p}^p \\ \leq \int_{\mathbb{R}_x}\int_{\mathbb{R}_\xi}|Q||f(t,x,\xi)-M(t,x,\xi)|^{p-1}d\xi dx. \quad (6.51)$$

Since $|Q|\in L^p([0,T],\mathbb{R}_x^d\times\mathbb{R}_\xi)$ and $|f(t,x,\xi)-M(t,x,\xi)|^{p-1}\in L^{\frac{p}{p-1}}$, with p and $\frac{p}{p-1}$ being conjugate exponents, we can use Hölder's inequality to get

$$\begin{aligned}\int_{\mathbb{R}_x}\int_{\mathbb{R}_\xi}|Q||f-M|^{p-1}d\xi dx &\leq \|Q\|_{V_p}\|(f-M)^{p-1}\|_{L^{p/p-1}(\mathbb{R}_x^d\times\mathbb{R}_\xi)}\\ &\leq \|Q\|_{V_p}\|f-M\|_{L^p(\mathbb{R}_x^d\times\mathbb{R}_\xi)}^{p-1}.\end{aligned} \quad (6.52)$$

Simplifying by $\|f-M\|_{L^p(\mathbb{R}_x^d\times\mathbb{R}_\xi)}^{p-1}$ we obtain

$$\frac{d}{dt}\|f(t,x,\xi)-M(t,x,\xi)\|_{V_p}+\lambda\|f(t,x,\xi)-M(t,x,\xi)\|_{V_p}\leq\|Q(t)\|_{V_p}. \quad (6.53)$$

This last inequality can be integrated between 0 and $T>0$ thanks to Lemma 6.3.8 and yields

$$\|f(T)-M(T)\|_{V_p}\leq\|f_0-M_0\|_{V_p}e^{-\lambda T}+\frac{1-e^{-\lambda T}}{\lambda}\sup_{0\leq t\leq T}\|Q(t)\|_{V_p}. \quad (6.54)$$

This completes the proof. □

In a second step, we want to relax the hypothesis on the data M in order to exploit fully the fact that important discontinuities can appear and the observer still converges (see Remark 6.3.7). For that purpose, we use space and time regularization techniques.

Theorem 6.3.9. *Let p=1,2. Let $M(t,x,\xi)\in C([0,T],V_p)$ and $f(t,x,\xi)\in C([0,T],V_p)$ be the solution of*

$$\begin{cases}\dfrac{\partial}{\partial t}f(t,x,\xi)+a(\xi)\cdot\nabla_x f(t,x,\xi)+\lambda f(t,x,\xi)=\lambda M(t,x,\xi),\\ f(t,x,\xi=0)=f_0(x,\xi).\end{cases} \quad (6.55)$$

Then,

$$\|f(T)-M(T)\|_{V_p}\underset{\lambda\to+\infty}{\longrightarrow}0.$$

Proof of Theorem 6.3.9. The key idea is to regularize the equations by convolution and apply the previous theorem to the smooth problem . Let ω be a regularizing kernel (see Definition A.1.1) and $\tilde{\omega}$ an asymmetric regularizing kernel (see Defintion A.2.1). From those kernels, we build two sequences of mollifiers (Defintion A.1.2) of compact support ϵ, in space for the first one and in time for the second one: $\omega_\epsilon(x)$ and $\tilde{\omega_\epsilon}(t)$. Recall that

asymmetry is required in time because $t > 0$ raises issues in the convolution operation. We define $M_\epsilon = M * \omega_\epsilon(x) * \tilde{\omega}_\epsilon(t)$ and $f_\epsilon = f * \omega_\epsilon(x) * \tilde{\omega}_\epsilon(t)$ where $*$ represents the convolution. Thanks to Propositions A.1.3 and A.2.2, we have f_ϵ, classical solution of

$$\begin{cases} \dfrac{\partial}{\partial t} f_\epsilon(t,x,\xi) + a(\xi)\cdot\nabla_x f_\epsilon(t,x,\xi) + \lambda f_\epsilon(t,x,\xi) = \lambda M_\epsilon(t,x,\xi), \\ f_\epsilon(t,x,\xi=0) = f_0(x,\xi) * \omega_\epsilon(x). \end{cases} \tag{6.56}$$

Then, the triangular inequality writes for all $T > 0$

$$\begin{aligned} &\|f(T) - M(T)\|_{V_p} \\ &\qquad \leq \|f(T) - f_\epsilon(T)\|_{V_p} + \|f_\epsilon(T) - M_\epsilon(T)\|_{V_p} + \|M_\epsilon(T) - M(T)\|_{V_p}. \end{aligned} \tag{6.57}$$

Invoking a classic theorem of mathematical analysis we can state for any $T > 0$

$$\begin{aligned} \|f(T) - f_\epsilon(T)\|_{V_p} &\underset{\epsilon\to 0}{\longrightarrow} 0, \\ \|M(T) - M_\epsilon(T)\|_{V_p} &\underset{\epsilon\to 0}{\longrightarrow} 0. \end{aligned} \tag{6.58}$$

A proof can be found in [35]. Let us concentrate on $\|f_\epsilon - M_\epsilon\|_{V_p}$. In order to apply the previous theorem, we need to show that the quantity $Q(t,x,\xi) = \partial_t M_\epsilon + a(\xi)\cdot\nabla_x M_\epsilon$ is bounded in V_p. Considering the compact support of $\tilde{\omega}$, a combination of Lemma A.1.4 and Jensen's inequality yields

$$\begin{aligned} \|a(\xi)\cdot\nabla_x M_\epsilon\|_{V_p} &\leq a_\infty \frac{\|M * \tilde{\omega}_\epsilon(t)\|_{V_p}}{\epsilon}, \\ &\leq a_\infty \frac{\|\int_{\mathbb{R}} M(t-s)\tilde{\omega}_\epsilon(s)ds\|_{V_p}}{\epsilon} \\ &\leq a_\infty \frac{\|\int_{-\epsilon}^{0} M(t-s)\tilde{\omega}_\epsilon^p(s)ds\|_{V_p}}{\epsilon} \\ &\leq a_\infty \frac{\left(\int_{-\epsilon}^{0} \|M(t-s)\|_{V_p}^p \tilde{\omega}_\epsilon^p(s)ds\right)^{1/p}}{\epsilon} \\ &\leq a_\infty \|\tilde{\omega}\|_{L^p(\mathbb{R})} \frac{\sup\limits_{t\leq s\leq t+\epsilon} \|M(s)\|_{V_p}}{\epsilon}. \end{aligned} \tag{6.59}$$

The same process on the second term leads to,

$$\begin{aligned} \|\partial_t M_\epsilon\|_{V_p} &= \|M * \omega_\epsilon * \partial_t\tilde{\omega}_\epsilon\|_{V_p} \\ &\leq \left(\int_{\mathbb{R}} \|M * \omega_\epsilon(t-s)\|_{V_p}^p |\partial_t\tilde{\omega}_\epsilon(s)|^p ds\right)^{1/p} \\ &\leq \sup_{t\leq s\leq t+\epsilon} \|M * \omega_\epsilon(s)\|_{V_p} \left(\int_{\mathbb{R}} |\partial_t\tilde{\omega}_\epsilon(s)|^p\right)^{1/p} \\ &\leq \sup_{t\leq s\leq t+\epsilon} \|M(s)\|_{V_p} \frac{\|\partial_t\tilde{\omega}\|_{L^p(\mathbb{R})}}{\epsilon}. \end{aligned}$$

Considering $\max \epsilon = 1$, we end up with the upper bound

$$\|\partial_t M_\epsilon(t,x,\xi) + a(\xi)\cdot\nabla_x M_\epsilon(t,x,\xi)\|_{V_p} \leq a_\infty \|\tilde{\omega}\|_{L^p(\mathbb{R})} \frac{\sup\limits_{t\leq s\leq t+1}\|M(s)\|_{V_p}}{\epsilon} + \frac{\sup\limits_{t\leq s\leq t+1}\|M(s)\|_{V_p}}{\epsilon}\|\partial_t\tilde{\omega}\|_{L^p(\mathbb{R})}. \quad (6.60)$$

Therefore we can apply Lemma 6.3.6 to f_ϵ and M_ϵ

$$\|f_\epsilon(T) - M_\epsilon(T)\|_{V_p} \leq \|f_{\epsilon,0} - M_{\epsilon,0}\|_{V_p} e^{-\lambda T} + \frac{1-e^{-\lambda T}}{\epsilon\lambda} \sup_{0\leq t\leq T+1}\|M(t)\|_{V_p}\left(a_\infty\|\tilde{\omega}\|_{L^p(\mathbb{R})} + \|\partial_t\tilde{\omega}\|_{L^p(\mathbb{R})}\right) \quad (6.61)$$

Using the property of convolution (i.e. $\forall f \in L^p(\mathbb{R}^d), \|f_\epsilon\|_{L^p} = \|f * \omega_\epsilon\|_{L^p} \leq \|f\|_{L^p}\|\omega_\epsilon\|_{L^1} = \|f\|_{L^p}$) we end up with

$$\|f_\epsilon(T) - M_\epsilon(T)\|_{V_p} \leq \|f_0 - M_0\|_{V_p} e^{-\lambda T} + \frac{1-e^{-\lambda T}}{\epsilon\lambda} \sup_{0\leq t\leq T+1}\|M(t)\|_{V_p}\left(a_\infty\|\tilde{\omega}\|_{L^p(\mathbb{R})} + \|\partial_t\tilde{\omega}\|_{L^p(\mathbb{R})}\right) \quad (6.62)$$

and

$$\|f_\epsilon(T) - M_\epsilon(T)\|_{L^1(\mathbb{R}_\xi\times\mathbb{R}_x)} \underset{\lambda\to+\infty}{\longrightarrow} 0. \quad (6.63)$$

The conclusion follows.

□

6.3.3 Noisy observations in the scalar case - linear coefficient

It is natural to consider that observations are noisy. Here we restrict our analysis to additive noise in the observer equation. Appropriate distribution spaces representing this phenomena are the dual Sobolev spaces. The noise is indeed not negligible in the strong L^2 norm because of its high oscillations, but it is smaller in a weaker $H^{-\alpha}$ norm. This modeling enables us to prove convergence theorems for velocity averaged quantities like $\rho_\psi(t,x) = \int_{\mathbb{R}_\xi} f(t,x,\xi)\psi(\xi)d\xi$ that are known to lie in a better space than the microscopic density $f(t,x,\xi)$. This property results from averaging lemmas [63, 64]. In the following, the proofs are based on the same ideas than those developed in [29, 63, 64].

Steady state

We begin with the steady state situation in the case of a linear coefficient for advection. This typically occurs in the kinetic formulation of Burgers' equation. The additive kinetic variable ξ represents then a multidimensional velocity, and we have $\xi \in \mathbb{R}^d$ (as $x \in \mathbb{R}^d$). As stated previously, the noise is an α^{th} space derivative of an L^2 function. Let us consider

the solution of

$$\xi \cdot \nabla_x f(x,\xi) + \lambda f(x,\xi) = \lambda M(x,\xi) + \lambda \frac{\partial^\alpha E}{\partial x^\alpha}, \quad E(t,x,\xi) \in V_2 \tag{6.64}$$

with

$$\xi \cdot \nabla_x M(x,\xi) = Q(x,\xi) \in V_2, \tag{6.65}$$

where α is a multi-index $(\alpha_1, \alpha_2, \dots \alpha_n)$ satisfying $|\alpha| = \alpha_1 + \alpha_2 + \ldots + \alpha_n$,

$$\frac{\partial^\alpha E}{\partial x^\alpha} = \frac{\partial^\alpha E}{\partial x_1^{\alpha_1} x_2^{\alpha_2} \dots x_n^{\alpha_n}}.$$

Remark 6.3.10. *We point out that the corruption of the data in a real situation is rather located on the macroscopic variables. It might be more realistic to translate this macroscopic noise at the kinetic level. However, this transcription is not straightforward and remains to be done. For now, we limit ourselves to the case where we introduce the noise directly on the kinetic observer equation.*

Let us denote $g(x,\xi) = f(x,\xi) - M(x,\xi)$ the error between the estimator and observations. Subtracting (6.64) and (6.65), the equation for g is

$$\xi \cdot \nabla_x g(x,\xi) + \lambda g(x,\xi) = \lambda \frac{\partial^\alpha E}{\partial x^\alpha} - Q(x,\xi), \tag{6.66}$$

with an explicit solution (Theorem 6.3.2)

$$g(x,\xi) = -\frac{1}{\lambda} \int_0^{+\infty} \left(Q(x - \frac{\xi}{\lambda} s, \xi) + \lambda \frac{\partial^\alpha E}{\partial x^\alpha}(x - \frac{\xi}{\lambda} s, \xi) \right) e^{-s} ds, \tag{6.67}$$

leading to the upper bound of the error in the L^2 norm

$$\|g\|_{V_2} \leq \frac{\|Q\|_{V_2}}{\lambda} + \|\partial^\alpha E\|_{V_2}. \tag{6.68}$$

As already mentioned in Remark 6.3.7, the nudging coefficient tends to filter the collision term. Nevertheless, it has no effect on the noise. It is then to be expected that in a usual norm as L^2, we do not get rid of noisy terms. But it is also worth noticing, that this noise is not amplified. This will be all the more important in the evolutionary case in the next section, as noise usually tends to increase with time.

By means of Fourier transform analysis, we try to obtain a better upper bound in a stronger norm for g, but considering a weaker norm for the noise. Let us denote by $\widehat{g}(k,\xi)$ the space Fourier transform of g

$$\widehat{g}(k,\xi) = \int_{\mathbb{R}^N} g(x,\xi) e^{ik\cdot x} dx. \tag{6.69}$$

$\widehat{E}$ and $\widehat{Q}$ are defined in the same manner. Moreover, we will work on the averaged quantity

$$\rho_\psi(t,x) = \int_{\mathbb{R}_\xi} g(t,x,\xi)\psi(\xi)d\xi, \tag{6.70}$$

where ψ is a smooth compactly supported function. We notice that

$$\widehat{\rho}_\psi(t,k) = \int_{\mathbb{R}_\xi} \widehat{g}(t,k,\xi)\psi(\xi)d\xi. \tag{6.71}$$

We claim that the averaged quantity ρ_ψ lies in a better space than $L^2([0,T], L^2(\mathbb{R}_x))$, and its homogeneous seminorm tends to zero when $\|E\|_{V_2}$ becomes smaller. This result is obtained by an asymptotic analysis in $\|E\|_{V_2}$. In the following theorem, $\|\rho\|_{\dot{H}^s(\mathbb{R}^d_k)}$ represents the homogeneous Sobolev norm of ρ.

Theorem 6.3.11. *Let $M(x,\xi) \in V_2$ be solution of (6.65) and $f(x,\xi) \in V_2$ be solution of the noisy data assimilation problem (6.64) for $|\alpha| < \frac{1}{2}$. Then, there exists γ, $0 < \gamma \leq 1 - 2|\alpha|$ and a constant K such that*

$$\|\widehat{\rho}_\psi\|^2_{\dot{H}^{\gamma/2}(\mathbb{R}_x)} \leq K\|\partial^\alpha E\|^2_{V_2}\left(\frac{\|E\|_{V_2}}{\|\partial^\alpha E\|^2_{V_2}}\right)^{\frac{\gamma}{1-|\alpha|}} + \mathrm{o}\left(\|E\|_{V_2}^{\frac{2+\gamma}{1-|\alpha|}}\right), \tag{6.72}$$

and therefore tends to 0 as $\|E\|_{V_2}$ tends to zero. This inequality is obtained for an optimal value of λ,

$$\lambda_{opt} = K\|Q\|_{V_2}\left(\frac{\|\partial^\alpha E\|^{2\alpha}_{V_2}}{\|E\|_{V_2}}\right)^{\frac{1}{1-\alpha}}, \tag{6.73}$$

where K is a constant.

Remark 6.3.12. *Let us focus here on the interest of this theorem. First of all, noisy observations represents a more realistic situation. Second of all, we have found a norm for the error that tends to zero even if the L^2 norm of the noise does not. We think here of a noise of type*

$$E(x) = \epsilon\cos(\frac{x}{\epsilon}), \quad \partial_\alpha E(x) = \epsilon^{1-\alpha}cos(\frac{x}{\epsilon} + \alpha\frac{\pi}{2}).$$

In this example, $\partial_\alpha E(x)$ may be big in L^2 norm, even if E is not. And eventually, we are capable of giving an expression of a bounded optimal λ. With the noise here, the theoretical results of Section 6.3.2 are no longer valid (λ cannot be taken as big as we want) and we need to carefully choose the nudging coefficient in order not to amplify the noise. See Section 6.3.7 for the numerical representation of this theorem on Burgers' equation.

Proof of Theorem 6.3.11. Performing a space Fourier transform on (6.66) yields

$$\xi \cdot ik\widehat{g} + \lambda\widehat{g} = -\widehat{Q} + \lambda k^\alpha \widehat{E}. \tag{6.74}$$

Then we can deduce an expression of the space Fourier transform of g:

$$\widehat{g} = \frac{-\widehat{Q}}{\lambda + i\xi \cdot k} + \lambda k^{\alpha} \frac{\widehat{E}}{\lambda + i\xi \cdot k}. \tag{6.75}$$

Young's inequality yields

$$|\widehat{\rho}_{\psi}(t,k)|^2 \leq 2 \left| \int_{\mathbb{R}_{\xi}} \frac{-\widehat{Q}(k,\xi)\psi(\xi)}{\lambda + i\xi \cdot k} d\xi \right|^2 + 2\lambda^2 |k|^{2|\alpha|} \left| \int_{\mathbb{R}_{\xi}} \frac{-\widehat{E}(k,\xi)\psi(\xi)}{\lambda + i\xi \cdot k} d\xi \right|^2. \tag{6.76}$$

Applying Cauchy-Schwarz inequality leads to

$$\begin{aligned} |\widehat{\rho}_{\psi}(t,k)|^2 &\leq \frac{2}{\lambda^2} \left| \int_{\mathbb{R}_{\xi}} \widehat{Q}^2(k,\xi) d\xi \right| \left| \int_{\mathbb{R}_{\xi}} \frac{\psi(\xi)^2}{1 + \frac{(\xi \cdot k)^2}{\lambda^2}} d\xi \right| + 2|k|^{2|\alpha|} \left| \int_{\mathbb{R}_{\xi}} \widehat{E}^2(k,\xi) d\xi \right| \left| \int_{\mathbb{R}_{\xi}} \frac{\psi(\xi)^2}{1 + \frac{(\xi \cdot k)^2}{\lambda^2}} d\xi \right| \\ &\leq 2\|\psi\|^2_{L^{\infty}(\mathbb{R}_{\xi})} C_{\psi} \frac{\lambda}{|k|} \left(\frac{1}{\lambda^2} \int_{\mathbb{R}_{\xi}} |\widehat{Q}|^2 d\xi + |k|^{2|\alpha|} \int_{\mathbb{R}_{\xi}} |\widehat{E}(k,\xi)|^2 d\xi \right). \end{aligned} \tag{6.77}$$

The last line uses the usual observation leading to averaging lemmas i.e.

$$\int_{\mathbb{R}_{\xi}} \frac{\psi(\xi)^2}{1 + \frac{(\xi \cdot k)^2}{\lambda^2}} d\xi \leq \|\psi\|^2_{L^{\infty}} C_{\psi} \frac{\lambda}{|k|}, \tag{6.78}$$

where C_{ψ} is constant related to the support of ψ. To prove it, we choose an orthonormal basis for the ξ space, with first vector $\xi_1 = \frac{k}{|k|}$. The integration in the orthogonal directions of ξ_1 yields the constant C_{ψ}. In the direction of k, the inequality reduces to the computation of

$$\int_{-\infty}^{\infty} \frac{1}{1 + (\xi_1 \frac{k}{|k|} \cdot \frac{k}{\lambda})^2} d\xi_1 = \int_{-\infty}^{\infty} \frac{1}{1 + \xi_1^2 \frac{|k|^2}{\lambda^2}} d\xi_1 = \frac{\lambda}{|k|} \int_{-\infty}^{\infty} \frac{1}{1 + \eta^2} d\eta = \pi \frac{\lambda}{|k|}. \tag{6.79}$$

Now let us choose γ such that $0 < \gamma < 1 - 2|\alpha|$. Then, for any $k_0 \in \mathbb{R}_+^*$ the upper bound of $|\rho_{\psi}|^2$ in (6.77) is clearly integrable over the domain $\mathcal{D}_{k_0} = \{k \in \mathbb{R}_k, s.t.\ |k| > k_0\}$ and its integration results in

$$\int_{\mathcal{D}_{k_0}} |k|^{\gamma} \left| \widehat{\rho}_{\psi}(t,k) \right|^2 dk \leq J(\lambda, k_0) \tag{6.80}$$

where

$$J(\lambda, k_0) = 2C_{\psi} \|\psi\|^2_{L^{\infty}(\mathbb{R}_{\xi})} \left(\|Q\|^2_{V_2} \frac{1}{\lambda} \frac{1}{k_0^{1-\gamma}} + \|E\|^2_{V_2} \lambda \frac{1}{k_0^{1-2|\alpha|-\gamma}} \right). \tag{6.81}$$

The optimization of this function with respect to λ leads to

$$\lambda_{opt}(k_0) = \frac{\|Q\|_{V_2}}{\|E\|_{V_2}} \frac{1}{k_0^{|\alpha|}}, \tag{6.82}$$

and

$$J(\lambda_{opt}(k_0), k_0) = \quad 4C_\psi \|\psi\|^2_{L^\infty(\mathbb{R}_\xi)} \left(\|Q\|_{V_2} \|E\|_{V_2} \frac{1}{k_0^{1-|\alpha|-\gamma}} \right). \tag{6.83}$$

Combining (6.83) with the L^2 upper bound (6.68),

$$\begin{aligned} \|\widehat{\rho}_\psi\|^2_{\dot{H}^{\gamma/2}(\mathbb{R}^d_k)} \leq & \quad 4C_\psi \|\psi\|^2_{L^\infty(\mathbb{R}_\xi)} \|Q\|_{V_2} \|E\|_{V_2} \frac{1}{k_0^{1-|\alpha|-\gamma}} \\ & \qquad + k_0^\gamma \left(2\frac{\|Q\|^2_{V_2}}{\lambda^2} + 2\|\partial^\alpha E\|^2_{V_2} \right) \\ \leq & \quad 4C_\psi \|\psi\|^2_{L^\infty(\mathbb{R}_\xi)} \|Q\|_{V_2} \|E\|_{V_2} \frac{1}{k_0^{1-|\alpha|-\gamma}} \\ & \qquad + 2k_0^\gamma \left(k_0^{2|\alpha|} \|E\|^2_{V_2} + \|\partial^\alpha E\|^2_{V_2} \right). \end{aligned} \tag{6.84}$$

The previous bound clearly admits a minimum in k_0 since $J(\lambda_{opt}, \cdot)$ is contintuous on $]0, +\infty[$ and

$$J(\lambda_{opt}(k_0), k_0) \underset{k_0 \to 0}{\longrightarrow} +\infty, \quad J(\lambda_{opt}(k_0), k_0) \underset{k_0 \to +\infty}{\longrightarrow} +\infty.$$

The estimation of this minimum and its argument is done by asymptotic analysis, considering that $\|E\|_{V_2}$ is small. Let us denote

$$K_1 = 2, \quad K_2 = 4C_\psi \|\psi\|^2_{L^\infty(\mathbb{R}_\xi)} \|Q\|_{V_2},$$

and

$$\begin{aligned} J(\lambda_{opt}(k_0), k_0) &= K_1 k_0^\gamma \|\partial^\alpha E\|^2_{V_2} + K_2 \|E\|_{V_2} \frac{1}{k_0^{1-|\alpha|-\gamma}} + \mathrm{o}\left(\|E\|^2_{V_2}\right) \\ &= J_2(k_0) + \mathrm{o}\left(\|E\|^2_{V_2}\right). \end{aligned} \tag{6.85}$$

The optimisation of J_2 with respect to k_0 leads to

$$\underset{k_0}{\operatorname{argmin}} J_2 = \left(\frac{K_2 (1-\alpha-\gamma)}{K_1 \gamma} \frac{\|E\|_{V_2}}{\|\partial^\alpha E\|^2_{V_2}} \right)^{\frac{1}{1-\alpha}} = K_3 \left(\frac{\|E\|_{V_2}}{\|\partial^\alpha E\|^2_{V_2}} \right)^{\frac{1}{1-\alpha}}, \tag{6.86}$$

and

$$\min J_2 = \left(K_1 K_3^\gamma + K_2 K_3^{|\alpha|+\gamma-1} \right) \|\partial^\alpha E\|^2_{V_2} \left(\frac{\|E\|_{V_2}}{\|\partial^\alpha E\|^2_{V_2}} \right)^{\frac{\gamma}{1-|\alpha|}}. \tag{6.87}$$

Moreover, taking into account the optimal value of k_0, the optimal λ is

$$\lambda_{opt} = \frac{1}{K_3} \frac{\|Q\|_{V_2} \|\partial^\alpha E\|^{\frac{2\alpha}{1-\alpha}}_{V_2}}{\|E\|^{\frac{1}{1-\alpha}}_{V_2}}. \tag{6.88}$$

□

Evolution case

The same study is extended to the evolution case. It uses the Fourier transform in x, ξ but not in t (see [29]). Therefore, it suits better functions defined on $[0,T]\times\mathbb{R}^d_x\times\mathbb{R}_\xi$.

We consider f the solution of

$$\partial_t f(t,x,\xi)+\xi\cdot\nabla_x f(t,x,\xi)+\lambda f(t,x,\xi)=\lambda M(t,x,\xi)+\lambda\frac{\partial^\alpha E}{\partial x^\alpha}, \tag{6.89}$$

with

$$\partial_t M(t,x,\xi)+\xi\cdot\nabla_x M(t,x,\xi)=Q(x,\xi,t)\in C([0,T],V_2). \tag{6.90}$$

Subtracting (6.89) and (6.90) and denoting $g=f-M$, we obtain

$$\partial_t g+\xi\cdot\nabla_x g+\lambda g=\lambda\frac{\partial^\alpha E}{\partial x^\alpha}-Q. \tag{6.91}$$

First of all, let us recall that in the case when the noise should be bounded in L^2, then, thanks to theorem 6.3.6, we have

$$\begin{aligned}\|g(t,x,\xi)\|_{V_2}\leq{}&\|g_0\|_{V_2}e^{-\lambda t}\\&+(1-e^{-\lambda t})\left(\frac{\|Q(t,x,\xi)\|_{V_2}}{\lambda}+\|\partial_\alpha E\|_{V_2}\right).\end{aligned} \tag{6.92}$$

Therefore, thanks to Young's inequality we obtain

$$\begin{aligned}\|g(t,x,\xi)\|^2_{V_2}\leq{}&3\|g_0\|^2_{V_2}e^{-2\lambda t}\\&+3(1-e^{-\lambda t})^2\left(\frac{\|Q(t,x,\xi)\|^2_{V_2}}{\lambda^2}+\|\partial_\alpha E\|^2_{V_2}\right).\end{aligned} \tag{6.93}$$

And eventually

$$\begin{aligned}\int_0^T\|g(t,x,\xi)\|^2_{V_2}dt\leq{}&\frac{3\|g_0\|^2_{V_2}}{2\lambda}\\&+3\left(\frac{\|Q(t,x,\xi)\|^2_{L^2([0,T],V_2)}}{\lambda^2}+\|\partial_\alpha E\|^2_{L^2([0,T],V_2)}\right).\end{aligned} \tag{6.94}$$

This last inequality tells us that we cannot approach the exact solution closer than the magnitude of the noise. Following Section 6.3.3 we denote $\widehat{g}(t,k,\xi)$ the space Fourier transform of g

$$\widehat{g}(t,k,\xi)=\int_{\mathbb{R}^N}g(t,x,\xi)e^{ik\cdot x}dx, \tag{6.95}$$

$\widehat{E}$ and $\widehat{Q}$ and $\widehat{\rho}_\psi$ are defined in the same manner. We now formulate the following theorem which proof is available in Section B.1.

Theorem 6.3.13. *Let $M(t,x,\xi)\in C([0,T],V_2)$ satisfy (6.90) and $f(t,x,\xi)\in C([0,T],V_2)$*

satisfy the noisy data assimilation problem (6.89)*. Then, there exists* β, $0 < \beta < 1$, *and* γ, $0 < \gamma < \beta - 2|\alpha|$ *such that*

$$\|\widehat{\rho}_\psi\|^2_{L^2([0,T],\dot{H}^{\gamma/2})} \leq K_1 \|\partial_\alpha E\|^{2(1-\gamma)}_{L^2([0,T],V_2)} \|g_0\|^{2\gamma}_{V_2} + \mathrm{o}\left(\|E\|_{L^2([0,T],V_2)}\right), \tag{6.96}$$

which is obtained for an optimal λ

$$\lambda_{opt} = K_2 \frac{\|Q\|_{L^2([0,T],V_2)}}{\|g_0\|^{2\alpha}_{V_2}} \frac{\|\partial_\alpha E\|^{2\alpha}_{L^2([0,T],V_2)}}{\|E\|_{L^2([0,T],V_2)}}. \tag{6.97}$$

where K_1 *and* K_2 *are constants.*

6.3.4 Noise stability in the scalar case - nonlinear coefficient

Let us now consider a nonlinear coefficient $a \in L^\infty_{loc}(\mathbb{R}_\xi, \mathbb{R}^d)$, $\xi \in \mathbb{R}$, which corresponds to the kinetic formulation of a general scalar conservation law of the form (6.19) with $p = 1$. In this situation, a non-degeneracy assumption is required to recover the regularity of averages in ξ. More precisely, for any direction $\sigma \in \mathbb{R}^{d-1}$, $a(\xi) \cdot \sigma$ has to be non constant to enable the averaging procedure to give regularity in x in the direction σ.

Steady state

We begin with the steady state situation. As stated previously, the noise is an α^{th} space derivative of an L^2 function. We consider the solution of

$$a(\xi) \cdot \nabla_x f(x,\xi) + \lambda f(x,\xi) = \lambda M(x,\xi) + \lambda \frac{\partial^\alpha E}{\partial x^\alpha}, \tag{6.98}$$

with

$$a(\xi) \cdot \nabla_x M(x,\xi) = Q(x,\xi) \in L^2(\mathbb{R}^N_x \times \mathbb{R}_\xi), \tag{6.99}$$

where a is a non-degenerate flux. Let us denote $g(x,\xi) = f(x,\xi) - M(x,\xi)$ the error between the estimator and observations. Subtracting (6.98) and (6.99), the equation for g is

$$a(\xi) \cdot \nabla_x g(x,\xi) + \lambda g(x,\xi) = \lambda \frac{\partial^\alpha E}{\partial x^\alpha} - Q(x,\xi), \tag{6.100}$$

with an explicit solution (Theorem 6.3.2)

$$g(x,\xi) = -\frac{1}{\lambda} \int_0^{+\infty} \left(Q(x - \frac{a(\xi)}{\lambda} s, \xi) + \lambda \frac{\partial^\alpha E}{\partial x^\alpha}(x - \frac{a(\xi)}{\lambda} s, \xi) \right) e^{-s} ds, \tag{6.101}$$

leading to the upper bound of the error in the L^2 norm

$$\|g\|_{V_2} \leq \frac{\|Q\|_{V_2}}{\lambda} + \|\partial^\alpha E\|_{V_2}. \tag{6.102}$$

Let us denote by $\widehat{g}(k,\xi)$, $\widehat{E}$, $\widehat{Q}$ and $\widehat{\rho}_\psi$ the space Fourier transforms of g, E, Q and ρ_ψ.

Theorem 6.3.14. *Let $M(x,\xi) \in V_2$ be solution of (6.99) and $f(x,\xi) \in V_2$ be solution of the noisy data assimilation problem (6.98). Then, there exists β, $0 < \beta < 1$, γ, $0 < \gamma < \beta - 2|\alpha|$ and a constant K such that*

$$\|\dot{\hat{\rho}}_\psi\|^2_{H^{\gamma/2}(\mathbb{R}_x)} \leq K_1 \|\partial^\alpha E\|^2_{V_2} \left(\frac{\|E\|^{2-\beta}_{V_2}}{\|\partial^\alpha E\|^2_{V_2}} \right)^{\frac{\gamma}{(|\alpha|+1)\beta - 2|\alpha|}} + \mathrm{o}\left(\|\widehat{E}\|_{V_2}^{\frac{(2-\beta)\gamma}{(|\alpha|+1)\beta-2|\alpha|}} \right), \tag{6.103}$$

which is obtained for an optimal λ

$$\lambda_{opt} = K_2 \|Q\|_{V_2} \left(\frac{\|\partial^\alpha E\|^{2\alpha}_{V_2}}{\|E\|^{\beta}_{V_2}} \right)^{\frac{1}{(\alpha+1)\beta - 2\alpha}}, \tag{6.104}$$

where K_1 and K_2 are constants.

Proof of Theorem 6.3.14. Performing a space Fourier transform on (6.100) yields

$$a(\xi) \cdot ik\widehat{g} + \lambda \widehat{g} = -\widehat{Q} + \lambda k^\alpha \widehat{E}. \tag{6.105}$$

Then we can deduce an expression of the space Fourier transform of g:

$$\widehat{g} = \frac{-\widehat{Q}}{\lambda + ia(\xi)\cdot k} + \lambda k^\alpha \frac{\widehat{E}}{\lambda + ia(\xi)\cdot k}. \tag{6.106}$$

Young's inequality yields

$$|\widehat{\rho}_\psi(t,k)|^2 \leq 2 \left| \int_{\mathbb{R}_\xi} \frac{-\widehat{Q}(k,\xi)\psi(\xi)}{\lambda + ia(\xi)\cdot k} d\xi \right|^2 + 2\lambda^2 k^{2\alpha} \left| \int_{\mathbb{R}_\xi} \frac{-\widehat{E}(k,\xi)\psi(\xi)}{\lambda + ia(\xi)\cdot k} d\xi \right|^2. \tag{6.107}$$

Applying Cauchy-Schwarz inequality leads to

$$\begin{aligned}
|\widehat{\rho}_\psi(t,k)|^2 \leq \quad & 2 \left| \int_{\mathbb{R}_\xi} \widehat{Q}^2(k,\xi) d\xi \right| \left| \int_{\mathbb{R}_\xi} \frac{\psi(\xi)^2}{\lambda^2 + (a(\xi)\cdot k)^2} d\xi \right| \\
& + 2\lambda^2 k^{2\alpha} \left| \int_{\mathbb{R}_\xi} \widehat{E}^2(k,\xi) d\xi \right| \left| \int_{\mathbb{R}_\xi} \frac{\psi(\xi)^2}{\lambda^2 + (a(\xi)\cdot k)^2} d\xi \right| \\
|\widehat{\rho}_\psi(t,k)|^2 \leq \quad & \frac{2}{\lambda^2} \left| \int_{\mathbb{R}_\xi} \widehat{Q}^2(k,\xi) d\xi \right| \left| \int_{\mathbb{R}_\xi} \frac{\psi(\xi)^2}{1 + \frac{(a(\xi)\cdot k)^2}{\lambda^2}} d\xi \right| \\
& + 2k^{2\alpha} \left| \int_{\mathbb{R}_\xi} \widehat{E}^2(k,\xi) d\xi \right| \left| \int_{\mathbb{R}_\xi} \frac{\psi(\xi)^2}{1 + \frac{(a(\xi)\cdot k)^2}{\lambda^2}} d\xi \right|.
\end{aligned} \tag{6.108}$$

Under non-degeneracy condition for the flux $a(\xi)$, we can state that there exists β, $0 < \beta \leq$

1, such that

$$|\widehat{\rho}_\psi(t,k)|^2 \leq \frac{2}{\lambda^2}\|\psi\|^2_{L^\infty(\mathbb{R}_\xi)}\int_{\mathbb{R}_\xi}|\widehat{Q}|^2 d\xi\left(\frac{\lambda}{|k|}\right)^\beta + 2\|\psi\|^2_{L^\infty(\mathbb{R}_\xi)}k^{2\alpha}\int_{\mathbb{R}_\xi}|\widehat{E}(k,\xi)|^2 d\xi\left(\frac{\lambda}{|k|}\right)^\beta$$
$$\leq 2\|\psi\|^2_{L^\infty(\mathbb{R}_\xi)}\left(\frac{1}{\lambda^{2-\beta}}\frac{1}{|k|^\beta}\int_{\mathbb{R}_\xi}|\widehat{Q}|^2 d\xi + \lambda^\beta\frac{1}{|k|^{\beta-2|\alpha|}}\int_{\mathbb{R}_\xi}|\widehat{E}(k,\xi)|^2 d\xi\right). \tag{6.109}$$

Now let us choose γ such that $\gamma < \beta - 2|\alpha|$. Then, the upper bound of $|\rho_\psi|^2$ is clearly integrable over the domain $\mathcal{D}_{k_0} = \{k \in \mathbb{R}_k, s.t.\ |k| > k_0\}$ for any $k_0 > 0$ and its integration results in

$$\int_{\mathcal{D}_{k_0}} |k|^\gamma |\rho_\psi|^2 dk \leq J(\lambda, k_0), \tag{6.110}$$

where

$$J(\lambda,k_0) = 2\|\psi\|^2_{L^\infty(\mathbb{R}_\xi)}\left(\|Q\|^2_{V_2}\frac{1}{\lambda^{2-\beta}}\frac{1}{k_0^{\beta-\gamma}} + \|E\|^2_{V_2}\lambda^\beta\frac{1}{k_0^{\beta-2|\alpha|-\gamma}}\right) \tag{6.111}$$

The optimization of this function with respect to λ leads to

$$\lambda_{opt}(k_0) = \sqrt{\frac{2-\beta}{\beta}}\frac{\|Q\|_{V_2}}{\|E\|_{V_2}}\frac{1}{k_0^{|\alpha|}}, \tag{6.112}$$

and

$$\begin{aligned} J(\lambda_{opt}(k_0),k_0) = \; & 2\|\psi\|^2_{L^\infty(\mathbb{R}_\xi)}\left(\|Q\|^2_{V_2}\frac{1}{k_0^{\beta-\gamma}}\left(\sqrt{\frac{\beta}{2-\beta}}\frac{k_0^{|\alpha|}\|E\|_{V_2}}{\|Q\|_{V_2}}\right)^{2-\beta}\right. \\ & \left. + \|E\|^2_{V_2}\frac{1}{k_0^{\beta-2|\alpha|-\gamma}}\left(\sqrt{\frac{2-\beta}{\beta}}\frac{\|Q\|_{V_2}}{k_0^{|\alpha|}\|E\|_{V_2}}\right)^\beta\right) \\ = \; & 2\|\psi\|^2_{L^\infty(\mathbb{R}_\xi)}\|Q\|^\beta_{V_2}\|E\|^{2-\beta}_{V_2}\frac{1}{k_0^{\beta(|\alpha|+1)-2|\alpha|-\gamma}}\left(\frac{2}{2-\beta}\left(\frac{2-\beta}{\beta}\right)^{\beta/2}\right). \end{aligned} \tag{6.113}$$

Combining (6.113) with the L^2 upper bound (6.102),

$$\begin{aligned} \|\dot{\hat{\rho}}_\psi\|^2_{H^{\gamma/2}(\mathbb{R}^d_k)} \leq \; & 2\|\psi\|^2_{L^\infty(\mathbb{R}_\xi)}\|Q\|^\beta_{V_2}\|E\|^{2-\beta}_{V_2}\frac{1}{k_0^{\beta(|\alpha|+1)-2|\alpha|-\gamma}}\left(\frac{2}{2-\beta}\left(\frac{2-\beta}{\beta}\right)^{\beta/2}\right) \\ & + k_0^\gamma\left(3\frac{\|Q\|^2_{V_2}}{\lambda^2} + 3\|\partial^\alpha E\|^2_{V_2}\right) \\ \leq \; & 2\|\psi\|^2_{L^\infty(\mathbb{R}_\xi)}\|Q\|^\beta_{V_2}\|E\|^{2-\beta}_{V_2}\frac{1}{k_0^{\beta(|\alpha|+1)-2|\alpha|-\gamma}}\left(\frac{2}{2-\beta}\left(\frac{2-\beta}{\beta}\right)^{\beta/2}\right) \\ & + k_0^\gamma\left(3\frac{\beta}{2-\beta}k_0^{2|\alpha|}\|E\|^2_{V_2} + 3\|\partial^\alpha E\|^2_{V_2}\right). \end{aligned} \tag{6.114}$$

The previous bound clearly admits a minimum since $J(\lambda_{opt}(\cdot),\cdot)$ is contintuous on $]0,+\infty[$ and

$$J(\lambda_{opt}(k_0),k_0) \underset{k_0\to 0}{\longrightarrow} +\infty, \quad J(\lambda_{opt}(k_0),k_0) \underset{k_0\to+\infty}{\longrightarrow} +\infty.$$

The estimation of this minimum and its argument is done by asymptotic analysis, considering that $\|E\|_{V_2}$ is small. Let us denote

$$K_1 = 3, \quad K_2 = 2\|\psi\|^2_{L^\infty(\mathbb{R}_\xi)}\|Q\|^\beta_{V_2}\left(\frac{2}{2-\beta}\left(\frac{2-\beta}{\beta}\right)^{\beta/2}\right),$$

and

$$\begin{aligned} J(\lambda_{opt}(k_0),k_0) &= K_1 k_0^\gamma \|\partial^\alpha E\|^2_{V_2} + K_2\|E\|^{2-\beta}_{V_2}\frac{1}{k_0^{\beta(|\alpha|+1)-2|\alpha|-\gamma}} + \mathrm{o}\left(\|E\|^2_{V_2}\right) \\ &= J_2(k_0) + \mathrm{o}\left(\|E\|^2_{V_2}\right). \end{aligned} \tag{6.115}$$

The optimisation of J_2 with respect to k_0 leads to

$$\begin{aligned} \underset{k_0}{\operatorname{argmin}} J_2 &= \left(\frac{K_2\left((|\alpha|+1)\beta-2|\alpha|-\gamma\right)}{K_1\gamma}\frac{\|E\|^{2-\beta}_{V_2}}{\|\partial^\alpha E\|^2_{V_2}}\right)^{\frac{1}{(|\alpha|+1)\beta-2|\alpha|}} \\ &= K_3\left(\frac{\|E\|^{2-\beta}_{V_2}}{\|\partial^\alpha E\|^2_{V_2}}\right)^{\frac{1}{(|\alpha|+1)\beta-2|\alpha|}}, \end{aligned} \tag{6.116}$$

and

$$\begin{aligned} \min J_2 &= K_1K_3^\gamma\|\partial^\alpha E\|^2_{V_2}\left(\frac{\|E\|^{2-\beta}_{V_2}}{\|\partial^\alpha E\|^2_{V_2}}\right)^{\frac{\gamma}{(|\alpha|+1)\beta-2|\alpha|}} \\ &\quad + K_2K_3^{2|\alpha|+\gamma-\beta(|\alpha|+1)}\|E\|^{2-\beta}_{V_2}\left(\frac{\|E\|^{2-\beta}_{V_2}}{\|\partial^\alpha E\|^2_{V_2}}\right)^{\frac{2|\alpha|+\gamma-\beta(|\alpha|+1)}{(|\alpha|+1)\beta-2|\alpha|}}, \\ \min J_2 &= \left(K_1K_3^\gamma + K_2K_3^{2|\alpha|+\gamma-\beta(|\alpha|+1)}\right)\|\partial^\alpha E\|^2_{V_2}\left(\frac{\|E\|^{2-\beta}_{V_2}}{\|\partial^\alpha E\|^2_{V_2}}\right)^{\frac{\gamma}{(|\alpha|+1)\beta-2|\alpha|}}. \end{aligned} \tag{6.117}$$

Besides, taking into account the optimal k_0, the optimal λ finally writes as follows

$$\lambda_{opt} = \sqrt{\frac{2-\beta}{\beta}}\frac{1}{K_3^\alpha}\|Q\|_{V_2}\left(\frac{\|\partial^\alpha E\|^{2\alpha}_{V_2}}{\|E\|^\beta_{V_2}}\right)^{\frac{1}{(\alpha+1)\beta-2\alpha}}. \tag{6.118}$$

□

Remark 6.3.15. *The proof of Theorem 6.3.14 is based on the finding of an optimal λ. The*

existence of an optimum is illustrated on Burgers' equation in Section 6.4.3, Figure 6.3.

Evolution case

The same study can be performed in the evolution case. It uses the Fourier transform in x, ξ but not in t (see [29]). Therefore, it suits better functions defined on $[0,T]\times\mathbb{R}^d_x\times\mathbb{R}_\xi$.

We consider f the solution of

$$\partial_t f(t,x,\xi)+a(\xi)\cdot\nabla_x f(t,x,\xi)+\lambda f(t,x,\xi)=\lambda M(t,x,\xi)+\lambda\frac{\partial^\alpha E}{\partial x^\alpha}, \tag{6.119}$$

with

$$\partial_t M(t,x,\xi)+a(\xi)\cdot\nabla_x M(t,x,\xi)=Q(x,\xi,t)\in C([0,T],L^2(\mathbb{R}^N_x\times\mathbb{R}_\xi)),. \tag{6.120}$$

Subtracting (6.119) and (6.120) and denoting $g=f-M$, we obtain

$$\partial_t g+a(\xi)\cdot\nabla_x g+\lambda g=\lambda\frac{\partial^\alpha E}{\partial x^\alpha}-Q. \tag{6.121}$$

First of all, let us recall that in the case where the noise should be bounded in L^2, then, thanks to Theorem 6.3.6, we have

$$\begin{aligned}\|g(t,x,\xi)\|_{V_2}\leq{}&\|g_0\|_{V_2}e^{-\lambda t}\\&+(1-e^{-\lambda t})\left(\frac{\|Q(t,x,\xi)\|_{L^2(\mathbb{R}^d_x\times\mathbb{R}_\xi}}{\lambda}+\|\partial_\alpha E\|_{V_2}\right).\end{aligned} \tag{6.122}$$

Therefore, thanks to Young's inequality we obtain

$$\begin{aligned}\|g(t,x,\xi)\|^2_{V_2}\leq{}&3\|g_0\|^2_{V_2}e^{-2\lambda t}\\&+3(1-e^{-\lambda t})^2\left(\frac{\|Q(t,x,\xi)\|^2_{V_2}}{\lambda^2}+\|\partial_\alpha E\|^2_{V_2}\right).\end{aligned} \tag{6.123}$$

And eventually

$$\begin{aligned}\int_0^T\|g(t,x,\xi)\|^2_{V_2}dt\leq{}&\frac{3\|g_0\|^2_{V_2}}{2\lambda}\\&+3\left(\frac{\|Q(t,x,\xi)\|^2_{V_2}}{\lambda^2}+\|\partial_\alpha E\|^2_{L^2([0,T],V_2)}\right).\end{aligned} \tag{6.124}$$

This last inequality tells us that we cannot approach the exact solution closer than the magnitude of the noise.

Following Section 6.3.4 we denote $\widehat{g}(t,k,\xi)$ the space Fourier transform of g

$$\widehat{g}(t,k,\xi)=\int_{\mathbb{R}^N}g(t,x,\xi)e^{ik\cdot x}dx, \tag{6.125}$$

$\widehat{E}$ and $\widehat{Q}$ are defined in the same manner. Moreover, we will work on the averaged quantity $\rho_\psi(t,x) = \int_{\mathbb{R}_\xi} g(t,x,\xi)\psi(\xi)d\xi$ where ψ is a smooth compactly supported function. We notice that $\widehat{\rho}_\psi(t,k) = \int_{\mathbb{R}_\xi} \widehat{g}(t,k,\xi)\psi(\xi)d\xi$. We claim that the averaged quantity ρ_ψ lies in a better space than $L^2([0,T],L^2(\mathbb{R}_x))$, and its homogeneous seminorm tends to zero when $\|E\|_{L^2}$ becomes smaller. Like in the linear case, we state the following theorem, which proof can be found in Section B.2

Theorem 6.3.16. *Let $M(t,x,\xi) \in C([0,T],V_2)$ satisfy (6.120) and $f(t,x,\xi) \in C([0,T],V_2)$ satisfy the noisy data assimilation problem(6.119). Then, there exists β, $0 < \beta \leq 1$, and γ, $0 < \gamma \leq \beta - 2|\alpha|$ and a constant K such that*

$$\begin{aligned}\|\widehat{\rho}_\psi\|^2_{L^2([0,T],\dot{H}^{\gamma/2}(\mathbb{R}_x))} \leq K\|\partial_\alpha E\|^2_{L^2}\left(\frac{\|E\|^{2(1-\beta)}_{L^2([0,T],V_2)}}{\|\partial_\alpha E\|^2_{L^2([0,T],V_2)}}\right)^{\frac{\gamma}{\beta-2\alpha(1-\beta)}} \\ + \mathrm{o}\left(\|E\|_{V_2}^{\frac{2(1-\beta)\gamma}{\beta-2\alpha(1-\beta)}}\right).\end{aligned} \tag{6.126}$$

6.3.5 Sampling operator in time in the scalar case

In the very theoretical case of complete and exact observations, as studied in Section 6.3.2, the conclusion is that the scalar nudging term can be chosen as big as possible and convergence is ensured. When adding noise, an optimal value for λ minimizes the covergence error, as explained in Section 6.3.3. Now, we want to model the fact that we may not have access to the exact observation at time t_k but only to some mean of it over a small period of time. For that purpose, we define a mollifier φ. We recall that φ is a smooth function on $\mathbb{R}$ satisfying

- φ is compactly supported,
- $\displaystyle\int_{\mathbb{R}} \varphi(s)ds = 1$,
- $\displaystyle\lim_{\sigma\to 0} \varphi_\sigma(s) = \lim_{\sigma\to 0} \frac{1}{\sigma}\varphi(\frac{s}{\sigma}) = \delta(s)$.

Let us choose

$$\varphi(s) = \begin{cases} Ce^{-1/(1-|s|^2)} & \text{if } |s| < 1 \\ 0 & \text{if } |s| \geq 1, \end{cases},$$

where the constant C is chosen such that the function satisfies the integral property. With the regularizing sequence $\{\varphi_\sigma,\ \sigma \in \mathbb{R}^+\}$ built from φ we have a series of functions with a compact support of length 2σ. Then, considering that data come from a hyperbolic conservation law of type (6.19) admitting a kinetic formulation on the density $M(t,x,\xi)$:

$$\partial_t M(t,x,\xi) + a(\xi)\cdot\nabla_x M(t,x,\xi) = Q(t,x,\xi), \tag{6.127}$$

for some collision term Q, we work with the following equation of the estimator:

$$\partial_t f(t,x,\xi) + a(\xi)\cdot\nabla_x f(t,x,\xi) + \lambda\sum_{k\in I}\varphi_\sigma(t-t_k)f(t_k,x,\xi) = \lambda\sum_{k\in I}\varphi_\sigma(t-t_k)M(t_k,x,\xi), \tag{6.128}$$

where $\{t_k,\, k\in I\}$ are the observation times.

Theorem 6.3.17. *Let us suppose that M is solution of (6.127) and f is solution of (6.128). Provided that* $\mathrm{Card}(k, t_k \le T-\sigma) \neq 0$*, then,*

$$\begin{aligned}\|f(T)-M(T)\|_{V_1} \le{}& \|f_0-M_0\|_{V_1} e^{-\lambda\,\mathrm{Card}(k,t_k\le T-\sigma)}\\ &+\sigma\|\partial_t(f-M)\|_{L^\infty_t(M^1_x(\mathbb{R}_x),L^1(\mathbb{R}_\xi))}\left(1-e^{-\lambda\,\mathrm{Card}(k,t_k\le T+\sigma)}\right)\\ &+\sup_{0<t\le T}\|Q(t)\|_{V_1}\frac{1-e^{-\lambda\,\mathrm{Card}(k,t_k\le T+\sigma)}}{\lambda}.\end{aligned} \tag{6.129}$$

Proof of Theorem 6.3.17. We perform the difference between (6.128) and (6.127) and begin with

$$\begin{aligned}&\partial_t(f-M)(t,x,\xi) + a(\xi)\cdot\nabla_x(f-M)(t,x,\xi)\\ &\qquad+\lambda\sum_{k\in I}\varphi_\sigma(t-t_k)(f-M)(t_k,x,\xi) = -Q(t,x,\xi).\end{aligned} \tag{6.130}$$

Multiplying by $\mathrm{sgn}(f-M)(t,x,\xi)$ leads to

$$\begin{aligned}&\partial_t|f-M| + a(\xi)\cdot\nabla_x|f-M|\\ &\qquad+\lambda\,\mathrm{sgn}(f-M)(t,x,\xi)\sum_{k\in I}\varphi_\sigma(t-t_k)(f-M)(t_k,x,\xi) \le |Q|.\end{aligned} \tag{6.131}$$

An integration in the space and velocity variable results in the inequality:

$$\begin{aligned}&\frac{d}{dt}\|(f-M)(t)\|_{V_1} + \lambda\int_{\mathbb{R}_x}\int_{\mathbb{R}_\xi}\sum_{k\in I}\varphi_\sigma(t-t_k)(f-M)(t_k,x,\xi)\,\mathrm{sgn}(f-M)(t,x,\xi)d\xi dx\\ &\qquad\le \|Q(t)\|_{V_1}.\end{aligned} \tag{6.132}$$

Using Fubini theorem to invert the integral and sum operators, the previous equation also

writes

$$\begin{aligned}\frac{d}{dt}\|(f-M)(t)\|_{V_1} &+ \lambda\sum_{k\in I}\varphi_\sigma(t-t_k)\|(f-M)(t)\|_{V_1}\\ &\leq \lambda\int_{\mathbb{R}_x}\int_{\mathbb{R}_\xi}\sum_{k\in I}\varphi_\sigma(t-t_k)\left[(f-M)(t,x,\xi)-(f-M)(t_k,x,\xi)\right]\operatorname{sgn}(f-M)(t,x,\xi)d\xi dx\\ &\quad+\|Q(t)\|_{V_1}\\ &\leq \lambda\int_{\mathbb{R}_x}\int_{\mathbb{R}_\xi}\sum_{k\in I}\varphi_\sigma(t-t_k)|(f-M)(t,x,\xi)-(f-M)(t_k,x,\xi)|d\xi dx+\|Q(t)\|_{V_1}.\end{aligned} \tag{6.133}$$

Let us assume now that $f-M$ is of time bounded variation. Then,

$$|(f-M)(t,x,\xi)-(f-M)(t_k,x,\xi)|\leq\left|\int_{t_k}^{t}\partial_\tau(f-M)(\tau,x,\xi)d\tau\right|.$$

At this point we have

$$\begin{aligned}\frac{d}{dt}\|(f-M)(t)\|_{V_1} &+ \lambda\sum_{k\in I}\varphi_\sigma(t-t_k)\|(f-M)(t)\|_{V_1}\\ &\leq \lambda\int_{\mathbb{R}_x}\int_{\mathbb{R}_\xi}\sum_{k\in I}\varphi_\sigma(t-t_k)\left|\int_{t}^{t_k}\partial_\tau(f-M)(\tau,x,\xi)d\tau\right|d\xi dx+\|Q(t)\|_{V_1}.\end{aligned} \tag{6.134}$$

Let us use Fubini theorem to get

$$\begin{aligned}\frac{d}{dt}\|(f-M)(t)\|_{V_1} &+ \lambda\sum_{k\in I}\varphi_\sigma(t-t_k)\|(f-M)(t)\|_{V_1}\\ &\leq \lambda\sum_{k\in I}\varphi_\sigma(t-t_k)\operatorname{sgn}(t-t_k)\int_{t_k}^{t}\int_{\mathbb{R}_x}\int_{\mathbb{R}_\xi}|\partial_\tau(f-M)|d\xi dx d\tau+\|Q(t)\|_{V_1}.\end{aligned} \tag{6.135}$$

Since $\partial_t(f-M)\in L^\infty_t(M^1_x(\mathbb{R}^d_x),L^1(\mathbb{R}_\xi))$, we can write

$$\begin{aligned}\frac{d}{dt}\|(f-M)(t)\|_{V_1} &+ \lambda\sum_{k\in I}\varphi_\sigma(t-t_k)\|(f-M)(t)\|_{V_1}\\ &\leq \lambda\sum_{k\in I}\varphi_\sigma(t-t_k)|t-t_k|\|\partial_t(f-M)\|_{L^\infty_t(M^1_x(\mathbb{R}^d_x))}+\|Q(t)\|_{V_1}.\end{aligned} \tag{6.136}$$

Moreover, because of the compact domain of each φ_σ we can state

$$\begin{aligned}\frac{d}{dt}\|(f-M)(t)\|_{V_1} &+ \lambda\sum_{k\in I}\varphi_\sigma(t-t_k)\|(f-M)(t)\|_{V_1}\\ &\leq \lambda\sigma\|\partial_t(f-M)\|_{L^\infty_t(M^1_x(\mathbb{R}_x))}\sum_{k\in I}\varphi_\sigma(t-t_k)+\|Q(t)\|_{V_1}.\end{aligned} \tag{6.137}$$

Using Lemma 6.3.8 we obtain

$$\begin{aligned}\|f(T)-M(T)\|_{L^1(\mathbb{R}_x)} &\leq \|f_0-M_0\|_{L^1(\mathbb{R}_x)} e^{-\lambda\int_0^T \sum_{k\in I}\varphi_\sigma(t-t_k)dt} \\ &+ \lambda\sigma\|\partial_t(f-M)\|_{L^\infty_t(M^1_x(\mathbb{R}_x),L^1(\mathbb{R}_\xi))}\int_0^T \sum_{k\in I}\varphi_\sigma(t-t_k)e^{-\lambda\int_t^T \sum_{k\in I}\varphi_\sigma(s-t_k)ds}dt \\ &+ \sup_{0<t\leq T}\|Q(t)\|_{V_1}\int_0^T e^{-\lambda\int_t^T \sum_{k\in I}\varphi_\sigma(s-t_k)ds}dt.\end{aligned} \tag{6.138}$$

Eventually, noticing that

$$\frac{d}{dt}e^{-\lambda\int_t^T \sum_{k\in I}\varphi_\sigma(s-t_k)ds} = \lambda\sum_{k\in I}\varphi_\sigma(t-t_k)e^{-\lambda\int_t^T \sum_{k\in I}\varphi_\sigma(s-t_k)ds},$$

we end up with

$$\begin{aligned}\|f(T)-M(T)\|_{L^1(\mathbb{R}_x\times\mathbb{R}_\xi)} &\leq \|f_0-M_0\|_{L^1(\mathbb{R}_x\times\mathbb{R}_\xi)} e^{-\lambda\int_0^T \sum_{k\in I}\varphi_\sigma(t-t_k)dt} \\ &+ \sigma\|\partial_t(f-M)\|_{L^\infty_t(M^1_x(\mathbb{R}_x),L^1(\mathbb{R}_\xi))}\left(1-e^{-\lambda\int_0^T \sum_{k\in I}\varphi_\sigma(t-t_k)dt}\right) \\ &+ \sup_{0<t\leq T}\|Q(t)\|_{V_1}\frac{1-e^{-\lambda\int_0^T \sum_{k\in I}\varphi_\sigma(t-t_k)dt}}{\lambda}.\end{aligned} \tag{6.139}$$

The conclusion follows. □

Remark 6.3.18. *From Theorem 6.3.17 we have the same remarks as we already did before. The error in the initial condition is still forgotten with time, as expected from hyperbolic conservation laws. The effect of the collision term is filtered by the nudging coefficient λ. However, the error in time introduced on the observations introduces a bias of order σ in the upper bound which cannot be ignored nor counter-balanced. But it is still worth noticing that λ does not amplify this error which is a very important point.*

6.3.6 Incomplete observations in space

In this section, a subdomain is defined, where assimilation towards data occur. We deal with a simplified 1D problem with boundary conditions and assuming that solutions are smooth. The first idea is to find the minimal time required for the information to spread over the whole domain and have an effect on the variables. In control theory, this is the observability problem, dealt with in a first paragraph. The second idea is to prove the stability of the problem by studying the error decay, which is analyzed in a second paragraph.

Observability

Let us study the periodic 1D problem over the domain $[0,1]$

$$\begin{cases} \partial_t f(t,x,\xi) + a(\xi)\cdot\nabla_x f(t,x,\xi) = \lambda(x)(M(t,x,\xi) - f(t,x,\xi)) \\ f(0,x,\xi) = f_0(x,\xi) \\ f(t,0,\xi) = f(t,1,\xi) \end{cases} \tag{6.140}$$

where the observations are supposed to come from the model

$$\begin{cases} \partial_t M(t,x,\xi) + a(\xi)\cdot\nabla_x M(t,x,\xi) = Q(t,x,\xi) \\ M(0,x,\xi) = M_0(x,\xi) \\ f(t,0,\xi) = f(t,1,\xi) \end{cases} \tag{6.141}$$

We are interested in the case $\lambda(x) = \lambda \mathbb{1}_{[a,b]}(x)$, $\lambda \in \mathbb{R}^+$, $0 < a < b < 1$. We consider $Q = 0$, ξ is supposed to be fixed. This assumption is not meaningless. It represents indeed the situation where no collision occur at the kinetic level, which translates at the macroscopic level into a situation where no shock occur.

The first concern is the observability of the situation at time $T > 0$, where observability is defined as follows in our case

Definition 6.3.19 (Observability condition)**.** *The Cauchy system* (6.140) *is observable if and only if*

$$\exists C \in \mathbb{R}_+^*, \forall u \text{ solution of the linear transport equation } (\lambda = 0),$$
$$C\int_0^T \|\lambda(x)u(x,t)\|^2_{L^2([0,1])} \geq \|u(0)\|^2_{L^2([0,1]} \tag{6.142}$$

This formally means that the information captured in the time lapse $[0,T]$ in the subdomain $[a,b]$ allows to reconstruct any initial condition. At fixed ξ, $(s, x + a(\xi)s)$ is the characteristic curve starting in x of the pure transport problem ($\lambda = 0$). The quantity $\int_0^t \mathbb{1}_{[a,b]}(x + a(\xi)s)ds$ represents the time that the particle starting at point x spends in interval $[a,b]$ between 0 and t. Let us call

$$X_{t,\xi}(x) = \int_0^t \mathbb{1}_{[a,b]}(x + a(\xi)s)ds.$$

We prove the following proposition:

Proposition 6.3.20. (6.140) *is observable* $\Leftrightarrow X^{inf}_{t,\xi} = \min_x X_{t,\xi} > 0$

Proof of Proposition 6.3.20. Let us show first that the condition $X^{inf}_{t,\xi} > 0$ (every characteristics spends time in the observed domain) is equivalent to $T > \frac{1-(b-a)}{|a(\xi)|}$. This shows that $a(\xi)$ should necessarily be non-zero, reflecting the fact that particles with speed 0 are not observable. On Figure 6.1 we represent the characteristics of constant postitive speed c in the periodic case on domain $[0,1]$. We see that the last characteristics to pass through the domain $[a,b]$ is the green one, starting right after point b. This happens if $T > \frac{1-(b-a)}{c}$.

□

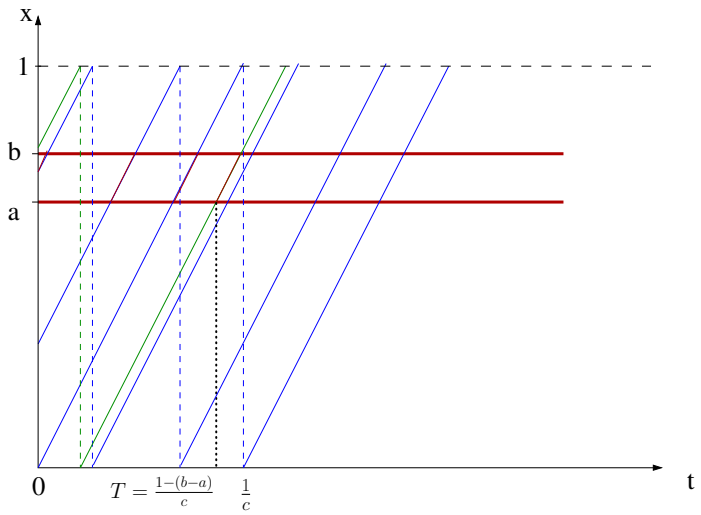

Figure 6.1: Characteristics of the problem. This figure shows the equivalence between both conditions $X_{t,\xi}^{inf} > 0$ and $T > \frac{1-(b-a)}{|a(\xi)|}$.

Error decay

Let us denote $g(t,x,\xi)$ the error between the observations and the estimator:

$$g(t,x,\xi) = f(t,x,\xi) - M(t,x,\xi).$$

Proposition 6.3.21. *Let $f(t,x,\xi)$ satisfy (6.140) and $M(t,x,\xi)$ satisfy (6.141) where $Q(t,x,\xi) = 0$. If the data assimilation problem (6.140) is observable, exponential stability in time is ensured as soon as $\lambda \geq \frac{t}{X_t^{inf}}$, where X_t^{inf} is defined in Section 6.3.6 i.e.*

$$\|g(t)\|_{V_2} \leq \|g_0\|_{V_2} e^{-\lambda X_t^{inf}}. \tag{6.143}$$

Proof of Proposition 6.3.21. Hence, subtracting (6.140) and (6.141) and calling $g(t,x,\xi) = f(t,x,\xi) - M(t,x,\xi)$ leads to

$$\begin{cases} \partial_t g(t,x,\xi) + a(\xi)\cdot\nabla_x g(t,x,\xi) = -\lambda(x) g(t,x,\xi) \\ g(0,x,\xi) = f_0(x,\xi) - M_0(x,\xi) = g_0(x,\xi) \\ g(t,0,\xi) = g(t,1,\xi) \end{cases} \tag{6.144}$$

(6.144) is equivalent to

$$\begin{cases} \dfrac{d}{dt} g(t,x+a(\xi)t,\xi) = -\lambda(x+a(\xi)t) g(t,x+a(\xi)t,\xi) \\ g(0,x,\xi) = g_0(x,\xi) \\ g(t,0,\xi) = g(t,1,\xi) \end{cases} \tag{6.145}$$

(6.145) integrates into

$$\begin{aligned} g(t, x + a(\xi)t, \xi) &= g_0(x, \xi) e^{-\int_0^t \lambda(x+a(\xi)s)ds} \\ &= g_0(x, \xi) e^{-\lambda \int_0^t \mathbb{1}_{[a,b]}(x+a(\xi)s)ds} \end{aligned} \tag{6.146}$$

Then, if $X_{t,\xi}$ has a positive lower bound $X_{t,\xi}^{inf}$ (if the system is observable),

$$\|g(t)\| \leq \|g_0\| e^{-\lambda X_t^{inf}}. \tag{6.147}$$

Therefore, an exponential decrease of the error is possible if $\lambda \geq \frac{t}{X_t^{inf}}$. □

Then it is possible to add the collision term in a second step. The analytical resolution of the error writes

$$\begin{aligned} &g(t, x + a(\xi)t, \xi) = \\ &e^{-\int_0^t \lambda(x+a(\xi)s)ds} \left(g_0(x, \xi) - \int_0^t Q(s, x + a(\xi)s, \xi) e^{\int_0^s \lambda(x+a(\xi)r)dr} ds \right) \end{aligned} \tag{6.148}$$

which also writes

$$\begin{aligned} g(t, x + a(\xi)t, \xi) = e^{-\int_0^t \lambda(x+a(\xi)s)ds} & g_0(x, \xi) \\ & + \int_0^t Q(s, x + a(\xi)s, \xi) e^{-\int_s^t \lambda(x+a(\xi)r)dr} ds \end{aligned} \tag{6.149}$$

However, it is not so clear how to treat the integral with the collision term, since we cannot extract the coefficient λ as easily as in the situation when it was constant. It raises the question to know if the coefficient can filter collisions everywhere, like in the case of complete observations at the beginning of this chapter, even if it is spatially constrained.

Remark 6.3.22. *This problem remains an open question and the sampling of observations in space in a more general context is future work.*

6.3.7 Numerical results

Numerical experiments of the kinetic nudging are performed first on a scalar conservation law, Burgers' equation. Further numerical results about the shallow water equations are presented in Section 6.4.3.

Discretization

We consider that observations satisfy the Burgers equation with homogeneous Dirichlet boundary conditions on the domain $[0,1]$

$$\begin{cases} \partial_t u + \partial_x \dfrac{u^2}{2} = 0 \\ u(0,x) = u_0(x) \\ u(t,0) = 0,\ u(t,1) = 0 \end{cases} \tag{6.150}$$

This problem with all its entropies is well represented by the kinetic model

$$\begin{cases} \partial_t \chi(\xi, u(t,x)) + \xi \partial_x \chi(\xi, u(t,x)) = \partial_\xi m(t,x,\xi) \\ \chi(\xi, u(0,x)) = \chi(\xi, u_0(x)) \\ \chi(\xi, u(t,0)) = \chi(\xi, u(t,1)) = 0 \end{cases} \tag{6.151}$$

Therefore, data assimilation at the kinetic level writes

$$\begin{cases} \partial_t f(t,x,\xi) + \xi \partial_x f(t,x,\xi) = \lambda(\chi(\xi, u(t,x)) - f(t,x,\xi)) \\ f(0,x,\xi) = f_0(x) \\ f(t,0,\xi) = f(t,1,\xi) = 0 \end{cases} \tag{6.152}$$

To solve this numerically, we develop a finite volume framework. The domain $[0,1]$ is divided into N cells centered on $x_i,\ i \in 0..N$. Then, we integrate (6.152) over $[x_{i-1/2}, x_{i-1/2}] \times [t^n, t^{n+1}]$. An explicit Euler scheme leads

$$f_i^{n+1} = f_i^n - \frac{\Delta t}{dx}\xi \left(f_{i+1/2}^n - f_{i-1/2}^n \right) + \lambda \Delta t \left(\chi(\xi, \overline{u}_i^n) - f_i^n \right) \tag{6.153}$$

The numerical fluxes are computed using a simple upwind scheme:

$$f_{i+1/2}^n = \begin{cases} f_i^n, & \text{for } \xi \geq 0 \\ f_{i+1}^n, & \text{for } \xi < 0 \end{cases}$$

This explicit scheme is only valid under the CFL condition

$$\Delta t \leq \left(\lambda + \frac{\sup \xi}{dx} \right)^{-1}.$$

An integration in ξ gives the macroscopic scheme for the estimator $\widehat{u}(t,x)$, which is basically the Osher-Engquist scheme

$$\begin{aligned} \widehat{u}_i^{n+1} = \widehat{u}_i^n - \frac{\Delta t}{dx} \Bigg(& \max(\widehat{u}_i^n, 0)\frac{\widehat{u}_i^n}{2} + \min(\widehat{u}_{i+1}^n, 0)\frac{\widehat{u}_{i+1}^n}{2} \\ & - \max(\widehat{u}_{i-1}^n, 0)\frac{\widehat{u}_{i-1}^n}{2} - \min(\widehat{u}_i^n, 0)\frac{\widehat{u}_i^n}{2} \Bigg) + \lambda \Delta t (u_i^n - \widehat{u}_i^n) \end{aligned} \tag{6.154}$$

In the end, the observer and the numerical scheme for the data assimilation is similar to what could have been done on the macroscopic conservation law directly. However, this framework paves the way for an interesting theoretical framework, making the most of what has already been around kinetic equations. But most of all, it is its extension to the case of hyperbolic systems in Section 6.4 that reveals its efficiency.

Results

We want to illustrate our mathematical result about noise stability (Theorem 6.3.11) on Burgers' equation. We add a deterministic noise to the data. As explained in the Remark 6.3.10, in practice the noise is on the macroscopic data. Let us choose

$$E(x) = \epsilon \cos(\frac{x}{\epsilon}), \quad \partial_\alpha E(x) = \epsilon^{1-\alpha} cos(\frac{x}{\epsilon} + \alpha\frac{\pi}{2}).$$

Therefore,

$$\|E\|_{L^2([0,1])} = \frac{\epsilon}{2}\sqrt{2 + \epsilon \sin(\frac{2}{\epsilon})}, \quad \|\partial_\alpha E\|_{L^2([0,1])} = \frac{\epsilon^{1-\alpha}}{2}\sqrt{2 + \epsilon \sin(\frac{2}{\epsilon})}.$$

The noise may then be non negligible in L^2 norm (as soon as $\alpha > 0$) whereas it is small in $H^{-\alpha}$. Initial condition is taken as follows

$$u(0,x) = \begin{cases} 1 & \text{if } \frac{1}{8} \leq x \leq \frac{1}{4} \\ 0 & \text{otherwise,} \end{cases},$$

while

$$\widehat{u}(0,x) = \begin{cases} 0.75 & \text{if } \frac{1}{12} \leq x \leq \frac{1}{6} \\ 0 & \text{otherwise.} \end{cases},$$

The parameters take the following values: $N = 100$, $\lambda = 100$, $\alpha = \frac{1}{4}$. The observations are partial in time: 30 observations are carried out between $t = 0$ and $t = 2$. The number of time steps is 320 which makes an observation ratio of 10%. The first row of Figure 6.2 shows the evolution of the observer if no assimilation occurred ($\lambda = 0$). We can see that the error introduced by a wrong initial condition is detrimental. Figure 6.2 shows the evolution of the data assimilation problem for two different values of ϵ. In the case $\epsilon = 0.02$, $\|\partial_\alpha E\|_{L^2([0,1])} = 4.0\,10^{-2}$, whereas $\|\partial_\alpha E\|_{L^2([0,1])} = 7.0\,10^{-3}$ for $\epsilon = 0.002$. In comparison, the norm of the initial solution is $\|u(0,\cdot)\|_{L^2([0,1])} = 4.0\,10^{-1}$. It converges rapidly to the global shape of the original problem. As stated previously, the noise introduced on the data cannot be forgotten, but it is not amplified.

The proof of the theorems about noise stability are centered around the search for an optimal λ, that can be expressed as a function of another parameter k_0, optimized later on (equations (6.112) and (B.48)). Figure 6.3 shows the existence of an optimal λ minimizing the homogeneous Sobolev seminorm. Moreover, it shows that the error tends to zero as ϵ tends to zero.

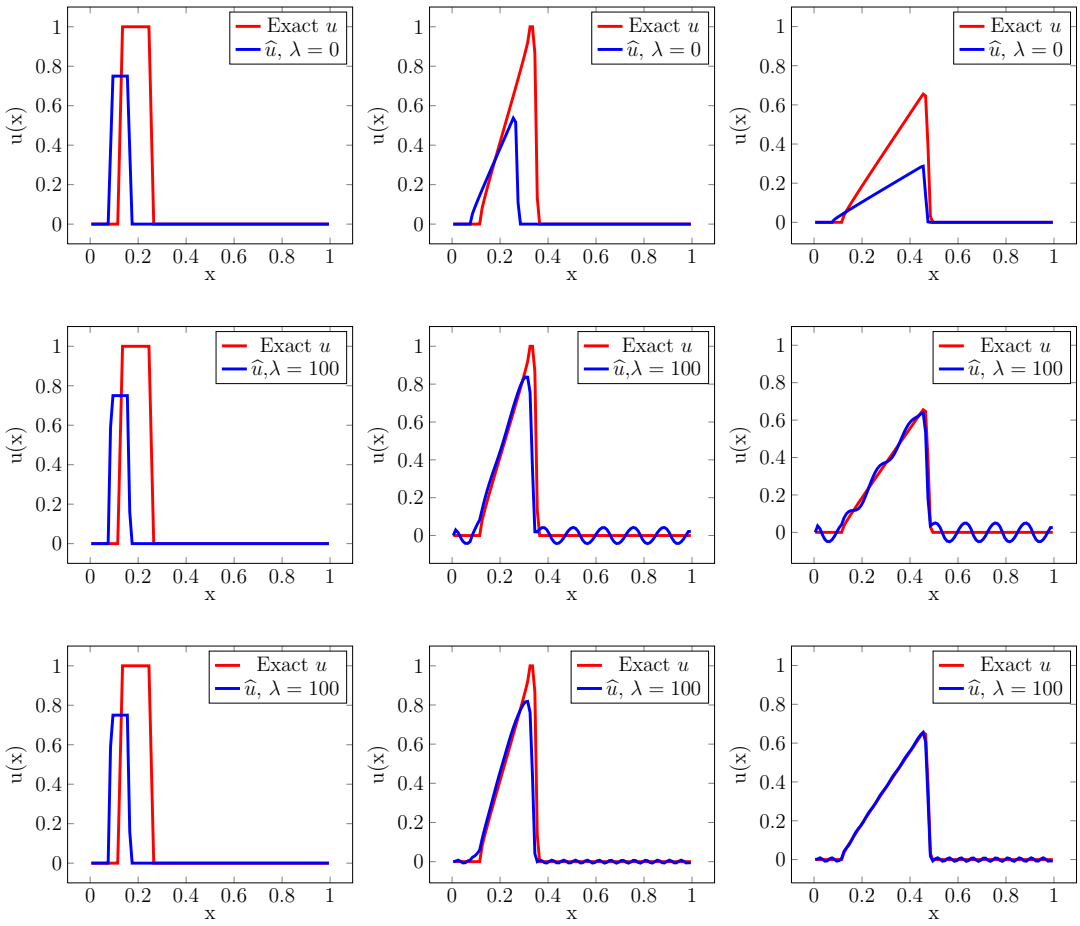

Figure 6.2: Top: Evolution of the data assimilation problem at time t =0.01, t = 0.2 and t = 0.5 in the case $\varepsilon = 0.02$. Bottom: Evolution of the data assimilation problem at time t =0.01, t = 0.2 and t = 0.5 in the case $\varepsilon = 0.002$.

6.4 Kinetic Luenberger observer on the Saint-Venant system

Systems in several space dimensions usually hardly give a kinetic formulation. They satisfy indeed a single entropy inequality instead of a whole family. And this is not enough to deduce the sign of the kinetic entropy defect measure in (6.27). Therefore, we introduce a weaker concept: the kinetic representation.

6.4.1 Kinetic representation of the Saint-Venant system

The kinetic representation only uses one entropy. It is much less demanding than the kinetic formulation. It enables to represent a hyperbolic system by integration of the underlying kinetic equation. Its main interest lies in the design of finite volume solvers. Since the kinetic representation does not admit a general writing, we choose to derive it on the Saint-Venant system.

As explained in the introduction of this thesis, the shallow water assumptions allows

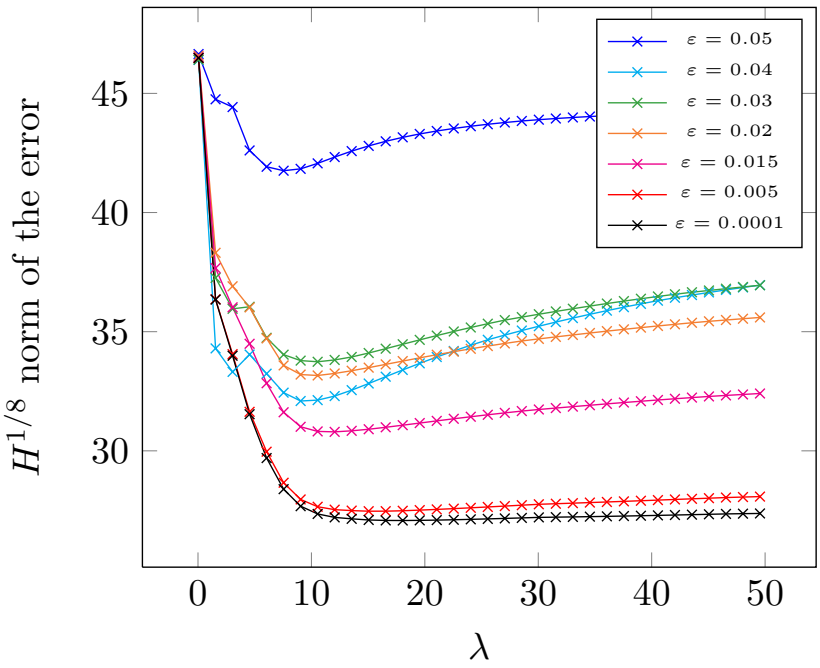

Figure 6.3: $H^{1/8}$ error between the observations and the model as a function of λ. We see on the one hand the existence of an optimal λ for any value of ε. Notice also the decrease of the error with ε.

to approximate the free surface Navier-Stokes equations under the form of a hyperbolic conservation law, the Saint-Venant system with topography source term, that we recall hereafter

$$\frac{\partial H}{\partial t} + \frac{\partial}{\partial x}\big(Hu\big) = 0 \tag{6.155}$$

$$\frac{\partial (Hu)}{\partial t} + \frac{\partial (Hu^2)}{\partial x} + \frac{g}{2}\frac{\partial H^2}{\partial x} = -gH\frac{\partial z_b}{\partial x} \tag{6.156}$$

where H and u respectively denote the water depth and the averaged velocity and z_b represents the bathymetry with $H = \eta - z_b$. We point out the difficulty of treating a nonlinear hyperbolic system, in comparison with scalar conservation laws. A review of control theory on the Saint-Venant system is available in [47], which uses non trivial tools like the return method, quasi static deformations, and leaves the reader with still open problems.

We call entropy solution to the Saint-Venant system, a weak solution which satisfies the entropy inequality given in the following theorem.

Theorem 6.4.1. *The system (6.155)-(6.156) is strictly hyperbolic for $H > 0$. It admits a mathematical entropy (which is also the energy)*

$$\zeta = \frac{Hu^2}{2} + \frac{gH(\eta + z_b)}{2}.$$

satisfying

$$\frac{\partial \zeta}{\partial t} + \frac{\partial G}{\partial x} \leq 0, \tag{6.157}$$

with

$$G = u\big(\zeta + g\frac{H^2}{2}\big).$$

We do not prove this theorem which relies on the classical theory of hyperbolic equations and simple algebraic calculation, see [49]. We just recall that for smooth solutions the inequality in (6.157) is an equality.

The system (6.155)-(6.157) admits a kinetic representation. We use another interpretation as the one given in the introduction. As explained in [111], many Gibbs equilibria can indeed replace the Maxwellian usually used in kinetic theory, as soon as it satisfies basic properties. The following is particularly suited for the design of efficient numerical schemes because it enables analytical integrations (see [9], [10]).

We first introduce a real function χ defined on $\mathbb{R}$, compactly supported and which has the following properties

$$\begin{cases} \chi(-w) = \chi(w) \geq 0 \\ \int_{\mathbb{R}} \chi(w)\ dw = \int_{\mathbb{R}} w^2 \chi(w)\ dw = 1 \end{cases} \tag{6.158}$$

define $k_3 = \int_{\mathbb{R}} \chi^3(w)\ dw$. We denote $[-w_\chi, w_\chi]$ the compact support of length $2w_\chi$ of the function χ. The simplest choice for χ is

$$\chi_1(z) = \frac{1}{2\sqrt{3}} 1_{|z|\leq\sqrt{3}}. \tag{6.159}$$

Another function deserves being mentioned too

$$\chi_0(z) = \frac{1}{\pi}\sqrt{1 - \frac{z^2}{4}}\, \mathbb{1}_{|z|\leq 2}. \tag{6.160}$$

It is indeed the minimizer of energy. We recall the lemma from [115] in a slightly different form

Lemma 6.4.2. *The minimization of the energy*

$$E(f, z_b) = \int_{\mathbb{R}} \left(\frac{\xi^2}{2} f(\xi) + \frac{g^2}{8} f(\xi)^3 + g z_b f(\xi) \right) d\xi \tag{6.161}$$

under the constraints

$$f \geq 0, \quad , \int_{\mathbb{R}} f(\xi) d\xi = H, \quad \text{and } \int_{\mathbb{R}} \xi f(\xi) d\xi = Hu \tag{6.162}$$

is reached for the function $M(t,x,\xi) = \frac{H}{c}\chi_0(\frac{\xi-u}{c})$*, with* χ_0 *defined by*

$$\chi_0(z) = \frac{1}{\pi}\sqrt{1-\frac{z^2}{4}}\mathbb{1}_{|z|\leq 2}. \tag{6.163}$$

It also permits analytical integration and we will use this one in the further numerical experiments. Now let us construct the density of particles $M(t,x,\xi)$ defined by a Gibbs equilibrium: the microscopic density of particles present at time t, at the abscissa x and with velocity ξ given by

$$M(t,x,\xi) = \frac{H}{c}\chi\left(\frac{\xi-u}{c}\right), \tag{6.164}$$

with $c = \sqrt{\frac{gH}{2}}$.

Then we have the following theorem

Theorem 6.4.3. *The functions* (H,u) *are strong solutions of the Saint-Venant system described by* (6.155)-(6.157) *if and only if the equilibrium* $M(t,x,\xi)$ *is solution of the kinetic equation*

$$\frac{\partial M}{\partial t} + \xi\cdot\nabla_x M - g\nabla_x z_b\cdot\nabla_\xi M = Q(t,x,\xi), \tag{6.165}$$

where $Q(x,t,\xi)$ *is a collision term satisfying*

$$\int_{\mathbb{R}} Q\ d\xi = \int_{\mathbb{R}} \xi Q\ d\xi = 0. \tag{6.166}$$

The solution is an entropy solution if additionally

$$\int_{\mathbb{R}}\left(\frac{\xi^2}{2}+\frac{g^2}{8k_3}M^2+gz_b\right)Q d\xi \leq 0. \tag{6.167}$$

Proof of theorem 6.4.3. From the definition (6.158), the proof is obvious calculating the quantities

$$\int_{\mathbb{R}}(6.165)\ d\xi, \quad \int_{\mathbb{R}}\xi(6.165)\ d\xi, \quad \text{and} \quad \int_{\mathbb{R}}\left(\frac{\xi^2}{2}+\frac{g^2}{8k_3}M^2+gz_b\right)(6.165)\ d\xi$$

and using (6.166) and (6.167). □

Remark 6.4.4. *The right hand side* $Q(t,x,\xi)$ *in the kinetic representation does not vanish in the smoothness region, whatever the choice of* χ*, as opposed to the measure* m *in Section 6.3.1.*

6.4.2 Convergence result for the Saint-Venant system

Let us deal now with a more practical case: data assimilation on the Saint-Venant system with a bounded source term. We prove that convergence towards a Saint-Venant solution

is possible when observing the water height only. This is the key point of our Saint-Venant study. For that reason, we define a kinetic density in the case we only have access to water height observations

$$\widetilde{M}(t,x,\xi) = \frac{H}{c}\chi\left(\frac{\xi-\widehat{u}}{c}\right), \tag{6.168}$$

where $H(t,x)$ are the observations and $\widehat{u}(t,x)$ is the velocity of macroscopic estimator (with the notations). At the kinetic level, the equation satisfied by the estimator density f can be written as follows

$$\partial_t f(t,x,\xi) + \xi\cdot\nabla_x f(t,x,\xi) - g\nabla_x z_b \nabla_\xi f(t,x,\xi) = \lambda(\widetilde{M}(t,x,\xi) - f(t,x,\xi)), \tag{6.169}$$

where z_b is the topography. Let us suppose that the solution f of (6.169) can also be written under the form of a Gibbs equilibrium using the macroscopic estimator $(\widehat{H}(t,x),\widehat{u}(t,x))$ i.e.

$$f(t,x,\xi) = \frac{\widehat{H}}{\widehat{c}}\chi(\frac{\xi-\widehat{u}}{\widehat{c}}), \tag{6.170}$$

Proposition 6.4.5. *Let $H(t,x)\in L^\infty([0,T]\times\mathbb{R}_x)$ be solution of (6.155) - (6.156), and $\widetilde{M}(t,x,\xi)$ be the Gibbs equilibrium built from it following (6.168). Let $f(t,x,\xi)$ satisfy (6.169), with the constraint of being of the form (6.170). Assuming some regularity on $\widetilde{M}$ defined by*

$$\partial_t\widetilde{M} + \xi\cdot\nabla_x\widetilde{M} + g\frac{\partial z_b}{\partial x}\left(\frac{\xi-u}{c^2}\right)\widetilde{M} = Q\in C([0,T],V_1) \tag{6.171}$$

then, $\exists\gamma>0$ such that $\forall T>0$

$$\|f(T)-\widetilde{M}(T)\|_{V_1} \le \|f_0-\widetilde{M_0}\|_{V_1}e^{-(\lambda-\gamma)T} + \sup_{0\le t\le T}\|Q(t)\|_{V_1}\frac{1-e^{-(\lambda-\gamma)T}}{\lambda-\gamma}. \tag{6.172}$$

Remark 6.4.6. *As in the scalar case, the upper bound consists of two terms. The first implies the initial conditions and disappears with time, as soon as $\lambda>\gamma$. The second is the filter on the collision term, which is useful once again as soon as $\lambda>\gamma$.*

Proof of Proposition 6.4.5. To begin the proof, we introduce another data assimilation problem, which is equivalent to (6.169)

$$\partial_t f(t,x,\xi) + \xi\cdot\nabla_x f(t,x,\xi) - g\nabla_x z_b\nabla_\xi\overline{f}(t,x,\xi) = \lambda(\widetilde{M}(t,x,\xi) - f(t,x,\xi)), \tag{6.173}$$

where $\overline{f}$ is defined hereafter

$$\overline{f}(t,x,\xi) = \frac{\widehat{H}}{\widehat{c}}\overline{\chi}(\frac{\xi-\widehat{u}}{\widehat{c}}), \tag{6.174}$$

and $\overline{\chi}$ satisfies

$$\begin{cases} \overline{\chi}(a) = \overline{\chi}(-a), \\ \displaystyle\int \overline{\chi}(z)dz = 1. \end{cases} \tag{6.175}$$

Given the properties of $\overline{\chi}$, an integration of (6.169) and (6.173) in the ξ variable results in the same macroscopic equations. Therefore working with (6.173) also leads to the right data assimilation problem. We choose the particular expression for $\overline{\chi}$:

$$\overline{\chi} = \int_z^{+\infty} \xi \chi(\xi) d\xi. \tag{6.176}$$

Hence, (6.173) simplifies into

$$\partial_t f(t,x,\xi) + \xi \cdot \nabla_x f(t,x,\xi) + g \nabla_x z_b \frac{\xi - u}{c^2} f(t,x,\xi) = \lambda(\widetilde{M}(t,x,\xi) - f(t,x,\xi)). \tag{6.177}$$

From the hypothesis on $\widetilde{M}(t,x,\xi)$ we have

$$\partial_t(f - \widetilde{M}) + \xi \cdot \nabla_x(f - \widetilde{M}) + (\lambda + g\frac{\partial z_b}{\partial x}\frac{\xi - u}{c^2})(f - \widetilde{M}) = -Q \tag{6.178}$$

Multiplying (6.178) by $\mathrm{sgn}(f(t,x,\xi) - \widetilde{M}(x,\xi))$ leads to

$$\partial_t|f - \widetilde{M}| + \xi \cdot \nabla_x|f - \widetilde{M}| + (\lambda + g\frac{\partial z_b}{\partial x}\frac{\xi - u}{c^2})|f - \widetilde{M}| \leq |Q|. \tag{6.179}$$

Assuming the source term is bounded yields

$$\partial_t|f - \widetilde{M}| + \xi \cdot \nabla_x|f - \widetilde{M}| + (\lambda - g\|\frac{\partial z_b}{\partial x}\|_{L^\infty(\mathbb{R}^d_x)}\frac{|\xi - u|}{c^2})|f - \widetilde{M}| \leq |Q| \tag{6.180}$$

Integrating (6.180) over the spatial and velocity variables we end up with

$$\frac{d}{dt}\int_{R_x}\int_{R_\xi} |f - \widetilde{M}| d\xi dx + \int_{R_x}\int_{R_\xi} (\lambda - g\|\frac{\partial z_b}{\partial x}\|_\infty \frac{|\xi - u|}{c^2})|f - \widetilde{M}| d\xi dx \\ \leq \int_{R_x}\int_{R_\xi} |Q| d\xi dx. \tag{6.181}$$

Since $\widetilde{M}$ and f are considered to be Gibbs equilibria of compact support in ξ we introduce Ω the support of M and ξ_{max} defined such that

$$\forall \xi \text{ s.t. } |\xi| \geq \xi_{max},\ f(t,x,\xi) = \widetilde{M}(t,x,\xi) = 0.$$

Besides, we consider that $u(t,x) \in L^\infty([0,T], R^d_x)$, $Q \in V_1$. We can therefore proceed to the next step by writing

$$\frac{d}{dt}\|f - \widetilde{M}\|_{V_1} + (\lambda - g\|\frac{\partial z_b}{\partial x}\|_\infty \frac{\xi_{max} + \|u\|_\infty}{c^2})\|f - \widetilde{M}\|_{V_1} \leq \|Q(t)\|_{V_1}. \tag{6.182}$$

let us denote

$$\gamma = g\|\frac{\partial z_b}{\partial x}\|_\infty \frac{\xi_{max} + \|u\|_\infty}{c^2}$$

Eventually,

$$\|f - \widetilde{M}\|_{V_1} \leq \|f_0 - \widetilde{M_0}\|_{V_1} e^{-(\lambda-\gamma)t} + \sup_{0\leq t\leq T} \|Q(t)\|_{V_1} \frac{1 - e^{-(\lambda-\gamma)t}}{\lambda - \gamma}. \tag{6.183}$$

And the convergence of f towards $\widetilde{M}$ is achieved for large λ. □

In a second step, we prove that the observation of H is enough to have convergence of f towards M, where M is defined as follows

$$M = \frac{H}{c} \chi\left(\frac{\xi - u}{c}\right). \tag{6.184}$$

This means that M is entirely built with observations (unlike $\widetilde{M}$) and we want to know if the problem defined by (6.169) leads to a convergence of $(\widehat{H}, \widehat{u})$ towards (H, u). This is the key point of the study on the Saint-Venant system.

Proposition 6.4.7. *Under the hypothesis of Prop.6.4.5, we have* $\forall\ T > 0$

$$\|f - M\|_{V_1} \underset{\lambda\to+\infty}{\longrightarrow} 0 \tag{6.185}$$

Proof of Proposition 6.4.7. The triangular inequality tells us that

$$\|f - M\|_{V_1} \leq \|f - \widetilde{M}\|_{V_1} + \|\widetilde{M} - M\|_{V_1} \tag{6.186}$$

We have already proved in Prop.6.4.5 that $\|f - \widetilde{M}\|_{V_1} \underset{\lambda\to+\infty}{\longrightarrow} 0$. It is clear that $\widetilde{M}$ is also one solution to the data assimilation problem

$$\frac{\partial \widetilde{M}}{\partial t} + \xi \cdot \nabla_x \widetilde{M} - g \frac{\partial z_b}{\partial x} \frac{\partial \widetilde{M}}{\partial \xi} = \lambda(M - \widetilde{M}), \tag{6.187}$$

Subtracting it with gives

$$\frac{\partial \delta}{\partial t} + \xi \cdot \nabla_x \delta - g \frac{\partial z_b}{\partial x} \frac{\partial \delta}{\partial \xi} = -\lambda \delta, \tag{6.188}$$

where $\delta = M - \widetilde{M}$. And since

$$\int_{\mathbb{R}} \delta(t, x, \xi)\ d\xi = H(t, x, \xi) - H(t, x, \xi) = 0,$$

the integration in ξ of (6.188) gives necessarily $u = \widehat{u}$ and therefore $\widetilde{M} = M$ (as soon as u is known at one point e.g. at one of the boundaries). And the proof is complete. □

Remark 6.4.8. *In other words, if (H, u) is a solution to the Saint-Venant system, there are no other solutions of the form $(H, \widehat{u})$ with $u \neq \widehat{u}$.*

6.4.3 Numerical results

Let us start first by some reminder of the techniques used for an appropriate discretization of the shallow water equations without assimilation. To approximate the solution of the Saint-Venant system (6.155)-(6.156), we use a finite volume framework. We assume that the computational domain is discretised by I nodes x_i. We denote C_i the cell of length $\Delta x_i = x_{i+1/2} - x_{i-1/2}$ with $x_{i+1/2} = (x_i + x_{i+1})/2$. For the time discretization, we denote $t^n = \sum_{k\leq n} \Delta t^k$ where the time steps Δt^k will be precised later though a CFL condition. The ratio between the space and time steps is $\sigma_i^n = \Delta t^n/\Delta x_i$. We denote $X_i^n = (H_i^n, q_i^n)$ the approximate solution at time t^n on the cell C_i with $q_i^n = H_i^n u_i^n$.

The hydrostatic reconstruction technique

The hydrostatic reconstruction consists in a modification of the bottom topography and the water depths at the cell interfaces, see [3]. More precisely the quantities $H^n_{i+1/2\pm}$ are defined by

$$H^n_{i+1/2-} = H_i^n + z_{b,i} - z_{b,i+1/2}, \quad H^n_{i+1/2+} = H^n_{i+1} + z_{b,i+1} - z_{b,i+1/2}. \tag{6.189}$$

with

$$\begin{aligned} z_{b,i+1/2} &= \max(z_{b,i}, z_{b,i+1}), \\ \Delta z_{b,i+1/2-} &= z_{b,i+1/2} - z_{b,i}, \\ \Delta z_{b,i-1/2+} &= z_{b,i-1/2} - z_{b,i}. \end{aligned} \tag{6.190}$$

A nonnegativity-preserving truncation of the leading order depths is also applied in (6.189)

$$H^n_{i+1/2\pm} = \max(0, H^n_{i+1/2\pm}). \tag{6.191}$$

Discrete scheme

To precise the numerical scheme, we deduce a finite volume kinetic scheme from the kinetic interpretation (6.165) of the Saint-Venant system. First, we define the discrete densities of particles M_i^n by

$$M_i^n = M_i^n(\xi) = \frac{H_i^n}{c_i^n}\chi\left(\frac{\xi - u_i^n}{c_i^n}\right), \tag{6.192}$$

with $c_i^n = \sqrt{\frac{gH_i^n}{2}}$. Then we propose a discretisation of (6.165) under the form

$$\begin{aligned} M_i^{n+1-} = M_i^n - \sigma_i^n \Bigg(& \xi M^n_{i+1/2} - \xi M^n_{i-1/2} - g\Delta z_{b,i+1/2-} \frac{\partial \overline{M}^n_{i+1/2-}}{\partial \xi} \\ & + g\Delta z_{b,i-1/2+} \frac{\partial \overline{M}^n_{i-1/2+}}{\partial \xi} \Bigg), \end{aligned} \tag{6.193}$$

with

$$\begin{aligned}
M^n_{i+1/2} &= M^n_{i+1/2-}\mathbb{1}_{\xi\geq 0} + M^n_{i+1/2+}\mathbb{1}_{\xi\leq 0},\\
M^n_{i+1/2-} &= \frac{H^n_{i+1/2-}}{c^n_{i+1/2-}}\chi\left(\frac{\xi-u^n_i}{c^n_{i+1/2-}}\right),\\
\overline{M}^n_{i+1/2-} &= \frac{H^n_i + H^n_{i+1/2-}}{2c^n_{i+1/2-}}\chi\left(\frac{\xi-u^n_i}{c^n_{i+1/2-}}\right),\\
\overline{M}^n_{i-1/2+} &= \frac{H^n_i + H^n_{i-1/2+}}{2c^n_{i-1/2+}}\chi\left(\frac{\xi-u^n_i}{c^n_{i-1/2+}}\right).
\end{aligned}$$

We rewrite the preceding scheme under the form

$$M^{n+1-}_i = M^n_i - \sigma^n_i\left(\mathcal{M}^n_{i+1/2} - \mathcal{M}^n_{i-1/2}\right), \tag{6.194}$$

with

$$\begin{aligned}
\mathcal{M}^n_{i+1/2} &= \xi M^n_{i+1/2} - g\Delta z_{b,i+1/2-}\frac{\partial \overline{M}^n_{i+1/2-}}{\partial\xi},\\
\mathcal{M}^n_{i-1/2} &= \xi M^n_{i-1/2} - g\Delta z_{b,i-1/2+}\frac{\partial \overline{M}^n_{i-1/2+}}{\partial\xi}.
\end{aligned}$$

The discrete scheme (6.194) does not take into account the collision term which relaxes M^{n+1-}_i to a Gibbs equilibrium so the quantity M^{n+1-}_i can not be written under the form (6.192). The collision term is used in a second step introducing a discontinuity at time t^{n+1} on M and replacing M^{n+1-}_i by an equilibrium

$$M^{n+1}_i = M^{n+1-}_i + \Delta t^n Q^n_i, \tag{6.195}$$

such that M^{n+1}_i is supposed to be of the form

$$M^{n+1}_i = M^{n+1}_i(\xi) = \frac{H^{n+1}_i}{c^{n+1}_i}\chi\left(\frac{\xi-u^{n+1}_i}{c^{n+1}_i}\right),$$

where H^{n+1}_i and u^{n+1}_i are computed using an integration of (6.194)

$$X^{n+1}_i = \begin{pmatrix} H^{n+1}_i \\ H^{n+1}_i u^{n+1}_i \end{pmatrix} = \int_{\mathbb{R}} \mathcal{K}(\xi) M^{n+1-}_i(\xi)\, d\xi, \tag{6.196}$$

with $\mathcal{K}(\xi)$ is the vector $\mathcal{K}(\xi) = (1,\xi)^T$. Notice that M^{n+1}_i is discontinuous in the sense that $M^{n+1}_i \neq M^{n+1-}_i$ whereas the macroscopic variables remain continuous $X^{n+1}_i = X^{n+1-}_i$.

Fluxes calculus

Using (6.196), we are now able to precise the numerical scheme for the Saint-Venant system (6.155)-(6.157)

$$X_i^{n+1} = X_i^n - \sigma_i^n \left(\mathcal{F}_{i+1/2}^n - \mathcal{F}_{i-1/2}^n \right), \tag{6.197}$$

with

$$\mathcal{F}_{i+1/2}^n = \int_{\mathbb{R}} \mathcal{K}(\xi) \mathcal{M}_{i+1/2}^n(\xi) \, d\xi. \tag{6.198}$$

Now, using (6.194), we are able to precise the computation of the fluxes introduced in the discrete macroscopic equations (4.70). If we denote

$$\mathcal{F}(X_{i+1/2}^n) = \left(\mathcal{F}_H(X_{i+1/2}^n), \mathcal{F}_q(X_{i+1/2}^n) \right)^T,$$

then we have

$$\begin{aligned} \mathcal{F}_H(X_{i+1/2}^n) = H_{i+1/2+}^n \int_{z \leq -\frac{u_{i+1}^n}{c_{i+1/2+}^n}} (u_{i+1}^n + z c_{i+1/2+}^n) \chi(z) \, dz \\ + H_{i+1/2-}^n \int_{z \geq -\frac{u_i^n}{c_{i+1/2-}^n}} (u_i^n + z c_{i+1/2-}^n) \chi(z) \, dz, \end{aligned} \tag{6.199}$$

$$\begin{aligned} \mathcal{F}_q(X_{i+1/2}^n) = H_{i+1/2+} \int_{z \leq -\frac{u_{i+1}^n}{c_{i+1/2+}^n}} (u_{i+1}^n + z c_{i+1/2+}^n)^2 \chi(z) \, dz \\ + H_{i+1/2-}^n \int_{z \geq -\frac{u_i^n}{c_{i+1/2-}^n}} (u_i^n + z c_{i+1/2-}^n)^2 \chi(z) \, dz + \frac{g \Delta z_{b,i+1/2-}}{2} (H_{i+1/2-}^n + H_i^n). \end{aligned} \tag{6.200}$$

Properties of the numerical scheme

The previous scheme exactly corresponds to the original reconstruction technique proposed by Audusse *et al.* [3] with a kinetic solver for the conservative part and therefore it is endowed with the properties depicted in [3, theorem 2.1]. We recall hereafter the statement of the theorem.

Theorem 6.4.9. *The kinetic flux for the homogenous Saint-Venant system is consistent, preserves the nonnegativity of the water depth and satisfies an in-cell entropy inequality corresponding to the entropy ζ in* (6.157)*. Then the finite volume scheme* (6.197) *with the definitions* (6.189),(6.190),(6.191),(6.196),(6.199) *and*(6.200)

(i) preserves the nonnegativity of the water depth,

(ii) preserves the steady state of a lake at rest $H + z_b = cst$,

(iii) is consistent with the Saint-Venant system (6.155)-(6.156)*,*

(iv) satisfies an in-cell entropy inequality associated to the entropy ζ defined in (6.157)

$$\frac{d}{dt}\zeta(X_i(t), z_{b,i}) + \sigma_i^n \left(G_{i+1/2}^n - G_{i-1/2}^n\right) \leq 0.$$

The preceding inequality is a semi-discrete version of (6.157).

Since the proof of the preceeding theorem is similar to the one given in [3, theorem 2.1], it is not detailed here.

Numerical scheme for the data assimilation problem

Let us deal now with the numerical scheme for the assimilation problem (6.169). Since the handling of the topography source terms with hydrostatic reconstruction has been explained in the previous section, we will only consider here the source term associated to the nudging term. We are working on

$$\partial_t f(t,x,\xi) + \xi \cdot \nabla_x f(t,x,\xi) = \lambda \left(\widetilde{M} - f\right), \tag{6.201}$$

for which we propose the two steps numerical scheme composed first of a transport stage

$$f_i^{n+1-} = f_i^n - \sigma_i^n \xi \left(f_{i+1/2}^n - f_{i-1/2}^n\right) + \Delta t^n \lambda \left(\widetilde{M}_i^n - f_i^n\right), \tag{6.202}$$

where the numerical fluxes are computed using a simple upwind scheme

$$f_{i+1/2}^n = \begin{cases} f_i^n, & \text{for } \xi \geq 0 \\ f_{i+1}^n, & \text{for } \xi < 0; \end{cases} \tag{6.203}$$

and a collapse stage that forces f_i^{n+1} to be of the form

$$f_i^{n+1} = \frac{\widehat{H}_i^{n+1}}{\widehat{c}_i^{n+1}} \chi\left(\frac{\xi - \widehat{u}_i^{n+1}}{\widehat{c}_i^{n+1}}\right). \tag{6.204}$$

As in the 1D case for Burgers' equation, this leads, by an integration against ξ of the first two moments, to a macroscopic scheme

$$\widehat{H}_i^{n+1} = \widehat{H}_i^n - \sigma_i^n \left(\left(\mathcal{F}_H(X_{i+1/2}^n) - \mathcal{F}_H(X_{i-1/2}^n)\right)\right) + \lambda \Delta t^n \left(H_i^n - \widehat{H}_i^n\right), \tag{6.205}$$

$$\begin{aligned} \widehat{H}_i^{n+1}\widehat{u}_i^{n+1} = \widehat{H}_i^n \widehat{u}_i^n - \sigma_i^n \left(\mathcal{F}_q(X_{i+1/2}^n) - \mathcal{F}_q(X_{i-1/2}^n)\right) \\ + \lambda \Delta t^n \left(H_i^n \widehat{u}_i^n - \widehat{H}_i^n \widehat{u}_i^n\right). \end{aligned} \tag{6.206}$$

Let us denote

$$e(f) = \frac{\xi^2}{2} f + \frac{g^2}{8k_3} f^3, \tag{6.207}$$

where $k_3 = \int_{\mathbb{R}} \chi^3(\omega) d\omega$,

$$\widehat{E}_i^n = \int_{\mathbb{R}} e(f_i^n)(\xi) d\xi \quad \text{and} \quad \widetilde{E}_i^n = \int_{\mathbb{R}} e(\widetilde{M}_i^n)(\xi) d\xi, \tag{6.208}$$

respectively the observer energy and the observations energy of cell i at time n, and

$$\Lambda_{i+1/2}^n = \int_{\mathbb{R}} \xi e(f_{i+1/2}^n)(\xi) d\xi, \tag{6.209}$$

the energy flux between cell i and cell $i+1$. Then we can state a deeper stability property than the positivity of the water height in the following theorem

Theorem 6.4.10. *Under the CFL condition*

$$\Delta t^n \leq \min_i \frac{\Delta x_i}{\lambda \Delta x_i + |\widehat{u}_i^n| + \widehat{c}_i}, \tag{6.210}$$

the finite volume scheme (6.202) *with the definition* (6.203) *preserves the non-negativity of the water height and admits the discrete entropy inequality:*

$$\widehat{E}_i^{n+1} \leq \widehat{E}_i^n - \sigma_i^n \left(\Lambda_{i+1/2}^n - \Lambda_{i-1/2}^n \right) + \lambda \Delta t^n \left(\widetilde{E}_i^n - \widehat{E}_i^n \right). \tag{6.211}$$

Proof. Proof of Theorem 6.4.10 Let us denote

$$f^+ = \max(f, 0) \quad \text{and} \quad f^- = \min(f, 0).$$

From (6.201), the scheme (6.202) with (6.203) leads to

$$f_i^{n+1-} = f_i^n - \sigma_i^n \xi^+ \left(f_i^n - f_{i-1}^n \right) - \sigma_i^n \xi^- \left(f_{i+1}^n - f_i^n \right) + \lambda \Delta t^n \left(\widetilde{M}_i^n - f_i^n \right), \tag{6.212}$$

which can be rewritten

$$f_i^{n+1-} = f_i^n \left(1 - \sigma_i^n \xi^+ + \sigma_i^n \xi^- - \lambda \Delta t^n \right) + \sigma_i^n \xi^+ f_{i-1}^n - \sigma_i^n \xi^- f_{i+1}^n + \lambda \Delta t^n \widetilde{M}_i^n. \tag{6.213}$$

Under the condition that

$$1 - \sigma_i^n |\xi| - \lambda \Delta t^n \leq 0, \tag{6.214}$$

which can be written under the form of the CFL condition

$$\Delta t^n \leq \min_{i \in \mathcal{I}} \frac{\Delta x_i}{\lambda \Delta x_i + |\widehat{u}_i^n| + \widehat{c}_i}, \tag{6.215}$$

the scheme (6.213) is a convex combination of $f_i^n, f_{i-1}^n, f_{i+1}^n$ and M_i^n. As a consequence, we can claim that if the initial condition is non-negative, and so are the observations, the density f_i^n remains positive for any time, *a fortiori* the water height. The scheme preserves the non-negativity of the water height. In the case where $f \geq 0$, it is a convex function,

which enables us to write for the convex combination (6.213)

$$e(f_i^{n+1-}) \leq \left(1 - \sigma_i^n \xi^+ + \sigma_i^n \xi^- - \lambda \Delta t^n\right) e(f_i^n) + \sigma_i^n \xi^+ e(f_{i-1}^n) - \sigma_i^n \xi^- e(f_{i+1}^n) + \lambda \Delta t^n e(\widetilde{M}_i^n) \quad (6.216)$$

And (6.216) is factorized again as

$$e(f_i^{n+1-}) = e(f_i^n) - \sigma_i^n \xi \left(e(f_{i+1/2}^n) - e(f_{i-1/2}^n)\right) + \lambda \Delta t^n \left(e(\widetilde{M}_i^n) - e(f_i^n)\right). \quad (6.217)$$

We integrate (6.217) with respect to ξ

$$\widehat{E}_i^{n+1-} \leq \widehat{E}_i^n + \sigma_i^n \left(\Lambda_{i+1/2}^n - \Lambda_{i-1/2}^n\right) + \lambda \Delta t^n \left(\widetilde{E}_i^n - \widehat{E}_i^n\right). \quad (6.218)$$

Eventually, Lemma 6.4.2 ensures that the minimum of energy is achieved for the Gibbs equilibrium of the form (6.204), authorizing us to write

$$\int_{\mathbb{R}} e(f_i^{n+1}) d\xi = \widehat{E}_i^{n+1} \leq \widehat{E}_i^{n+1-} \leq \widehat{E}_i^n - \sigma_i^n \left(\Lambda_{i+1/2}^n - \Lambda_{i-1/2}^n\right) + \lambda \Delta t^n \left(\widetilde{E}_i^n - \widehat{E}_i^n\right). \quad (6.219)$$

□

With the discrete entropy inequality (6.211), we can deduce an upper bound of the total energy. For this computation, we will consider that we are able to impose the kinetic boundary conditions f_0^n and f_{N+1}^n such that at the macroscopic level

$$\Lambda_{1/2}^n = \Lambda_{N+1/2}^n \quad (6.220)$$

Therefore, we can sum over all cells $i \in \{1..N-1\}$ and we get rid of the entropy fluxes as soon as σ_i^n is uniform in space (does not depend on i), ending up with

$$\widehat{\mathcal{E}}^{n+1} \leq \widehat{\mathcal{E}}^n + \lambda \Delta t^n \left(\widetilde{\mathcal{E}}^n - \widehat{\mathcal{E}}^n\right), \quad (6.221)$$

where $\widehat{\mathcal{E}}^n = \sum_{i \in I} \widehat{E}_i^n$ and $\widetilde{\mathcal{E}}^n = \sum_{i \in I} \widetilde{E}_i^n$. This also writes

$$\widehat{\mathcal{E}}^{n+1} \leq (1 - \lambda \Delta t^n) \widehat{\mathcal{E}}^n + \lambda \Delta t^n \widetilde{\mathcal{E}}^n. \quad (6.222)$$

Using the fact that $1 - \mu \leq e^{-\mu}$, $\forall \mu \geq 0$, we obtain

$$\widehat{\mathcal{E}}^{n+1} \leq e^{-\lambda \Delta t^n} \widehat{\mathcal{E}}^n + \lambda \Delta t^n \widetilde{\mathcal{E}}^n. \quad (6.223)$$

An easy induction leads to

$$\widehat{\mathcal{E}}^{n+1} \leq e^{-\lambda \sum_{k=0}^{n} \Delta t^k} \widehat{\mathcal{E}}^0 + \lambda \sum_{k=0}^{n} e^{-\lambda \left(\sum_{l=k+1}^{n} \Delta t^l \right)} \Delta t^k \widetilde{\mathcal{E}}^k. \tag{6.224}$$

$$\widehat{\mathcal{E}}^{n+1} \leq e^{-\lambda t^{n+1}} \widehat{\mathcal{E}}^0 + \lambda \sum_{k=0}^{n} e^{-\lambda (t^{n+1} - t^{k+1})} \Delta t^k \widetilde{\mathcal{E}}^k. \tag{6.225}$$

Remark 6.4.11. *We notice that if λ tends to infinity in (6.225), with the CFL condition (6.210), we end up with*

$$\widehat{\mathcal{E}}^{n+1} \leq \widetilde{\mathcal{E}}^n. \tag{6.226}$$

The convergence of $\widehat{\mathcal{E}}^n$ towards $\widetilde{\mathcal{E}}^n$ suggested by Proposition 6.4.5, and, even better towards $\widetilde{\mathcal{E}}^n$ suggested by Proposition 6.4.7 is not straightforward. We do not detail it here but it will appear in the publication.

Simulations

In order to show how the kinetic Luenberger observer converges to non trivial equilibria, the first test case in two dimensions are the Thacker solutions [138]. Those are analytical periodic solutions to the Saint-Venant system in a parabolic bowl for which the free surface always remains a straight line. They are quite difficult to handle numerically, because of the presence of numerous drying and flooding areas in time. The domain is thus the onedimensional parabolic bowl determined by

$$z_b(x) = \frac{h_m}{a^2} \left(\left(x - \frac{L}{2} \right)^2 - a^2 \right),$$

where $a = 1.0$, $L = 4.0$ and $h_m = 0.5$. Our reference solution, which will serve as observations, starts with an initial water height

$$H(0, x) = \max(0, -h_m/a^2((x + 1/2)^2 - a^2)),$$

and null velocity $u(0, x) = 0$. This makes the surface a straight line of equation $\eta(x) = \frac{-h_m}{a^2}(4x - 0.25)$. The assimilated problem on the contrary starts from an equilibria

$$\widehat{H}(0, x) = max(0, -z_b(x)),$$

$u(0, x) = 0$, such that the surface has equation $\eta(x) = 0$. The domain is divided into 300 cells and the simulation lasts 15 seconds. Exact observations are carried out over the spatial interval $[1.5, 2.5]$ (25% of the domain) and every 0.05s. Figure 6.4 shows snapshots of the evolution of an observer towards an analytical Thacker solution. Visually at least, the observer seems to converge quite fast towards the observations. Then, we study the relative error between the exact height and the observer's height. In order to illustrate the

different convergence results with respect to λ, we repeat the experiment for several values of the nudging coefficient. Figure 6.5 shows the result in the case where observations are exact, but partial in space and time. We obtain two rapidly decreasing curves, which goes approximately to zero when λ gets bigger (the residual error is due to the discretization of the numerical scheme). This is what was expected from Proposition 6.4.5: without noise, the bigger λ, the better. However, this assessement is not true numerically as λ influences badly the time step (6.210). Figure 6.6 shows the same situation, when the noise already used in Section 6.3.7 is added to data ($\varepsilon^{1-\alpha}\cos(\frac{x}{\varepsilon})$, with $\varepsilon = 0.1$ and $\alpha = 0.25$). Even if Theorem 6.3.11 did not apply to systems of conservation laws with source terms, we see clearly here that there is an optimal λ (here around 13), balancing the fact that the gain improves the match with data but also amplifies the noise. We notice also that the L^1 error norm does not tend to zero, since it cannot get rid of the perturbations added on the data.

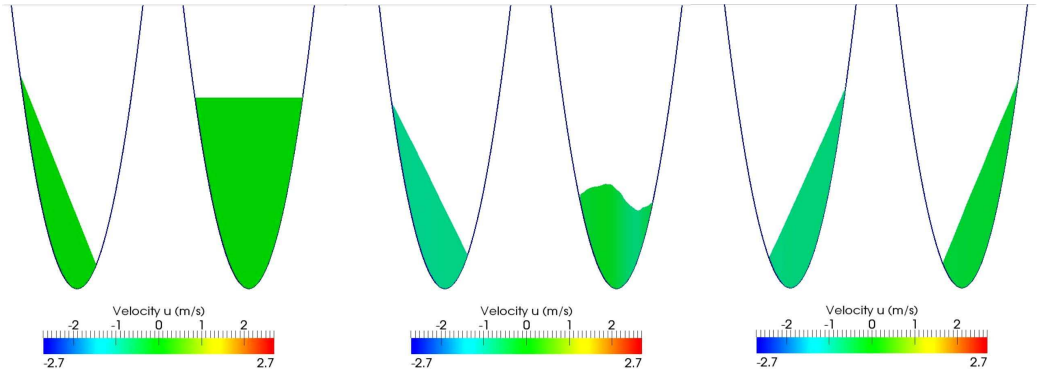

Figure 6.4: Evolution of Thackers solution at $t = 0$s, $t = 2$s and $t = 5$s. For each time, the left plot is the reference solution and the right plot is the observer. To give a better insight, an animation can viewed on my website http://www.ljll.math.upmc.fr/ Boulanger/?page=animation.

Then, we propose a numerical test of our kinetic Luenberger observer on the non-hydrostatic Saint-Venant system detailed in [36], that we recall here without proof.

$$\frac{\partial H}{\partial t} + \frac{\partial}{\partial x}(Hu) = 0, \tag{6.227}$$

$$\frac{\partial (Hu)}{\partial t} + \frac{\partial (Hu^2)}{\partial x} + \frac{\partial (Hp)}{\partial x} = -p|_b \frac{\partial z_b}{\partial x} + p^a \frac{\partial \eta}{\partial x}, \tag{6.228}$$

$$w = -(z - z_b)\frac{\partial u}{\partial x} + \frac{\partial z_b}{\partial x} u, \tag{6.229}$$

$$Hp = Hp^a + \frac{g}{2}H^2 + \frac{\partial}{\partial t}\int_{z_b}^{\eta}\int_{z}^{\eta} w dz' dz + \frac{\partial H^2}{\partial t}\left(H\frac{\partial u}{\partial x} - \frac{\partial z_b}{\partial x}u\right), \tag{6.230}$$

$$p|_b = p^a + gH + \frac{\partial}{\partial t}\int_{z_b}^{\eta} w dz + 2\frac{\partial H}{\partial t}\left(H\frac{\partial u}{\partial x} - \frac{\partial z_b}{\partial x}u\right) \tag{6.231}$$

No theoretical work has yet been pursued by the authors about data assimilation on this system, but we extended the result on the observer built for the Saint-Venant system, where

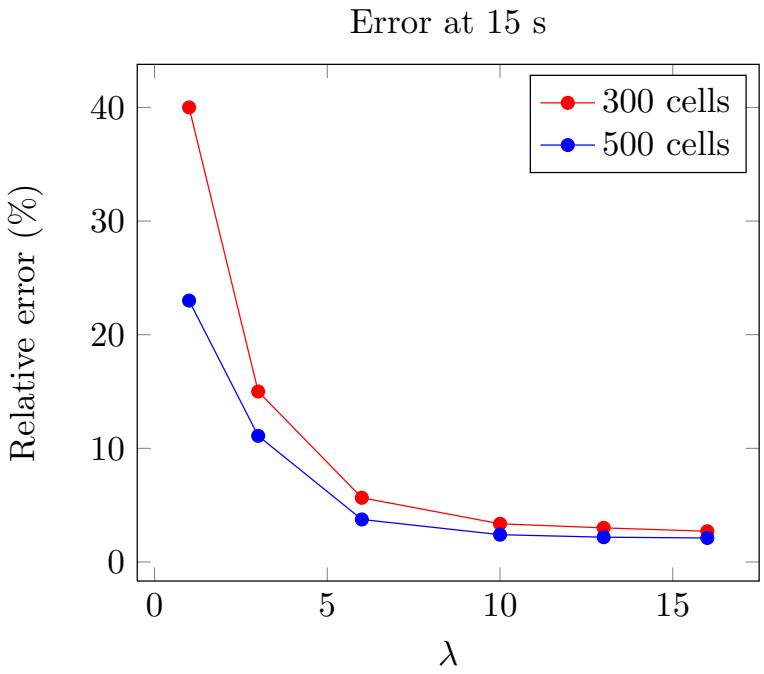

Figure 6.5: Thackers solution. Relative error $\frac{\|\widehat{H}-H\|_{L^1}}{\|H\|_{L^1}}$ for different values of λ.

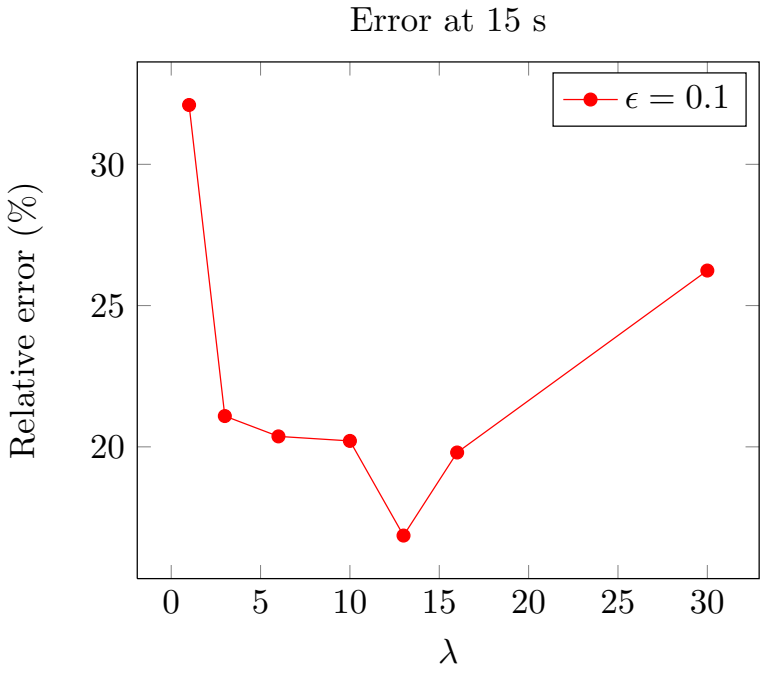

Figure 6.6: Thackers noisy solution. Relative error $\frac{\|\widehat{H}-H\|_{L^1}}{\|H\|_{L^1}}$ for different values of λ in the case where a noise is added to the observations.

only the water height was required. The context is now a bidimensional 30m long pond, with the bottom topography

$$z_b(x) = \begin{cases} z_0, & \text{for } x \leq 6 \\ z_0 + \dfrac{z_M - z_0}{6}(x-6), & \text{for } 6 \leq x < 12 \\ z_M & \text{for } 12 \leq x \leq 14 \\ z_M + \dfrac{z_0 - z_M}{3}(x-14) & \text{for } 14 \leq x \leq 17 \\ z_0 & \text{for } 17 \leq x \leq 30, \end{cases}$$

where $z_0 = -0.4$, $z_M = -0.1$. The domain is divided into 400 cells, and the simulation lasts 20s. Observations are made on the whole domain in space and time, but only on $H(t,x)$. Contrary to what was done for Thackers solutions, an interpolation in time is carried out between two measurements to provide an observation value every 0.05s. Figure 6.7 and Figure 6.8 show the compared evolution of the reference simulation on the left, and of the observer, on the right. Both simulations started with completely different initial conditions. The reference initial condition is, for $x_{max} = 30$ and $\eta_1 = 0.2$

$$\begin{cases} H_0(x) = \eta_1 - z_b(x) + 0.3e^{-(x-0.75x_{max})^2} \\ Hu_0(x) = 0.3\sqrt{g(\eta_1 - z_b(x))}e^{-(x-0.75x_{max})^2}, \end{cases} \tag{6.232}$$

While the observer begins with a completely different water height, for $\eta_2 = 1$ this time

$$\begin{cases} H_0(x) = \eta_2 - z_b(x) \\ Hu_0(x) = 0.3\sqrt{g(\eta_1 - z_b(x))}e^{-(x-0.75x_{max})^2}, \end{cases} \tag{6.233}$$

Once again, the convergence of the observer seems visually correct. We propose in Figure 6.9 a plot of the relative error between exact and complete observations in space, every 0.08 s or 0.04s. Even if, once again, our results do not apply to this system, we can see that the observer built only from the knowledge of the water height is also efficient in this case. The decrease of the error with λ is obtained like for Thackers solutions. We may also notice that the time between two measurements influences the error, as it provides a better interpolation process.

6.5 Discussion

In this chapter, we proposed a new method for data assimilation on hyperbolic conservation laws. After the introduction of some required background in kinetic theory that may seem complicated, we end up with a quite simple process based on a Luenberger observer. Usually, when tackling a problem on hyperbolic balance laws, the scalar case permits the development of a great theoretical framework, that is unfortunately hardly extendable to systems. In our case, theoretical results on hyperbolic scalar conservation laws are developed and validated numerically in a first part. Then, in a second part we work on the Saint-Venant

system. Though the theory is less satisfying, we can still build an efficient observer on the shallow water equations and provide an entropy satisfying numerical scheme to handle it. However, when dealing with more complex system like the non-hydrostatic Saint-Venant system or even the free surface hydrostatic Navier-Stokes equations, no proofs are available for now. Nevertheless, we were able to extrapolate our method on those systems and the results are encouraging. Further perpectives of this work may include the building of a Kalman filter and the use of relative entropy theory to prove more convergence results in time. Besides, we can also think of applying our method to other existing data assimilation strategies.

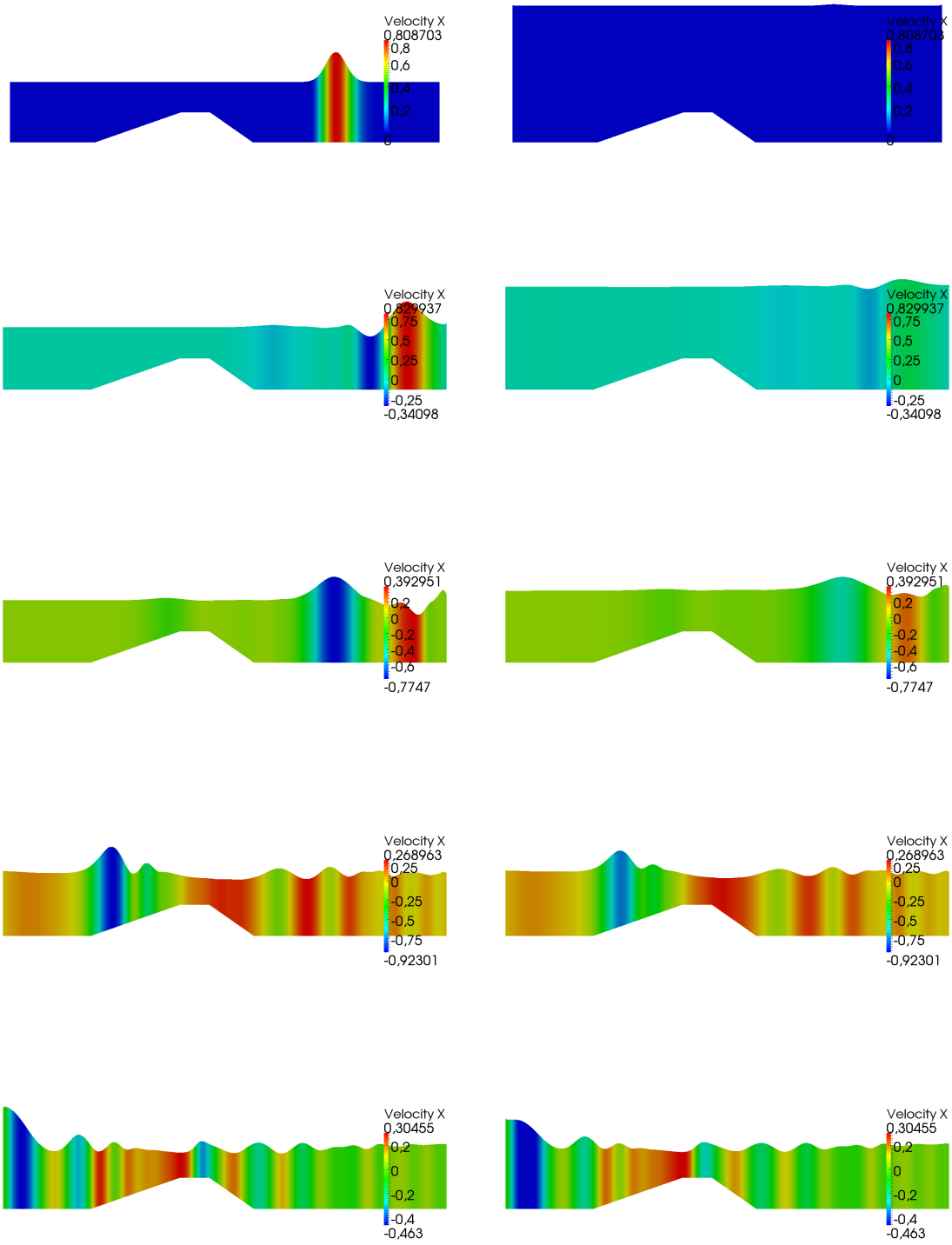

Figure 6.7: Snapshots of data assimilation on the non-hydrostatic Saint-Venant system, compared to the reference simulation for the horizontal velocity.To give a better insight, an animation can viewed on my website http://www.ljll.math.upmc.fr/ Boulanger/?page=animation.

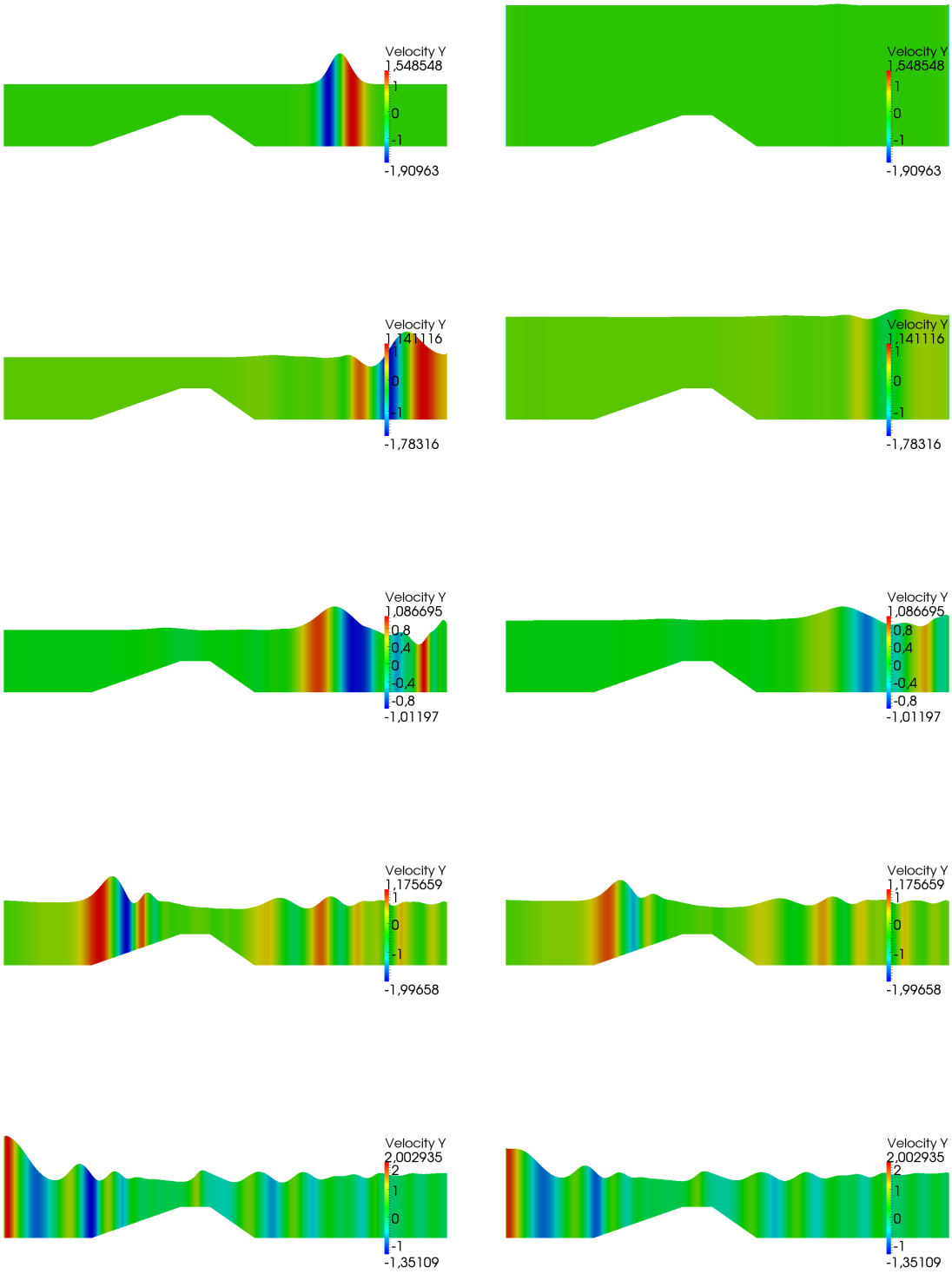

Figure 6.8: Snapshots of data assimilation on the non-hydrostatic Saint-Venant system, compared to the reference simulation for the vertical velocity.To give a better insight, an animation can viewed on my website http://www.ljll.math.upmc.fr/ Boulanger/?page=animation.

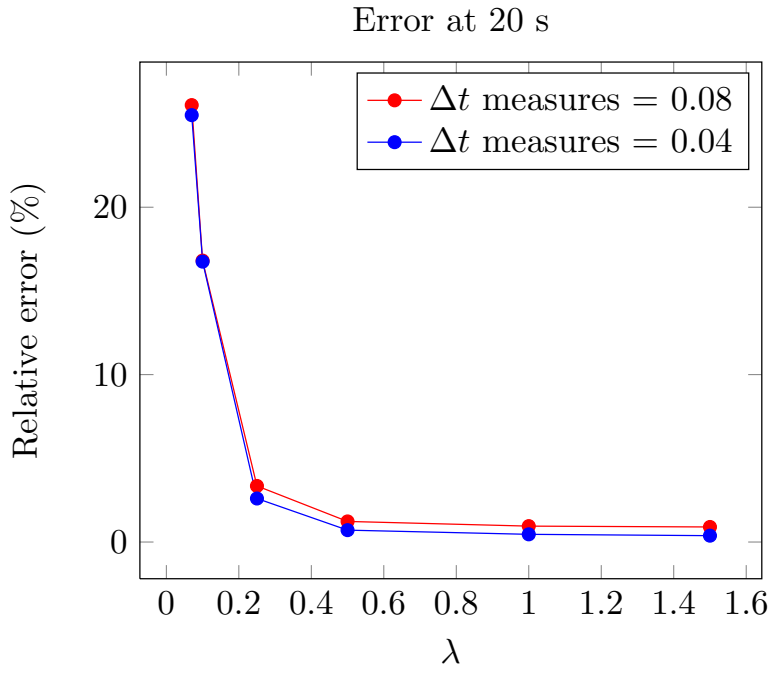

Figure 6.9: Relative error $\frac{\|\widehat{H}-H\|_{L^1}}{\|H\|_{L^1}}$ for different values of λ for the non-hydrostatic Saint-Venant system. Two observations time steps are tested.

Regularization of hyperbolic equations

A

A.1 Regularization of hyperbolic equations (space)

Definition A.1.1. *A regularizing kernel is a function satisfying the following properties*

$$\omega \in \mathcal{D}(\mathbb{R}^d), \quad \omega \geq 0, \quad \int_{\mathbb{R}^d} \omega = 1 \tag{A.1}$$

We regularize functions by convolution by setting

$$f * \omega(x) = \int_{\mathbb{R}^d} f(x-y)\omega(y)dy = \int_{\mathbb{R}^d} f(y)\omega(x-y)dy$$

We precise that for $f \in L^1(\mathbb{R}^d)$, we have $f * \omega \in L^1(\mathbb{R}^d)$.

Definition A.1.2. *We call mollifier any sequence of functions (ω_ϵ) such that*

$$\omega_\epsilon \in \mathcal{D}(\mathbb{R}^d), \quad Supp\ \omega_\epsilon \subset B(0,\epsilon), \quad \int_{\mathbb{R}^d} \omega_\epsilon = 1, \quad \omega_\epsilon \geq 0\ over\ \mathbb{R}^d. \tag{A.2}$$

Given a regularizing kernel ω, we build a mollifier:

$$\omega_\epsilon = \frac{1}{\epsilon^d}\omega(\frac{x}{\epsilon}).$$

Proposition A.1.3. *Let ω be a regularizing kernel, $M \in C([0,T], L^1(\mathbb{R}^d_x \times \mathbb{R}_\xi))$ and $f_0 \in L^1(\mathbb{R}^d_x \times \mathbb{R}_\xi)$. Let $f \in C([0,T], L^1(\times\mathbb{R}^d_x \times \mathbb{R}_\xi))$ $\forall T > 0$ be a weak solution of*

$$\partial_t f(t,x,\xi) + a(\xi) \cdot \nabla_x f(t,x,\xi) + \lambda f(t,x,\xi) = M(t,x,\xi) \tag{A.3}$$

Then $f * \omega$ belongs to $C^1(R^+; L^1(\mathbb{R}_\xi) \times C^1(\mathbb{R}^d_x))$ and is a classical solution to (A.3) for a regularized right hand side $M * \omega$ and an initial data $f_0 * \omega$.

Proof of Proposition A.1.3. The aim here is to prove the C^1 differentiability in time of f_ω, the rest being obvious. The proof is inspired from regularization processes about weak solutions to parabolic equations in [114](Chap.3). By definition of a weak solution, we have for a test function $\Phi \in \mathcal{D}([0,\infty] \times \mathbb{R}^d_x \times \mathbb{R}_\xi)$

$$\int_0^\infty \int_{\mathbb{R}^{d+1}} \left(\partial_t f + a(\xi) \cdot \nabla_x f + \lambda f\right) \Phi(t,x,\xi) dx d\xi dt = \int_0^\infty \int_{\mathbb{R}^{d+1}} \lambda M \Phi(t,x,\xi) dx d\xi dt \tag{A.4}$$

An integration by parts leads to

$$\begin{aligned}\int_0^\infty \int_{\mathbb{R}^{d+1}} \left(-\partial_t \Phi - a(\xi) \cdot \nabla_x \Phi + \lambda \Phi\right) f(t,x,\xi) dx d\xi dt = &\int_0^\infty \int_{\mathbb{R}^{d+1}} \lambda M \Phi(t,x,\xi) dx d\xi dt \\ &+ \int_{\mathbb{R}^{d+1}} f_0(x,\xi) \Phi(0,x,\xi) dx d\xi\end{aligned} \tag{A.5}$$

We use the test function $\Phi(t,x,\xi) = \phi(t)\psi(\xi)\omega(y-x)$ with $y \in \mathbb{R}^d$ a fixed vector, $\phi \in \mathbb{R}^+$ and $\psi \in \mathbb{R}$ given test functions and ω a regularizing kernel. Following (A.4) we start with

$$\begin{aligned}&-\int_0^\infty \int_{\mathbb{R}^{d+1}} \left[f(t,x,\xi)\omega(y-x)\psi(\xi)\partial_t\phi(t) + f(t,x,\xi)a(\xi)\cdot\nabla_x\omega(y-x)\psi(\xi)\phi(t)\right] dx d\xi dt \\ &+ \int_0^\infty \int_{\mathbb{R}^{d+1}} \lambda f(t,x,\xi)\omega(y-x)\psi(\xi)\phi(t) dx d\xi dt \\ &= \int_0^\infty \int_{\mathbb{R}^{d+1}} \lambda M(t,x,\xi)\omega(y-x)\psi(\xi)\phi(t) dx d\xi dt - \int_{\mathbb{R}^{d+1}} f_0(x,\xi)\psi(\xi)\omega(y-x)\phi(0) dx d\xi\end{aligned} \tag{A.6}$$

Let us denote $f_\omega(t,x,\xi) = f * \omega$ and $M_\omega(t,x,\xi) = M * \omega$. Both functions are smooth in x. Putting apart the ξ integral which can be factorized in each term, and changing the name of the space variable from y to x, (A.6) reduces to (for a.e. ξ)

$$\begin{aligned}\int_0^\infty -f_\omega(t,x,\xi)\partial_t\phi dt = &\int_0^\infty \left[a(\xi)\cdot\nabla_x f_\omega(t,x,\xi) + \lambda\left(M_\omega(t,x,\xi) - f_\omega(t,x,\xi)\right)\right]\phi(t) dt \\ &+ f_\omega(0,x,\xi)\phi(0)\end{aligned} \tag{A.7}$$

In order to conclude on the time C^1-differentiability of f_ω, we proceed as follows. Let $T > 0$ and consider the function $\phi(t) = \mathbb{1}_{0\le t\le T}$. We build a series of admissible test functions from it, satisfying the properties:

$$\phi_n \in \mathcal{D}(\mathbb{R}^+), \quad \phi_n \text{ decreasing }, \quad \phi_n(t) \le \phi(t), \quad \phi_n(t) = 1 \text{ on } \left[0, T - \frac{1}{n}\right].$$

Using ϕ_n as test function in (A.7) we end up with

$$\int_0^\infty -f_\omega(t,x,\xi)\partial_t\phi_n(t)dt = \int_0^\infty \left[a(\xi)\cdot\nabla_x f_\omega(t,x,\xi) + \lambda\left(M_\omega(t,x,\xi) - f_\omega(t,x,\xi)\right)\right]\phi_n(t)dt + f_\omega(0,x,\xi) \tag{A.8}$$

We set $H = a(\xi)\cdot\nabla_x f_\omega(t,x,\xi) + \lambda\left(M_\omega(t,x,\xi) - f_\omega(t,x,\xi)\right)$. By the Lebesgue Dominated Convergence Theorem applied to H, we have

$$\int_0^\infty H(t,x,\xi)\phi_n(t)dt + f_\omega(0,x,\xi) \underset{n\to+\infty}{\longrightarrow} \int_0^T H(t,x,\xi)dt + f_\omega(0,x,\xi)$$

In the same manner, choosing ϕ_n for each Lebesgue point T,

$$\int_0^\infty -f_\omega(t,x,\xi)\partial_t\phi_n(t)dt \underset{n\to+\infty}{\longrightarrow} f_\omega(T,x,\xi).$$

Hence,

$$f_\omega(x,\xi,T) = \int_0^T H(t,x,\xi)dt + f_\omega(0,x,\xi) \tag{A.9}$$

This proves that $f_\omega \in C(\mathbb{R}^+)$. Besides, $\nabla_x f_\omega = f * \nabla_x\omega$ and time continuity of H follows. *A fortiori* $f_\omega \in C^1(\mathbb{R}^+)$. □

Lemma A.1.4. *Let $M \in L^p(\mathbb{R}^d)$ with $1 \le p \le \infty$ and ω_ϵ a mollifier. We define $M_\epsilon = M * \omega_\epsilon$. Then*

$$\|\nabla_x M_\epsilon\|_{L^p} = \left(\sum_{i=1}^d \|\partial_{x_i} M_\epsilon\|_{L^p}^p\right)^{1/p} \le C\frac{\|M\|_{L^p}}{\epsilon}.$$

Proof of Lemma A.1.4. First of all, let us notice that $\nabla M_\epsilon = \nabla\left(M * \omega_\epsilon\right) = M * \nabla\omega_\epsilon$ and $\partial_{x_i} M_\epsilon = M * \partial_{x_i}\omega_\epsilon$. Moreover, since $M \in L^p(\mathbb{R}^d)$ and $\partial_{x_i}\omega_\epsilon \in L^1(\mathbb{R}^d)$, we know from a classical theorem on convolution (see [35] for instance)that $\nabla M_\epsilon \in L^2$ and

$$\|\partial_{x_i} M_\epsilon\|_{L^p} \le \|M\|_{L^p}\|\partial_{x_i}\omega_\epsilon\|_{L^1}.$$

Eventually, computing $\|\partial_{x_i}\omega_\epsilon\|_{L^1}$ we find

$$\begin{aligned}\|\partial_{x_i}\omega_\epsilon\|_{L^1} &= \int_{\mathbb{R}^d} |\partial_{x_i}\omega_\epsilon(x)|dx \\ &= \frac{1}{\epsilon^{n+1}}\int_{\mathbb{R}^d} |\partial_{x_i}\omega(\frac{x}{\epsilon})|dx \\ &= \frac{1}{\epsilon}\int_{\mathbb{R}^d} |\partial_{z_i}\omega(z)|dz\end{aligned} \tag{A.10}$$

We end up with

$$\|\partial_{x_i} M_\epsilon\|_{L^p} \le \int_{\mathbb{R}^d} |\partial_{z_i}\omega(z)|dz\frac{\|M\|_{L^p}}{\epsilon},$$

and this concludes the proof. □

A.2 Regularization of hyperbolic equations (time)

Regularization in time introduces a technical issue because $t > 0$ and a simple convolution with a regularizing kernel of previous section is not possible. That is why we introduce an asymmetric regularizing kernel $\tilde{\omega}$.

Definition A.2.1. *An asymmetric regularizing kernel $\tilde{\omega}$ is a function satisfying the properties:*

$$\tilde{\omega} \in \mathcal{D}(\mathbb{R}^d), \quad \tilde{\omega} \leq 0, \quad \tilde{\omega}(s) = 0 \text{ for } s \geq 0, \quad \int_{\mathbb{R}^d} \omega = 1 \tag{A.11}$$

Then the regularization by convolution of a function $f(t) : \mathbb{R}^+ \longrightarrow \mathbb{R}$ is made in the following way

$$\tilde{\omega} *_t f(t) = \int_{\mathbb{R}} \tilde{\omega}(t-s) f(s) ds. \tag{A.12}$$

(A.12) is indeed well defined because $t - s$ needs to be greater than 0. This leads, for $t \geq 0$, to $s \geq 0$.

Proposition A.2.2. *Let ω be a symetric regularizing kernel, and $\tilde{\omega}$ be an asymmetric regularizing kernel, $M \in C([0,T], L^1(\mathbb{R}^d_x \times \mathbb{R}_\xi))$ and $f_0 \in L^1(\mathbb{R}^d_x \times \mathbb{R}_\xi)$. Let $f \in C([0,T], L^1(\mathbb{R}^d_x \times \mathbb{R}_\xi)) \forall T > 0$ be a weak solution of*

$$\partial_t f(t,x,\xi) + a(\xi) \cdot \nabla_x f(t,x,\xi) + \lambda f(t,x,\xi) = M(t,x,\xi) \tag{A.13}$$

Then $f *_x \omega *_t \tilde{\omega}$ belongs to $C^1(R^+; L^1(\mathbb{R}_\xi) \times C^1(\mathbb{R}^d_x))$ and is a classical solution to (A.13) for a regularized right hand side $M *_x \omega *_t \tilde{\omega}$ and an initial data $f_0 *_x \omega$.

Proof. The problem here is the recovery of the initial data. The proof is based on the same tools as previous proof. We do not detail it here. □

Proofs of noise theorems - instationary case

B

B.1 Proof of Theorem 6.3.13

Applying the space Fourier transform to (6.121) leads to

$$\partial_t \widehat{g} + \xi \cdot (ik)\widehat{g} + \lambda \widehat{g} = \lambda k^\alpha \widehat{E} - \widehat{Q}, \tag{B.1}$$

where $k^\alpha = \prod_{i=1}^N k_i^{\alpha_i}$. Solving this equation in the sense of distributions we get

$$\begin{aligned} \widehat{g}(t,k,\xi) &= \widehat{g}_0(k,\xi) e^{-(\lambda + ik\cdot\xi)t} \\ &\quad + \int_0^t e^{-(\lambda+ik\cdot\xi)s} \left(\lambda k^\alpha \widehat{E}(t-s,k,\xi) - \widehat{Q}(t-s,k,\xi) \right) ds \end{aligned} \tag{B.2}$$

Therefore, multiplying (B.2) by ψ and integrating in ξ we get

$$\begin{aligned} \widehat{\rho}_\psi(t,k) &= e^{-\lambda t} \int_{\mathbb{R}_\xi} e^{-ik\cdot\xi t} \widehat{g}_0(k,\xi)\psi(\xi) d\xi \\ &\quad + \int_0^t e^{-\lambda s} \int_{\mathbb{R}_\xi} e^{-ik\cdot\xi s} \left(\lambda k^\alpha \widehat{E}(s,k,\xi)\psi(\xi) - \widehat{Q}(t,k,\xi)\psi(\xi) \right) d\xi ds \end{aligned} \tag{B.3}$$

Let us define now the operator $\mathcal{F}$ which is the Fourier transform in x and ξ

$$\mathcal{F}(f)(k,v) = \int_{\mathbb{R}} e^{-i\xi\cdot v} \widehat{f}(k,\xi) d\xi. \tag{B.4}$$

We can rewrite (B.3)

$$\widehat{\rho}_\psi(t,k) = e^{-\lambda t} \mathcal{F}(g_0\psi)(k,kt) + \int_0^t e^{-\lambda s} \mathcal{F}\left(\lambda \frac{\partial^\alpha E}{\partial x^\alpha}\psi - Q\psi \right)(t-s,k,ks) ds \tag{B.5}$$

Young's inequality provides

$$\begin{aligned}|\widehat{\rho}_\psi(t,k)|^2 \leq\ & 2e^{-2\lambda t}|\mathcal{F}(g_0\psi)(k,kt)|^2 \\ & + 2\left|\int_0^t e^{-\lambda s}\mathcal{F}\left(\lambda\frac{\partial^\alpha E}{\partial x^\alpha}\psi - Q\psi\right)(t-s,k,ks)ds\right|^2\end{aligned} \tag{B.6}$$

Then we use Cauchy Schwartz inequality with weight $e^{-\lambda t}$ to get

$$\begin{aligned}|\widehat{\rho}_\psi(t,k)|^2 \leq\ & 2e^{-2\lambda t}|\mathcal{F}(g_0\psi)(k,kt)|^2 \\ & + 2\left(\int_0^t e^{-\lambda s}ds\right)\int_0^t e^{-\lambda s}\left|\mathcal{F}\left(\lambda\frac{\partial^\alpha E}{\partial x^\alpha}\psi - Q\psi\right)(t-s,k,ks)\right|^2 ds\end{aligned} \tag{B.7}$$

We obtain, with a change of variable $\tau = t - s$

$$\begin{aligned}\int_0^T |\widehat{\rho}_\psi(t,k)|^2 dt \leq\ & 2\int_0^T e^{-2\lambda t}|\mathcal{F}(g_0\psi)(k,kt)|^2 dt \\ & + \frac{2}{\lambda}\int_0^T\int_0^t e^{-\lambda s}\left|\mathcal{F}\left(\lambda\frac{\partial^\alpha E}{\partial x^\alpha}\psi - Q\psi\right)(t-s,k,ks)\right|^2 dsdt \\ \leq\ & 2\int_0^T e^{-2\lambda t}|\mathcal{F}(g_0\psi)(k,kt)|^2 dt \\ & + \frac{2}{\lambda}\int_0^T\int_0^T e^{-\lambda s}\left|\mathcal{F}\left(\lambda\frac{\partial^\alpha E}{\partial x^\alpha}\psi - Q\psi\right)(\tau,k,ks)\right|^2 dsd\tau\end{aligned} \tag{B.8}$$

Using the estimate

$$\forall s \geq 0,\ e^{-\lambda s} \leq 1, \tag{B.9}$$

we can write

$$\begin{aligned}\int_0^T |\widehat{\rho}_\psi(t,k)|^2 dt \leq\ & 2\int_0^T |\mathcal{F}(g_0\psi)(k,kt)|^2\, dt \\ & + \frac{2}{\lambda}\int_0^T\int_0^T \left|\mathcal{F}\left(\lambda\frac{\partial^\alpha E}{\partial x^\alpha}\psi - Q\psi\right)(\tau,k,ks)\right|^2 dsd\tau\end{aligned} \tag{B.10}$$

We proceed to the substitution $z = |k|t$ in the first integral and $z = |k|s$ in the second one.

$$\begin{aligned}\int_0^T |\widehat{\rho}_\psi(t,k)|^2 dt \leq\ & \frac{2}{|k|}\int_0^{|k|T}\left|\mathcal{F}(g_0\psi)(k,\frac{k}{|k|}z)\right|^2 dz \\ & + \frac{2}{\lambda|k|}\int_0^T\int_0^{|k|T}\left|\mathcal{F}\left(\lambda\frac{\partial^\alpha E}{\partial x^\alpha}\psi - Q\psi\right)(\tau,k,\frac{k}{|k|}z)\right|^2 dsd\tau \\ \leq\ & \frac{2}{|k|}\int_{-\infty}^{+\infty}\left|\mathcal{F}(g_0\psi)(k,\frac{k}{|k|}z)\right|^2 dz \\ & + \frac{2}{\lambda|k|}\int_0^T\int_{-\infty}^{+\infty}\left|\mathcal{F}\left(\lambda\frac{\partial^\alpha E}{\partial x^\alpha}\psi - Q\psi\right)(\tau,k,\frac{k}{|k|}z)\right|^2 dsd\tau\end{aligned} \tag{B.11}$$

Now let us introduce the following trace lemma.

Lemma B.1.1. *Let $\Phi \in H^s(\mathbb{R}^d_\xi)$ with $s > \frac{d-1}{2}$. Then, for any $\sigma \in \mathbb{R}^d$ such that $|\sigma| = 1$,*

$$\|\Phi(\sigma z)\|_{L^2(z\in\mathbb{R})} \leq C_{d,s}\|(Id - \Delta_\xi)\Phi\|_{L^2(\mathbb{R}^d_\xi)} \tag{B.12}$$

Proof of Lemma B.1.1. See [29]. □

Then, applying Lemma B.1.1 for each integral in z and Plancherel's inequality, we end up with

$$\begin{aligned}
\int_0^T |\widehat{\rho}_\psi(t,k)|^2 dt \leq{}& \frac{2C_{d,s}}{|k|}\int_{\mathbb{R}_\xi} |\widehat{g}_0(k,\xi)\psi|^2 (1+|\xi|^2)^s d\xi \\
&+ 2C_{d,s}\frac{\lambda}{|k|}\int_0^T\int_{\mathbb{R}_\xi} \left|k^\alpha \widehat{E}(t,k,\xi)\psi\right|^2 (1+|\xi|^2)^s d\xi dt \\
&+ \frac{2C_{d,s}}{\lambda|k|}\int_0^T\int_{\mathbb{R}_\xi} \left|\widehat{Q}(t,k,\xi)\psi\right|^2 (1+|\xi|^2)^s d\xi dt \\
&\leq 2C_{d,s}\|\psi(\xi)(1+\xi^2)^{s/2}\|^2_{L^\infty(\mathbb{R}^d_\xi)} \left(\frac{1}{|k|}\int_{\mathbb{R}_\xi} |\widehat{g}_0(k,\xi)|^2 d\xi \right. \\
&\left. + \frac{\lambda}{|k|^{1-2|\alpha|}}\int_0^T\int_{\mathbb{R}_\xi} \left|\widehat{E}(t,k,\xi)\right|^2 d\xi dt + \frac{1}{\lambda|k|}\int_0^T\int_{\mathbb{R}_\xi} \left|\widehat{Q}(t,k,\xi)\right|^2 d\xi dt\right)
\end{aligned} \tag{B.13}$$

Let γ be such that $0 < \gamma < 1 - 2|\alpha|$. Then,

$$\begin{aligned}
\int_0^T |k|^\gamma |\widehat{\rho}_\psi(t,k)|^2 dt \leq{}& 2C_{d,s}\|\psi(\xi)(1+\xi^2)^{s/2}\|^2_{L^\infty(\mathbb{R}^d_\xi)} \left(\frac{1}{|k|^{1-\gamma}}\int_{\mathbb{R}_\xi} |\widehat{g}_0(k,\xi)|^2 d\xi \right. \\
&+ \frac{\lambda}{|k|^{1-2|\alpha|-\gamma}}\int_0^T\int_{\mathbb{R}_\xi} \left|\widehat{E}(t,k,\xi)\right|^2 d\xi dt \\
&\left. + \frac{1}{\lambda|k|^{1-\gamma}}\int_0^T\int_{\mathbb{R}_\xi} \left|\widehat{Q}(t,k,\xi)\right|^2 d\xi dt\right)
\end{aligned} \tag{B.14}$$

and we can integrate in k over the domain $\mathcal{D}_{k_0} = \left\{k \in \mathbb{R}^d_k \text{ such that } |k| > k_0, k_0 \in \mathbb{R}^{+*}\right\}$. We obtain

$$\begin{aligned}
\int_0^T |k|^\gamma |\widehat{\rho}_\psi(t,k)|^2 dt \leq{}& 2C_{d,s}\|\psi(\xi)(1+\xi^2)^{s/2}\|^2_{L^\infty(\mathbb{R}^d_\xi)} \left(\frac{1}{|k_0|^{1-\gamma}}\|g_0\|^2_{V_2} \right. \\
&\left. + \frac{\lambda}{|k_0|^{1-2|\alpha|-\gamma}}\|E\|^2_{L^2([0,T],V_2)} + \frac{1}{\lambda|k_0|^{1-\gamma}}\|Q\|^2_{L^2([0,T],V_2)}\right)
\end{aligned} \tag{B.15}$$

Let us denote

$$J(\lambda,k_0)=2C_{d,s}\|\psi(\xi)(1+\xi^2)^{s/2}\|^2_{L^\infty(\mathbb{R}^d_\xi)}\left(\frac{1}{|k_0|^{1-\gamma}}\|g_0\|^2_{V_2}\right.\\ \left.+\frac{\lambda}{|k_0|^{1-2|\alpha|-\gamma}}\|E\|^2_{L^2([0,T],V_2)}+\frac{1}{\lambda|k_0|^{1-\gamma}}\|Q\|^2_{L^2([0,T],V_2)}\right) \tag{B.16}$$

The function $J(\cdot,k_0)$ is continuous on $]0,+\infty[$, with

$$J(\lambda,k_0)\underset{\lambda\to 0}{\longrightarrow}+\infty,\quad J(\lambda,k_0)\underset{\lambda\to+\infty}{\longrightarrow}+\infty.$$

Then it admits a minimum in λ reached for $\lambda_{opt}(k_0)$, characterized by

$$\frac{dJ}{d\lambda}(\lambda_{opt}(k_0),k_0)=0. \tag{B.17}$$

The unique positive solution is

$$\lambda_{opt}(k_0)=\frac{\|Q\|_{L^2([0,T],V_2)}}{\|E\|_{L^2([0,T],V_2)}k_0^{|\alpha|}} \tag{B.18}$$

Thus,

$$\int_0^T\int_{\mathcal{D}_{k_0}}|k|^\gamma|\widehat{\rho}_\psi(t,k)|^2dkdt\le 2C_{d,s}\|\psi(\xi)(1+\xi^2)^{s/2}\|^2_{L^\infty(\mathbb{R}^d_\xi)}\left(\frac{1}{|k_0|^{1-\gamma}}\|g_0\|^2_{V_2}\right.\\ \left.+\frac{2}{|k_0|^{1-|\alpha|-\gamma}}\|Q\|_{L^2([0,T],V_2)}\|E\|_{L^2([0,T],V_2)}\right) \tag{B.19}$$

We also have

$$\int_0^T\int_{\mathbb{R}^N_k}|k|^\gamma|\widehat{\rho}_\psi(t,k)|^2dkdt=\int_0^T\int_{\mathcal{D}_{k_0}}|k|^\gamma|\widehat{\rho}_\psi(t,k)|^2dkdt\\ +\int_0^T\int_{\mathcal{B}_{k_0}}|k|^\gamma|\widehat{\rho}_\psi(t,k)|^2dkdt \tag{B.20}$$

with

$$\int_0^T\int_{\mathcal{B}_{k_0}}|k|^\gamma|\widehat{\rho}_\psi(t,k)|^2dkdt\le k_0^\gamma\int_0^T\int_{\mathbb{R}^N_k}|\widehat{\rho}_\psi(t,k)|^2dkdt \tag{B.21}$$

and

$$\int_0^T\int_{\mathbb{R}^N_k}|\widehat{\rho}_\psi(t,k)|^2dkdt\le\frac{3\|g_0\|^2_{V_2}}{2\lambda}\\ +3\left(\frac{\|Q(t,x,\xi)\|^2_{L^2([0,T],V_2)}}{\lambda^2}+\|\partial_\alpha E\|^2_{L^2([0,T],V_2)}\right) \tag{B.22}$$

Eventually,

$$\begin{aligned}\int_0^T \int_{\mathbb{R}_k^d} |\widehat{\rho}_\psi(t,k)|^2 dk dt \leq 2C_{d,s}\|\psi(\xi)(1+\xi^2)^{s/2}\|^2_{L^\infty(\mathbb{R}_\xi^d)} \left(\frac{1}{|k_0|^{1-\gamma}} \|g_0\|^2_{V_2} \right. \\ \left. + \frac{2}{|k_0|^{1-|\alpha|-\gamma}} \|Q\|_{L^2([0,T],V_2)} \|E\|_{L^2([0,T],V_2)} \right) \\ + 3k_0^\gamma \|\partial_\alpha E\|^2_{L^2([0,T],V_2)} + 3\|E\|^2_{L^2([0,T],V_2)} k_0^{2|\alpha|+\gamma} \\ + \frac{3}{2} \frac{\|g_0\|^2_{V_2} \|E\|_{L^2([0,T],V_2)}}{\|Q\|_{L^2([0,T],V_2)}} k_0^{|\alpha|+\gamma}\end{aligned} \tag{B.23}$$

Considering the upper bound above as a function of k_0, let us call it $L(k_0)$. The existence of the global minima is given by the fact that

$$L(k_0) \underset{k_0 \to 0}{\longrightarrow} +\infty, \quad L(k_0) \underset{k_0 \to +\infty}{\longrightarrow} +\infty$$

Since an analytical resolution of the optimization problem is not feasible, we give an estimation of it by asymptotic analysis, considering $\|E\|_{L^2([0,T],V_2)}$ small. We see here that the balance is between two constant terms, since

$$\begin{aligned} L(k_0) &= 2C_{d,s}\|\psi(\xi)(1+\xi^2)^{s/2}\|^2_{L^\infty(\mathbb{R}_\xi^d)} \left(\frac{1}{|k_0|^{1-\gamma}} \|g_0\|^2_{V_2} \right) + k_0^\gamma \|\partial_\alpha E\|^2_{L^2([0,T],V_2)} \\ &\quad + \mathrm{o}\left(\|E\|_{L^2([0,T],V_2)}\right) \\ &= K_1 \|g_0\|^2_{V_2} \frac{1}{|k_0|^{1-\gamma}} + K_2 k_0^\gamma \|\partial_\alpha E\|^2_{L^2([0,T],V_2)} + \mathrm{o}\left(\|E\|_{L^2([0,T],V_2)}\right) \\ &= L_2(k_0) + \mathrm{o}\left(\|E\|_{L^2([0,T],V_2)}\right). \end{aligned} \tag{B.24}$$

Therefore,

$$\underset{k_0}{\operatorname{argmin}}\, L_2 = \frac{1-\gamma}{\gamma} \frac{K_1}{K_2} \frac{\|g_0\|^2_{V_2}}{\|\partial_\alpha E\|^2_{L^2([0,T],V_2)}}. \tag{B.25}$$

Getting back to λ, we include the expression of the optimal k_0 in (B.18) and we have

$$\lambda_{opt} = \left(\frac{(1-\gamma)K_1}{\gamma K_2} \right)^\alpha \frac{\|Q\|_{L^2([0,T],V_2)} \|\partial_\alpha E\|^{2\alpha}_{L^2([0,T],V_2)}}{\|E\|_{L^2([0,T],V_2)} \|g_0\|^{2\alpha}_{V_2}}. \tag{B.26}$$

And the upper-bound of the error is

$$\begin{aligned}\int_0^T \int_{\mathbb{R}_k^d} |k|^\gamma |\widehat{\rho}_\psi(t,k)|^2 dk dt \leq K_2 \left(\frac{K_1}{K_2} \right)^\gamma \frac{(1-\gamma)^{\gamma-1}}{\gamma^\gamma} \|\partial_\alpha E\|^{2(1-\gamma)}_{L^2([0,T],V_2)} \|g_0\|^{2\gamma}_{V_2} \\ + \mathrm{o}\left(\|E\|_{L^2([0,T],V_2)}\right)\end{aligned} \tag{B.27}$$

B.2 Proof of Theorem 6.3.16

Applying the space Fourier transform to (6.121) leads to

$$\partial_t \widehat{g} + a(\xi)\cdot(ik)\widehat{g} + \lambda\widehat{g} = \lambda k^\alpha \widehat{E} - \widehat{Q}, \tag{B.28}$$

where $k^\alpha = \prod_{i=1}^N k_i^{\alpha_i}$. Solving this equation in the sense of distributions we get

$$\begin{aligned}\widehat{g}(t,k,\xi) &= \widehat{g}_0(k,\xi)e^{-(\lambda+ik\cdot a(\xi))t} \\ &\quad + \int_0^t e^{-(\lambda+ik\cdot a(\xi))s}\left(\lambda k^\alpha \widehat{E}(t-s,k,\xi) - \widehat{Q}(t-s,k,\xi)\right)ds\end{aligned} \tag{B.29}$$

Therefore, multiplying (B.29) by ψ and integrating in ξ we get

$$\begin{aligned}\widehat{\rho}_\psi(t,k) &= e^{-\lambda t}\int_{\mathbb{R}_\xi} e^{-ik\cdot a(\xi)t}\widehat{g}_0(k,\xi)\psi(\xi)d\xi \\ &\quad + \int_0^t e^{-\lambda s}\int_{\mathbb{R}_\xi} e^{-ik\cdot a(\xi)s}\left(\lambda k^\alpha \widehat{E}(s,k,\xi)\psi(\xi) - \widehat{Q}(t,k,\xi)\psi(\xi)\right)d\xi ds\end{aligned} \tag{B.30}$$

Let us define now the operator $\mathcal{G}$ which plays the role of the Fourier transform in x and ξ

$$\mathcal{G}(f)(k,v) = \int_{\mathbb{R}} e^{-ia(\xi)\cdot v}\widehat{f}(k,\xi)d\xi. \tag{B.31}$$

We can rewrite (B.30)

$$\widehat{\rho}_\psi(t,k) = e^{-\lambda t}\mathcal{G}(g_0\psi)(k,kt) + \int_0^t e^{-\lambda s}\mathcal{G}\left(\lambda\frac{\partial^\alpha E}{\partial x^\alpha}\psi - Q\psi\right)(t-s,k,ks)ds \tag{B.32}$$

Young's inequality provides

$$\begin{aligned}|\widehat{\rho}_\psi(t,k)|^2 &\le 2e^{-2\lambda t}|\mathcal{G}(g_0\psi)(k,kt)|^2 \\ &\quad + 2\left|\int_0^t e^{-\lambda s}\mathcal{G}\left(\lambda\frac{\partial^\alpha E}{\partial x^\alpha}\psi - Q\psi\right)(t-s,k,ks)ds\right|^2\end{aligned} \tag{B.33}$$

Then we use Cauchy Schwartz inequality with weight $e^{-\lambda t}$ to get

$$\begin{aligned}|\widehat{\rho}_\psi(t,k)|^2 &\le 2e^{-2\lambda t}|\mathcal{G}(g_0\psi)(k,kt)|^2 \\ &\quad + 2\left(\int_0^t e^{-\lambda s}ds\right)\int_0^t e^{-\lambda s}\left|\mathcal{G}\left(\lambda\frac{\partial^\alpha E}{\partial x^\alpha}\psi - Q\psi\right)(t-s,k,ks)\right|^2 ds\end{aligned} \tag{B.34}$$

We obtain

$$\begin{aligned}\int_0^T |\widehat{\rho}_\psi(t,k)|^2 dt \leq \;& 2\int_0^T e^{-2\lambda t}|\mathcal{G}(g_0\psi)(k,kt)|^2 dt \\ & + \frac{2}{\lambda}\int_0^T\int_0^t e^{-\lambda s}\left|\mathcal{G}\left(\lambda\frac{\partial^\alpha E}{\partial x^\alpha}\psi - Q\psi\right)(t-s,k,ks)\right|^2 ds dt \\ \leq \;& 2\int_0^T e^{-2\lambda t}|\mathcal{G}(g_0\psi)(k,kt)|^2 dt \\ & + \frac{2}{\lambda}\int_0^T\int_0^T e^{-\lambda s}\left|\mathcal{G}\left(\lambda\frac{\partial^\alpha E}{\partial x^\alpha}\psi - Q\psi\right)(\tau,k,ks)\right|^2 ds d\tau\end{aligned} \tag{B.35}$$

Using the estimate

$$\forall s \geq 0,\ e^{-\lambda s} \leq \frac{1}{1+\lambda^2 s^2}, \tag{B.36}$$

we can write

$$\begin{aligned}\int_0^T |\widehat{\rho}_\psi(t,k)|^2 dt \leq\; & 2\int_0^T \frac{1}{1+\lambda^2 t^2}\left|\mathcal{G}(g_0\psi)(k,kt)\right|^2 dt \\ & + \frac{2}{\lambda}\int_0^T\int_0^T \frac{1}{1+\lambda^2 s^2}\left|\mathcal{G}\left(\lambda\frac{\partial^\alpha E}{\partial x^\alpha}\psi - Q\psi\right)(\tau,k,ks)\right|^2 ds d\tau\end{aligned} \tag{B.37}$$

We proceed to the substitution $z = |k|t$ in the first integral and $z = |k|s$ in the second one.

$$\begin{aligned}\int_0^T |\widehat{\rho}_\psi(t,k)|^2 dt \leq\; & \frac{2}{|k|}\int_0^{|k|T} \frac{1}{1+\frac{\lambda^2 z^2}{|k|^2}}\left|\mathcal{G}(g_0\psi)(k,\frac{k}{|k|}z)\right|^2 dz \\ & + \frac{2}{\lambda|k|}\int_0^T\int_0^{|k|T} \frac{1}{1+\frac{\lambda^2 z^2}{|k|^2}}\left|\mathcal{G}\left(\lambda\frac{\partial^\alpha E}{\partial x^\alpha}\psi - Q\psi\right)(\tau,k,\frac{k}{|k|}z)\right|^2 ds d\tau \\ \leq\; & \frac{2}{|k|}\int_{-\infty}^{+\infty} \frac{1}{1+\frac{\lambda^2 z^2}{|k|^2}}\left|\mathcal{G}(g_0\psi)(k,\frac{k}{|k|}z)\right|^2 dz \\ & + \frac{2}{\lambda|k|}\int_0^T\int_{-\infty}^{+\infty} \frac{1}{1+\frac{\lambda^2 z^2}{|k|^2}}\left|\mathcal{G}\left(\lambda\frac{\partial^\alpha E}{\partial x^\alpha}\psi - Q\psi\right)(\tau,k,\frac{k}{|k|}z)\right|^2 ds d\tau\end{aligned} \tag{B.38}$$

Now let us recall the following lemma which gives an estimate of the oscillatory integral $\mathcal{G}$.

Lemma B.2.1. *Let $b : \mathbb{R} \to \mathbb{R}$ be a measurable function, and $\psi \in L^2(\mathbb{R})$. We assume that there exists a nondecreasing function h such that*

$$\forall u \in \mathbb{R}, \forall \epsilon > 0, \quad \int_{u<b(v)<u+\epsilon} |\psi(v)|^2 dv \leq f(\epsilon). \tag{B.39}$$

Then, for any $\gamma > 0$ and $f \in L^2(\mathbb{R})$,

$$\|\frac{1}{\sqrt{1+\gamma^2 z^2}}\int_{\mathbb{R}} e^{-izb(\xi)} f(\xi)\psi(\xi)\|^2_{L^2(z\in\mathbb{R})} \leq \frac{2\pi}{\gamma}\int_0^\infty e^{-t} h(\gamma t) dt \|f\|_{L^2(\mathbb{R})} \tag{B.40}$$

Proof of Lemma B.2.1. See [29]. □

We choose the function ψ such that

$$\forall \sigma \in \S^{N-1}, \forall u \in \mathbb{R}, \forall \epsilon > 0, \quad \int_{u<a(\xi)\cdot\sigma<u+\epsilon} |\psi(\xi)|^2 d\xi \leq K\epsilon^{\beta} \tag{B.41}$$

for some K and $0 < \beta \leq 1$. Then, applying Lemma B.2.1 with $\gamma = \frac{\lambda}{|k|}$, $b(\xi) = a(\xi) \cdot \frac{k}{|k|}$, $h(\epsilon) = K\epsilon^{\beta}$, we end up with

$$\begin{aligned}
\int_0^T |\widehat{\rho}_{\psi}(t,k)|^2 dt &\leq 4\pi K \int_{\mathbb{R}_\xi} |\widehat{g}_0(k,\xi)|^2 \, d\xi \frac{\lambda^{\beta-1}}{|k|^{\beta}} \\
&\quad + 4\pi K \int_0^T \int_{\mathbb{R}_\xi} \left| \lambda k^{\alpha} \widehat{E}(t,k,\xi) - \widehat{Q}(t,k,\xi) \right|^2 d\xi dt \\
&\leq 4\pi K \int_{\mathbb{R}_\xi} |\widehat{g}_0(k,\xi)|^2 \, d\xi \frac{\lambda^{\beta-1}}{|k|^{\beta}} \\
&\quad + 4\pi K \int_0^T \int_{\mathbb{R}_\xi} \lambda^2 k^{2\alpha} |\widehat{E}(t,k,\xi)|^2 + |\widehat{Q}(t,k,\xi)|^2 d\xi dt
\end{aligned} \tag{B.42}$$

Eventually we can write (since $k^{2\alpha} \leq |k|^{2|\alpha|}$)

$$\begin{aligned}
\int_0^T |\widehat{\rho}_{\psi}(t,k)|^2 dt &\leq 4\pi K \int_{\mathbb{R}_\xi} |\widehat{g}_0(k,\xi)|^2 \, d\xi \frac{\lambda^{\beta-1}}{|k|^{\beta}} \\
&\quad + 4\pi K \frac{\lambda^{\beta} |k|^{2|\alpha|}}{|k|^{\beta}} \int_0^T \int_{\mathbb{R}_\xi} |\widehat{E}(t,k,\xi)|^2 d\xi dt \\
&\quad + 4\pi K \frac{\lambda^{\beta-2}}{|k|^{\beta}} \int_0^T \int_{\mathbb{R}_\xi} |\widehat{Q}(t,k,\xi)|^2 d\xi dt
\end{aligned} \tag{B.43}$$

Let γ be such that $0 < \gamma \leq \beta - 2|\alpha|$. Then,

$$\begin{aligned}
\int_0^T |k|^{\gamma} |\widehat{\rho}_{\psi}(t,k)|^2 dt &\leq 4\pi K \int_{\mathbb{R}_\xi} |\widehat{g}_0(k,\xi)|^2 \, d\xi \frac{\lambda^{\beta-1}}{|k|^{\beta-\gamma}} \\
&\quad + 4\pi K \frac{\lambda^{\beta} |k|^{2|\alpha|+\gamma}}{|k|^{\beta}} \int_0^T \int_{\mathbb{R}_\xi} |\widehat{E}(t,k,\xi)|^2 d\xi dt \\
&\quad + 4\pi K \frac{\lambda^{\beta-2}}{|k|^{\beta-\gamma}} \int_0^T \int_{\mathbb{R}_\xi} |\widehat{Q}(t,k,\xi)|^2 d\xi dt
\end{aligned} \tag{B.44}$$

and we can integrate in k over the domain $\mathcal{D}_{k_0} = \left\{ k \in \mathbb{R}_k^d \text{ such that } |k| > k_0, k_0 \in \mathbb{R}^{+*} \right\}$.

We obtain

$$\begin{aligned}\int_0^T \int_{\mathcal{D}_{k_0}} |k|^\gamma |\widehat{\rho}_\psi(t,k)|^2 dkdt \leq 4\pi K \int_{\mathbb{R}_k}\int_{\mathbb{R}_\xi} |\widehat{g}_0(k,\xi)|^2 \, d\xi dk \frac{\lambda^{\beta-1}}{k_0^{\beta-\gamma}} \\ + 4\pi K \frac{\lambda^\beta k_0^{2|\alpha|+\gamma}}{k_0^\beta} \int_0^T \int_{\mathbb{R}_k}\int_{\mathbb{R}_\xi} |\widehat{E}(t,k,\xi)|^2 d\xi dkdt \\ + 4\pi K \frac{\lambda^{\beta-2}}{k_0^{\beta-\gamma}} \int_0^T \int_{\mathbb{R}_k}\int_{\mathbb{R}_\xi} |\widehat{Q}(t,k,\xi)|^2 d\xi dkdt\end{aligned} \tag{B.45}$$

Let us denote

$$\begin{aligned}J(\lambda,k_0) = 4\pi K \frac{\lambda^{\beta-1}}{k_0^{\beta-\gamma}} \int_{\mathbb{R}_k}\int_{\mathbb{R}_\xi} |\widehat{g}_0(k,\xi)|^2 \, d\xi dk \\ + 4\pi K \frac{\lambda^\beta k_0^{2|\alpha|+\gamma}}{k_0^\beta} \int_0^T \int_{\mathbb{R}_k}\int_{\mathbb{R}_\xi} |\widehat{E}(t,k,\xi)|^2 d\xi dkdt \\ + 4\pi K \frac{\lambda^{\beta-2}}{k_0^{\beta-\gamma}} \int_0^T \int_{\mathbb{R}_k}\int_{\mathbb{R}_\xi} |\widehat{Q}(t,k,\xi)|^2 d\xi dkdt\end{aligned} \tag{B.46}$$

The function $J(\cdot, k_0)$ is continuous on $]0,+\infty[$, with

$$J(\lambda,k_0) \underset{\lambda\to 0}{\longrightarrow} +\infty, \quad J(\lambda,k_0) \underset{\lambda\to+\infty}{\longrightarrow} +\infty.$$

Then it admits a minimum in λ reached for $\lambda_{opt}(k_0)$, caracterized by

$$\frac{dJ}{d\lambda}(\lambda_{opt},k_0) = 0. \tag{B.47}$$

The unique positive solution is

$$\lambda_{opt}(k_0) = \frac{(1-\beta)}{2\beta} \frac{\|g_0\|_{V_2}^2}{\|E\|^2_{L^2([0,T],V_2)} k_0^{2|\alpha|}} \left(1 + \sqrt{1 + \frac{4\beta(2-\beta)k_0^{2|\alpha|}}{(\beta-1)^2} \frac{\|Q\|^2_{L^2([0,T],V_2)}\|E\|^2_{L^2([0,T],V_2)}}{\|g_0\|^4_{V_2}}}\right) \tag{B.48}$$

Denoting

$$f(E,Q,k_0) = \left(1 + \sqrt{1 + \frac{4\beta(2-\beta)k_0^{2|\alpha|}}{(\beta-1)^2} \frac{\|Q\|^2_{L^2([0,T],V_2)}\|E\|^2_{L^2([0,T],V_2)}}{\|g_0\|^4_{V_2}}}\right), \tag{B.49}$$

with $f(E,Q,k_0) \underset{\|E\|_{L^2([0,T],V_2)}\to 0}{\longrightarrow} 2$, we end up with

$$\begin{aligned}
&\int_0^T \int_{\mathcal{D}_{k_0}} |k|^\gamma |\widehat{\rho}_\psi(t,k)|^2 dkdt \\
&\quad \leq 4\pi K \left(\frac{2\beta}{1-\beta}\right)^{1-\beta} f^{\beta-1}(E,Q,k_0) \|g_0\|_{V_2}^{2\beta} \|E\|_{L^2([0,T],V_2)}^{2(1-\beta)} k_0^{2\alpha(1-\beta)+\gamma-\beta} \\
&\quad + 4\pi K \left(\frac{1-\beta}{2\beta}\right)^{\beta} f^{\beta}(E,Q,k_0) \|g_0\|_{V_2}^{2\beta} \|E\|_{L^2([0,T],V_2)}^{2(1-\beta)} k_0^{2\alpha(1-\beta)+\gamma-\beta} \\
&\quad + 4\pi K \left(\frac{2\beta}{1-\beta}\right)^{2-\beta} f^{\beta-2}(E,Q,k_0) \frac{\|Q\|_{L^2([0,T],V_2)}^2}{\|g_0\|_{V_2}^{2(2-\beta)}} \|E\|_{L^2([0,T],V_2)}^{2(2-\beta)} k_0^{2\alpha(2-\beta)+\gamma-\beta}
\end{aligned} \tag{B.50}$$

We also have

$$\begin{aligned}
\int_0^T \int_{\mathbb{R}_k^N} |k|^\gamma |\widehat{\rho}_\psi(t,k)|^2 dkdt &= \int_0^T \int_{\mathcal{D}_{k_0}} |k|^\gamma |\widehat{\rho}_\psi(t,k)|^2 dkdt \\
&\quad + \int_0^T \int_{\mathcal{B}_{k_0}} |k|^\gamma |\widehat{\rho}_\psi(t,k)|^2 dkdt
\end{aligned} \tag{B.51}$$

with

$$\int_0^T \int_{\mathcal{B}_{k_0}} |k|^\gamma |\widehat{\rho}_\psi(t,k)|^2 dkdt \leq k_0^\gamma \int_0^T \int_{\mathbb{R}_k^N} |\widehat{\rho}_\psi(t,k)|^2 dkdt \tag{B.52}$$

and

$$\begin{aligned}
\int_0^T \int_{\mathbb{R}_k^N} |\widehat{\rho}_\psi(t,k)|^2 dkdt &\leq \frac{3\|g_0\|_{V_2}^2}{2\lambda} \\
&\quad + 3\left(\frac{\|Q(t,x,\xi)\|_{L^2([0,T],\mathbb{R}_x^d\times\mathbb{R}_\xi)}^2}{\lambda^2} + \|\partial_\alpha E\|_{L^2([0,T],V_2)}^2\right)
\end{aligned} \tag{B.53}$$

Eventually,

$$\begin{aligned}
&\int_0^T \int_{\mathbb{R}_k^N} |\widehat{\rho}_\psi(t,k)|^2 dk dt \\
&\quad \leq 4\pi K \left[\left(\frac{2\beta}{1-\beta} \right)^{1-\beta} f^{\beta-1}(E,Q,k_0) \|g_0\|_{V_2}^{2\beta} \|E\|_{L^2([0,T],V_2)}^{2(1-\beta)} k_0^{2\alpha(1-\beta)+\gamma-\beta} \right. \\
&\quad + \left(\frac{1-\beta}{2\beta} \right)^{\beta} f^{\beta}(E,Q,k_0) \|g_0\|_{V_2}^{2\beta} \|E\|_{L^2([0,T],V_2)}^{2(1-\beta)} k_0^{2\alpha(1-\beta)+\gamma-\beta} \\
&\quad \left. + \left(\frac{2\beta}{1-\beta} \right)^{2-\beta} f^{\beta-2}(E,Q,k_0) \frac{\|Q\|_{L^2([0,T],V_2)}^2}{\|g_0\|_{V_2}^{2(2-\beta)}} \|E\|_{L^2([0,T],V_2)}^{2(2-\beta)} k_0^{2\alpha(2-\beta)+\gamma-\beta} \right] \\
&\quad + 3k_0^{\gamma} \|\partial_\alpha E\|_{L^2([0,T],V_2)}^2 \\
&\quad + 3 \left(\frac{2\beta}{1-\beta} \right)^2 f(E,Q,k_0)^{-2} \frac{\|Q\|_{L^2([0,T],V_2)}^2}{\|g_0\|_{V_2}^4} k_0^{\gamma+4\alpha} \|E\|_{L^2([0,T],V_2)}^4 \\
&\quad + 3 \frac{\beta}{1-\beta} \frac{1}{\|g_0\|_{V_2}^2} f(E,Q,k_0)^{-1} k_0^{\gamma+2\alpha} \|E\|_{L^2([0,T],V_2)}^2
\end{aligned} \tag{B.54}$$

Considering the upper bound above as a function of k_0, let us call it $L(k_0)$. The existence of the global minima is given by the fact that

$$L(k_0) \underset{k_0 \to 0}{\longrightarrow} +\infty, \quad L(k_0) \underset{k_0 \to +\infty}{\longrightarrow} +\infty$$

Since an analytical resolution of the optimization problem is not feasible, we give an estimation of it by asymptotic analysis, considering $\|E\|_{L^2([0,T],V_2)}$ small. In that case, we can give an approximation of

$$\begin{aligned}
f(E,Q,k_0) &= \left(1 + \sqrt{1 + \frac{4\beta(2-\beta)k_0^{2|\alpha|}}{(\beta-1)^2} \frac{\|Q\|_{L^2([0,T],V_2)}^2 \|E\|_{L^2([0,T],V_2)}^2}{\|g_0\|_{V_2}^4}} \right) = 1 + \sqrt{1 + D\|E\|_{L^2([0,T],V_2)}^2} \\
&= 2 + \frac{D}{2} \|E\|_{L^2([0,T],V_2)}^2 + \mathrm{o}\left(\|E\|_{L^2([0,T],V_2)}^2 \right),
\end{aligned} \tag{B.55}$$

and thus

$$f^n(E,Q,k_0) = 2^n \left(1 + \frac{nD}{4} \|E\|_{L^2([0,T],V_2)}^2 \right), \quad \forall n \in \mathbb{R}^+. \tag{B.56}$$

Let us denote

$$K_1 = 3, \quad K_2 = 4\pi K \left(\frac{1-\beta}{\beta} \right)^{\beta} \|g_0\|_{V_2}^{2\beta} \left(1 + \frac{\beta}{1-\beta} \right)$$

$$\begin{aligned}
L(k_0) &= K_1 k_0^{\gamma} \|\partial_\alpha E\|_{L^2([0,T],V_2)}^2 + K_2 k_0^{2\alpha(1-\beta)+\gamma-\beta} \|E\|_{L^2([0,T],V_2)}^{2(1-\beta)} + \mathrm{o}\left(\|E\|_{L^2([0,T],V_2)}^{2(1-\beta)} \right) \\
&= L_2(k_0) + \mathrm{o}\left(\|E\|_{L^2([0,T],V_2)}^{2(1-\beta)} \right)
\end{aligned} \tag{B.57}$$

The optimisation of L_2 with respect to k_0 leads to

$$\begin{aligned}\underset{k_0}{\operatorname{argmin}} L_2 &= \left(\frac{(2\alpha(1-\beta)+\gamma-\beta)K_2}{\gamma K_1}\frac{\|E\|^{2(1-\beta)}_{L^2([0,T],V_2)}}{\|\partial_\alpha E\|^2_{L^2([0,T],V_2)}}\right)^{\frac{1}{\beta-2\alpha(1-\beta)}} \\ &= K_3\left(\frac{\|E\|^{2(1-\beta)}_{L^2([0,T],V_2)}}{\|\partial_\alpha E\|^2_{L^2([0,T],V_2)}}\right)^{\frac{1}{\beta-2\alpha(1-\beta)}}\end{aligned} \tag{B.58}$$

And finally,

$$\min L_2 = \left(K_1K_3^{\gamma}+K_2K_3^{2\alpha(1-\beta)+\gamma-\beta}\right)\|\partial_\alpha E\|^2_{L^2([0,T],V_2)}\left(\frac{\|E\|^{2(1-\beta)}_{L^2([0,T],V_2)}}{\|\partial_\alpha E\|^2_{L^2([0,T],V_2)}}\right)^{\frac{\gamma}{\beta-2\alpha(1-\beta)}} \tag{B.59}$$

Moreover, we can state that the optimal λ should be close to

$$\lambda_{opt} \approx \frac{1-\beta}{2\beta}\|g_0\|^2_{V_2}\left(\frac{\|\partial_\alpha E\|^{4\alpha}_{V_2}}{\|E\|^{2\beta}_{L^2([0,T],V_2)}}\right)^{\frac{1}{\beta-2|\alpha|(1-\beta)}} \tag{B.60}$$

Bibliography

[1] E. Audusse. *Modelisation hyperbolique et analyse numerique pour les ecoulements en eaux peu profondes.* PhD thesis, Université Pierre et Marie Curie - Paris VI, 2004.

[2] E. Audusse. A multilayer saint-venant model: derivation and numerical validation. *Discrete Contin. Dyn. Syst. Ser. B*, 5(2):189–214, 2005.

[3] E. Audusse, F. Bouchut, M.-O. Bristeau, R. Klein, and B. Perthame. A fast and stable well-balanced scheme with hydrostatic reconstruction for Shallow Water flows. *SIAM J. Sci. Comput.*, 25(6):2050–2065, 2004.

[4] E. Audusse, F. Bouchut, M.-O. Bristeau, R. Klein, and B. Perthame. A fast and stable well-balanced scheme with hydrostatic reconstruction for shallow water flows. *SIAM J. Sci. Comput.*, 25(6):2050–2065, June 2004.

[5] E. Audusse and M.-O. Bristeau. Transport of pollutant in shallow water flows : A two time steps kinetic method. *ESAIM: M2AN*, 37(2):389–416, 2003.

[6] E. Audusse and M.-O. Bristeau. A well-balanced positivity preserving second-order scheme for shallow water flows on unstructured meshes. *J. Comput. Phys.*, 206(1):311–333, 2005.

[7] E. Audusse and M.-O. Bristeau. Finite-volume solvers for a multilayer saint-venant system. *Int. J. Appl. Math. Comput. Sci.*, 17(3):311–320, October 2007.

[8] E. Audusse, M.-O. Bristeau, and A Decoene. Numerical simulations of 3d free surface flows by a multilayer saint-venant model. *International journal for numerical methods in fluids*, 56(3):331–350, 2008.

[9] E. Audusse, M-O Bristeau, M. Pelanti, and J. Sainte-Marie. Approximation of the hydrostatic navier–stokes system for density stratified flows by a multilayer model: Kinetic interpretation and numerical solution. *Journal of Computational Physics*, 230(9):3453–3478, 2011.

[10] E. Audusse, M.-O. Bristeau, B. Perthame, and J. Sainte-Marie. A multilayer saint-venant system with mass exchanges for shallow water flows. derivation and numerical

validation. *ESAIM: Mathematical Modelling and Numerical Analysis*, 45(01):169–200, 2011.

[11] D. Auroux and J. Blum. Back and forth nudging algorithm for data assimilation problems. *Comptes Rendus Mathematique*, 340(12):873–878, 2005.

[12] D. Auroux and J. Blum. Back and forth nudging algorithm for data assimilation problems. *Comptes Rendus Mathematique*, 340(12):873 – 878, 2005.

[13] D. Auroux, J. Blum, et al. A nudging-based data assimilation method: the back and forth nudging (bfn) algorithm. *Nonlinear Processes in Geophysics*, 15:305–319, 2008.

[14] D. Auroux and M. Nodet. The back and forth nudging algorithm for data assimilation problems : theoretical results on transport equations. *ESAIM: Control, Optimisation and Calculus of Variations*, 18:318–342.

[15] S.-D. Ayata, M. Lévy, O. Aumont, A. Sciandra, J. Sainte-Marie, A. Tagliabue, and O. Bernard. Phytoplankton growth formulation in marine ecosystem models: should we take into account photo-acclimation and variable stochiometry in oligotrophic areas? *Journal of Marine Systems*, 2012.

[16] M. Baklouti, F. Diaz, C. Pinazo, V. Faure, and B. Queguiner. Investigation of mechanistic formulations depicting phytoplankton dynamics for models of marine pelagic ecosystems and description of a new model. *Progress in Oceanography*, 71(1):1–33, 2006.

[17] C. Bardos and O. Pironneau. A formalism for the differentiation of conservation laws. *Comptes Rendus Mathematique*, 335(10):839–845, 2002.

[18] C. Bardos and O. Pironneau. Data assimilation for conservation laws. *Methods and Applications of Analysis*, 12(2):103–134, 2005.

[19] A.-J.-C. Barré de Saint-Venant. Théorie du mouvement non permanent des eaux, avec application aux crues des rivières et à l'introduction des marées dans leur lit. *Comptes Rendus des Séances de l'Académie des Sciences. Paris.*, 73:147–154, 1871.

[20] R.E. Bellman. *Dynamic Programming*. Princeton University Press, 1957.

[21] A. Bensoussan. *Filtrage optimal des systèmes linéaires*. Dunod, 1971.

[22] O. Bernard. Hurdles and challenges for modelling and control of microalgae for co2 mitigation and biofuel production. *Journal of Process Control*, 21(10):1378 – 1389, 2011.

[23] O. Bernard and J.-L. Gouzé. Transient behavior of biological loop models, with application to the Droop model. *Mathematical Biosciences*, 127(1):19–43, 1995.

[24] O. Bernard and J.-L. Gouzé. Global qualitative behavior of a class of nonlinear biological systems: application to the qualitative validation of phytoplankton growth models. *Artif. Intel.*, 136:29–59, 2002.

[25] C. Bertoglio, D. Chapelle, M.A. Fernández, J-F. Gerbeau, and P. Moireau. State observers of a vascular fluid-structure interaction model through measurements in the solid. *Comput. Meth. Appl. Mech. Engrg*, 256(2013):149–168, 2011.

[26] J. Blum, F.-X. Le Dimet, and I. M. Navon. Data assimilation for geophysical fluids. In R. Temam and J. Tribbia, editors, *Handbook of Numerical Analysis: Computational Methods for the Atmosphere and the Oceans*. Elsevier, 2008.

[27] P. Bonneton, E. Barthelemy, F. Chazel, R. Cienfuegos, D. Lannes, F. Marche, and M. Tissier. Recent advances in serre–green naghdi modelling for wave transformation, breaking and runup processes. *European Journal of Mechanics-B/Fluids*, 30(6):589–597, 2011.

[28] F. Bouchut. An introduction to finite volume methods for hyperbolic conservation laws. In *ESAIM: Proceedings*, volume 15, pages 1–17, 2005.

[29] F. Bouchut and L. Desvillettes. Averaging lemmas without time fourier transform and application to discretized kinetic equations. In *Proceedings of the Royal Society of Edinburgh-A-Mathematics*, volume 129, pages 19–36. Cambridge Univ Press, 1999.

[30] F. Bouchut, V. Zeitlin, et al. A robust well-balanced scheme for multi-layer shallow water equations. *Discrete and Continuous Dynamical Systems-Series B*, 13(4):739–758, 2010.

[31] A.-C. Boulanger and J. Sainte-Marie. Analytical solutions for the free surface hydrostatic Euler equations. *Commun. Math. Sci.*, 11(4):993–1010, 2013.

[32] J.-F. Bourgat, P. Le Tallec, F. Mallinger, B. Perthame, and Y. Qiu. Coupling boltzmann and navier-stokes. Research Report RR-2281, INRIA, 1994. Projet MENUSIN.

[33] J. Boussinesq. Théorie de l'intumescence liquide appelée onde solitaire ou de translation se propageant dans un canal rectangulaire. *Comptes Rendus Acad. Sci (Paris)*, 72:755–759, 1871.

[34] Y. Brenier. Homogeneous hydrostatic flows with convex velocity profiles. *Nonlinearity*, 12(3):495–512, 1999.

[35] H. Brézis. *Functional Analysis, Sobolev Spaces and Partial Differential Equations*, volume XIV of *Universitext*. Springer, 2010.

[36] M.-O. Bristeau, N Goutal, and J. Sainte-Marie. Numerical simulations of a non-hydrostatic shallow water model. *Computers and Fluids*, 47(1):51 – 64, 2011.

[37] M.-O. Bristeau and J. Sainte-Marie. Derivation of a non-hydrostatic shallow water model; Comparison with Saint-Venant and Boussinesq systems. *DCDS(B)*, 10(4):733–759, 2008.

[38] M. Castro, J. Macías, and C. Parés. A q-scheme for a class of systems of coupled conservation laws with source term. application to a two-layer 1-d shallow water system. *ESAIM: Mathematical Modelling and Numerical Analysis*, 35(01):107–127, 2001.

[39] M.J. Castro, J.A. Garcıa-Rodrıguez, J.M. González-Vida, J. Macıas, C. Parés, and M.E. Vázquez-Cendón. Numerical simulation of two-layer shallow water flows through channels with irregular geometry. *Journal of Computational Physics*, 195(1):202–235, 2004.

[40] V. Casulli. A semi-implicit finite difference method for non-hydrostatic, free-surface flows. *International Journal for Numerical Methods in Fluids*, 30(4):425–440, 1999.

[41] C. Cercignani. *The Boltzmann equation*. Springer, 1988.

[42] D. Chapelle, N. Cîndea, M. de Buhan, and P. Moireau. Exponential convergence of an observer based on partial field measurements for the wave equation. *Mathematical Problems in Engineering*, (581053):1–12, 2012.

[43] D. Chapelle, N. Cîndea, and P. Moireau. Improving convergence in numerical analysis using observers - the wave-like equation case. *Mathematical Models and Methods in Applied Sciences*, 22, 2012. In press, doi:10.1142/S0218202512500406.

[44] D. Chapelle, M. Fragu, V. Mallet, and P. Moireau. Fundamental principles of data assimilation underlying the verdandi library: applications to biophysical model personalization within euheart. *Medical & Biological Eng & Computing*, pages 1–13, 2012.

[45] Y. Chisti. Biodiesel from microalgae. *Biotechnology Advances*, 25:294–306, 2007.

[46] D. Christodoulou. The euler equations of compressible fluid flow. *Bulletin of the American Mathematical Society*, 44(4):581–602, 2007.

[47] J.-M. Coron. *Control and nonlinearity*, volume 136. American Mathematical Soc., 2009.

[48] G.P. Cressman. An operational objective analysis system. *Monthly Weather Review*, 87(10):367–374, 1959.

[49] C.M. Dafermos. *Hyperbolic conservation laws in continuum physics*, volume 325. Springer Verlag, 2005.

[50] A. Decoene, L. Bonaventura, E. Miglio, and F. Saleri. Asymptotic derivation of the section-averaged shallow water equations for natural river hydraulics. *Mathematical Models and Methods in Applied Sciences*, 19(03):387–417, 2009.

[51] R.J. DiPerna, P.-L. Lions, and Y. Meyer. Lp regularity of velocity averages. In *Annales de l'institut Henri Poincaré (C) Analyse non linéaire*, volume 8, pages 271–287. Gauthier-Villars, 1991.

[52] M.R. Droop. Vitamin B_{12} and marine ecology. IV. the kinetics of uptake growth and inhibition in *Monochrysis lutheri*. *J. Mar. Biol. Assoc.*, 48(3):689–733, 1968.

[53] M.R. Droop. 25 years of algal growth kinetics, a personal view. *Botanica marina*, 16:99–112, 1983.

[54] R.C. Dugdale. Nutrient limitation in the sea: dynamics, identification and significance. *Limnol. Oceanogr.*, 12:685–695, 1967.

[55] A. Ern, S. Piperno, and K. Djadel. A well-balanced runge–kutta discontinuous galerkin method for the shallow-water equations with flooding and drying. *International journal for numerical methods in fluids*, 58(1):1–25, 2008.

[56] S. Esposito, V. Botte, D. Iudicone, and M. Ribera d'Alcala. Numerical analysis of cumulative impact of phytoplankton photoresponses to light variation on carbon assimilation. *J Theor Biol*, 261(3):361–371, 2009.

[57] P.G. Falkowski and J.A. Raven. *Aquatic photosynthesis*. Biology-earth science. Princeton University Press, 2007.

[58] S. Ferrari and F. Saleri. A new two-dimensional shallow water model including pressure effects and slow varying bottom topography. *ESAIM: Mathematical Modelling and Numerical Analysis*, 38(02):211–234, 2004.

[59] T. Gallouët, J.-M. Hérard, and N. Seguin. Some approximate godunov schemes to compute shallow-water equations with topography. *Computers & Fluids*, 32(4):479–513, 2003.

[60] R.J. Geider, H.L. MacIntyre, and T.M. Kana. A dynamic regulatory model of phytoplanktonic acclimation to light, nutrients, and temperature. *Limnol Oceanogr*, 43:679–694, 1998.

[61] J.-F. Gerbeau and B. Perthame. Derivation of viscous saint-venant system for laminar shallow water; numerical validation. *Discrete and Continuous Dynamical Systems-series B*, 1:89–102, 2001.

[62] E. Godlewski and P.A. Raviart. *Numerical approximation of hyperbolic systems of conservation laws*, volume 118. Springer, 1996.

[63] F. Golse, P.-L. Lions, B. Perthame, and R. Sentis. Regularity of the moments of the solution of a transport equation. *Journal of functional analysis*, 76(1):110–125, 1988.

[64] F. Golse, B. Perthame, and R. Sentis. Un resultat de compacite pour les equations de transport et application au calcul de la valeur propre principale de i'operateur de transport cr acad sc. *T*, 301:l, 1985.

[65] F. Golse, B. Perthame, and R. Sentis. Un résultat de compacité pour l'équation de transport et application au calcul de la valeur propre principale d'un opérateur de transport. *R. Acad. Sc, 301, 341*, 344, 1985.

[66] A.E. Green and P.M. Naghdi. A derivation of equations for wave propagation in water of variable depth. *Journal of Fluid Mechanics*, 78(02):237–246, 1976.

[67] J.M. Greenberg and A.-Y. Leroux. A well-balanced scheme for the numerical processing of source terms in hyperbolic equations. *SIAM Journal on Numerical Analysis*, 33(1):1–16, 1996.

[68] E. Grenier. On the derivation of homogeneous hydrostatic equations. *ESAIM: Mathematical Modelling and Numerical Analysis*, 33(05):965–970, 1999.

[69] J. U. Grobbelaar, C. J. Soeder, and E. Stengel. Modeling algal productivity in large outdoor cultures and waste treatment systems. *Biomass*, 21:297–314, 1990.

[70] H. Guterman, A. Vonshak, and S. Ben-Yaakov. A macromodel for outdoor algal mass production. *Biotechnology & Bioengineering*, 35(8):809–819, 1990.

[71] G. Haine and K. Ramdani. Reconstructing initial data using observers. *Numer Math*, pages 1–37, August 2011.

[72] B.P. Han. Photosynthesis-irradiance response at physiological level: a mechanistic model. *Journal of Theoretical Biology*, 213(2):121–127, 2001.

[73] B.P. Han. A mechanistic model of algal photoinhibition induced by photodamage to photosystem-ii. *Journal of theoretical biology*, 214(4):519–527, FEB 21 2002.

[74] J.-M. Hervouet. *Hydrodynamics of Free Surface Flows: Modelling With the Finite Element Method*. John Wiley & Sons, 2007.

[75] J.E. Hoke and R.A. Anthes. The initialization of numerical models by a dynamic-initialization technique(fluid flow models for wind forecasting). *Monthly Weather Review*, 104:1551–1556, 1976.

[76] David D Houghton and Akira Kasahara. Nonlinear shallow fluid flow over an isolated ridge. *Communications on Pure and Applied Mathematics*, 21(1):1–23, 1968.

[77] D. L. Huggins, R. H. Piedrahita, and T. Rumsey. Analysis of sediment transport modeling using computational fluid dynamics (cfd) for aquaculture raceways. *Aquacultural Engineering*, 31(3-4):277–293, 2004.

[78] D. L. Huggins, R. H. Piedrahita, and T. Rumsey. Use of computational fluid dynamics (cfd) for aquaculture raceway design to increase settling effectiveness. *Aquacultural Engineering*, 33(3):167–180, 2005.

[79] P.-E. Jabin and B. Perthame. Regularity in kinetic formulations via averaging lemmas. *ESAIM: Control, Optimisation and Calculus of Variations*, 8:761–774, 2002.

[80] S. C. James and V. Boriah. Modeling algae growth in an open-channel raceway. *J Comput Biol*, 17(7):895–906, 2010.

[81] S. Jin. A steady-state capturing method for hyperbolic systems with geometrical source terms. *ESAIM: Mathematical Modelling and Numerical Analysis*, 35(04):631–645, 2001.

[82] T. Katsaounis and C. Makridakis. Relaxation models and finite element schemes for the shallow water equations. In *Hyperbolic Problems: Theory, Numerics, Applications*, pages 621–631. Springer, 2003.

[83] B. Khobalatte and B. Perthame. Maximum principle on the entropy and minimal limitations for kinetic schemes. Research Report RR-1628, INRIA, 1992. Projet MENUSIN.

[84] B. Khobalatte and B. Perthame. Maximum principle on the entropy and second-order kinetic schemes. *mathematics of computation*, 62(205):119–131, 1994.

[85] D. J. Korteweg and G. de Vries. Xli. on the change of form of long waves advancing in a rectangular canal, and on a new type of long stationary waves. *The London, Edinburgh, and Dublin Philosophical Magazine and Journal of Science*, 39(240):422–443, 1895.

[86] M. D. Kruskal and N. J. Zabusky. Exact invariants for a class of nonlinear wave equations. *Journal of Mathematical Physics*, 7:1256, 1966.

[87] K. Lange and F. J. Oyarzun. The attractiveness of the Droop equations. *Math. Biosci.*, 111(2):261–278, 1992.

[88] P. D. Lax. Integrals of nonlinear equations of evolution and solitary waves. *Communications on pure and applied mathematics*, 21(5):467–490, 1968.

[89] F.-X. Le Dimet and O. Talagrand. Variational algorithms for analysis and assimilation of meteorological observations: theoretical aspects. *Tellus A*, 38(2):97–110, 2010.

[90] A.-Y. Leroux. Riemann solvers for some hyperbolic problems with a source term. In *ESAIM: Proceedings*, volume 6, pages 75–90, 1999.

[91] R.J. LeVeque. Balancing source terms and flux gradients in high-resolution godunov methods: the quasi-steady wave-propagation algorithm. *Journal of computational physics*, 146(1):346–365, 1998.

[92] R.J. LeVeque. *Finite volume methods for hyperbolic problems*, volume 31. Cambridge university press, 2002.

[93] T. Levi-Civita. Determination rigoureuse des ondes permanentes d'ampleur finie. *Mathematische Annalen*, 93(1):264–314, 1925.

[94] P.L. Lions, B. Perthame, and E. Tadmor. A kinetic formulation of multi-dimensional scalar conservation laws and related equations. *Journal of the American Mathematical Society*, 7(1):169–192, 1994.

[95] K. Liu. Locally distributed control and damping for the conservative systems. *SIAM J. Control Optim.*, 35(5):1574–1590, 1997.

[96] D.G. Luenberger. *Determining the State of a Linear with Observers of Low Dynamic Order*. PhD thesis, Stanford University, 1963.

[97] D.G. Luenberger. An introduction to observers. *IEEE Transactions on Automatic Control*, 16:596–602, 1971.

[98] H.-P. Luo and M.H. Al-Dahhan. Analyzing and modeling of photobioreactors by combining first principles of physiology and hydrodynamics. *Biotechnology & Bioengineering*, 85(4):382–393, 2004.

[99] I. MacDonald, M.J. Baines, N.K. Nichols, and P.G. Samuels. Comparisons of some steady state saint-venant solvers for some test problems with analytic solutions. *Numerical Analysis Report*, 2:95, 1995.

[100] I. MacDonald, M.J. Baines, N.K. Nichols, and P.G. Samuels. Steady open channel test problems with analytic solutions. *Numerical analysis report*, 3:95, 1995.

[101] F. Marche. Derivation of a new two-dimensional viscous shallow water model with varying topography, bottom friction and capillary effects. *European Journal of Mechanics-B/Fluids*, 26(1):49–63, 2007.

[102] F.B. Metting. Biodiversity and application of microalgae. *Journal of Industrial Microbiology & Biotechnology*, 17:477 – 489, 1996.

[103] P. Moireau, D. Chapelle, and P. Le Tallec. Filtering for distributed mechanical systems using position measurements: Perspectives in medical imaging. *Inverse Problems*, 25(3):035010 (25pp), 2009.

[104] I.M. Navon. Data assimilation for numerical weather prediction : a review. In S.K. Park and L. Xu, editors, *Data Assimilation for Atmospheric, Oceanic, and Hydrologic Applications*, volume XVIII. Springer, 2009.

[105] C. Parés and M. Castro. On the well-balance property of roe's method for nonconservative hyperbolic systems. applications to shallow-water systems. *ESAIM: mathematical modelling and numerical analysis*, 38(05):821–852, 2004.

[106] L Pawlowski. *Modelisation de l'incorporation du carbone photosynthetique en environnement marin pilote par ordinateur*. PhD thesis, Paris VI University, 2004.

[107] J. C. H. Peeters and P. Eilers. The relationship between light intensity and photosynthesis: a simple mathematical model. *Hydrobiol. Bull.*, 12:134–136, 1978.

[108] M. Pelanti, F. Bouchut, and A. Mangeney. A roe-type scheme for two-phase shallow granular flows over variable topography. *ESAIM: Mathematical Modelling and Numerical Analysis*, 42(05):851–885, 2008.

[109] I. Perner, C. Posten, and J. Broneske. Cfd-aided optimization of a plate photobioreactor for cultivation of microalgae. *Chemie Ingenieur Technik*, 74:865– 869, 2002.

[110] I. Perner-Nochta and C. Posten. Simulations of light intensity variation in photobioreactors. *Journal of Biotechnology*, 131:276– 285, 2007.

[111] B. Perthame. Boltzmann type schemes for gas dynamics and the entropy property. *SIAM Journal on Numerical Analysis*, 27(6):1405–1421, 1990.

[112] B. Perthame. *Kinetic formulation of conservation laws*. Oxford lecture series in mathematics and its applications. Oxford University Press, 2002.

[113] B. Perthame. Mathematical tools for kinetic equations. *Bulletin of the American Mathematical Society*, 41(2):205–244, 2004.

[114] B. Perthame. *Growth, reaction, movement and diffusion from biology*. February 2012.

[115] B Perthame and C Simeoni. A kinetic scheme for the saint-venant system with a source term. *Calcolo*, 38(4):201–231, 2001.

[116] B. Perthame and P.E. Souganidis. A limiting case for velocity averaging. In *Annales Scientifiques de l'Ecole Normale Supérieure*, volume 31, pages 591–598. Elsevier, 1998.

[117] B. Perthame and E. Tadmor. A kinetic equation with kinetic entropy functions for scalar conservation laws. *Comm. Math. Phys*, pages 501–517, 1991.

[118] J. Pruvost, L. Pottier, and J. Legrand. Numerical investigation of hydrodynamic and mixing conditions in a torus photobioreactor. *Chemical Engineering Science*, 61:4476–4489, 2006.

[119] A.J. Pullan, N.P. Smith, and P.J. Hunter. An anatomically based model of transient coronary blood flow in the heart. *SIAM Journal on Applied mathematics*, 62(3):990–1018, 2002.

[120] D.I. Pullin. Direct simulation methods for compressible inviscid ideal-gas flow. *Journal of Computational Physics*, 34(2):231–244, 1980.

[121] K. Ramdani, M. Tucsnak, and G. Weiss. Recovering the initial state of an infinite-dimensional system using observers. *Automatica*, 46(10):1616–1625, 2010.

[122] L.F. Richardson and S. Chapman. *Weather prediction by numerical process*. Dover publications New York, 1965.

[123] A. Ritter. Die fortpflanzung de wasserwellen. *Zeitschrift Verein Deutscher Ingenieure*, 36(33):947–954, 1892.

[124] L. Rodolfi, G. C. Zittelli, N. Bassi, G. Padovani, N. Biondi, G. Bonini, and M. R. Tredici. Microalgae for Oil: Strain Selection, Induction of Lipid Synthesis and Outdoor Mass Cultivation in a Low-Cost Photobioreactor. *Biotechnol. Bioeng.*, 102(1):100–112, 2009.

[125] R. Rosello Sastre, Z. Coesgoer, I. Perner-Nochta, P. Fleck-Schneider, and C. Posten. Scale-down of microalgae cultivations in tubular photo-bioreactors - a conceptual approach. *Journal of Biotechnology*, 132:127– 133, 2007.

[126] J. Sainte-Marie. Vertically averaged models for the free surface euler system. derivation and kinetic interpretation. *Math. Models Methods Appl. Sci. (M3AS)*, 21(3):459–490, 2011.

[127] R.H. Sanders and K.H. Prendergast. The possible relation of the 3-kiloparsec arm to explosions in the galactic nucleus. *The Astrophysical Journal*, 188:489–500, 1974.

[128] A. Sciandra and P. Ramani. The limitations of continuous cultures with low rates of medium renewal per cell. *J. Exp. Mar. Biol. Ecol.*, 178:1–15, 1994.

[129] K. Sompech, Y. Chisti, and T. Srinophakun. Design of raceway ponds for producing microalgae. *Biofuels*, 3(4):387–397, 2012.

[130] D.R. Stauffer, R. David, and J.-W. BAO. Optimal determination of nudging coefficients using the adjoint equations. *Tellus A*, 45(5):358–369, 1993.

[131] D.R. Stauffer and N.L. Seaman. Use of four-dimensional data assimilation in a limited-area mesoscale model. part i: Experiments with synoptic-scale data. *Monthly Weather Review*, 118(6):1250–1277, 1990.

[132] J.J. Stoker. The formation of breakers and bores the theory of nonlinear wave propagation in shallow water and open channels. *Communications on Pure and Applied Mathematics*, 1(1):1–87, 1948.

[133] J.J. Stoker. *Water waves: The mathematical theory with applications*. Wiley-Interscience, 2011.

[134] A.D. Stroock, S.K.W. Dertinger, A. Ajdari, I. Mezić, H.A. Stone, and G.M. Whitesides. Chaotic mixer for microchannels. *Science*, 295(5555):647–651, 2002.

[135] A. Sukenik, P.G. Falkowski, and J. Bennett. Potential enhancement of photosynthetic energy conversion in algal mass culture. *Biotechnology & Bioengineering*, 30(8):970–977, 1987.

[136] A. Sukenik, R.S. Levy, Y. Levy, P.G. Falkowski, and Z. Dubinsky. Optimizing algal biomass production in an outdoor pond: a simulation model. *Journal of Applied Phycology*, 3:191–201, 1991.

[137] R. Temam. *Navier-Stokes equations: theory and numerical analysis*, volume 343. Oxford University Press, 2001.

[138] W. C. Thacker. Some exact solutions to the nonlinear shallow-water wave equations. *Journal of Fluid Mechanics*, 107(1):499–508, 1981.

[139] E.F. Toro. *Riemann solvers and numerical methods for fluid dynamics: a practical introduction*. Springer, 2009.

[140] C. Vejrazka, M. Janssen, M. Streefland, and R. H. Wijffels. Photosynthetic efficiency of chlamydomonas reinhardtii in flashing light. *Biotechnology and Bioengineering*, 108(12):2905–2913, 2011.

[141] A. Vidard, F.-X. Le Dimet, and A. Piacentini. Optimal determination of nudging coefficients. *Tellus Series A: Dynamic meteorology and oceanography*, 55(1):1–15, 2003.

[142] G.B. Whitham. *Linear and nonlinear waves*, volume 42. Wiley-interscience, 2011.

[143] R.H. Wijffels and M.J. Barbosa. An outlook on microalgal biofuels. *Science*, 329(5993):796–799, 2010.

[144] P. J. B. Williams and L. M. L. Laurens. Microalgae as biodiesel and biomass feedstocks: Review and analysis of the biochemistry, energetics and economics. *Energy Environ. Sci.*, 3:554–590, 2010.

[145] X. Zou, I.M. Navon, and F.-X. LeDimet. An optimal nudging data assimilation scheme using parameter estimation. *Quarterly Journal of the Royal Meteorological Society*, 118(508):1163–1186, 1992.